A study of microviscosity in liquid crystals using laser tweezers

A thesis submitted to the University of Manchester for the degree of

Doctor of Philosophy

in the Faculty of Engineering and Physical Sciences

2012

Jennifer Louise Sanders

School of Physics and Astronomy

Contents

Final word count: 40,021

List of Figures

List of Tables

Nomenclature

Symbol	Definition	Unit	Page

Latin Symbols

Symbol	Definition	Unit	Page
A	Area	m	68
$\mathtt{A}$	Natural logarithmic ratio of dynamic viscosity		149
$\mathbb{A}$	Amplitude of displacement function	m	131
a	Coefficient of weighting factor ζ		149
B	Magnetic field amplitude	T	67
$\mathbf{B}$	Magnetic field vector	T	67
b	coefficient of weighting factor ζ		149
$\mathtt{C}$	Normalisation constant of Gaussian distribution $G(x)$		74
CP	Centre point	pixels	121
c	Speed of light	m / s	67
D_0	Free diffusion coefficient	m^2 / s	82
d	Diameter	m	68
d_T	Diameter of trapping beam	m	108
d_i	Image distance	m	112
d_o	Object distance	m	112
E	Electric field amplitude	V / m	67
$\mathbf{E}$	Electric field vector	V / m	67

Symbol	*Definition*	*Unit*	*Page*
E	Energy	J	67
E_r	Ericksen number		95
$\mathbf{E}_{th}$	Threshold electric field vector	V / m	95
$\mathbf{F}_v$	Micrometer reading of neutral density filter	mm	122
$\mathbf{F}$	Total trapping force; $\mathbf{F}_{scat} + \mathbf{F}_{grad}$	N	70
$\mathbf{F}_B$	Thermal force	N	72
$\mathbf{F}_S$	Stokes' viscous drag force	N	72
$\mathbf{F}_T$	Optical trapping force	N	72
$\mathbf{F}_{esc}$	Escape force; minimum force required to cause a particle to escape from an optical trap	N	174
$\mathbf{F}_{grad}$	Gradient force	N	68
$\mathbf{F}_{max}$	Maximum optical trapping force	N	174
$\mathbf{F}_{scat}$	Scattering force	N	68
$\mathcal{F}_d$	Frank free energy density	J / m^3	94
$\mathcal{F}_{el}$	Elastic energy	J	96
$\mathcal{F}_s$	Surface anchoring energy	J	96
f	Frequency	Hz	67
f_c	Corner frequency	Hz	77
f_{eff}	Effective focal length	m	109
f_{obj}	Focal length of microscope objective lens	m	109
G(x)	Gaussian distribution		74
g	Acceleration due to gravity	m / s^2	85
H$_i$	Hermite polynomial (order i)		42
H(x)	Position histogram		74
HG$_{mn}$	Hermite-Gaussian beam (radial and azimuthal mode indices m,n)		42
HM$_m$	Helical Mathieu beam (order m)		43

Symbol	Definition	Unit	Page
h	Planck's constant	m^2 kg / s	67
h	Thickness	m	88
I	Intensity	W / m^2	68
I	Current	A	122
I_{th}	Threshold intensity	W / m^2	95
J$_m$	Bessel beam (order m)		42
K_i	Frank elastic constant, $i = 1, 2, 3$; splay, twist, bend	N	94
k_{B}	Boltzmann's constant	kg m^2 / s^2	73
L$_{pl}$	Laguerre polynomial (radial and azimuthal mode indices p, l)		42
LG$_{pl}$	Laguerre-Gaussian beam (radial and azimuthal mode indices p, l)		41
ℓ	Combined thickness of immersion oil and coverslip		109
M	Magnification		121
m	Mass	kg	72
m_{g}	Mass of glycerol	kg	150
m_{w}	Mass of water	kg	150
N	Number of reflectance spectra maxima		100
NA	Numerical Aperture		107
n	Refractive index		61
n_{e}	Extraordinary refractive index		88
n_{m}	Refractive index of medium		69
n_{o}	Ordinary refractive index		88
n_{p}	Refractive index of particle		69
$\hat{n}$	Liquid crystal director		88
P	Probability density		73
P	Power	W	68

Symbol	Definition	Unit	Page
$\mathbf{P}$	Polarisation density	A s / m^2	90
P_{rad}	Radiation pressure	kg / m s^2	67
P_{T}	Optical trapping power	W	122
p	Momentum	kg m / s	67
p_i	Pixel value 0 – 255 (black – white)		120
Q	Optical trapping efficiency		84
q	Lens translation	m	112
R	Fresnel reflection coefficient		69
Re	Reynold's number		52
r	Radius	m	72
$\mathbf{S}$	Poynting vector	W / m^2	68
$\langle S \rangle$	Time-averaged $\mathbf{S}$; irradiance	W / m^2	68
S_0	Initial value of power spectrum	m^2 / Hz	77
$S_{\text{B}}(f)$	Power spectrum due to Brownian motion	m^2 / Hz	77
S_{c}	Power at corner frequency f_{c} and half of S_0	m^2 / Hz	77
S_{ii}	Sum of squares of pixels, $i = x, y, z$	pixels^2	120
$S_x(f)$	Power spectrum of $\mathbf{x}(t)$	m^2 / Hz	77
$S_{\text{v}}(f)$	Uncalibrated power spectrum	V^2 / Hz	115
T	Absolute temperature	K or °C	73
T	Fresnel transmission (refraction) coefficient		69
T_{c}	Clearing temperature of liquid crystal; temperature of anisotropic-isotropic liquid crystal transition	°C	89
U	Potential	J	73
V	Volume	m^3	85
V_{g}	Volume of glycerol	m^3	150
V_{w}	Volume of water	m^3	150

Symbol	*Definition*	*Unit*	*Page*
V	Detector signal	V	115
v	Shear flow	cP	91
$\mathbf{v}$	Velocity	m / s	72
$\mathbf{v}_{\text{esc}}$	Escape velocity; velocity of surrounding fluid, or sample stage, when a particle is released from an optical trap	m / s	174
v_∞	Velocity scale	m / s	95
W	Anchoring energy	J / m^2	96
$\mathbf{X}(f)$	Fourier transform of $\mathbf{x}(t)$	Hz	77
X, Y	Pixel co-ordinates	pixels	120
x_0	Optical trap centre or equilibrium position	m	74
$\mathbf{x}$	Displacement vector	m	72
$\mathbf{x}_{\text{max}}$	Maximum displacement from optical trap centre	m	174
$\langle x^2 \rangle$	Positional variance	m^2	73
$\langle x(t+\tau)x(t) \rangle$	Autocorrelation function (ACF) of $x(t)$	m^2	80
$\langle \Delta x^2(\tau) \rangle$	Mean square displacement (MSD) of $x(t)$	m^2	82
Z_{T}	Trap depth	m	83

Greek Symbols

α	One-half angular aperture of objective	° or rad	107
α_i	Leslie coefficient, $i = 1, 2, ...5$		90
β	Detector sensitivity	V / m	115
γ	Viscous drag coefficient	N s / m	72
γ_i	Rotational viscosity coefficient, $i = 1, 2$		93
$\gamma_\parallel$	Lateral drag coefficient	N s / m	83
$\gamma_\perp$	Axial drag coefficient	N s / m	83

Symbol	*Definition*	*Unit*	*Page*
$\Delta\varepsilon$	Dielectric anisotropy		90
$\Delta\vartheta$	Phase difference between light rays emerging from a birefringent material	° or rad	89
Δn	Birefringence; $n_\mathrm{e} - n_\mathrm{o}$		88
$\Delta\mathbf{p}$	Momentum change	kg m / s	70
δn	Refractive index between particle and medium		185
ε	Material permittivity		90
ε_0	Permittivity of free space	$\mathrm{A}^2\ \mathrm{s}^4$ / kg m^3	67
$\varepsilon_\parallel$	Material permittivity parallel to $\hat{n}$		90
$\varepsilon_\perp$	Material permittivity perpendicular to $\hat{n}$		90
ζ	Dynamic viscosity weighting factor		149
η	Dynamic fluid viscosity	N s / m^2	72
η_i	Mięsowicz coefficients, $i = 1, 2, 3$		91
η_g	Dynamic viscosity of glycerol	cP	149
η_w	Dynamic viscosity of water	cP	149
η_wg	Dynamic viscosity of water–glycerol mixture	cP	149
$\eta_\mathrm{eff}^\parallel$	Effective viscosity parallel to $\hat{n}$	cP	91
$\eta_\mathrm{eff}^\perp$	Effective viscosity perpendicular to $\hat{n}$	cP	91
θ	Angle of $\hat{n}$ relative to shear flow v	° or rad	91
ϑ	Angle of incidence of a light ray impinging on the surface of a particle	° or rad	70
κ	Optical trap stiffness	N / m	72
λ	Wavelength	m	67
μ_0	Permeability of free space	m kg / $\mathrm{s}^2\ \mathrm{A}^2$	67
μ_x, μ_y	Particle centroid co-ordinates	m	120
∇v	Shear flow gradient	cP	91
ν	Flow viscosity	cP	98

Symbol	Definition	Unit	Page
ν_{wg}	Kinematic viscosity of water–glycerol mixture	$\mathrm{m^2 / s}$	150
ξ_{a}	Surface anchoring parameter		96
ρ	Density	$\mathrm{kg / m^3}$	85
ρ_{g}	Density of glycerol	$\mathrm{kg / m^3}$	150
ρ_{w}	Density of water	$\mathrm{kg / m^3}$	150
ρ_{wg}	Density of water–glycerol mixture	$\mathrm{kg / m^3}$	150
σ	Standard deviation	$[units]$	74
σ^2	Variance	$[units]^2$	74
τ	Correlation time	s	80
τ_{c}	Decay, corner or trap relaxation time	s	80
ϕ	Angle of $\hat{n}$ relative to shear flow gradient ∇v	° or rad	91
φ	Angle of refraction of a light ray refracted at the surface of a particle	° or rad	70
Φ_{m}	Mass fraction		149
χ_{e}	Electric susceptibility		89
ω	Oscillation frequency	Hz	131

Units

cP	CentiPoise	10^{-3} Pa s	97
uu	User units (Position reading in *StageControl.vi*)		114

Acronyms

ACF	Autocorrelation function	$\mathrm{m^2}$	80
AFM	Atomic Force Microscope / Microscopy		47

Symbol	*Definition*	*Unit*	*Page*
AOD	Acousto-optic Deflector		45
BFP(I)	Back Focal Plane (Interferometry)		79
CCD	Charge-Coupled Devide		107
CGH	Computer Generated Hologram		44
CMOS	Complementary Metal Oxide Semiconductor		107
CoM	Centre of mass		119
DLL	Dynamic-Link Library		120
DOE	Diffractive Optical Element		44
DPSS	Diode Pumped Solid State		103
EF	Escape Force		174
EOD	Electro-optic Deflector		45
EQ	Equipartition		128
FIONA	Fluorescence Imaging with One Nanometer Accuracy		57
GO	Geometrical Optics		144
HG	Hermite-Gaussian		42
HM	Helical Mathieu		43
HOTs	Holographic Optical Tweezers		46
HSVM	High Speed Video Microscopy		117
IPA	Isopropyl alcohol		100
IR	Infrared		38
LC	Liquid Crystal		58
LCD	Liquid Crystal Display		59
LCE	Liquid Crystal Emulsion		60
LG	Laguerre-Gaussian		41
LOC	Lab-on-a-chip		51
µTAS	Micro Total Analytical Systems		52

Symbol	*Definition*	*Unit*	*Page*
MDT	Microfluidic Diagnostic Technology		52
MSD	Mean Square Displacement	m^2	82
MWNT	Multi-Walled Nanotube		49
NA	Numerical Aperture		107
Nd:YVO$_4$	Neodymium Doped Yttrium Orthovanadate		103
NDF	Neutral Density Filter		105
NIR	Near-Infrared		38
NLC	Nematic Liquid Crystal		59
NSOM	Near-field Scanning Optical Microscope / Microscopy		57
OAM	Orbital Angular Momentum		40
ODP	Optically Driven Pump		49
OFM	Optofluidic Microscope / Microscopy		57
OFT	Optical Fréedericksz Transition		95
OTMS	Octadecyltrimethoxysilane (Silane)		99
PDMS	Poly(dimethylsiloxane)		46
pN	pico-Newton	N	68
POC	Point-of-care		52
PS	Polystyrene (bead)		73
PSD	Power Spectral Density	m^2 / Hz	77
PSF	Point Spread Function		46
PSU	Power Supply Unit		122
PVA	Polyvinyl alcohol		99
QPD	Quadrant Photodiode		115
RBC	Red Blood Cell		55
RNAP	RNA Polymerase		55
RO	Ray Optics		68

Symbol	*Definition*	*Unit*	*Page*
ROI	Region of Interest		119
SAM	Spin Angular Momentum		40
SC	Silica (bead) made of borosilicate or soda lime glass		98
SERS	Surface-Enhanced Raman Scattering		53
SLM	Spatial Light Modulator		40
SNR	Signal-to-Noise Ratio		124
SP	Surface Plasmon		58
SWNT	Single-Walled Nanotube		49
TEM_{00}	Fundamental transverse laser mode		70
VD	Viscous Drag		131
WG	Water–Glycerol		148

The University of Manchester

ABSTRACT OF THESIS submitted by Jennifer Louise Sanders
for the Degree of Doctor of Philosophy and entitled
A study of microviscosity in liquid crystals using laser tweezers. April 2012

The dynamic response characteristics of a liquid crystal (LC) device are dependent upon its viscosity coefficients which are particularly important for optimising LC devices. Micron-sized polystyrene and silica particles are dispersed in two nematic LC mixtures; MLC-6648 and MLC-6609, with homeotropic and planar alignment. The microfluidic behaviour of the LC is investigated using a computer-controlled laser tweezing system, where particle tracking is performed using high-speed video microscopy. Laser tweezers rely upon momentum conservation and radiation pressure exerted by light to manipulate and rotate micron-size particles and cells, including *E.coli*, DNA, dielectric colloids in a selection of media, such as water and liquid crystals. The technique can measure picoNewton (pN) forces with pN accuracy. The laser tweezing system is built around a commerically available, inverted optical microscope and employs an Nd:YVO$_4$ laser operating at a wavelength λ of $1064\,\mathrm{nm}$. Prior to performing any measurements in LCs, power, position and trap stiffness calibration in three dimensions is completed using both active and passive techniques. The laser tweezing system is initially used for microviscometry measurements in water–glycerol (WG) mixtures with varying glycerol concentration since the relationship between viscosity and glycerol concentration is well characterised. Both active and passive methods are employed to determine the effective viscosity coefficients parallel and perpendicular to the LC director $\hat{n}$; $\eta_{\mathrm{eff}}^{\parallel}$ and $\eta_{\mathrm{eff}}^{\perp}$, respectively. Measurements are made in the low Reynolds and Ericksen number regimes, where viscosity is described by Stokes' law and reorientation of $\hat{n}$ is considered negligible. The anisotropic nature of the LC's viscosity is successfully observed using active and passive microviscometry. As expected, for both MLC-6648 and MLC-6609, $\eta_{\mathrm{eff}}^{\perp} > \eta_{\mathrm{eff}}^{\parallel}$ for cells with both homeotropic and planar alignment. Values are in good agreement with the bulk flow viscosities quoted by the manufacturer and, in the case of MLC-6648, are consistent with measurements made using laser tweezers under the same conditions. For MLC-6609, the data deviate when comparing with values published in the literature. However, those values were measured using a shear flow measurement technique not in the low Ericksen number regime. Factors affecting measurement of η_{eff} in LCs using laser tweezers are discussed, including reorientation of $\hat{n}$ due to the trapping laser beam, anchoring of $\hat{n}$ at the particle surface and accuracy of particle tracking. The results illustrate that system's capability to detect microscopic changes in anisotropic viscosity of LCs through observation of the dynamics of optically trapped particles.

Declaration

No portion of the work referred to in this thesis has been submitted in support of an application for another degree or qualification of this or any other university or other institution of learning.

Copyright

(i) The author of this thesis (including any appendices and/or schedules to this thesis) owns certain copyright or related rights in it (the "Copyright") and she has given The University of Manchester certain rights to use such Copyright, including for administrative purposes.

(ii) Copies of this thesis, either in full or in extracts and whether in hard or electronic copy, may be made **only** in accordance with the Copyright, Designs and Patents Act 1988 (as amended) and regulations issued under it or, where appropriate, in accordance with licensing agreements which the University has from time to time. This page must form part of any such copies made.

(iii) The ownership of certain Copyright, patents, designs, trade marks and other intellectual property (the "Intellectual Property") and any reproductions of copyright works in the thesis, for example graphs and tables ("Reproductions"), which may be described in this thesis, may not be owned by the author and may be owned by third parties. Such Intellectual Property and Reproductions cannot and must not be made available for use without the prior written permission of the owner(s) of the relevant Intellectual Property and/or Reproductions.

(iv) Further information on the conditions under which disclosure, publication and commercialisation of this thesis, the Copyright and any Intellectual Property and/or Reproductions described in it may take place is available in the University IP Policy[1], in any relevant Thesis restriction declarations deposited in the University Library, The University Library's regulations[2] and in The University's policy on Presentation of Theses.

---

[1] URL: www.campus.manchester.ac.uk/medialibrary/researchoffice/graduate education/g-pres-theses-pgr.pdf

[2] URL: www.manchester.ac.uk/library/aboutus/regulations

Jennifer Louise Sanders   31

Quotes

"*Mini Me, stop humping the "laser".*"

"*You know, I have one simple request. And that is to have sharks with frickin' laser beams attached to their heads!*"

<div align="right">

Dr. Evil in *Austin Powers* (1997 & 1999)

</div>

Mr. Potato Head: *Hey, a laser! How come **you** don't have a laser, Woody?*
Woody: *It's not a laser! It's a little light bulb that blinks!*
Hamm: *What's with him?*
Mr. Potato Head: *Laser envy.*

<div align="right">

Toy Story (1995)

</div>

"*If I were creating the world I wouldn't mess about with butterflies and daffodils. I would have started with lasers, eight o'clock, Day One!*"

<div align="right">

Evil in *Time Bandits* (1981)

</div>

Sheldon: *In 1917 when Albert Einstein established the theoretic foundation for the laser in his paper "Zur Quantentheorie der Strahlung"* [1], *his fondest hope was that the resultant device be bitchin'.*
Zack: *Mission accomplished.*

<div align="right">

Big Bang Theory: The Lunar Excitation (#3.23, 2010)

</div>

"*We shall call you Laser Jen! POW POW!*"

<div align="right">

Jennifer Gupta and Nadya Kunawicz
of *JBCA, The University of Manchester* (2008)

</div>

☞ **bitchin'** [**bich-***uhn*] ***adjective***, *slang*
meaning: wonderful, marvellous, spectacularly good

Acknowledgments

For those who know me, this thesis has been a long time coming, perhaps in excess of 26 years, depending on your point of view. And there are so many people in my life that have made it possible and helped along the way that I would like to thank and acknowledge; most definitely more than I am able to mention here, but I shall make an attempt.

First and foremost, I would like to express my sincere gratitude to my supervisor, Dr. Mark Dickinson, for the support during the PhD, for his patience, motivation, enthusiasm and expert knowledge. I am deeply indebted to Prof. Helen Gleeson, who provided so much help, motivation and invaluable contribution throughout the research and writing of this thesis. I also wish to acknowledge the funding provided by EPSRC.

I would like to express my appreciation for the expertise, assistance and facilities provided by Prof. Miles Padgett, Head of the Optics group at the University of Glasgow, and his team including Richard Bowman and Graham Gibson. Thank you to Manchester's Nonlinear and Liquid Crystal Physics Group, past and present; Nicholas Roberts, Thomas Cronin, Paul Brimicombe, Simon Siemianowski, Yiming Yang and Sarabjot Kaur, for being so welcoming and incredibly helpful with all things liquid crystal. Thank you to Andrew Harrison for his guidance, words of advice and expert proof-reading. Oh, and for increasing the optical trapping expertise two-fold merely by his arrival into the Photon Science Institute (PSI) at Manchester.

Nadya Kunawicz and Jennifer Gupta; thank you for all the fun demonstrating times in first year lab and just for being awesome! Thank you to everyone in the Photon Physics research group, past and present, especially to Stuart Stubbs, Graham Dinsdale, Colin Mercer, James Sanders (hey bro!), Sarah Jhumka and

Daniel Espinobarro. A very special thank you to Matt Davies. A special thank you to Alexander Knight-Percival, for so many things, including all his wonderful help with LabVIEW and my general ignorance; and Matthew Harvey, Ben Cowsill, Timothy Butters, Phil Stewart, Cecilia Choi and Oleg Aslanidi for providing such wonderful company in and/or outside of my windowless lab. I am thankful to Amy Freund for her kind words and thoughtful nature. Thank you to the Jodrell Bank Centre for Astrophysics research group, specifically Nadya Kunawicz, Jennifer Gupta, Mike Peel, Paul Woods and Dave Jones; for allowing my infiltration into JBCA; JBCAles, albeit as an imposter, was so much fun!

Everybody needs a little help from their friends and I am so grateful to have such wonderful friends; Hussein Farook, Rainbow Ho, Janice Cheng, Sarah Keith, Stephen Beebee, and Terry and Yan Chiu. Thank you to Andrew Abu-Muharib, Claire Dooley and Stephen Gallagher; a.k.a. 'The Clique', for their invaluable friendship and for the ridiculous amount of laughs these past two years, and hopefully many more to come. You have been wonderful friends, especially during the crazy days of writing the thesis! To Rakan Sleiman; thank you, for everything.

And last, but by no means least, my family. All this would have been impossible without my absolute best friends; Mom, Dad, my siblings Victoria, James and Johnathan, my brother-in-law Simon and my beautiful nephew Lucas James. Their unwavering confidence in me has been my constant inspiration and their unconditional love, my greatest strength.

Dedication

For my wonderful parents.

Supporting Work

Sanders, J.L., Gleeson, H.F., Yang, Y. and Dickinson, M.R., Pushing, pulling and twisting liquid crystal systems; exploring new directions with laser manipulation (2012), INVITED PAPER, TALK GIVEN BY H.F. GLEESON, Royal Society Meeting: New frontiers in anisotropic fluid-particle composites. Discussion meeting paper to be published in *Philosophical Transactions of the Royal Society A: Mathematical, Physical and Engineering Sciences* (proof shown in Appendix B).

Sanders, J.L., Gleeson, H.F. and Dickinson, M.R., A study of microviscosity of liquid crystals using laser tweezers (2012), Royal Society Meeting: New frontiers in anisotropic fluid-particle composites, POSTER PRESENTATION.

Sanders, J.L., Dickinson, M.R. and Gleeson, H.F., Laser tweezers for determining anisotropic local shear viscosity coefficients of nematic liquid crystals, *Proc. SPIE* **7762**, 776221 (2010) ORAL AND POSTER PRESENTATION, AND CONFERENCE PROCEEDING PAPER DOI: 10.1117/12.862853.

Sanders, J.L., Dickinson, M.R. and Gleeson, H.F., *Laser tweezers and anisotropic viscosity of nematic liquid crystals*, International Symposium 'Frontiers in Photon Science', Manchester, UK (Oct 2010) POSTER PRESENTATION.

Sanders, J.L., Dickinson, M.R. and Gleeson, H.F., *Nematic liquid crystal anisotropic viscosity and laser tweezers*, Photon10, Southampton, UK (Aug 2010) POSTER PRESENTATION.

Chapter 1

Introduction

Optical trapping, as a means to manipulate and study micron-sized dielectric particles, has advanced significantly since the first steps towards the technology were taken more than 40 years ago by Arthur Ashkin [2]. Since the successful demonstration of the first single-beam optical trap for dielectric particles by Ashkin *et al.* in 1986 [3], '*laser tweezers*' — the popular name when referring to optical trapping — have become one of the most popular techniques employed for manipulating such particles and determining their characteristics, resulting in the proliferation of further innovative optical trapping technologies. The range of laser tweezing applications is rapidly growing, with the current focus on biological and microanalytical systems as well as the integration of laser tweezers with already well established investigative techniques [4].

This chapter aims to establish the historial background of optical trapping, giving a brief synopsis of the relevant literature and popular research methods. It also endeavours to ultimately identify how the research in this thesis can contribute to the fields of optical trapping, microfluidics and liquid crystal physics, and address some of the unanswered questions.

1.1   Historical background

Conventional laser tweezers employ the radiation pressure created by a tightly focussed laser beam impinging on the surface of microscopic particles. However,

even before the use of the word '*laser*' by Gordon Gould in a 1959 conference paper [5] and construction of the first laser — a ruby laser — by Theodore Maiman in 1960 [6], two publications in 1901 by Lebedev [7], and Nichols and Hull [8] provided independent demonstrations of the existence of radiation pressure using a focussed arc lamp [9, 10].

It was Arthur Ashkin who pioneered optical manipulation whilst working at Bell Telephone Laboratories during the 1970s and 1980s where he used transparent particles in transparent media to observe and employ radiation pressure. Ashkin's first paper in 1969 [2], in which he demonstrates light-guided particle motion due to radiation pressure, established the field of optical trapping. The experiment was relatively simple; illuminating a sample of $10\,\mu m$ transparent latex spheres suspended in water using a weakly focussed, few-mW Argon ion laser beam with a wavelength of $514.5\,nm$ and a Gaussian beam profile.

A host of publications subsequently followed [11–18], including the levitation of particles as described in a paper by Ashkin and Diedzic in 1971 [11], in which the beam was inverted such that the radiation pressure was balanced by the force due to gravity, and optical levitation of charged and neutral liquid droplets [13]. Ultimately, the 1986 paper by Ashkin *et al.* [3] cemented the field of optical trapping with the demonstration of the first single-beam 3D optical trap, i.e. complete 3D confinement in the axial *and* transverse directions. Compared with the low index lenses used up until this point, colloids of glass, polystyrene and silica ($\sim 25\,nm - 10\,\mu m$) dispersed in water were trapped using a high numerical aperture microscope objective lens. A popular implementation of laser tweezers based on Ashkin's early experiments is shown in Fig. 1.1.

Ashkin soon recognised the potential of optical trapping for biological applications and, in a 1987 paper with Diedzic [19], used laser tweezers to manipulate viruses and bacterica, including *Escherichia coli*, also using an Argon ion laser beam with a wavelength of $514.5\,nm$. However, it was soon realised visible light was easily absorbed by biological samples leading to their optical damage (termed '*opticution*') but absorb weakly in the near-infrared (NIR) region of the electromagnetic spectrum. So, in a second 1987 paper, Ashkin, Dziedzic and Yamane [20] employed an Nd:YAG infrared laser to significantly reduce optical damage of living cells. This wavelength range is now typical in biological applications of optical trapping. [10]
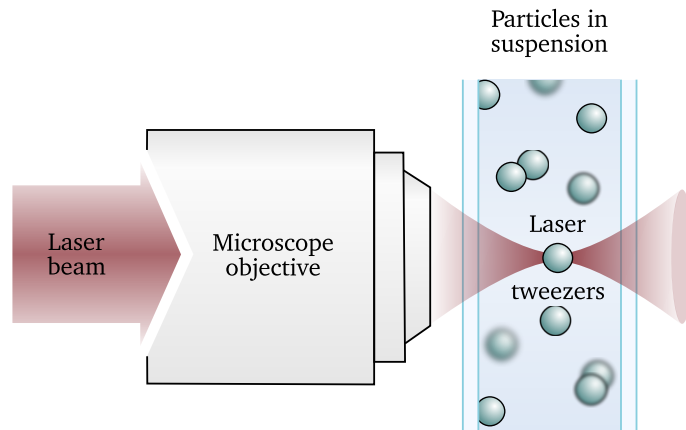
Figure 1.1: A popular implementation of laser tweezers; a tightly focussed laser beam using a microscope objective lens with a high numerical aperture to optically trap particles in suspension.

The field of optical trapping soon began to expand and a multitude of publications ensued. Further details of the history and development of optical trapping can be found in comprehensive reviews by McGloin [9], Padgett, Molloy and McGloin [10] and Ashkin himself [21].

1.2 Current state of laser tweezers

Further research into the development or application of laser tweezers has seen phenomenal interest; at the time of writing, Ashkin's original 1970 paper [2] had over 1,900 citations and his 1986 paper [3] being cited almost 3,000 times! In addition, several publications exist geared towards undergraduates understanding and experimenting with optical tweezers [22–27], illustrating the acceptance of the technique into mainstream optics.

In June 2010, marking more than a century of related research[7, 8], a book providing a comprehensive introduction to the theory, methods and applications of laser tweezers was published. *Optical Tweezers: Methods and Applications* by Padgett, Molloy and McGloin [10] comprises reprints of approximately 60 landmark publications and refers to more than 400 pieces of related literature.

The scope of achievements with laser tweezers continues to expand as the technique progresses alongside and in partnership with contemporary technology. At the start of 2011, a publication detailed the use of an Apple iPad — a thin,

tablet computer controlled via a multi-touch display — to control multiple particles with laser tweezers [28]. The *iTweezers* interface can wirelessly control a computer which hosts and runs the optical trapping software, hence overcoming the limitations of mouse-based interfaces. At the end of 2011, researchers in Germany developed a microscopic heat engine; a Stirling engine, whose piston mechanism is powered by an optically trapped particle, as described in the *Nature Physics* publication by Blickle and Bechinger [29].

The start of 2012 has already seen the '*nanoear*'; a trapped 60 nm gold nanoparticle as an acoustic receiver. Ohlinger et al. [30] introduced sound waves to the surrounding liquid media by either heating surrounding gold nanoparticles or via a loudspeaker, and observed the effect on the nanoparticle's position fluctuations and their frequency response.

1.3   Novel beams for optical manipulation

Higher order beams, which have been employed in laser tweezers with some interesting results, are usually referred to as '*optical vortices*' [31] often generated using a spatial light modulator (SLM), producing a plethora of different beam modes. Some popular novel beams are described below and shown in Fig. 1.2.

As described in a comprehensive journal article by Yao and Padgett [33], rotating light beams possess angular momentum. An important distinction exists depending on their rotation as they propagate: if every polarization vector rotates, the light possesses *spin* angular momentum (SAM); if the phase structure rotates, the light has *orbital* angular momentum (OAM), whose magnitude can be many times greater than the spin. It was recognised that, like spin, OAM should be quantised in units of $\hbar$ per photon. It is emphasised that the angular momentum arises from the light surrounding the singularity at the centre, not the singularity itself. For circularly polarised light, the intrinsic spin of each photon is aligned giving an angular momentum of $\sigma\hbar$ per photon, where $\sigma = \pm 1$ for left and right handed polarisation, respectively [34]. It is possible to derive the quantisation of spin and orbital angular momentum using Maxwell's equations. In most cases, they remain distinct quantities. The ability to produce beams which carry OAM in a standard optics laboratory has been a realisation in the

(a) **Laguerre-Gaussian beams**

LG$_{00}$ LG$_{01*}$ LG$_{10}$ LG$_{01}$ LG$_{03}$

(b) **Hermite-Gaussian beams**

HG$_{00}$ HG$_{01}$ HG$_{02}$ HG$_{10}$ HG$_{22}$

(c) **Bessel beams**

J$_0$

(d) **Helical Mathieu beams**

HM$_0$ HM$_2$ HM$_6$ HM$_9$ HM$_{12}$
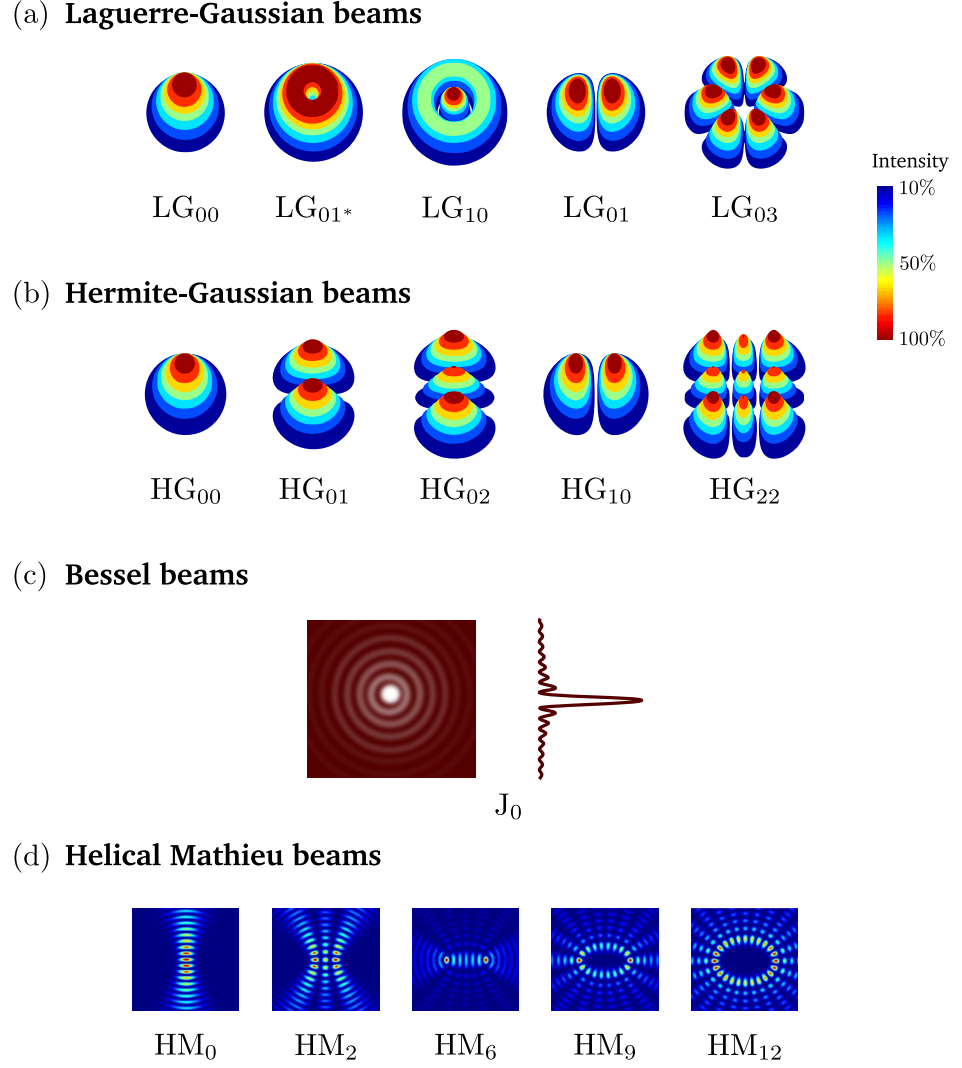
Figure 1.2: Intensity distribution of novel beams for optical trapping. (a) Laguerre-Gaussian LG$_{pl}$ beams, (b) Hermite-Gaussian HG$_{mn}$ beams — where the fundamental mode of both LG and HG beams is a Gaussian beam TEM$_{00}$ — (c) Bessel beams J$_m$, and (d) Helical Mathieu HM$_m$ beams [32].

last 20 years [33].

Laguerre-Gaussian beams

Laguerre-Gaussian (LG) beams are circularly symmetric beams with higher order transverse modes and possess an OAM of $l\hbar$ per photon [34]. Each mode LG$_{pl}$ (whose radial electric field is proportional to the product of a Gaussian and an

associated Laguerre polynominal L_{pl} [35]) is characterised by a radial mode index p, which determines the radial structure, and an azimuthal mode index l, giving an OAM of $l\hbar$ per photon to describe its phase structure or *helicity* [33, 36]. They have helical wavefronts, annular intensity profiles and carry an orbital angular momentum which, as shall be seen later in Section 1.5.1, is why they are often used for rotating trapped particles [37].

LG beams, a selection of which are shown in Fig. 1.2, have been used to improve axial trapping [38] and to trap low index particles [39] such that rather than being repelled, they are confined to the centre of the beam; the area devoid of light. LG modes with $l = 0$ and $p > 0$, resulting in a single intensity minima at the centre, are referred to as '*doughnut*' modes as illustrated by LG_{01*} in Fig. 1.2. They have been employed in optical trapping in the past to trap and form ring patterns of 20 μm hollow glass spheres in water [40].

Hermite-Gaussian beams

Analogous to LG beams, the radial electric field of a Hermite-Gaussian (HG) beam is proportional to the product of a Gaussian and an associated Hermite polynomial H_i, where each mode HG_{mn} is characterised by two mode indices m and n which describe the order of H_i in the x and y directions, respectively [34]. Figure 1.2 illustrates the intensity distributions of a selection of HG modes.

In addition to using an SLM, LG modes can be generated by converting HG mode beams with a pair of identical cylindrical lenses [41] and, despite them being a non-standard choice compared to other novel beams, a rotating high-order HG beam has been employed to trap and rotate red blood cells [42].

Bessel beams

Bessel beams satisfy the Helmholtz equation and, since their intensity profile remains unchanged along the propagation direction, are referred to as propagation invariant or '*non-diffracting*' beams [36, 43]. They also carry angular momentum along their axis of propagation. A Bessel beam J_m should, in theory, have a sharp on-axis peak and be free of divergence but only approximations to this can be created experimentally, such as focussing a Gaussian beam through an axicon;

a conical prism [44]. This technique has been employed to create a zeroth-order Bessel beam and manipulate a selection of particles such as 1–5 µm silica spheres, elongated glass fragments, Chinese hamster chromosomes and *E. coli* [44]. The beam profile and radial intensity distribution of a zeroth-order Bessel beam is shown in Fig. 1.2. Bessel beams have also been used to improve optical trapping capabilities [38].

Helical Mathieu beams

Helical Mathieu (HM) beams are also solutions to the Helmholtz equation, specifically in elliptical co-ordinates, and are non-diffracting beams which possess orbital angular momentum. Each HM_m mode is characterised by order m, a selection of which are shown in Fig. 1.2. They have been used to induce controlled rotation of 3 µm polystyrene beads in a solution of heavy water D_2O, via the transfer of OAM [45].

The elliptical symmetry of HM beams makes them ideal for trapping and orientating elongated objects, as shown by the trapping of rod-like silica particles [32]. Another property of HM beams are their self-healing nature, i.e. they rebuild their transversal intensity distribution after any disruption from (small) obstacles [32], thereby facilitating multiple particles stacking in the z direction, which can then be rotated and potentially employed in microfluidics.

1.4   Multitrapping

Using multiple optical traps has become a well-established and increasingly popular technique, with publications continuing to highlight development. Several options exist for creating multiple optical traps, from acousto- and electro-optic deflection, rapid switching of galvanometer-controlled mirrors and deformable mirrors to multiple laser sources, diffractive optical elements and holographic optical tweezers. All of these fall into two main implementation methods; continuous re-positioning or *time-sharing* of a single beam, or the splitting of a single beam creating multiple simultaneous traps.

Time-sharing systems have limited functionality. However, provided the re-

fresh rate of each trap exceeds the trap's resonant frequency, time-shared traps are indistinguishable from true multi-beam traps; any lower and trap strength modulation becomes detectable in particle motion. This limits the number of traps to approximately 10 due to the restriction on refresh rate to tens of kHz [10].

The generation of multiple, individual traps is typically created in one of two ways; using the combination of computer generated holograms (CGHs) and an SLM, or using a real diffractive optical element (DOE), both of which allow manipulation in three dimensions. However, whilst DOEs may be cost effective, SLMs are superior due to their versatility and instant customisability compared with the static nature of DOEs.

Methods and equipment for both types of multitrapping shall now be described in further detail.

Deformable Mirrors

Deformable mirrors are adaptive devices consisting of actuators whose position is altered by the application of electric or magnetic fields. One might consider them to be grouped within the SLM family alongside the liquid crystal variety, with a high light efficiency but a lower resolution, e.g. 30–200 actuators. [46]

Deformable mirrors are mainly used in adaptive optics to correct for aberrations e.g. in astronomy and microscopy [47], but are also used within laser tweezing experiments [48, 49] where spherical aberrations notably affect the optical trap strength at significant trapping depths from the coverslip surface [36].

Galvo-mirrors

Galvanometer-controlled, or '*galvo*' mirrors, can be computer controlled to create multiple optical traps by rapidly scanning a single laser beam between multiple positions and became one of the first approaches for beam-steering in laser tweezers [50]. The beam should revisit each of the trapped particles at a sufficient rate to ensure the object does not diffuse a significant distance [37].

Galvo-mirrors have been used to trap up to seven $2\,\mu$m particles at any one time [51], and have also been used in combination with an SLM [52] in which the

SLM created the optical trap array and the galvo-mirrors allowed for its quick and smooth translation. Whilst they may offer a fast scanning rate, e.g. 1–2 kHz, large deflection angles and negligible power losses at relatively low cost, they have a low response time, e.g. 100 µs, afford a very limited number of traps in only two dimensions and are prone to wobble and jitter [50, 53, 54].

Acousto- and Electro-Optic Deflectors

Acousto-optic deflectors (AODs) and electro-optic deflectors (EODs) cause an angular deviation of a single beam to create two or more adjacent traps which can be computer-controlled [55–58].

An AOD acts as a Bragg grating such that an acoustic wave travelling at ultrasonic frequencies through the crystal diffracts the first-order of the incident beam [54]. Visscher, Brakenhoff and Krol [54] achieved a switching frequency of 21–31 MHz with a maximum trap seperation of ∼10 µm. However, AODs have relatively low diffraction efficiency, e.g. a maximum of 80 %, which is often changeable over the acoustic bandwidth. This creates significant variation, e.g. 10–15 %, in optical trap stiffness depending on angular deflection. Similar to galvo-mirrors, AODs are susceptible to hysteresis which can result in the manifestation of artifacts within the position signal [59].

EODs apply an electric field to an electro-optic material which induces a linear refractive index gradient to deflect the beam [54]. Compared with AODs, the optical alignment of EODs is more straightforward. They also provide improved light throughput (as much as 90 %), a switching frequency around 10 MHz, and reduced deflection-angle errors [50, 54, 58]. EODs can however be problematic due to wavefront distortions caused by crystal imperfections and low seperation of trapping beams, e.g. ∼1 µm [54].

Diffractive Optical Elements

A DOE or '*mask*' creates multiple beams by modification of the phase or amplitude of the input beam. They are advantageous as they are inexpensive, easy to integrate and commercially available. Unfortunately, they are limited by their static nature and as such, tend to be designed for specific applications. Diffractive

optics have been successfully integrated with laser tweezers to generate multiple optical traps, such as a 4×4 array [60], and an optical lattice for optical sorting of particles in microfluidic channels [61].

Spatial Light Modulators

An alternative method for creating multiple traps is presented in the form of holographic optical tweezers (HOTs) by the use of an SLM; a computer controlled DOE made of a liquid crystal which allows the point spread function (PSF) of each optical trap to be individually addressed [62, 63]. SLMs are a very popular choice for multiple laser tweezers and have been employed for translating multiple particles in two [64] and three dimensions [65]. The active area of a typical SLM is around $2\,cm^2$, with upto 2 million pixels and operates by modulation of the incident beam's phase or amplitude [46].

Depending on the compute- generated hologram applied to the SLM, a number of different optical trap configurations can be created. These include generation of novel beams for OAM transfer inducing particle rotation and of course, single optical traps if desired. They can also be used for aberration correction as employed by Cizmar, Mazilu and Dholakia to optically trap $5\,\mu m$ polystyrene spheres dispersed in a highly turbid and diffusive media; a sample of poly(dimethylsiloxane (PDMS) with a thickness of $40\,\mu m$ [66]. SLMs can be integrated with a number of different control interfaces including finger-tip control [67], a force feedback joystick [68] and as mentioned previously, an Apple iPad very recently [28].

The choice of alogorithm for hologram generation depends on the degree of computational power available; such as using the computers graphics card where it's possible to create on the order of 100 traps at 100's of Hz [69] or dividing the SLM into regions allowing traps to be controlled without recalculation of the entire hologram. Each alogrithm has limitations including significant trap strength variations requiring further hologram iterations [63, 70].

For further information on SLMs in optical microscopy and lab on chip devices, see references [46, 63].

1.5   Applications

Firstly, since comparison is often made between laser tweezers and a range of other micromanipulation techniques, including magnetic tweezers [71] and atomic force microscopy (AFM) [72, 73], Table 1.1 compares the important parameters for these three main micromanipulation techniques, listing their typical applications and some of their features.

Laser tweezers are attractive to a wide range of research areas and established techniques due to their applicability and ease of integration. With the continued research investment into the field of optical trapping and the development of laser tweezing techniques and tools, the list of applications continues to grow. This section will detail four applications of interest; optical spanners, microfluidics, biological and medical applications, and liquid crystals.

1.5.1   Optical spanners

Since light can possess angular momentum in addition to linear momentum, laser tweezers are also used to rotate trapped particles; a technique often referred to as '*optical spanners*' or an optical wrench. Optical spanners have been developed and used for a range of applications including microfluidic pumps [74], micro-machines [75] and a microviscometer [76, 77]. Both spin and orbital angular momentum can be transferred to a trapped particle to produce different effects. The transfer of spin angular momentum results in the particle spinning about its own axis, whilst a transfer of orbital angular momentum causes the particle to orbit around the beam's axis due to helical wavefronts [78]. Daria, Go and Bachor [78] illustrated this effect by transferring both linear and orbital angular momentum to hollow glass spheres using a dynamic array of optical vortices, inducing circular orbital motion of the particle around the vortex.

Particle rotation can also be generated by trapping birefringent particles with linearly polarised light as reported now more than a decade ago by Higurashi, Dawadi and Ito [79] using a linearly polarised TEM_{00} beam to rotate fluorinated polyimide (PMDA/TFDB). Several publications employing birefringent particles have followed. Examples include controlling the polarisation of the optical trapping beam with an SLM to transfer spin angular momentum to rotate and align an

Table 1.1: Comparison of micromanipulation techniques. This table compares the important parameters for three of the main micromanipulation techniques; laser tweezers, magnetic tweezers and atomic force microscopy (AFM) [72, 73].

	Laser Tweezers	Magnetic Tweezers	AFM
Spatial resolution (nm)	0.1 – 2	5 – 10	0.5 – 1
Temporal resolution (s)	10^{-4}	$10^{-1} - 10^{-2}$	10^{-3}
Stiffness (pN/nm)	0.005 – 1	$10^{-3} - 10^{-6}$	$10 - 10^5$
Force range (pN)	0.1 – 100	$10^{-3} - 10^{-2}$	$10 - 10^4$
Displacement range (nm)	$0.1 - 10^5$	$5 - 10^4$	$0.5 - 10^4$
Probe size (µm)	0.25 – 10	0.5 – 5	100 – 250
Typical applications	▷ 3D manipulation	▷ Tethered assay	▷ High-force pulling and interaction assays
Features	▷ Tethered assay ▷ Interaction assay ▷ Low-noise, low-drift dumbbell geometry	▷ DNA topology ▷ Force clamp ▷ Bead rotation ▷ Specific interactions	▷ High-resolution imaging
Limitations	▷ Photodamage ▷ Sample heating ▷ Nonspecific	▷ No manipulation	▷ Non-specific ▷ Large minimal force ▷ Large high-stiffness probe

array of birefringement calcite fragments [80] and applying circularly polarised light to vaterite particles [76, 81] or elliptically polarised light to calcite particles [82].

The development of optically driven pumps (ODPs) has been reported for efficient fluid transport [83]. OPDs are produced when a dielectric particle is trapped and spin angular momentum, in addition to orbital angular momentum, is transferred to the particle. The net result is particle rotation with frequencies ranging from around 4 Hz [84] to a few hundred Hz, where rotation frequency is proportional to the power of the trapping laser [85]. However, this relationship is not altogether linear which suggests an additional variable parameter [77]. Leach *et al.* [74] reported the creation of one such ODP. A circularly polarised beam was used to transfer spin angular momentum to trapped birefringent particles of vaterite to induce counter-propagating rotation and subsequent fluid flow within the surrounding fluid of the microfluidic channel. Successful rotation of vaterite particles with a diameter of 5–7 µm was observed generating increased fluid flow in close proximity to the rotating particles. A 1 µm diameter 'pump bead' was observed to travel between the two rotating vaterite particles with a maximum rate of 8.3 µm/s in the microfluidic channel.

Micron-sized droplets of liquid crystal, naturally birefringent materials, have also been rotated using linearly polarised light, as shall be discussed in further detail in Section 1.5.5.

A range of different particle shapes have been fabricated and employed to create optical spanners, a selection of which are shown in Fig. 1.3. In addition to the rotation of spherical beads described above (Fig. 1.3(a)), laser tweezers have been used to trap and rotate nanorods and nanotube materials like those shown in Fig. 1.3(b), such as CuO nanorods [86], nanotube bundles [87, 88] and palladium-decorated carbon nanotubes [89]. Two varieties of nanotube exist; single walled and multi-walled nanotubes, SWNTs and MWNTs, respectively [90, 91] and both have been observed to spin using circularly polarised infrared light via transfer of angular momentum when placed in a dual-beam optical trap [92]. If a cylindrical object is placed at the centre of the optical trap, it orientates itself to a position of lowest energy; that is, lying along the laser beam axis or '*end on*' in the trap i.e. perpendicular to the sample plane. Cylindrical rods outside the optical trap's centre, but still trapped, do the opposite and are perpendicular to the

laser beam axis i.e. parallel to the sample plane. This means assymetric nanorods can be rotated regardless of the polarisation of the trapping beam making laser tweezers a particularly attractive technique, holding promise for optically driven nanorotor technology [93]. If an ensemble of two cylindrical objects is simultaneously trapped, one will rotate in this '*end on*' orientation whilst the other will rotate perpendicular to it [94]. Horizontal trapping of dielectric microrods using multiple HOTs has recently been reported by Carberry *et al.* [95] as a tool for force microscopy, and very recently by Phillips *et al.* [96] to perform high-speed tracking of their rotational and translational motion.

(a) Bead
diameter: 0.5–10 μm

(b) Nanorod and
Carbon nanotube
diameter: 20–100 nm,
length: 300 nm–20 μm

(c) Microcog
diameter: 10 μm
length: 0.5 μm

(d) Micromotor
diameter: 10 μm
length: 2 μm

(e) Microgear
Unspecified size

(f) Microstructure
length: 8 μm
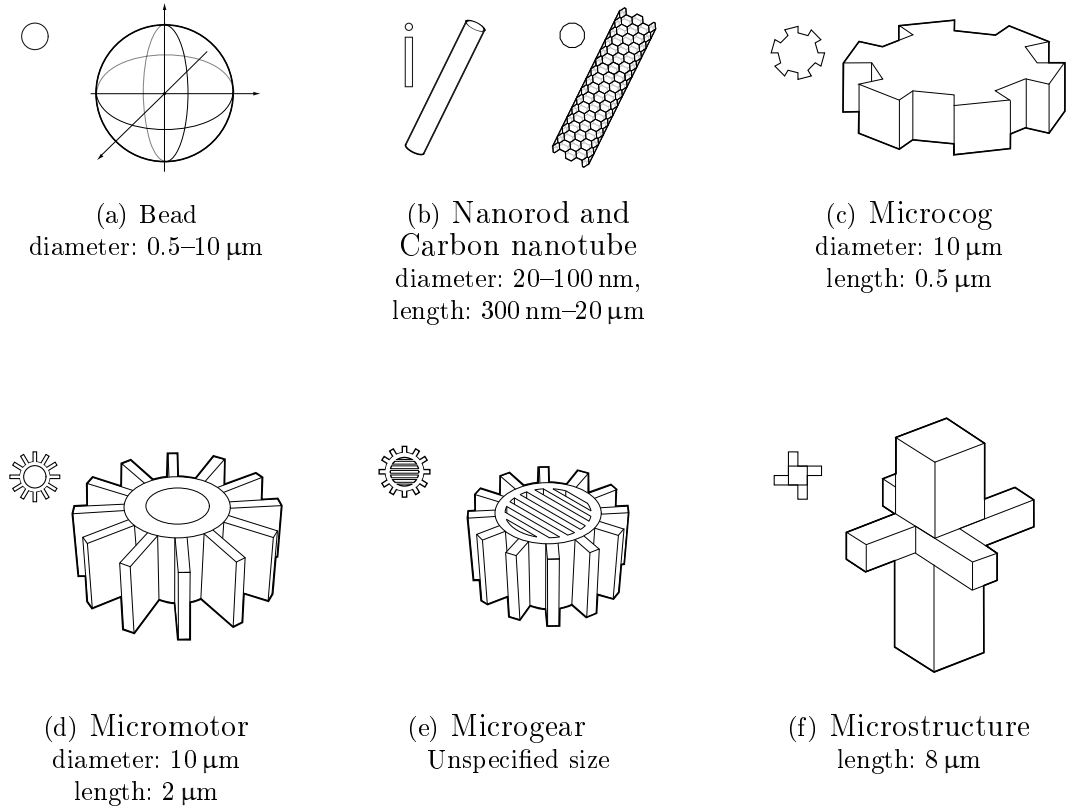
Figure 1.3: Different particle shapes developed and employed for optical spanners: (a) bead, (b) nanorod (left) and carbon nanotube (right), (c) microcog, (d) micromotor, (e) microgear and (f) microstructure. *See the text for details.*

In an experiment by Friese *et al.* [97], birefringent fragments of calcite were rotated in circularly polarised light to induce rotation of a microfabricated element or '*microcog*' (Fig. 1.3(c)). Optical torque is transferred to the microcog due to the surrounding fluid motion and, with the calcite fragment rotating clockwise,

the microcog rotates anti-clockwise. This demonstrated significant potential for producing rotorary components of optically-driven micromachines.

Following this, a fiber-optically delivered light beam was used to rotate a micromotor (Fig. 1.3(d)) [98], and beams with linearly and circularly polarised light have both been employed to rotate microgears (Fig. 1.3(e)). The microgears were fabricated using '*form birefringence*' — a difference in refractive index due to the internal shape of the fabricated structure — amd one microgear was observed to induce the rotation of a second optically trapped microgear in close proximity. These would provide an extremely useful mechanism in a micromachine [99].

Finally, Rubinsztein-Dunlop and colleagues provided a significant contribution in the development of optical spanners [75–77, 81, 85, 97, 100–104], culminating in the use of shape birefringence for rotation in laser tweezers. Asavei *et al.* [102] designed, fabricated and rotated microstructures using an LG beam. The initial design for the microstructure was an off-set cross and stalk with four-fold rotational symmetry as shown in Fig. 1.3(f) [103], which was modified slightly in a subsequent and recent conference proceeding paper alongside other shape alternatives [104].

1.5.2 Microfluidics

Microfluidics is the study of fluids on the micron scale in so-called microfluidic devices, whose channel dimensions range from 10–100 µm [105]. It forms the basis of a whole range of research and technology, including '*lab-on-chip*' (LOC) technologies, cell sorting and micromachines [74]. Applications began with microanalytical methods and devices which offered low cost, small volumes of both reagent and sample, and reduced footprint. Microfluidic research in the 1990's was also motivated by the aim of developing portable devices and systems for use in warfare to detect threats posed by biological and chemical weapons [105]. A wide range of microfluidic systems are functional as laboratory demonstrations but there are however, some which are commercially available technologies, such as screening for protein crystallisation [106–108].

Whilst microfluidics, the science, is well established, whether microfluidics, the technology, shall realise its full potential and have widespread use depends on successful methods for integration with a selection of other technologies. Mi-

crofluidic systems for chemical synthesis, for instance, has proved incompatible as the popular choice of polymer for microfluidic systems, PDMS [109], is easily dissolved or degraded by many organic solvents. Microfluidic research offers commercial opportunities for a range of industries; pharmaceutical, agricultural, security and food safety, if the desire for devices to be reproducible and easy to use is satisfied [105].

Major research is being undertaken to generate LOC technologies and devices which allow laboratory or '*factory*' operations to be performed on a small scale, dealing with volumes as small as picolitres of analyte, for biological and chemical applications [77, 105]. These technologies and devices are also referred to as μTAS; micro total analytical systems, the goal of which is manipulation and characterisation of small sample volumes of biological liquids, such as human tears, on a device the size of a chip [77, 83]. At the mesoscopic scale; a scale at which discussions of atomic behaviour can be neglected, the macroscopic theory of fluid flow is inapplicable. Dealing with these small liquid volumes places us in the low Reynold's number (Re) regime, where viscosity characteristics and diffusion effects dominate under laminar flow conditions in the absence of turbulence [36, 105]. Further understanding of the effects at the micron-scale offers insight into nanofluidics.

Aspirations for microfluidic technology include further development of microfluidic diagnostic technology (MDT) for medical devices. These include portable point-of-care (POC) medical devices used for rapid medical diagnosis in developing, and developed, parts of the globe [110] such as optically driven micromachines [111] and microrotors which allow transport through microfluidic channels via laser tweezers [94].

For biomedical analysis, it is often necessary to isolate single (or clusters of) cells from a large mixture, therefore fundamental microfluidic devices are designed to perform recognition, sorting and counting of particles or cells [112]. Such processes can be achieved using a variety of techniques, often in unison, including integrated optical waveguiding [111] or optical fibres, parallel processing using multiple independent laser tweezers [109], and laser induced fluorescence and digital imaging processing [112]. However, overall success is often a compromise between achieving simple and low-cost fabrication techniques, and high accuracy and increased yield [112].

1.5.3   Biological and medical applications

Laser tweezers are of particular interest to the biological sciences as, up until the birth of optical trapping, biological research relied upon results for bulk biological samples [36]. This section will briefly discuss how laser tweezers have been applied in a biological and medical arena but several review articles [53, 72, 73, 110, 113–117] and book sections [10, 118] are available for a more detailed description.

Laser tweezing studies involving biological systems have ranged from manipulation of goldfish photoreceptor cells to examine their sensitivity to polarised light [119] to obtaining surface-enhanced Raman scattering (SERS) spectra of optically trapped bacterial spores [120]. However, it is single-molecule manipulation which has been transformed by laser tweezers as, in exchange for insight into the molecule under investigation, it is straightforward to image a trapped bead and calibrate the laser tweezing system [36, 118]. As mentioned in Section 1.1, laser tweezers have been used to manipulate bacteria and viruses [19] as well as single cells [20]. Based on this early research, it is now standard practice to employ infrared trapping beams to avoid causing optical cell damage, since these wavelengths experience low absorption in biological tissue [20].

More than 15 years ago, Svoboda *et al.* [121] used laser tweezers to directly observe stepping of the motor protein kinesin, which moves along microtubule filaments, discovering it moved in 8 nm steps. In comparison, Allersma *et al.* [122] used interferometric optical tweezers to measure the displacement and average axial velocity of beads coated in ncd motor protein — a kinesin-related motor protein — to study its motility [122].

Biological molecules, such as DNA and proteins, are often too small to be directly trapped. In such a case, trapped beads — such as polystyrene or latex microspheres, for example — can be attached to molecules of interest [4] where the microsphere is coated with antibodies [10]. In this arrangement, the trapped bead is referred to as an '*anchor*' or '*handle*' as shown in Fig. 1.4 which depicts three of the several different arrangements for single molecule manipulation. Each of the arrangements pictured measures the displacement of the *handle* — the bead held in the laser tweezers — allowing the motion, properties and processes of the molecule to be studied in detail. They are implemented with a DNA molecule, for example, as follows;

▷ **Surface-tethered assay**: one end of the DNA molecule is attached to the *handle* in the laser tweezers whilst the other end is tethered to the coverslip surface.

▷ **Dual-trap dumbbell assay**: both ends of the DNA molecule are attached to the surface of optically trapped beads. Force is applied to the DNA molecule through the controlled lateral motion of the optical trap, and therefore one bead, whilst the other optical trap is held stationary [59].

▷ **Micropipette-tethered dumbbell assay**: both ends of the DNA molecule are attached to the surface of beads; one held by a micropipette and the other optically trapped. Force is applied to the DNA molecule through the controlled lateral motion of the micropipette, and therefore one bead, whilst the other optical trap remains stationary.

(a) Surface-tethered assay

(b) Dual-trap dumbbell assay

(c) Micropipette-tethered assay
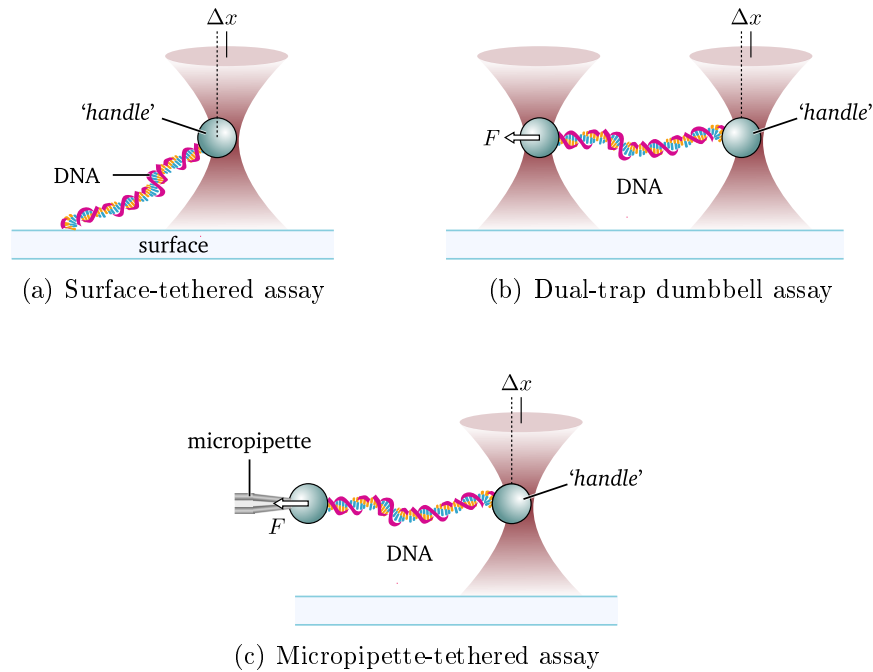
Figure 1.4: Optical tweezers and single-molecule studies in three different arrangements: (a) surface-tethered assay, (b) dual-trap dumbbell assay and (c) micropipette-tethered assay. Adapted from [72, 118].

In work by Abbondanzieri *et al.* [123], single molecules of *E. coli* were optically

trapped to observe base pair stepping of RNA polymerase* along DNA, achieving ångström-level resolution. The research was developed further by using a force-clamping technique to track transcription, also with ångström-level resolution, i.e. single-base pair resolution, of RNA polymerase using single molecules of *E. coli* RNA polymerase, where both ends of a DNA molecule are held in a dual-trap dumbbell assay arrangement [59, 125].

More recently, laser tweezers have been combined firstly with scanning probe microscopy to study DNA-protein interactions with nm-resolution; in an arrangement based on the pipette-tethered assay arrangement, where the tension within the DNA molecule is probed and the individual proteins located [126]. Secondly, incorporation of laser tweezers with confocal fluorescence and Raman spectroscopy has provided physical and chemical information about individual trapped protein aggregates, such as their transition temperature [127]. Researchers who demonstrated axial stretching of a DNA molecule under constant mechanical force and measuring its force-extension relationship believe their work makes molecular length scales more accessible [128].

Notable research has been conducted which incorporates laser tweezers in order to study erythrocytes or red blood cells (RBCs) including early research (mentioned previously in Section 1.3) where RBCs were optically trapped and rotated using a high-order HG beam. A dual optical tweezer arrangement has very recently been employed to manipulate RBCs, measure their membrane viscosity and gain information about their protein interaction. This therefore facilitated insight into cell agglutination, or '*clumping*' [129], and their elasticity and adhesion [130].

Ghosh *et al.* [131] used an optically driven micromotor to optically trap individual RBCs whose normal biconcave disc shape was observed to fold into a rod-like shape and rotate in a circularly polarised trapping beam. They demonstrated folding and rotation occurs at a critical trapping power, thus applying a proportional torque, with the RBC displaying birefringent properties in its folded state. The Brownian motion and associated power spectra of optically trapped normal RBCs and those infected with malaria has also been studied. The difference in power spectra between healthy and infected cells appeared independent

---

* RNA polymerase (RNAP) is the enzyme responsible for producing RNA by copying information from DNA [124].

of the stage and duration of the infection [132]. The development and advance of the research holds significant promise for efficient disease detection.

Whilst laser tweezers are conventionally applied through glass substrates, as they are transparent to visible light, researchers at the Massachusetts Institute of Technology (MIT) were the first to successfully trap and manipulate individual cells on the surface of a microchip [133]. Several *E. coli* cells were trapped and arranged on the surface of a silicon chip, as silicon is transparent to infrared light, to form the letters 'MIT' and plastic beads were arranged in hexagonal shapes near the silicon surface. Conversely, researchers at Berkeley demonstrated the use of optoelectronic tweezers which use electric forces for trapping as opposed to optical forces. As many as 15,000 independently addressable traps, created using spatial light modulation, were used to manipulate nm-scale particles, including *E. coli* [134].

Similarly, laser tweezers appeal to the medical sciences due to their minimally invasive nature. They have been employed for a variety of medical research studies including investigation of the interaction and attachment forces that occur between medical implant surfaces and bone forming cells at the implant site. This offers further understanding of the healing process after implant surgery and should be indicative of the future success of medical implants [135]. Wang *et al.* [136] performed cellular analysis on cancer cells using optical tweezers. Particle motion, induced due to scanning across the sample with the optical trapping beam, was observed without requiring biological markers which are often necessary for analytical experiments and techniques such as fluorescence spectroscopy.

In a 2001 paper, Guck *et al.* [137] reported the development of a method of stretching optically trapped particles using two opposed, non-focussed beams; termed the '*optical stretcher*'. The device allowed viscoelastic properties of dielectric materials to be measured and successfully deformed human RBCs and mouse fibroblasts, the most common cells in connective tissue which play an important role in wound healing. It was possible to stretch an RBC beyond the linear regime from a radius of 3.36 μm to 6.13 μm; an increase of $\approx 80\,\%$, which returned to its original shape with a reduction in laser power. In later research by Guck and colleagues [138], the optical stretcher, in combination with non-contact microfluidic delivery, was successfully employed to investigate the elasticity and optical deformability of mouse fibroblasts and human breast epithelial cells during their

progression from a normal to cancerous state.

Most biological applications involve incorporation of laser tweezers with other scientific techniques. The combination of two techniques can offer increased precision, applicability to a wide range of biological molecules and the ability to perform in-depth studies of individual particles resulting in many promising developments. An example includes the union of laser tweezers with the fluorescence detection technique, FIONA — fluorescence imaging with one nanometer accuracy [139] — Raman spectroscopy for studying a range of particles, some of which include metal particles, paints, gas bubbles and living cells [140, 141].

Heng *et al.* [142] employed an optofluidic microscope (OFM), used for transporting liquids within microfluidic channels, to improve upon the resolution offered by a near-field scanning optical microscope (NSOM). The OFM employs a nanoaperture grid — 100 nm sized apertures spaced by 25 μm — combined with laser tweezers to offer sub-wavelength resolution ($\sim$110 nm) microscopy at smaller scales. Micron-sized pollen spores and polystyrene beads were trapped and the light, travelling first through the nanoaperture grid and then through the sample, were imaged. Here, the laser tweezers allow precise particle translation across the two dimensional nanoaperture grid as opposed to a traditional translation stage. However, the microfluidic channel still experiences vibration resulting in reduced image resolution, and the OFM would benefit from an increased frame rate and reduced footprint.

1.5.4   Micromanipulation with surface plasmons

Research continues in earnest to extend optical trapping down to the nanometre scale where success would allow the ultra-accurate positioning of single nano-objects, offering potential application in many fields of science. One possible strategy is using metallic nanostructures to control light at the sub-wavelength scale to create nano-optical traps [143].

Conventional optical tweezers are formed at the diffraction-limited focus of a laser beam. Reducing the size of the trapped particle, such that one is operating in the Rayleigh regime ($d \ll \lambda$), hinders stable optical confinement, where there is a decrease in (i) the magnitude of the restoring force, resulting in a shallower trapping potential well and (ii) the damping force due to a reduction in viscous

drag. This ultimately allows the particle to more easily escape from the optical trap [143]. Diffraction prevents confinement of propagating light beyond a fraction of its wavelength. However, recent advances in nano-optics have circumvented this limitation, where evanescent fields can be concentrated well beyond the diffraction limit.

Surface plasmon (SP) traps are advantageous over conventional 3D optical traps as they allow the same trapping efficiency to be achieved using much less laser power and is thus, promising for fragile objects without destroying or damaging them e.g. biological specimen [144]. In addition, they do not require any bulk optics, operate with substantially reduce laser intensities, and allow controllable selectivity for specimen size [145]. SP tweezers were first implemented experimentally using a glass surface decorated by micrometre-sized gold disks [146, 147]. The patterned surface was illuminated by an unfocussed infrared laser beam. The incident evanescent field pushed polystyrene beads at the glass-water interface, guiding them towards the trapping region of the surface. Grigorenko *et al.* [148] were able to create nanometric optical tweezers using a pair of gold nanopillars ($d \sim 100$–400 nm) fabricated on a glass substrate to create well-defined, 3D plasmonic traps. The gap between each pair (140 nm) essentially determines the trap size and the maximum impulse that can be imparted to the trapped object. It can be reduced down to as little as 10 nm using nanolithography. They were able to trap 200 nm polystyrene beads immersed in glycerol [144].

For more detail, the reader is directed to comprehensive review articles on plasmon tweezers by Juan, Righini and Quidant [143] and Righini, Girard and Quidant [145].

1.5.5   Laser tweezers and liquid crystals

A liquid crystal (LC) is a thermodynamic phase of condensed matter, often referred to as *mesophase* [149], with some degree of order as given by the director $\hat{n}$. They create impressive and often colourful microscopy images like those shown in Fig. 1.5 due to their birefringent and anisotropic properties.

There are several different phases of liquid crystal, defined by the degree of orientational order present which exists in at least one direction, and with at least one degree of anisotropy present. The research in this thesis focuses on nematic
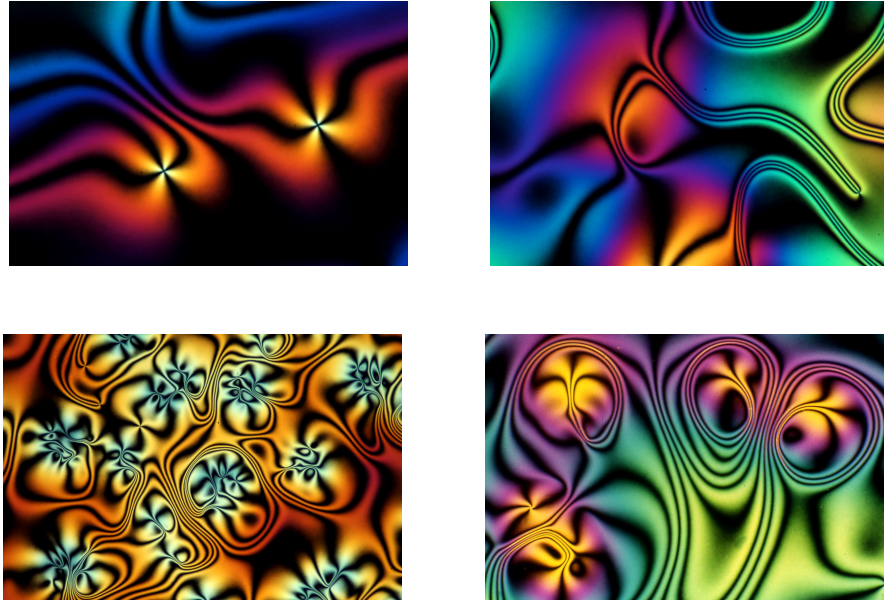
Figure 1.5: Polarisation microscopy images of a thin (1–2 μm thickness) film of liquid crystal spread across the isotropic fluid glycerine and open to air. The dark bands are areas of director distortion, caused by the two different interfaces, where the director is parallel to either the polariser or analyser [150].

liquid crystals (NLCs), those with long range orientational order in one direction. A more detailed description of the theory governing LCs and their properties will be provided in Chapter 3.

Liquid crystals were first discovered by Austrian botanist, Freidrich Reinitzer in 1888 following the observation of two melting points of cholesteryl benzoate, between which he observed irridescent colors. Two years later in 1890, Physicist Otto Lehmann constructed a polarising microscope with a temperature-controlled (hot) stage; now a standard piece of equipment in liquid crystal research. Fabrication of the first liquid crystal structure, the twisted-nematic on which today's liquid crystal display (LCD) technology is based, occurred in 1911 by Charles Mauguin in France. Liquid crystal research continued in earnest and the advent of LCDs, including wristwatches and pocket calculators, catapulted LCs into an arena of technological development beyond research simply for the benefit of understanding. A detailed description of the discovery of LCs and the subsequent development of LCD technology can be found in reference [151].

It is possible to optically trap colloids dispersed in liquid crystal, micron-sized

liquid crystals droplets, and LC topological defects or '*disclinations*' [152–154]; a region where the molecular alignment is altered by external forces e.g. electric or magnetic fields, and the walls of the container in which the LC sits. Hence, improvements in laser tweezing techniques have an influence on the progress of condensed matter research, specifically colloidal and liquid crystal science [155]. Conversely, liquid crystal research can also compliment and benefit biological research; many biological molecules also form anisotropic phases, such as DNA, cellulose, cell membranes and lipids, amongst others [156]. LCs have themselves been used for optical trapping in the form of a LC lens [157] and LC adaptive optical elements [158, 159], not to mention they form the basis of a SLM.

Liquid crystal droplets

Advances and understanding of LC emulsions (LCEs) — micro-droplets of LC, coated with a surfactant, dispersed in an isotropic liquid [160] — through optical manipulation establishes the potential of liquid crystals for optically driven micromachines. In a 1996 paper, Tamai, Ito and Masuhara [161] reported second- and third-harmonic generation from optically trapped micron-sized nematic and ferroelectric liquid crystal droplets dispersed in water. This was closely followed in 1999 with Juodkazis *et al.* [162] reporting the rotation of optically trapped nematic liquid crystal droplets with circularly polarised light. Further work by the same group detailed the dependence of rotation frequency on droplet size [163] and the efficiency of optical torque transfer to droplets [164].

There have been several further reports demonstrating optical trapping and rotation of LC droplets in suspension including nematic droplets with circularly polarised light [165–167], chiral nematic droplets with linearly polarised light [167–169], dye-doped nematic droplets using circularly and elliptically polarised light [84] and smectic† liquid crystal droplets in circularly polarised light [170]. Interestingly, liquid crystal droplets have recently been used to fabricate micronsized liquid crystal cylinders which were rotated in circularly polarised laser tweezers to measure the viscosity of the composite LC [171].

Spinning LC droplets have also been employed to measure the viscosity of

---

† For a liquid crystal in the smectic phase, the molecules exhibit orientational order, as seen in the nematic phase, but also translational order where they tend to arrange themselves in relatively defined layers.

the host medium, such as heavy water D_2O [172, 173]. More recently, an optical fibre laser tweezers arrangement, which more strongly focuses the light within high-index colloids compared with silica for example, was employed to trap, rotate and monitor the rotation of NLC droplets [174]. The trapping laser beam transfers optical torque to the LC droplet and its electric field induces molecular reorganisation within the LC droplet [175]. Gleeson, Wood and Dickinson [167] dismissed wave-plate behaviour as the mechanism solely responsible for observing LC droplet rotation but cited other possible mechanisms for the optical angular momentum transfer, including anisotropic scattering, absorption and the optical Fréedericksz transition. The reasons for the underlying physical processes continue to remain elusive and of interest.

Colloids in liquid crystalline media

Unusual behaviour exhibited by colloids and colloidal dispersions, of which paints, milk and fogs are examples, introduces the prospect of self-assembled photonic devices [176]. The introduction of colloids into a LC produces novel anisotropic structures, as discussed by Poulin *et al.* [177, 178] with Meeker *et al.* [179] showing it is possible to create colloid-liquid crystal composites at volume fractions greater than 2 % with potential for switchable display technologies.

Iwashita and Tanaka [180] were the first to report optical trapping of colloids dispersed in LC media in 2003 with silica beads in a lyotropic LC, followed in 2004 by optical trapping of colloids in a thermotropic LC by Yada, Yamamoto and Yokoyama [181]. As shall be seen in Chapter 2, for successful optical trapping it is necessary for the refractive index of the particle to exceed that of the host medium i.e. $n_p > n_m$. However, when optically trapping colloids within a LC, the trapping laser introduces long range deformations of the LC director $\hat{n}$, causing it to reorientate itself. This alters the refractive index difference between the trapped particle and the host LC medium. Collaborating researchers from Slovenia and Ukraine [176, 182, 183] illustrated this effect with successful optical trapping of silica particles whose refractive indices were lower than both refractive indices of the NLC host medium, with an index contrast of at least $n_p - n_{LC} = 0.09$ and as much as $n_p - n_{LC} = 0.37$. This 'forbidden' trapping can be attributed to (i) a distortion of the NLC director around the surface of the colloid, creating a high-index '*cloud*' or '*corona*' which can be trapped, or (ii) laser-induced local melting

of the NLC, creating a '*ghost*' colloid located at the centre of the optical trap with which the real colloid interacts. Potential applications of this technique include optically-tunable photonic crystals and optically-driven micropumps [184].

Temperature effects are of significant importance in LC research since they can change the refractive indices and therefore, birefringence [186]. These effects are particularly important when performing laser tweezing experiments since the popular choice of an infrared trapping source can induce heating, and therefore melting, of the LC. Tatarkova *et al.* [185] demonstrated the laser-induced heating of nematic LC 5CB, whose phase transition occurs at a temperature $\sim 36°$C. The laser created regions in which the LC was in the isotropic phase. Figure 1.6 shows a white light image (viewed between crossed polarisers) of

Figure 1.6: White light image, viewed between crossed polarisers, of 5CB with the optical trap located at the centre showing laser-heating induced isotropic '*bubble*' [185].

5CB with the optical trap located at the centre. The surrounding dark green region corresponds to the overheated isotropic '*bubble*'. The boundary seperating the isotropic bubble and the regularly orientated nematic (light green, approximately at room temperature) is well defined, where the observed Newton colours illustrate the change in local birefringence. Presence of an isotropic bubble also appeared to affect the motion of any surrounding colloids.

Viscosity in liquid crystals

Defining LC characteristics play a particularly significant role in improving LCD technologies [187]. For example, determining a twisted nematic LC's rotational viscosity coefficient or describing fluid flow, or '*back-flow*', effects [188] are critical for improving LCD efficiency since they influence the device's response times. Computer models for predicting back-flow effects often require several anisotropic viscosity coefficients, termed '*back-flow coefficients*', which can be determined via their relation to shear viscosity coefficients measurable in classical flow experiments [188, 189]. The effect of back-flow has itself been employed to optically trap colloids [190], illustrating that progress in understanding both LC back-flow

and optical trapping in LCs can be mutually beneficial. Temperature effects on back-flow in vertically aligned LCDs has been investigated [191], which should be taken into account in order to improve the performance of these devices.

In the past, viscosity coeffcients have been determined by studying LC flow through a capillary via the application of a magnetic field and observing pressure differences [192, 193]. Pasechnik *et al.* [189] employed a decay flow method; inducing shear flow with optically controlled pressure differences, to determine back-flow viscosities for the LC mixture MLC-6609. For the majority of new LCs generated for LCD technology, research often focuses upon determining LC refractive indices whilst other quantities, including viscosity coefficients, remain unknown. Ignoring such back-flow effects in LCDs allows poor prediction of their functionality and limits progress.

As in isotropic fluids, viscosity in LCs can be determined by observing the viscous, or Stokes', drag experienced by a particle moving through a fluid [166–169]. The Stokes' drag is highly non-linear for particles in a nematic solvent; the colloid (acting as a quadrupole) finds it easier to diffuse parallel to $\hat{n}$ than perpendicular to it [194, 195]. Further research by Verhoeff *et al.* [196] quantised this direction-dependent Stokes' drag. They demonstrated that for a colloid moving through a NLC, the viscous drag parallel to $\hat{n}$ was larger than the drag perpendicular to $\hat{n}$ by a factor of two. Gleeson *et al.* [167] employed the viscous drag technique with laser tweezers to measure the effective viscosities of LC mixture MLC-6648 for motion parallel and perpendicular to $\hat{n}$. The values allowed inference of the anchoring strength of colloidal particles within the LC mixture which was in good agreement with prediction. The research was the first to obtain viscosity measurements for this LC mixture therefore offering an opportunity for comparison and further understanding, leading to a recent proceedings publication by Sanders, Dickinson and Gleeson [197].

Colloids dispersed in a LC undergo a range of interesting interactions where laser tweezers have been employed to investigate them [198] alongside detailed theoretical treatments [199]. Due to elastic distortions of the director around the particle, they can experience a mutual attraction or repulsion [200]. In close promiximity e.g. at interparticle seperations of three particle diameters, the interaction overcomes Brownian motion producing an attraction or repulsion depending on their seperation relative to the director. These experiments conducted in

nematic bulk, observed colloidal aggregation such as chain-formation and complex structures. Recent research has gone on to investigate the effect of temperature and cell thickness on the interparticle forces between two colloids in a NLC [201].

Magneto-optic tweezers, a technique directly comparable with laser tweezers as discussed previously, have also been employed to study these colloid-liquid crystal interactions [202]. Attractive and repulsive forces between two spheres immersed in a NLC were observed depending on sample thickness. Due to the quadrupolar interaction between the two colloids, they would be repelled in samples whose thickness was comparable to the bead size but attracted in thicker samples to form clusters, relating also to the change in director orientation around the colloid. Development of this technique offers a viable technique for determination of a LC's viscosity.

Dierking, Biddulph and Matthews [203] reported the translation of microspheres dispersed in NLC along $\hat{n}$ upon application of an electric field. They were able to demonstrate the velocity of this '*electromigration*' was directly proportional to electric field amplitude presumably owing to the adsorption of surface charges by the colloid. These results are complimented by similar observations in a thin planar nematic cell, but with particle velocity inversely proportional to the frequency of the AC field, to produce close-packed crystalline colloidal structures [204]. Conversely, Dierking *et al.* [205] later showed electromigration of colloids dispersed in ferroelectric smectic LCs occurs along the plane of the smectic layer, almost perpendicular to $\hat{n}$. Their velocities were observed to be independent of electric field amplitude but directly proportional to increasing temperature i.e. an associated decrease in the LC's viscosity. These results indicate the promise of yet another technique for measuring LC viscosity.

1.6   Research context

Established techniques of liquid crystal research conduct macroscopic investigations since they examine the bulk liquid crystal. Therefore, there is a strong call for microscopic, local investigations. Research involving LC-colloidal dispersions expands the knowledge and understanding of LCs and their anisotropic nature. Whilst there has been experimentation into LC viscosity with laser tweezers using the viscous drag force method, passive observation of anisotropic Brownian mo-

tion of colloids in liquid crystalline media by analysing associated power spectra in the frequency domain remains to be presented.

Observation of an optically trapped particle's Brownian motion in a viscoelastic media with unknown frictional behaviour, such as a LC, is not suitable for calibrating optical tweezers. This is reserved for well understood viscous media, such as water, to employ a purely passive calibration method [206]. However, this warrants exploration into the idea that passive methods could be employed to understand and characterise the behaviour of viscoelastic media, including LCs. This is the motivation for the research conducted and reported in this thesis.

1.7   Thesis outline

The research detailed within this report uses laser tweezers to study microfluidics of isotropic and anisotropic nano-particulate suspensions including colloids dispersed in liquid crystals. This research has potential relevance and benefit to current technology and research, such as soft-condensed matter, biological or medical research concerned with liquid systems, cell-sorting and lab-on-chip devices, optical micromachines and molecular motors.

This thesis is comprised of three parts, the first describes the theory behind optical tweezers and the analytical methods employed, along with the theory and practicalities of liquid crystals, found in Chapters 2 and 3, respectively. The second part describes the arrangement and characterisation of the optical tweezing system, and the materials used in Chapter 4. The final part presents and discusses the results of laser tweezers employed in isotropic and simple systems, water–glycerol mixtures and liquid crystals, followed by a summary of the conclusions that can be drawn and suggested future work in Chapters 5 to 8, respectively.

Introduced in Chapter 2 is the theory governing optical trapping in the ray optics regime followed by a description of the statistical methods employed both for calibration and analysis of experimental data.

Chapter 3 details the theory, key definitions and practicalities of liquid crystals, specifically nematic liquid crystals, relevant to laser tweezers and the work undertaken. This chapter also provides the specifications for the liquid crystals

and colloids used, reasons for choosing them and outlines the sample preparation process.

The design and optical arrangement of the laser tweezing system is described in Chapter 4 where the important components are discussed in detail. Particular attention is paid to the technique employed for particle tracking; high-speed video microscopy.

Chapter 5 contains the results of laser tweezing in isotropic systems, more specifically optically manipulating polystyrene beads in water to calibrate the laser tweezing system. Three methods are employed for trap stiffness calibration; one active and two passive techniques. An attempt is made to quantify effects due to the proximity of a surface to an optically trapped particle and spherical aberration of the optical trap. The effect of particle size and refractive index are also investigated. The results provide characterisation of the laser tweezers prior to performing experiments in anisotropic media.

Chapter 6 presents the results of laser tweezing experiments performed in water–glycerol mixtures with varying glycerol concentration. These results provide a measure of the suitability of the laser tweezing system for microviscometry, where water–glycerol mixtures are well characterised.

The results of laser tweezing in liquid crystals are contained in Chapter 7 with optical manipulation of polystyrene and silica beads in two different liquid crystals with both homoetropic and planar alignment. This chapter shows results and comparison of passive and active microviscometry. Values of effective viscosity coefficients of the two liquid crystals are given. A discussion is provided on factors affecting laser tweezing experiments in liquid crystals, including director distortion, surface anchoring and accurate particle tracking.

Finally, Chapter 8 summaries the important results and conclusions drawn of the conducted research followed by suggestions for future experimental work to be carried out. Details of the alignment procedure for this laser tweezing system are given in Appendix A. Presented in Appendix B is a proof of the Royal Society Discussion Meeting paper: 'Pushing, pulling and twisting liquid crystal systems; exploring new directions with laser manipulation'.

Chapter 2

Laser Tweezers and Statistical Methods

This chapter details the theoretical basis for optical confinement, including trapping efficiency and Faxén's correction for an object close to an interface. The statistical methods chosen for analysis of the data presented in this thesis are outlined, with special attention being paid to power spectral density analysis.

2.1   Optical theory

Laser tweezers exploit the nature of photons which carry a momentum p,

$$p = \frac{\mathtt{E}}{c} = \frac{h}{\lambda} \tag{2.1}$$

where $\mathtt{E} = hf$ is the energy of a photon with frequency f and wavelength λ, and h is Planck's constant. The resultant momentum imparted to microscopic particles in an optical trap is referred to as *radiation pressure*. The radiation pressure P_{rad} due to an electromagnetic wave incident on a surface is equal to the wave's energy;

$$P_{\mathrm{rad}} = \frac{1}{2}\left(\varepsilon_0 E^2 + \frac{B^2}{\mu_0}\right) \tag{2.2}$$

where E and B are the amplitude of the electric and magnetic field vectors, **E** and **B**, respectively, ε_0 is the permittivity of free space and μ_0 is the perme-

ability of free space. This can also be expressed in terms of the magnitude of the Poynting vector, $S = | \mathbf{S} |$,

$$P_{\text{rad}} = \frac{S}{c} \tag{2.3}$$

where $\mathbf{S} = \frac{1}{\mu_o} \mathbf{E} \times \mathbf{B}$. The time-averaged value of $\langle S \rangle$ is *irradiance* and is defined as the power P incident on a surface with unit area A, but is commonly referred to as intensity I.

Laser tweezers can measure forces over a range of 1-100 pico-Newtons (pN) with pN accuracy [113] using a variety of different methods. The differing theories that describe how an object can be optically trapped depends upon the particle size relative to the trapping laser wavelength λ. Particles with a diameter $d > \lambda$, are considered to be in the **Mie regime** where the trapping forces can be understood in terms of geometrical ray optics.

Comparatively, trapping of particles with $d < \lambda$ is described by the **Rayleigh regime** using Rayleigh scattering theory, where the particle is treated as an electromagnetic dipole [36]. Optical trapping has been successfully established for both Mie and Rayleigh particles [207, 208]. In practice, laser tweezers are employed in an intermediate regime where neither model provides a perfectly accurate quantitative description [38, 209].

This thesis focusses on particles described by the **ray optics** (RO) **regime** where, in some instances, $d \approx \lambda$ (in this case, $\lambda = 1.064 \, \mu\text{m}$), whilst theory of the Rayleigh regime can be found elsewhere [53, 210].

2.1.1   Ray optics regime

The most widely adopted setup to generate laser tweezers uses an objective lens to tightly focus a laser beam, which ensures complete three-dimensional confinement. The overall trapping force experienced by the trapped particle is conventionally described by two constituent forces; the *scattering force* $\mathbf{F}_{\text{scat}}$, and the *gradient force* $\mathbf{F}_{\text{grad}}$, both due to radiation pressure. The scattering force is due to photons travelling along the direction of laser beam propagation and tends to push objects along this direction, even in the absence of a stable trap. The gradient force is due to the variation in intensity across the focussed laser beam profile and acts to pull the particle toward the region of greatest intensity, occurring at

the optical trap's focus [4].

A particle is trapped when the gradient force overcomes the scattering force, $\mathbf{F}_{\mathrm{grad}} > \mathbf{F}_{\mathrm{scat}}$, but the scattering force may cause some displacement of the trapping position [122]. It is still possible to trap if $\mathbf{F}_{\mathrm{grad}} < \mathbf{F}_{\mathrm{scat}}$ by using inverted trapping, where the scattering force can be balanced by gravitational forces. An inverted trapping arrangement is employed for the experiments in this thesis.

Optical trapping occurs only when the particle's refractive index n_{p} is greater than the refractive index of the surrounding medium n_{m}; $n_{\mathrm{p}} > n_{\mathrm{m}}$. If this condition is reversed ($n_{\mathrm{p}} < n_{\mathrm{m}}$), $\mathbf{F}_{\mathrm{grad}}$ repels the particle away from the optical trap focus [21, 53].

Let us examine a single light ray of the trapping beam with optical power P whose photon momentum per second is given by $n_{\mathrm{m}}\mathtt{P}/c$. As can be seen in Fig. 2.1, when this ray impinges on the surface of a particle with refractive index n_{p}, a portion of its optical power is reflected to produce ray PR and the remainder is refracted (or transmitted) giving rise to ray PT.
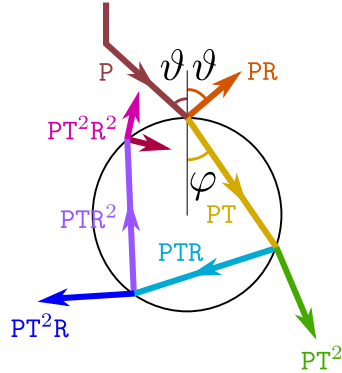
Figure 2.1: Ray optics diagram for a single trapping beam ray P impinging on the surface of a particle giving rise to reflected and refracted (or transmitted) rays PR, PT, PT^2, PTR, PT^{2}R, PTR^2, PT^{2}R^2, and so on. The angle of incidence and refraction are given by ϑ and φ, respectively. (Figure adapted from [211] and [212].)

The photon momentum per second for the reflected ray, PR is $n_{\mathrm{m}}\mathtt{PR}/c$ whilst that associated with the refracted ray PT is thus $n_{\mathrm{p}}\mathtt{PT}/c$ where R and T are the Fresnel coefficients for reflection and refraction, respectively [213]. The trapping force felt by the particle due to the subsequent reflection and refraction of *this* impinging ray is given by

$$\mathbf{F}_{\mathtt{P}} = \frac{n_{\mathrm{m}}\mathtt{P}}{c}\left\{\hat{\mathbf{k}}_{\mathrm{i}} - \mathtt{R}\hat{\mathbf{k}}_{\mathrm{r}} - \mathtt{T}\frac{n_{\mathrm{p}}}{n_{\mathrm{m}}}\hat{\mathbf{k}}_{\mathrm{t}}\right\}, \tag{2.4}$$

where $\hat{\mathbf{k}}_{\mathrm{i}}$, $\hat{\mathbf{k}}_{\mathrm{r}}$ and $\hat{\mathbf{k}}_{\mathrm{t}}$ are unit vectors describing the propagation direction of the incident, reflected and transmitted ray, respectively.

The total trapping force $\mathbf{F}$ felt by the trapped particle — the combination of $\mathbf{F}_{\text{scat}}$ and $\mathbf{F}_{\text{grad}}$ — is the vector sum of contributions due to the reflected ray $\mathtt{PR}$ and the infinite transmitted (refracted) rays; $\mathtt{PT}^2$, $\mathtt{PTR}$, $\mathtt{PT}^2\mathtt{R}$, $\mathtt{PTR}^2$, $\mathtt{PT}^2\mathtt{R}^2$, and so on, as given by

$$
\begin{aligned}
\mathbf{F} &= \mathbf{F}_{\text{scat}} + \mathbf{F}_{\text{grad}} \\
\mathbf{F} &= \frac{n_{\text{m}}\mathtt{P}}{c}\left\{1 + \mathtt{R}\cos(2\vartheta) - \frac{\mathtt{T}^2\left[\cos(2\vartheta - 2\varphi) + \mathtt{R}\cos(2\vartheta)\right]}{1 + \mathtt{R}^2 + 2\mathtt{R}\cos(2\varphi)}\right\}\hat{\mathbf{k}}_{\parallel} \\
&\quad + \frac{n_{\text{m}}\mathtt{P}}{c}\left\{\mathtt{R}\cos(2\vartheta) - \frac{\mathtt{T}^2\left[\sin(2\vartheta - 2\varphi) + \mathtt{R}\sin(2\vartheta)\right]}{1 + \mathtt{R}^2 + 2\mathtt{R}\cos(2\varphi)}\right\}\hat{\mathbf{k}}_{\perp}
\end{aligned}
\tag{2.5}
$$

where ϑ is the angle of incidence and φ is the angle of refraction as shown in Fig. 2.1. Here, $\hat{\mathbf{k}}_{\parallel}$ and $\hat{\mathbf{k}}_{\perp}$ are unit vectors parallel and perpendicular to the direction of the incident ray [211, 212].

The role of $\mathbf{F}_{\text{grad}}$ in the ray optics regime is illustrated in Fig. 2.2 where the direction of light propagation is parallel and the spatial light gradient is perpendicular to the beam axis, z, respectively. For a particle displaced from the z-axis of a Gaussian TEM_{00} mode laser beam (Fig. 2.2(a)), two rays $\mathbf{p}_1$ and $\mathbf{p}_2$ impinging on its surface differ in intensity. Hence, their associated momentum changes $\Delta\mathbf{p}_1$ and $\Delta\mathbf{p}_2$, respectively differ in magnitude, such that $\Delta\mathbf{p}_1 > \Delta\mathbf{p}_2$. Consequently, the particle experiences both a resultant momentum change $\Delta\mathbf{p}_x$ and; due to the conservation of momentum, a lateral restoring force $\mathbf{F}_{\text{grad}}$ so as to oppose the particle's lateral displacement.

For a particle displaced above or below the trap focus (Figs. 2.2(b) and 2.2(c), respectively) rays $\mathbf{p}_1$ and $\mathbf{p}_2$ are of approximately equal intensity, where their individual momentum changes, $\Delta\mathbf{p}_1$ and $\Delta\mathbf{p}_2$, respectively, are equal and opposite. Thus, the particle experiences a resultant momentum change $\Delta\mathbf{p}_z$ resulting in an axial restoring force $\mathbf{F}_{grad}$ towards the optical trap focus in opposition to the particle's axial displacement.

2.2   Statistical Analysis

Calibration of an optical trap for position and optical trap strength — or stiffness — can be performed using various techniques as mentioned in Chapter 1 and

(a) Lateral gradient force $\mathbf{F}_{\text{grad}}$.

(b) Axial gradient force downwards $\mathbf{F}_{\text{grad}}$.

(c) Axial gradient force upwards $\mathbf{F}_{\text{grad}}$.
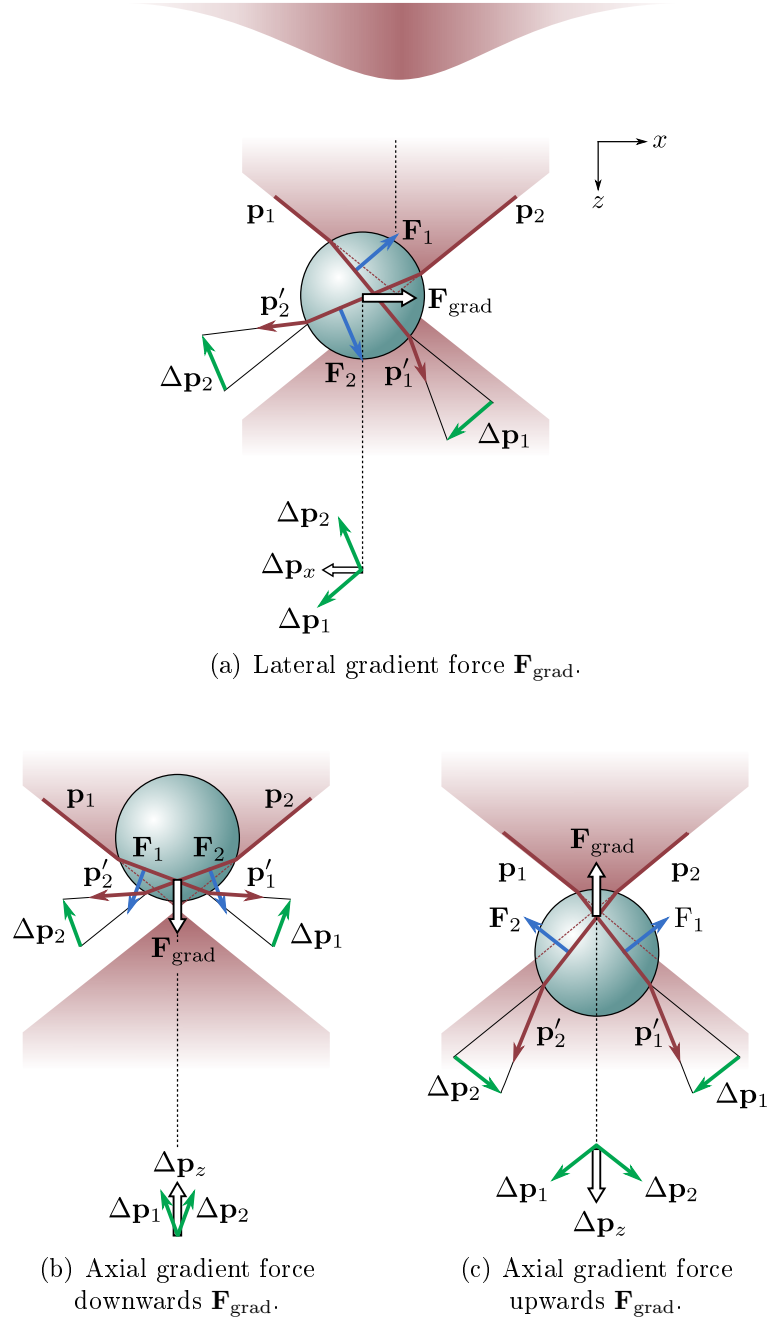
Figure 2.2: Optical trapping in the ray optics regime where particle diameter $d \approx \lambda$. The Gaussian intensity profile of the optical trapping beam creates a gradient force $\mathbf{F}_{\text{grad}}$ which acts to pull the particle towards the region of greatest intensity where (a) shows the *lateral* $\mathbf{F}_{\text{grad}}$ due to the varying intensity of the impinging rays $\mathbf{p}_1$ and $\mathbf{p}_2$ for a particle displaced from the laser beam axis (z-axis). Whilst (b) and (c) show the *axial* $\mathbf{F}_{\text{grad}}$ acting on a particle displaced above and below the trap focus, respectively. The scattering force $\mathbf{F}_{\text{scat}}$ acting in the direction of beam propagation is not shown. (Figure adapted from [209] and [211].)

described in a comprehensive review article by Neuman and Block [53]. This section examines the Langevin equation of motion to further quantify the forces experienced by an optically trapped particle followed by the theory of frequency and time-domain analysis.

2.2.1   Langevin equation of motion

An optical trap is analogous to a Hookean spring where the particle behaves like an overdamped harmonic oscillator for small displacements and the optical potential is harmonic about the equilibrium position. The motion of an optically trapped particle can be described by the one-dimensional Langevin equation,

$$m\ddot{\mathbf{x}}(t) + \gamma\dot{\mathbf{x}}(t) + \kappa\mathbf{x}(t) = \mathbf{F}_{\mathrm{B}}(t) \tag{2.6}$$

where $\mathbf{x}(t)$ is a vector representing the particle's displacement from the optical trap centre as a function of time, m is its mass, γ is the viscous drag coefficient of the fluid surrounding the trapped particle, κ is the optical trap stiffness and $\mathbf{F}_{\mathrm{B}}(t)$ is the force due to thermal fluctuations.

The first term (left) represents the inertial force. Typical optical trapping experiments are performed in the limit of low Reynolds number $\mathrm{Re} \ll 1$, where viscous forces dominate over inertial forces and the system is heavily overdamped. In this regime, this term is several orders of magnitude smaller than any frictional forces, meaning this term can be considered negligible.

The second term represents the viscous drag force and Stokes' law: a spherical particle moving through a viscous fluid at velocity $\mathbf{v} \equiv \dot{\mathbf{x}}$ will experience a Stokes' viscous drag force $\mathbf{F}_{\mathrm{S}} = \gamma\mathbf{v}$, where the viscous drag coefficient $\gamma = 6\pi\eta r$; η is the dynamic fluid viscosity of the surrounding medium and r is particle radius. This expression is valid for a Newtonian fluid where η is constant.

The third term in Eq. (2.6) describes the optical restoring force $\mathbf{F}_{\mathrm{T}} = -\kappa\mathbf{x}$ in one dimension where κ, optical trap stiffness, is analogous to the spring constant [25]. The axial trap stiffness κ_z is weaker than the trap stiffness in the lateral directions κ_x and κ_y since the trapped particle will scatter the light such that the potential becomes asymmetric. $\mathbf{F}_{\mathrm{T}}$ acts to counteract the particle's displacement and restore it to its equilibrium position at the centre of the optical

trap. It also optically confines the particle such that low frequency fluctuations are curtailed but high frequency vibrations due to thermal fluctuations still occur. As previously stated, the force due to thermal fluctuations, or Brownian motion, acting on the particle is given by $\mathbf{F}_{\mathrm{B}}(t)$ in Eq. (2.6) where $\langle \mathbf{F}_{\mathrm{B}}(t) \rangle = 0$.

The *viscous drag force method* of position calibration employs the drag force component of Eq. (2.6). The technique applies a known $\mathbf{F}_{\mathrm{S}}$ until the particle is released from the optical trap. At this point, the Stokes' viscous drag force and the optical trapping force are equivalent $\mathbf{F}_{\mathrm{S}} = \mathbf{F}_{\mathrm{T}}$ which allows κ to be calculated if η is known, or vice versa. At low Reynold's number, this is the same as keeping the trapped bead fixed and moving the surrounding medium.

Comparatively, the full Langevin equation, Eq. (2.6), is integral to performing position and trap stiffness calibration, whether using frequency or time domain analysis, or Boltzmann statistics and equipartition theorem. The theoretical basis for each technique shall be described in the following sections, using the position time series of an optically trapped $2\,\mu\mathrm{m}$ polystyrene (PS) as illustration.

2.2.2 Equipartition and Boltzmann statistics

The equipartition of energy states that each degree of freedom in thermal equilibrium has $k_{\mathrm{B}}T/2$ of thermal energy where k_{B} is Boltzmann's constant and T is absolute temperature. Equating this to the thermal energy of an optically trapped particle in a harmonic potential yields the following relation

$$\frac{1}{2}k_{\mathrm{B}}T = \frac{1}{2}\kappa \left\langle x^2 \right\rangle \tag{2.7}$$

where $\left\langle x^2 \right\rangle$ is the particle's *positional variance*, or the distribution of positions visited by the trapped particle during thermal fluctuations [214].

For an optically trapped particle, the probability density of finding the particle at a given position x within a potential $U(x)$ is described by Boltzmann statistics, as given by

$$P(x) \propto \exp\left(-\frac{U(x)}{k_{\mathrm{B}}T}\right). \tag{2.8}$$

We expect $P(x)$ to be proportional to the histogram of particle positions $H(x)$;

$$U(x) = -k_B T \ln\left[H(x)\right] + k_B T \ln C' \tag{2.9}$$

where the second term, a potential offset with constant C', can be neglected [215].

For small displacements from the equilibrium position x_0 — that is, the trap centre — the potential well can be approximated by a harmonic potential

$$U(x) = \frac{1}{2}\kappa_x (x - x_0)^2 \tag{2.10}$$

where an equivalent expression exists in the y direction. Despite the optical trapping force possibly being weaker with an asymmetric potential, the parabolic potential approximation can also be applied in the z direction and experimental data to support this can be seen in Chapter 4.

Using Eqs. (2.8) to (2.10), one can derive an expression for $P(x)$. Hence, the x histogram is defined such that

$$H(x) \propto P(x) = C \exp\left(-\frac{\kappa_x}{2k_B T}(x - x_0)^2\right) \tag{2.11}$$

which describes a Gaussian distribution given by

$$G(x) = \mathcal{C} \exp\left(-\frac{(x - \mu_x)^2}{2\sigma_x^2}\right), \tag{2.12}$$

with mean μ_x, standard deviation σ_x and normalisation constant $\mathcal{C}$. Comparing $G(x)$ with $H(x)$ in Eq. (2.11), we deduce $\mu_x = x_0$ and $\kappa_x = k_B T / \langle x^2 \rangle$ since $\sigma_x^2 \equiv \langle x^2 \rangle$. This is the same result as given in Eq. (2.7).

Experimentally, this approach requires the position of the particle to be recorded as a function of time, as shown in Fig. 2.3 for a $2\,\mu m$ PS bead optically trapped in water. The histogram of positions visited by the particle $H(x)$ is then fitted to a Gaussian distribution to determine $\langle x^2 \rangle$, as shown in Fig. 2.4(a).

Observing the particle's positional variance is a simple and common technique for determining κ and does not require a value for γ, meaning this method is independent of host media and trapped particle. The technique is susceptible to instrumental noise and drift, which, as shall be seen later in Chapter 4, will in-
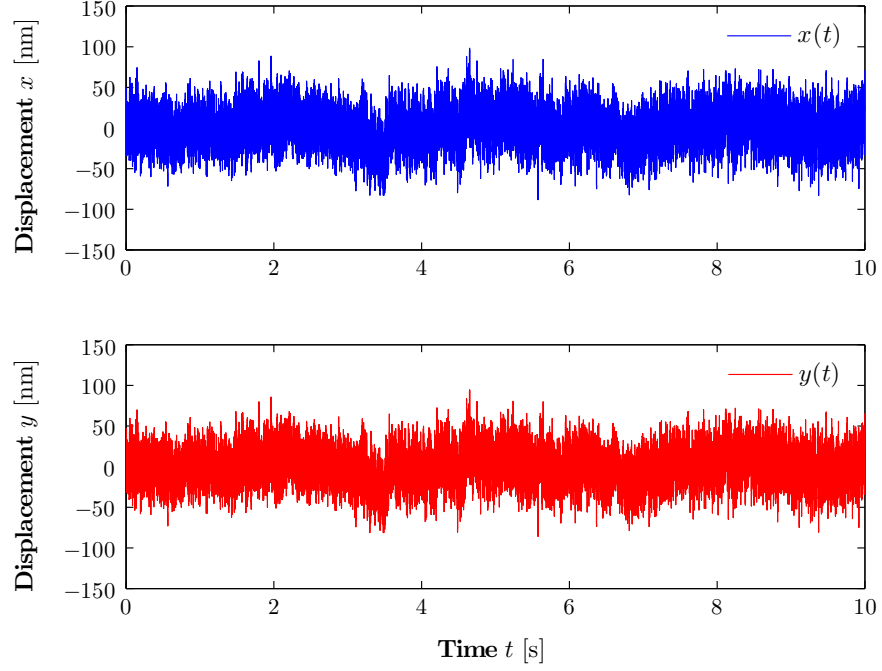
Figure 2.3: Position time series, $x(t)$ and $y(t)$ for an optically trapped $2\,\mu\mathrm{m}$ polystyrene (PS) bead in water.

crease the positional variance and therefore, underestimate κ [53, 54, 118], whilst low pass filtering will have the opposite effect [53].

For particle positions far from x_0, $U(x)$ is no longer harmonic and therefore, a Gaussian distribution is inadequate to describe it. To solve this and improve accuracy, the parabola can be fit to the central region of the potential well — where $U(x)$ *is* harmonic — corresponding to $\pm 1\sigma$, represented by the dashed lines in Fig. 2.4(b).

2.2.3   Power spectral density analysis

Let us return now to the Langevin equation, Eq. (2.6), and consider the over-damped regime, where we neglect the inertial term, such that,

$$\gamma\dot{\mathbf{x}} + \kappa\mathbf{x}(t) = \mathbf{F}_{\mathrm{B}}(t). \tag{2.13}$$

Using an appropriate Fourier transformation, the magnitude of the particle's position fluctuations can be transformed from the time domain t to the frequency
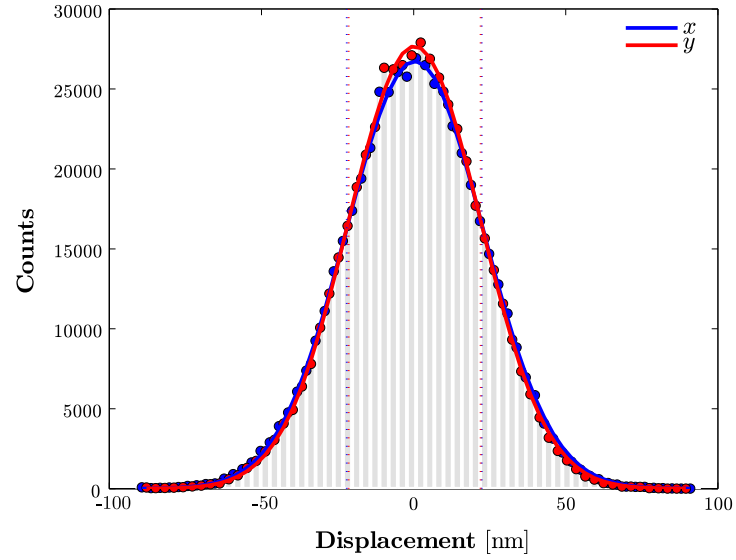
(a)
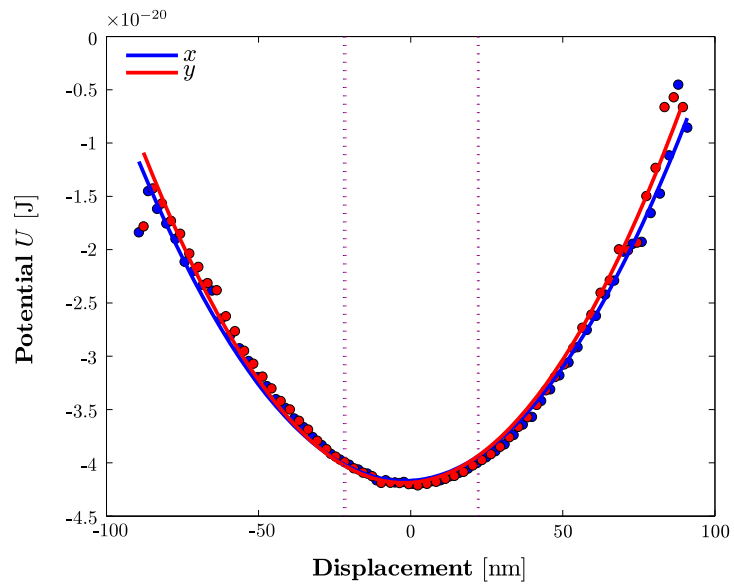
(b)

Figure 2.4: (a) Gaussian distribution of positions visited by am optically trapped bead and (b) the associated optical potential for the time series shown in Fig. 2.3. The dashed lines correspond to $\pm 1\sigma$.

domain f;

$$\mathbf{x}(t) = \int_{-\infty}^{\infty} \mathbf{X}(f) e^{-2\pi i f t} \, \mathrm{d}f \tag{2.14}$$

where $\mathbf{X}(f)$ denotes the Fourier transform of $\mathbf{x}(t)$. Figure 2.3 shows a typical position time series $\mathbf{x}(t)$ (and $\mathbf{y}(t)$) for an optically trapped particle. We can also write the Fourier transform of the particle's velocity $\dot{\mathbf{x}}$ as

$$\dot{\mathbf{x}}(t) = -2\pi i f \int_{-\infty}^{\infty} \mathbf{X}(f) e^{-2\pi i f t} \, \mathrm{d}f = -2\pi i f \mathbf{X}(f). \tag{2.15}$$

Therefore, if we take the Fourier transform of both sides of the Langevin equation in the overdamped regime Eq. (2.13) and factorise, we obtain the following expression,

$$2\pi\gamma \left(f_c - if \right) \mathbf{X}(f) = \mathbf{F}_{\mathrm{B}}(f) \tag{2.16}$$

where the ratio between the trap stiffness and drag coefficient is given by the *corner frequency* f_{c}:

$$f_{\mathrm{c}} = \frac{\kappa}{2\pi\gamma} \tag{2.17}$$

which describes the characteristic roll frequency of the optical trap shown in Fig. 2.5. More specifically, it defines the difference between optical trapping and thermal fluctuations. Now, taking the square modulus of Eq. (2.16) one obtains,

$$4\pi^2\gamma^2 \left(f_{\mathrm{c}}^2 + f^2 \right) |\mathbf{X}(f)|^2 = |\mathbf{F}_{\mathrm{B}}(f)|^2 \tag{2.18}$$

where the power spectrum of $x(t)$ is defined as $S_x(f) = |X(f)|^2$ and the power spectrum due to Brownian motion $S_{\mathrm{B}}(f) = |F_{\mathrm{B}}(f)|^2$. Taking into account that $S_{\mathrm{B}}(f)$ is a constant equal to $4\gamma k_{\mathrm{B}}T$, with an average value $\langle S_{\mathrm{B}}(f) \rangle = 0$ [216], Eq. (2.18) can be rewritten such that the power spectral density (PSD) is given by

$$S_x(f) = \frac{k_{\mathrm{B}}T}{\gamma\pi^2 \left(f_{\mathrm{c}}^2 + f^2 \right)} \; . \tag{2.19}$$

Equation (2.19) has an approximate Lorentzian profile as shown in Fig. 2.5. The figure illustrates two distinct regions of power-frequency relationship, where the shift between them is characterised by f_{c}; the point at which the power of thermal motion is half its initial value S_0, i.e. $S_{\mathrm{c}} = S_0/2$ [122]. More specifically, for frequencies $f \ll f_{\mathrm{c}}$, the particle is confined by the optical trap and the PSD remains approximately constant such that $S_x(f) \approx S_0 = 4\gamma k_{\mathrm{B}}T/\kappa^2$, as per Eq.

(a)

(b)
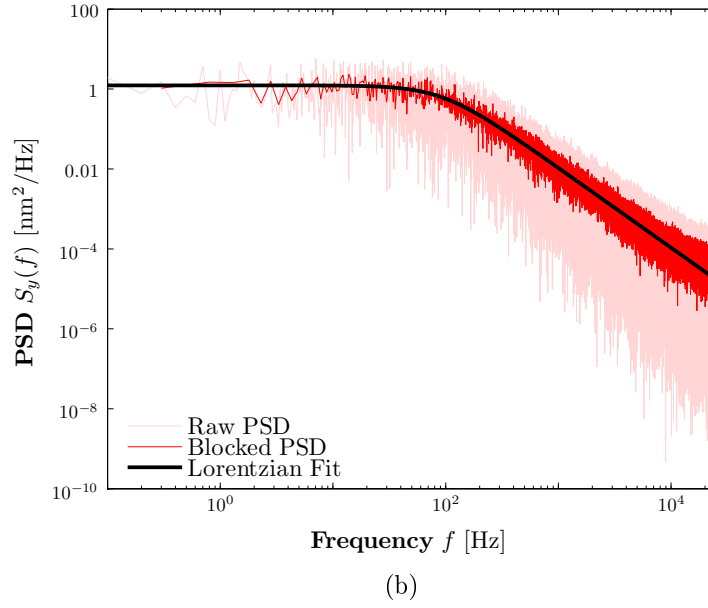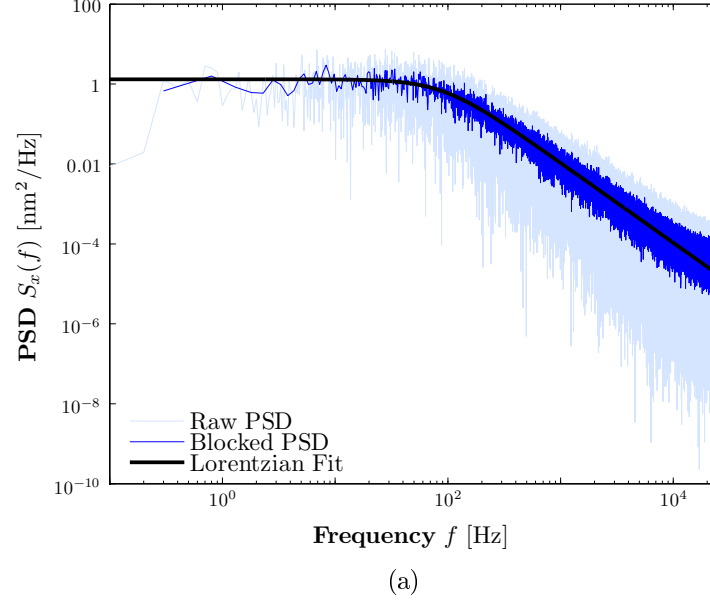
Figure 2.5: Power Spectral Density (PSD) for the (a) x and (b) y directions for the time series shown in Fig. 2.3. At low frequencies $f \ll f_c$, the PSD becomes approximately constant where $S_x(f) \approx S_0$. For high frequencies $f \gg f_c$, $S_x(f)$ is proportional to $1/f^2$ giving a slope of -2, as expected for free diffusion [216].

(2.19). Whereas, for frequencies $f \gg f_{\mathrm{c}}$, the particle experiences only Brownian motion and as such, the PSD $S_x(f)$ is proportional to $1/f^2$ giving a slope of -2, as expected for free diffusion. Thus, it is apparent that for short timescales, the particle does not strongly feel the effect of optical confinement. [216]

Furthermore, if trapping power $\mathsf{P}_1 < \mathsf{P}_2$, the PSD output and f_c is affected such that $f_{\mathrm{c}_1} < f_{\mathrm{c}_2}$ meaning $\kappa_1 < \kappa_2$, as defined by Eq. (2.17). This is an intuitive result with a stronger trapping power producing a stiffer trap, subsequently decreasing the positional variance due to thermal fluctuations $\langle x^2 \rangle$, and is illustrated in several references [197, 217–221].

As mentioned in Chapter 1, an optically trapped particle's PSD can be used for calibration of position and optical trap stiffness. Equation (2.19) allows κ to be determined from f_{c}, using a calculated value for γ. This is typically performed by recording the intensity variation of the trapping beam with a position sensitive detector, such as a quadrant photodiode, referred to as back focal plane interferometry (BFPI). This method requires the voltage signal produced by the detector to be converted to particle displacement relative to the trap centre.

Video-based tracking methods can also be used provided the bandwidth is sufficient to accurately record the PSD at least one order of magnitude above f_{c} [53, 72]; on the order of kHz. One might also wish to account for video-image motion blur as described by Wong and Halvorsen [222].

The theory and application of both methods; back focal plane interferometry and high-speed video microscopy, are described in further detail as part of the Optical Setup in Chapter 4 which also includes the details of calibration for this work.

In a system where the medium viscosity is unknown, a combination of optical potential and PSD analysis can be used, to first calculate κ and f_{c}, respectively. From Eq. (2.17), and remembering the equipartition theorem of Eq. (2.7) gives $\kappa = k_{\mathrm{B}} T / \langle x^2 \rangle$, viscosity can be calculated using

$$\eta = \frac{k_{\mathrm{B}} T}{12 \pi^2 r \langle x^2 \rangle f_{\mathrm{c}}} \tag{2.20}$$

where the drag coefficient $\gamma = 6 \pi \eta r$ has been incorporated.

2.2.4   Autocorrelation

For a particle in a harmonic potential well, the overdamped Langevin equation Eq. (2.13) can be solved for $x(t)$ to give its autocorrelation function (ACF), which decays exponentially as shown by the circles in Fig. 2.6 and given by

$$\langle x(t + \tau)x(t)\rangle = \langle x^2 \rangle \exp\left(-\frac{\tau}{\tau_{\mathrm{c}}}\right) \tag{2.21}$$

where τ is the correlation time and τ_{c} is the decay time — also known as the corner or trap relaxation time — defined as

$$\tau_{\mathrm{c}} = \frac{\gamma}{\kappa} \ . \tag{2.22}$$

Substituting $\gamma = 6\pi\eta r$ and $\kappa = k_{\mathrm{B}}T/\langle x^2 \rangle$ into Eq. (2.22) allows viscosity to be calculated from the ACF using

$$\eta = \frac{\tau_{\mathrm{c}} k_{\mathrm{B}} T}{6\pi r \langle x^2 \rangle} \ . \tag{2.23}$$

At $\tau = 0$, Eq. (2.21) becomes $\langle x^2 \rangle$ illustrating free diffusion whilst at long time scales $\tau \to \infty$, the autocorrelation function $\langle x(t + \tau)x(t)\rangle \to 0$ as the particle is confined by the optical trap. Incidentally, Eq. (2.22) can also be expressed as $\tau_{\mathrm{c}} = 1/2\pi f_{\mathrm{c}}$, thus producing the same result as Eq. (2.20), where η is calculated using the PSD and f_c.

As trapping power, and hence κ, is increased, the ACF's maximum value decreases to give a shorter τ_{c} as shown in experiments by Czerwinski, Richardson and Oddershede [223] and Gibson *et al.* [217]. This is in perfect agreement with Eq. (2.22) where κ is inversely proportional to τ_{c}.

When the ACF is normalised to unity, the technique does not rely on the exact calibration of the position detection but works on the assumption that the trapped particle is confined within a harmonic potential.

(a)

(b)
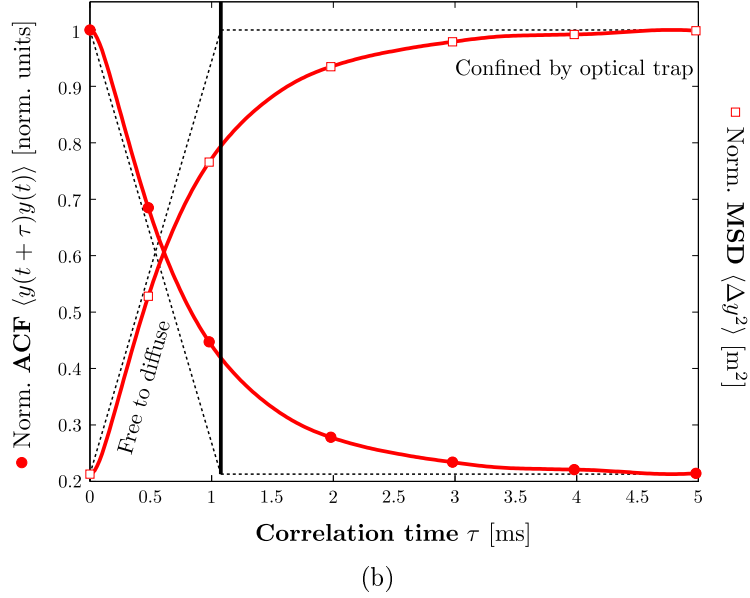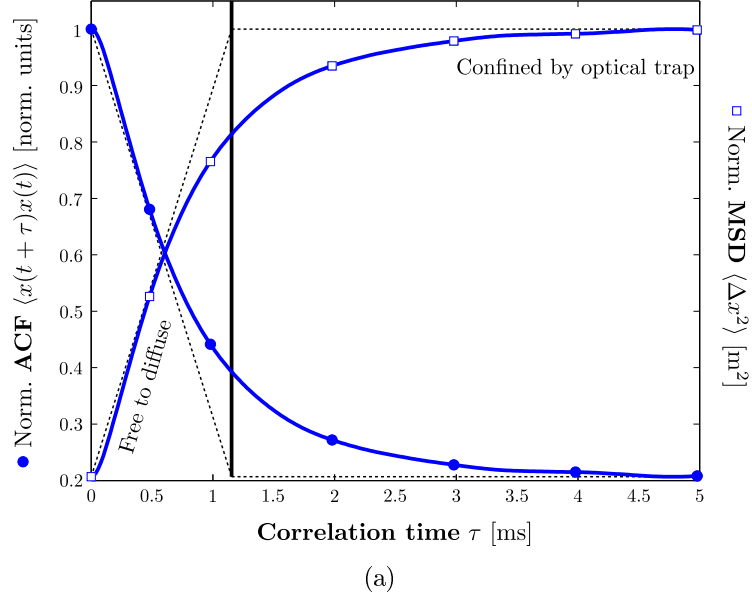
Figure 2.6: Normalised autocorrelation (filled circles) and mean squared displacement (open squares) functions for (a) x and (b) y directions for the time series shown in Fig. 2.3. The dashed lines indicate the cross over between free diffusion and optical confinement to give the corner decay time τ_{c}, represented by the solid black line.

2.2.5   Mean square displacement

The mean square displacement (MSD) of $x(t)$ is given by

$$\left\langle \Delta x^2(\tau) \right\rangle = \left\langle [x(t+\tau) - x(t)]^2 \right\rangle \tag{2.24}$$

where τ is again the correlation time. The MSD for the time series shown in Fig. 2.3 can be seen in Fig. 2.6. The MSD can also be related to the ACF given by Eq. (2.21);

$$\left\langle \Delta x^2(\tau) \right\rangle = 2 \left\langle x^2 \right\rangle - 2 \left\langle x(t+\tau)x(t) \right\rangle \tag{2.25}$$

which by substitution yields

$$\left\langle \Delta x^2(\tau) \right\rangle = \frac{2k_\mathrm{B}T}{\kappa} \left[1 - \exp\left(-\frac{\kappa\tau}{\gamma} \right) \right]. \tag{2.26}$$

As shown in Fig. 2.6 and from Eq. (2.26), when $\tau = 0$, the MSD is also zero; $\left\langle \Delta x^2(\tau) \right\rangle = 0$. For $0 < \tau < \tau_\mathrm{c}$, the particle freely diffuses and the MSD grows linearly; $\left\langle \Delta x^2 \right\rangle = 2D_0\tau$, where the free diffusion coefficient $D_0 = k_\mathrm{B}T/\gamma$ is given by the Stokes-Einstein relation. Finally, for $\tau \to \infty$, the MSD will plateau at $\left\langle \Delta x^2(\tau) \right\rangle = 2k_\mathrm{B}T/\kappa$ as it feels the effect of the optical confinement. As trapping power, and hence κ, is increased, the MSD plateau value decreases to give a shorter τ_c, also agreeing with Eq. (2.22). [224]

Fitting the exponential expression in Eq. (2.26) to experimental data to determine D_0 or τ_c allows the viscosity to calculated by

$$\eta = \frac{k_\mathrm{B}T}{6\pi D_0 r} = \frac{\kappa\tau_\mathrm{c}}{6\pi r} \ . \tag{2.27}$$

Incidentally, for a loglog plot of the MSD, the gradient lies between 0 and 1, corresponding to a purely elastic or purely viscous material, respectively. Hence, a gradient lying within this range will be that of a viscoelastic material [225].

2.3   Faxén's correction

The hydrodynamical Stokes' drag force $\mathbf{F}_S$ felt by a trapped particle increases with greater proximity to a surface, such as the microscope coverslip, for example. This effect occurs both in the lateral and axial directions. The lateral and axial drag coefficients, $\gamma_{x,y} \equiv \gamma_\parallel$ and $\gamma_z \equiv \gamma_\perp$, respectively, are modified as given by Schäffer, Nørrelykke and Howard [226]:

$$\gamma_\parallel = \frac{6\pi\eta r}{1 - \dfrac{9r}{16Z_\mathrm{T}} + \dfrac{r^3}{8Z_\mathrm{T}^3} - \dfrac{45r^4}{256Z_\mathrm{T}^4} - \dfrac{r^5}{16Z_\mathrm{T}^5}} \tag{2.28}$$

$$\gamma_\perp = \frac{6\pi\eta r}{1 - \dfrac{9r}{8Z_\mathrm{T}} + \dfrac{r^3}{2Z_\mathrm{T}^3} - \dfrac{57r^4}{100Z_\mathrm{T}^4} + \dfrac{r^5}{5Z_\mathrm{T}^5} + \dfrac{7r^{11}}{200Z_\mathrm{T}^{11}} - \dfrac{r^{12}}{25Z_\mathrm{T}^{12}}} \tag{2.29}$$

where Z_T is the distance between the trapped particle and the plane surface or, more specifically (and as before), trap depth. For $Z_\mathrm{T} \to \infty$, $\gamma_\parallel = \gamma_\perp = \gamma \equiv 6\pi\eta r$; the bulk drag coefficient corresponding to Stokes' drag with viscosity η.

The effect a trapped particle's proximity to a surface has on γ can be seen in Fig. 2.7, where the ratio between γ given by Stokes' Law and the corrected drag coefficients $\gamma_\parallel$ and $\gamma_\perp$ are plotted as a function of trap depth Z_T.

The values are calculated using Eqs. (2.28) and (2.29) with $r = 3\,\mu\mathrm{m}$ and $\eta = 0.8999\,\mathrm{mPa\,s}$ (the accepted value for the viscosity of water at $25\,°\mathrm{C}$). The top axis indicates the dimensionless ratio of trap depth to bead radius; Z_T/r. It can be seen that as the particle approaches the surface, i.e. when $Z_\mathrm{T} \to r$ and thus, $Z_\mathrm{T}/r \to 1$ the drag coefficient increases signifi-
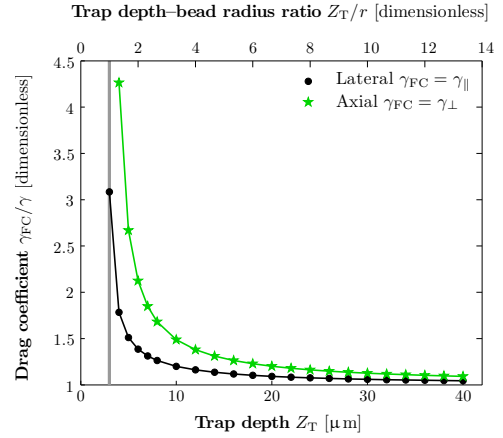
Figure 2.7: The effect on the Stokes' viscous drag coefficient γ due to a trapped particle being in close proximity to a surface. As the bead approaches the surface, the drag coefficient increases significantly, more so in the axial direction.

cantly, more so in the axial direction. Comparatively, as the bead moves far away from the surface such that $Z_\mathrm{T} \gg r$, any effect on γ due to the surface reaches a minimia, where $\gamma/\gamma_\parallel$ and $\gamma/\gamma_\perp$ both tend toward 1.

Tolić-Nørrelykke, Berg-Sørensen and Flyvbjerg [227] describe the use of a Matlab program to account for a frequency-dependent hydrodynamic effect in the theoretical power spectrum when fitting to experimental data. Alternatively, one can use Stokes' drag coefficient with Faxén's correction applied, $\gamma_\parallel$ or $\gamma_\perp$, whilst using an uncorrected theoretical power spectrum.

2.4   Trapping efficiency

The force exerted by a laser beam with power $\mathtt{P}$ travelling through a medium with refractive index n_m is given by

$$\mathbf{F} = Q\frac{n_\mathrm{m}\mathtt{P}}{c} \tag{2.30}$$

where Q is the optical trapping efficiency; a dimensionless constant of proportionality which can be thought of as the fraction of incident power used to exert an optical force. Q accounts for beam parameters, such as spot size, wavelength, and beam profile; and optical properties of the trapped particle, including its size, shape and mass, and refractive index relative to the surrounding medium [38, 228, 229]. For plane waves incident on a perfectly absorbing particle, $Q = 1$.

The quantity $n_\mathrm{m}\mathtt{P}/c$ is the laser beam's total linear momentum flux [38, 211]. Hence, Eq. (2.30) shows an increase in $\mathbf{F}$ is proportional to increases in $\mathtt{P}$, n_m or Q. It is not always possible to maximise each of these quantities. For example, the magnitude of the trapping laser power becomes important for systems which are susceptible to photodamage, such as biological samples, and the refractive index of the host medium is often restricted. For small dielectric or metal particles, $0.03 < Q < 0.1$.

We can derive expressions for Q in the lateral and axial directions, Q_{xy} and Q_z, respectively. Q_{xy} is determined using the viscous drag force method as described

above. Therefore, equating Eq. (2.30) with the viscous drag force $\mathbf{F}_S$ yields

$$Q_{xy} = \frac{c}{n_{\mathrm{m}}\mathsf{P}} \, 6\pi\eta r v_{\mathrm{release}} \tag{2.31}$$

where v_{release} is the velocity at which the particle is released from the optical trap.

To determine Q_z, the trapping power is decreased until the trapped particle 'falls' from the optical trap. The axial trapping efficiency is given by

$$Q_z = \frac{c}{n_{\mathrm{m}}\mathsf{P}_{\mathrm{min}}} \, (\rho_{\mathrm{p}} - \rho_{\mathrm{m}}) \, V_{\mathrm{p}} \, g \tag{2.32}$$

where ρ_{p} and ρ_{m} are the densities of the particle and medium, respectively, V_{p} is the particle's volume and g is the acceleration due to gravity [230]. Here, $\mathsf{P}_{\mathrm{min}}$ is the minimum power required to overcome gravity and to achieve successful axial trapping [38, 231]. When $\mathsf{P} < \mathsf{P}_{\mathrm{min}}$, the particle is pushed out by the scattering force $\mathbf{F}_{\mathrm{scat}}$ [231].

2.5   Measurement and calculation

For clarity, Fig. 2.8 summarises each of the techniques employed in this research; the equipartition (EQ), viscous drag (VD), power spectral density (PSD) and escape force (EF) methods. The equations used, the measurements made and the quantities obtained are shown. The method(s) chosen will depend on the known or desired quantities.

Weighted linear regression was performed using a least squares fitting procedure in Matlab [232] and, where appropriate, figures display the goodness of fit paramater, χ^2. Error expressions were derived from the propagation of errors and their individual quantities combined in quadrature. Any further details necessary are given in the appropriate sections.

2.6   Summary

This chapter details has presented the theoretical basis for laser tweezers with specific focus on the ray optics regime. The statistical methods were summarised,

(a) **EQ method**
Passive

Using:
$$\tfrac{1}{2}k_{\mathrm{B}}T = \tfrac{1}{2}\kappa\left\langle x^2\right\rangle \quad (2.7)$$

Measures:
1. $\mathbf{x}$ bead displacement
2. $\left\langle x^2\right\rangle$ variance

Gives:
Trap stiffness κ

(b) **VD method**
Active

Stokes' Force = Trapping Force
$$\mathbf{F}_{\mathrm{S}} = 6\pi\eta r\mathbf{v}$$
$$\mathbf{F}_{\mathrm{T}} = \kappa\mathbf{x} \quad (2.6)$$

Measures:
1. $\mathbf{v}$ stage velocity
2. $\mathbf{x}$ bead displacement

Gives:
Viscosity η
or
Trap stiffness κ

(c) **PSD method**
Passive

Using:
$$\kappa = 2\pi\gamma f_{\mathrm{c}} \quad (2.17)$$
$$\eta = \frac{k_{\mathrm{B}}T}{12\pi^2 r\langle x^2\rangle f_{\mathrm{c}}} \quad (2.20)$$

Measures:
1. $\mathbf{x} \to \mathrm{FFT} \to f_{\mathrm{c}}$
2. $\left\langle x^2\right\rangle$ from ACF

Gives:
Viscosity η
or
Trap stiffness κ

(d) **EF method**
Active

Trapping Force = Escape Force
$$\mathbf{F}_{\max} = 6\pi\eta r\mathbf{v}_{\mathrm{esc}} \quad (7.2)$$
$$= \frac{Qn_{\mathrm{m}}\mathbf{P}_{\mathrm{T}}}{c} \quad (2.30,\ 7.3)$$

Measures:
1. $\mathbf{v}_{\mathrm{esc}}$ escape velocity
2. $\mathbf{P}_{\mathrm{T}}$ trapping power

Gives:
Viscosity η

Figure 2.8: Flow diagram summarising each of the techniques employed in this research; (a) EQ: equipartition method, (b) VD: viscous drag method, (c) PSD: power spectral density method and (d) EF: escape force method. Each method details the relationships used (with reference to relevant equation numbers in brackets), which variables are measured and the quantities obtained.

derived from the Langevin equation of motion, with details of power spectral density analysis. Trapping efficiency and surface proximity to an optically trapped particle were discussed. Finally, a flow diagram detailing each of the four methods employed in this research; specifically the quantities measured and calculated, provides a clear reference.

Chapter 3

Liquid Crystals Background and Methods

At this stage, it is important to introduce key definitions, theoretical concepts, physical characteristics and practical techniques related to liquid crystal physics. This section will also provide the specifications of the chosen liquid crystals and colloids and detail the sample preparation process.

A liquid crystal (LC) phase is a *mesomorphic phase*; it forms an intermediate phase whose mechanical and symmetry properties are between that of the solid crystalline and isotropic liquid phases.

Two main types of liquid crystal exist; *thermotropic* and *lyotropic*. Thermotropic LCs have small organic molecules, typically rod or disk-shaped, whose mesomorphic behaviour depends on temperature. Lyotropic LCs can be comprised of a mixture of molecules whose behaviour depends on both the concentration of the species present and the temperature. [149] There are also chromonic liquid crystals, or chromonics, which belong to a class of lyotropic liquid crystals. They generally consist of rigid, plank-shaped or blade-like molecules and form due to the self-organisation of aromatic compounds with ionic or hydrophilic groups in aqueous solutions [233].

This research focuses on nematic liquid crystals (NLCs), which are thermotropic mesophases consisting of rod shaped molecules with one axis significantly longer than the other two. This causes the nematic molecules — also known as nematogens — to collectively lie with their long axes pointing along one

$\hat{n}$
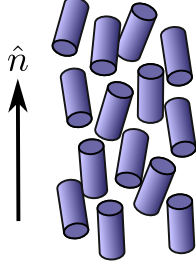
Figure 3.1: A nematic liquid crystal consists of rod shaped molecules with one axis significantly longer than the other two. Thus, the nematic molecules, or nematogens, collectively align themselves in one general direction given by the director $\hat{n}$ whilst their position remains uncorrelated.

particular direction whilst their positions are uncorrelated, as shown in Fig. 3.1. The average direction along which the nematic molecules align is known as the '*director*' denoted by $\hat{n}$, where $\hat{n}$ and $-\hat{n}$ are indistinguishable. [234, 235]

3.1 Anisotropic properties

Nematic materials are inherently anisotropic due to the orientational order present resulting in the manifestation of several anisotropic properties such as birefringence, dielectric anisotropy and anisotropic viscosity, which will be described below.

3.1.1 Birefringence

Optically, anisotropy presents itself as *birefringence*; light passing through the liquid crystal will experience a different refractive index depending on its orientation relative to $\hat{n}$. Light polarised perpendicular to the optic axis, and hence $\hat{n}$, will experience the *ordinary* refractive n_{o} whilst light polarised parallel to the optic axis and $\hat{n}$ will experience the *extraordinary* refractive index n_{e}. These components are often referred to as the *o*-ray (fast component) and *e*-ray (slow component), respectively.

The light rays emerging from a birefringent material of thickness $\mathtt{h}$ experiences a phase difference as given by

$$\Delta\vartheta = \frac{2\pi\mathtt{h}\Delta n}{\lambda} \tag{3.1}$$

where the material's birefringence $\Delta n = n_{\mathrm{e}} - n_{\mathrm{o}}$, and λ is the wavelength [236]. Birefringent materials are employed for phase retardation where varying the thick-
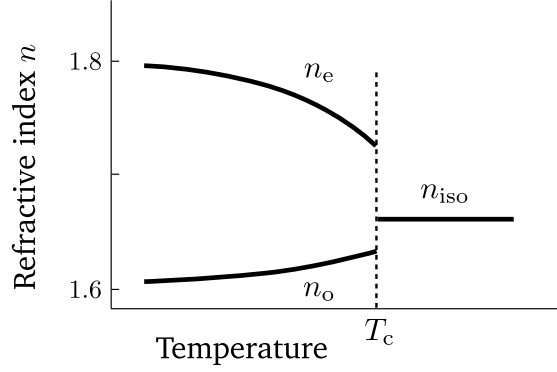
Figure 3.2: Refractive index as a function of temperature. The ordinary and extraordinary refractive indices are given by n_o and n_e, respectively whilst n_{iso} denotes the isotropic refractive index. T_c is the clearing temperature. Values given are just for illustration.

ness allows control over the phase shift and hence the polarisation of the emerging light.

Refractive index is temperature dependent as shown in Fig. 3.2; which can result in temperature dependent birefringence also. Again, as the thermal energy of the system increases with temperature, increased fluctuation of the molecular orientation occurs. Therefore, as the temperature of the nematic material increases, Δn decreases until the system becomes optically isotropic at the transition, or *clearing* temperature T_c.

Electric and magnetic fields can be applied to manipulate $\hat{n}$ and therefore control the effective Δn as employed in LCD technology.

3.1.2 Dielectric anisotropy

Dielectric properties relate the response of a material to the application of an electric field **E** which, when applied to a LC, can alter its refractive index via the induction of a dipole moment.

The permittivity of a material describes its polarisability in response to **E** and is given by

$$\varepsilon = \varepsilon_0 \chi_e \tag{3.2}$$

where ε_0 is the permittivity of free space and χ_e the electric susceptibility. For small electric fields, the dipole moment per unit volume, or *polarisation density*

$\mathbf{P} = \varepsilon \mathbf{E}$ [236, 237].

Similar to a nematic's refractive index, ε differs depending on the direction relative to $\hat{n}$. Thus, a dielectric anisotropy $\Delta\varepsilon$ results, which can be positive or negative, defined as

$$\Delta\varepsilon = \varepsilon_{\parallel} - \varepsilon_{\perp} \tag{3.3}$$

where $\varepsilon_{\parallel}$ is the permittivity parallel to $\hat{n}$ and $\varepsilon_{\perp}$ is perpendicular to $\hat{n}$. The larger $\Delta\varepsilon$, the smaller the electric field required to invoke a response from the LC. As with birefringence, dielectric anisotropy is temperature dependent as shown in Fig. 3.3.
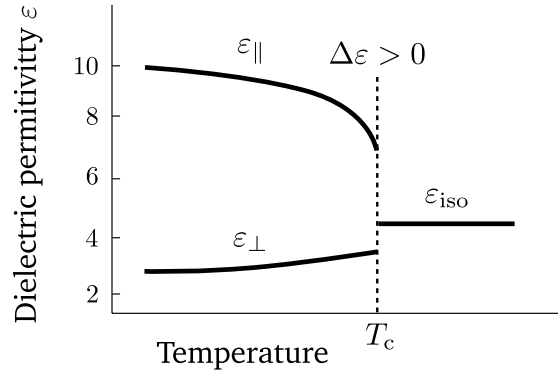
Figure 3.3: Dielectric permittivity of a nematic with dielectric anisotropy $\Delta\varepsilon > 0$ as a function of temperature. The permittivities parallel and perpendicular to $\hat{n}$ are given by $\varepsilon_{\parallel}$ and $\varepsilon_{\perp}$, respectively whilst $\varepsilon_{\mathrm{iso}}$ denotes the isotropic permittivity. T_{c} is the clearing temperature. Values given are just for illustration.

3.1.3   Anisotropic viscosity

The relationship between $\hat{n}$ and the NLC's fluid velocity, termed '*nematodynamics*', is described by the Ericksen-Leslie equations which include five independent Leslie coefficients α_i where $i = 1, 2, ...5$. Solutions to these equations are paramount for determining LCD switching times. As mentioned in Section 1.5.5, these are typically calculated by determining effective viscosities in shear flow experiments; applying shear to a LC sample cell, in which $\hat{n}$ is aligned electrically or magnetically.

The effective viscosity η, of a LC medium is given by

$$\eta(\theta, \phi) = \eta_1 \sin^2 \theta \cos^2 \phi + \eta_2 \cos^2 \theta + \eta_3 \sin^2 \theta \sin^2 \phi + \eta_{12} \sin^2 \theta \cos^2 \theta \cos^2 \phi \quad (3.4)$$

where η_1, η_2 and η_3 are the three principal anistropic viscosity coefficients, also known as the Mięsowicz viscosity coefficients, concerned with back-flow effects in a NLC and thus, switching times of an NLC device. As shown in Fig. 3.4, the angles θ and ϕ define the orientation of $\hat{n}$ relative to shear flow v and its gradient ∇v. η_{12} is the anisotropic viscosity coefficient associated with $\hat{n}$ not being parallel to either v or ∇v [238].
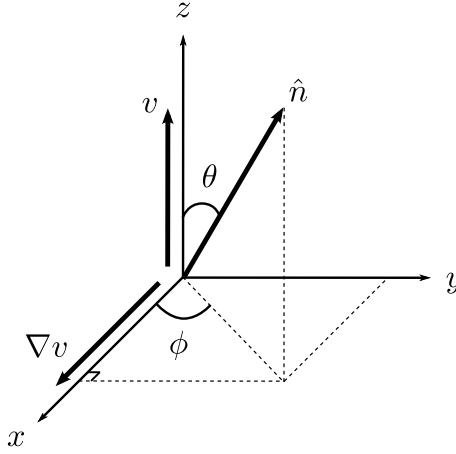
Figure 3.4: Orientation of the LC director $\hat{n}$ relative to the flow velocity v and flow velocity gradient ∇v.

The Mięsowicz viscosity coefficients are defined in terms of the Leslie coefficients as follows

$$\eta_1 = \frac{\alpha_4 + \alpha_5 - \alpha_2}{2}, \quad (3.5)$$

$$\eta_2 = \frac{\alpha_3 + \alpha_4 + \alpha_6}{2}, \quad (3.6)$$

$$\eta_3 = \frac{\alpha_4}{2}, \quad (3.7)$$

$$\eta_{12} = \alpha_1. \quad (3.8)$$

The relevant geometries in a laser tweezers setup can be seen in Fig. 3.5.

Interestingly, in a 3D scenario, the anistropic viscosity coefficients η_1 and η_3 occur simultaneously and are inseparable, so are given by effective viscosity $\eta_{\text{eff}}^{\perp}$ i.e. perpendicular to $\hat{n}$ whilst η_2 is given by $\eta_{\text{eff}}^{\parallel}$; parallel to $\hat{n}$. Experiments with

(a) Mięsowicz viscosity coefficient η_1 where $\hat{n} \perp v$, $\hat{n} \parallel \nabla v$ as in a cell with planar alignment.

(b) Mięsowicz viscosity coefficient η_2 where $\hat{n} \parallel v$, $\hat{n} \perp \nabla v$ as in a cell with homeotropic alignment.

(c) Mięsowicz viscosity coefficient η_3 where $\hat{n} \perp v$, $\hat{n} \perp \nabla v$ as in a cell with planar alignment.
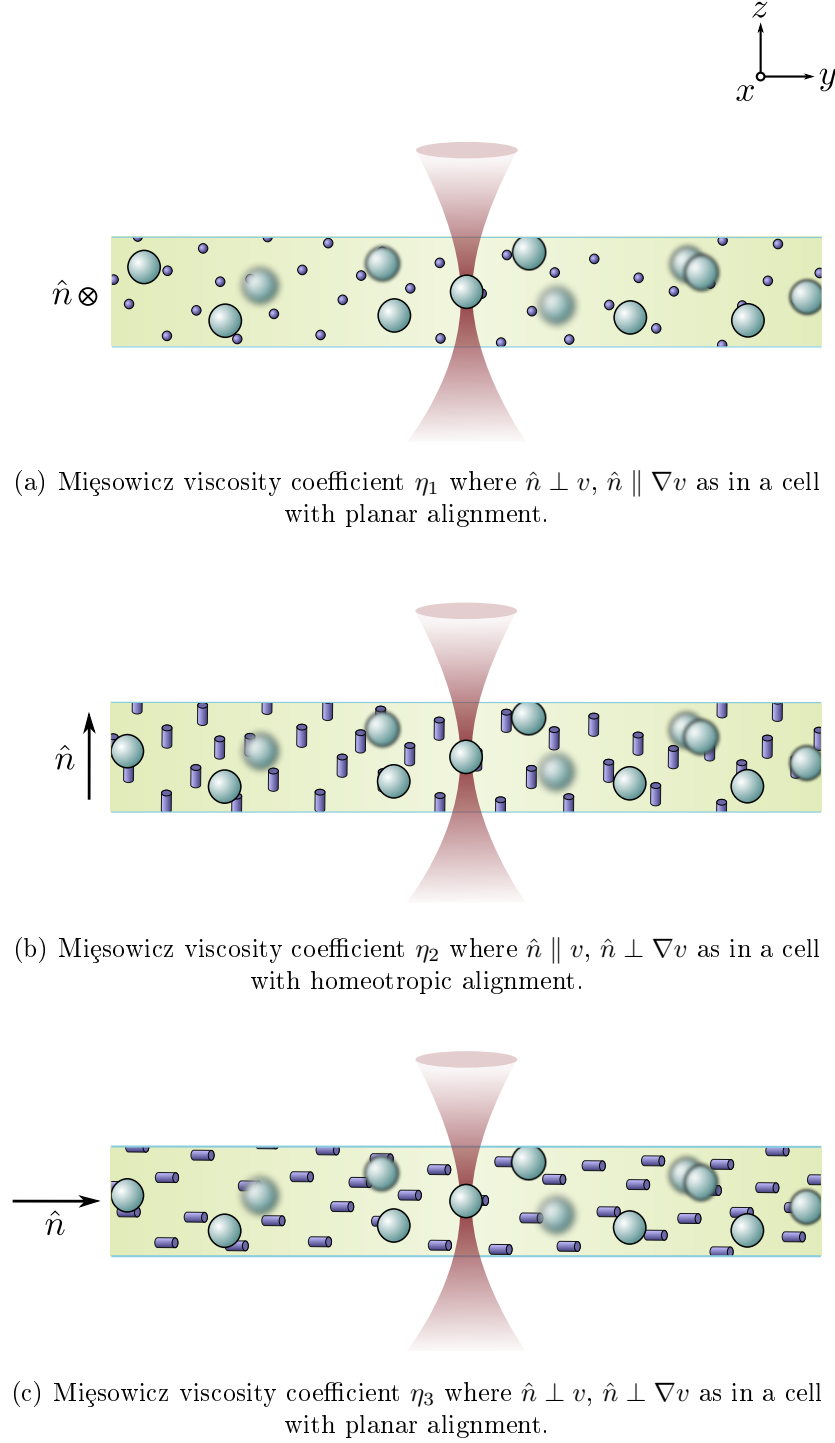
Figure 3.5: The geometry for an optically trapped colloid in a nematic LC medium illustrating the definition of Mięsowicz anisotropic viscosity coefficients (a) η_1, (b) η_2 and (c) η_3 defined in terms of $\hat{n}$ relative to flow velocity v and its gradient ∇v. The effective viscosity $\eta_{\text{eff}}^{\perp}$ describes the combination of η_1 and η_3, whilst $\eta_{\text{eff}}^{\parallel}$ describes η_2, which are are perpendicular and parallel to $\hat{n}$, respectively.

Table 3.1: Relationship between the three planes in a LC cell and its orientation relative to LC director $\hat{n}$. The reader should also refer to Fig. 3.5.

	Planar	Homeotropic
$x \parallel \hat{n}$	$x \perp \hat{n}$	$x \perp \hat{n}$
$y \perp \hat{n}$	$y \parallel \hat{n}$	$y \perp \hat{n}$
$z \perp \hat{n}$	$z \perp \hat{n}$	$z \parallel \hat{n}$

laser tweezers allow measurement of $\eta_{\text{eff}}^{\perp}$ and $\eta_{\text{eff}}^{\parallel}$ where the viscous drag force method has previously been employed for this [167, 168].

It is also possible to determine $\eta_{\text{eff}}^{\parallel}$ and $\eta_{\text{eff}}^{\perp}$ of a LC, leading to η_1, η_2 and η_3, by observing three dimensional position fluctuations of an optically trapped colloid immersed in the LC. As illustrated in Fig. 3.5, for a homeotropic cell, fluctuations occurring in the z direction are parallel to $\hat{n}$, whilst those in the x and y directions are both perpendicular to $\hat{n}$. In a planar cell, fluctuations in the z direction are perpendicular to $\hat{n}$. Depending on the orientation of the planar cell, either the x or y will be parallel to $\hat{n}$. These relationships are also given in Table 3.1.

The following expression allows all Leslie coefficients to be calculated

$$\eta_4 = \eta_3 + \frac{1}{2}(\eta_1 + \eta_2 + 2\eta_3) + \frac{1}{4}\eta_{12}. \tag{3.9}$$

In addition, in order to design efficient LCDs, rotational effects on the NLC should be considered where the viscosity coefficients associated with rotation of $\hat{n}$ are given by γ_1 and γ_2, also defined in terms of the Leslie coefficients;

$$\gamma_1 = \alpha_3 - \alpha_2, \tag{3.10}$$

$$\gamma_2 = \alpha_3 + \alpha_2. \tag{3.11}$$

The aim of the work presented in this thesis will be to measure effective viscosity coefficients parallel and perpendicular to $\hat{n}$; $\eta_{\text{eff}}^{\perp}$ and $\eta_{\text{eff}}^{\parallel}$, respectively.

3.2 Viscoelastic properties

Molecular reorientation can occur when a sufficiently large electric field overcomes the anchoring and viscoelastic properties of a LC. However, this is particularly difficult to achieve at material interfaces, where strong inter-molecular surface anchoring exists. This section describes director distortions, the response of a NLC to an applied electric field and its behaviour following the introduction of colloids.

3.2.1 Director distortion

Gradual director distortion throughout the bulk LC can occur, where the class of distortion depends on its direction relative to $\hat{n}$. The Frank free energy density in a nematic LC describes the amount of director distortion and is given by

$$\mathcal{F}_{\mathrm{d}} = \frac{1}{2}\left[K_1(\nabla \cdot \hat{n})^2 + K_2(\hat{n} \cdot \nabla \times \hat{n})^2 + K_3(\hat{n} \times \nabla \times \hat{n})^2\right] \qquad (3.12)$$

where K_1, K_2 and K_3 are the Frank elastic constants corresponding to the three distortions possible in a LC; splay, twist and bend, respectively whose geometries are shown in Fig. 3.6 [236]. They are typically on the order of 10^{-11}N [234].

(a) Splay   (b) Twist   (c) Bend
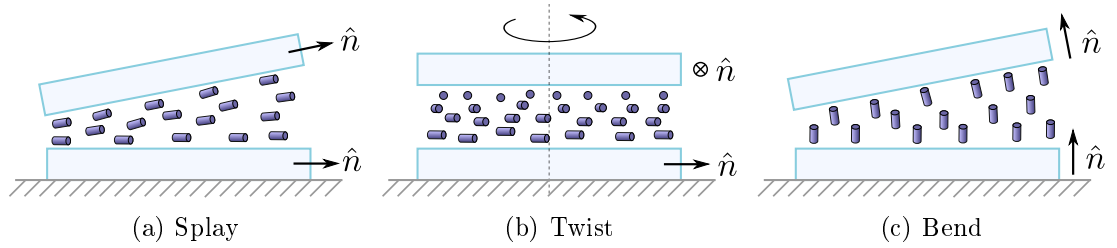
Figure 3.6: Schematic of nematic LC director $\hat{n}$ distortion; (a) splay (b) twist and (c) bend [235, 239].

3.2.2 Fréedericksz transition

The point at which the restoring forces within the LC can be overcome by an electric field is defined as the Fréedericksz transition [236]. The applied field

causes a director distortion across the nematic material, provided the field exceeds some threshold value defined as

$$\mathbf{E}_{\text{th}} = \frac{\pi}{\mathtt{h}} \sqrt{\frac{K_i}{\varepsilon_0 \Delta \varepsilon}} \tag{3.13}$$

where K_i corresponds to the elastic constants with $i = 1, 2, 3$ and as before, $\mathtt{h}$ is the thickness of the nematic material. The director remains undistorted if $\mathbf{E} < \mathbf{E}_{\text{th}}$. Gradual director distortions across the bulk occur once $\mathbf{E} > \mathbf{E}_{\text{th}}$. A derivation for $\mathbf{E}_{\text{th}}$ can be found in [149].

It is possible to induce the Fréedericksz transition optically, known as the optical Fréedericksz transition (OFT), if the NLC is irradiated by a laser beam [240]. Similarly, the OFT occurs when a laser beam with a sufficiently large intensity I above a threshold value I_{th} enters the system. The OFT can be employed to trap colloids with low refractive index relative to those of the LC in a scenario which would otherwise produce a repulsive rather than attractive optical force [176, 182].

3.2.3 Ericksen number E_{r}

The Ericksen number E_{r} is a dimensionless quantity describing the ratio of viscous to elastic forces in a nematic LC;

$$E_{\text{r}} = \frac{\alpha_4 v_\infty r}{2 K_i} \tag{3.14}$$

where v_∞ and r are velocity and length scales e.g. the velocity and radius of a colloid immersed in the NLC, and α_4 is a Leslie coefficient [237]. At low Ericksen number $E_{\text{r}} \ll 1$, elastic forces exceed viscous forces and so any elastic distortions of the director due to the flow field are considered negligible.

3.2.4 Colloid behaviour within a nematic liquid crystal

Particles introduced into a NLC create a director distortion across the bulk where the behaviour of the colloid-LC composite depends on the competition between molecular anchoring at the surface of the colloid and the NLC's bulk elasticity.

An initially uniform $\hat{n}$ will be largely unaffected by colloids with weak surface

anchoring. However, those with strong surface anchoring, $\hat{n}$ will be distorted in order to accommodate the colloid's surface anchoring to minimise the free energy in the system [168]. These director distortions introduce defects, including point defects, also referred to as '*hedgehogs*', and line defects, or *disclinations*.

Figure 3.7 illustrates the types of surface anchoring and the associated defects induced. If the surface anchoring of $\hat{n}$ is planar, two point defects, referred to as '*boojums*', are created as shown in Fig. 3.7(a). Homeotropic surface anchoring (i.e. normal to the colloid surface), creates a radial director structure. Weak homeotropic surface anchoring creates a Saturn-ring defect, as shown in Fig. 3.7(b) whilst strong homeotropic surface anchoring generates a satellite defect (Fig. 3.7(c)).

The ratio between surface anchoring energy at the colloid surface $\mathcal{F}_s$ and elastic energy of the nematic $\mathcal{F}_{el}$ is given by the following dimensionless anchoring parameter

$$\xi_a = \frac{\mathcal{F}_{el}}{\mathcal{F}_s} = \frac{Wr}{K_i} \tag{3.15}$$

where r is particle radius, W is the anchoring energy on the particle and K_i is the appropriate Frank elastic constant (typically $W{\sim}1$ pN/m and $K_i{\sim}10$ pN) [241]. For strong anchoring $\xi_a \gg 1$ resulting in topological defects whereas for weak anchoring $\xi_a \ll 1$, where $\hat{n}$ is only distorted close to the colloid surface.

The addition of colloids to a nematic LC can also affect the clearing temperature T_c where an increase in particle concentration can lead to a decrease in T_c [242].

(a) Point defect   (b) Saturn-ring   (c) Satellite
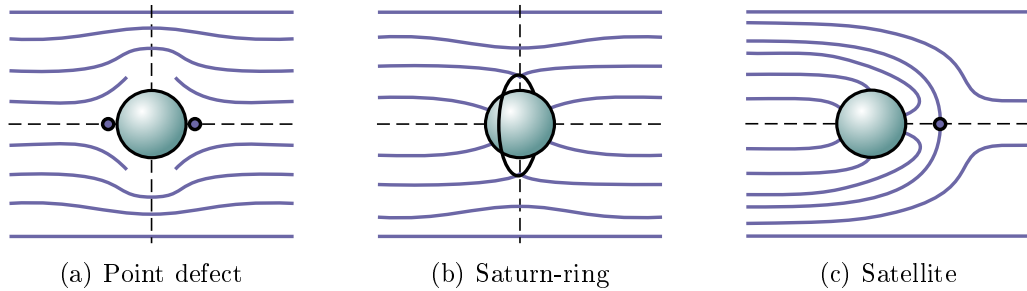
Figure 3.7: Surface anchoring of nematic LC director $\hat{n}$; (a) point defect illustrates planar alignment at surface of colloid whilst (b) Saturn-ring defect indicates weak homeotropic surface anchoring and (c) satellite defect indicates strong homeotropic surface anchoring.

3.3 Liquid crystal cells

The liquid crystal cells used in this work consisted of microspheres dispersed in aligned nematic LC mixture. The cells themselves were created from two coverslips separated by spacers and sealed with UV sensitive glue. The LC cell is then adhered to a microscope slide using nail varnish. Cell thickness was then measured using reflectance spectroscopy.

The fabrication of each LC cell was extensive. In addition to an intensive cleaning procedure, it was necessary to calculate and measure the ratio of microspheres to liquid crystal, disperse the colloids in the LC using an ultrasound bath and apply an alignment layer to the cell surfaces. After assembling each cell, the unfilled cell thickness was measured using reflectance spectroscopy and each cell was then loaded with the LC-colloid mixture. Each process is described in further detail in the following subsections beginning with the LC materials and colloids chosen.

One should note that the refractive indices of the LCs and colloidal materials are quoted for a given wavelength of light but will of course be dispersive media, i.e. their refractive index is wavelength-dependent. This wavelength dependency is described by the Sellmeier equations [243]. In addition, the values are also quoted for a given temperature where refractive index can vary with temperature.

3.3.1 Liquid crystalline materials

In order to optically trap colloids within a medium with refractive index n_{m}, it is important to adhere to the criterion $n_{\mathrm{m}} < n_{\mathrm{p}}$ where n_{p} is the refractive index of the particle being trapped.

When concerned with trapping in a liquid crystal, nematic materials with a low Δn facilitate efficient trapping at a depth of tens of microns into the LC cell. This becomes more difficult in nematic materials with a high birefringence [155].

Therefore, care was taken when choosing appropriate liquid crystalline materials. Table 3.2 details the important specifications of the liquid crystalline materials chosen to act as the host medium; MLC-6609 and MLC-6648, both

Table 3.2: Important paramaters of chosen nematic LCs; birefringence Δn, extraordinary and ordinary refractive indices n_e and n_o, dielectric anisotropy $\Delta \varepsilon$, clearing temperature T_c and flow viscosity ν. $1\,cP = 0.001\,Pas$. Refractive indices are determined at $589\,nm$ and $20\,°C$. Manufactured by Merck [244].

	Δn	n_e	n_o	$\Delta \varepsilon$	T_c [°C]	ν [cP]
MLC-6648	0.0701	1.5457	1.4756	*Unavailable*	90.5	19
MLC-6609	0.0777	1.5514	1.4737	-3.7	91.5	20

manufactured by Merck [244]. The liquid crystal should also have (a) a reasonable viscosity to allow colloidal motion, (b) a significant difference between n_p and n_m to ensure successful optical trapping, and (c) a high clearing temperature T_c to avoid the laser's thermal heat inducing the phase transition.

3.3.2 Colloidal materials and preparation

It was important to choose colloids with suitable parameters allowing them to be optically trapped under the condition $n_m < n_p$. Shown in Table 3.3 are important physical specifications for the colloids chosen for dispersing within the nematic LCs; polystyrene (PS) spheres and borosilicate (or soda lime glass) spheres. The PS beads came pre-dispered in water so it was necessary for these to be dried prior to dispersing them in LC, whereas the silica (SC) beads were pre-dried.

3.3.3 Liquid crystal alignment

It was necessary to treat the surfaces of the LC cell to control the orientation of $\hat{n}$. It is possible to align $\hat{n}$ parallel, perpendicular and at some angle to the cell surface; planar, homeotropic and tilted alignment, respectively. Tilted alignment was not employed for this work so only the techniques for achieving planar and homeotropic alignment will be described. Once the coverslips were assembled to create cells and filled with the LC-colloid mixture, successful alignment could be verified, as described in Section 3.3.6.

Table 3.3: Important paramaters of chosen colloids. The coefficient of variation (CV) refers to the size variation of a bead population and is the % ratio of the standard deviation to mean diameter.

Nominal	Diameter d (μm) (CV)	Density ρ (g/cm^3)	Refractive index n	Dielectric constant ε
POLYSTYRENE SPHERES			*PolySciences* [245]	
2 μm	1.914 (3.8 %)			
3 μm	2.909 (4.7 %)			
6 μm	5.658 (5.4 %)	1.05	1.59	~ 2.6
10 μm	9.14 (7.8 %)			
SILICA SPHERES			*ThermoScientific* [246]	
2 μm	2.0 (30 %)	2.50		
5 μm	5.1 (12 %)		1.56	5.8
8 μm	8.0 (13 %)	2.55		
10 μm	10.1 (11 %)			

3.3.3.1 Planar alignment

Mechanical rubbing of the cell surface with a polymer applied to it with paper or cloth is a simple method employed to achieve planar, or homogenous, alignment of the LC, providing strong anchoring [239].

Polyvinyl alcohol (PVA) was the polymer chosen to create the planar alignment layer. Each coverslip was spin-coated with 4 drops of PVA solution in water at a rate of 60 rps. The coverslip was then baked at ∼130 °C for 10 minutes and, after cooling, was rubbed unidirectionally with a velvet cloth roller approximately 10 times.

3.3.3.2 Homeotropic alignment

Liquid crystal cells can be homeotropically aligned via the application of a surfactant to the cell surfaces, such as silanes which are organic molecules. Octadecyltrimethoxysilane (OTMS) or Silane was the surfactant chosen to create homeotropic alignment. A drop of OTMS was dissolved in deionised water, sonicated for 10–15 minutes, followed by the addition of 5 ml of ethanol and sonicated further. It was important to sonicate the OTMS until fully dispersed creating a

cloudy solution otherwise an uneven alignment layer may result. Each coverslip was 'dipped' into the OTMS mixture for approximately 20 seconds with any excess removed with isopropyl alcohol (IPA). The alignment was fixed by baking the coverslip at ~100 °C for 2–5 minutes and then at 120–150 °C for a further 60 minutes.

3.3.4 Assembling cells

Two coated coverslips were sandwiched together — displaced slightly to allow for filling by capillary action — using Kapton spacers with an approximate length and width of 2.5 cm and 3 mm, respectively. The cells were adhered using UV sensitive glue and once the cell had been filled with the LC-colloid mixture, the cell edges were sealed with UV cured glue. During this, the cell area containing the LC-colloid mixture was protected from the UV light source e.g. with black card, to avoid the LC being destroyed.

3.3.5 Measuring cell thickness

Reflectance spectroscopy was used to measure the thickness, h of each cell before any LC-colloid mixture was loaded. The theory of the technique is founded in the intereference of white light fringes [247]. The thickness is calculated as follows;

$$h = \frac{N\lambda_1\lambda_2}{2(\lambda_2 - \lambda_1)} \qquad (3.16)$$

where N is the number of spectrum maxima, and λ_1 and λ_2 are the wavelengths associated with the initial and final maxima, respectively. An idealised reflectance spectra can be seen in Fig. 3.8.

LC cells that are symmetrical (square) compared with those which are asymmetrical (rectangular) may tend to dip in the centre as their support, provided by the spacers along the edge, against the weight of the coverslip is further away. Therefore, it was decided, rather than taking one measurement at some arbitrary point of the cell, readings at the centre as well as towards the four corners of the cell should be taken to calculate an average cell thickness.
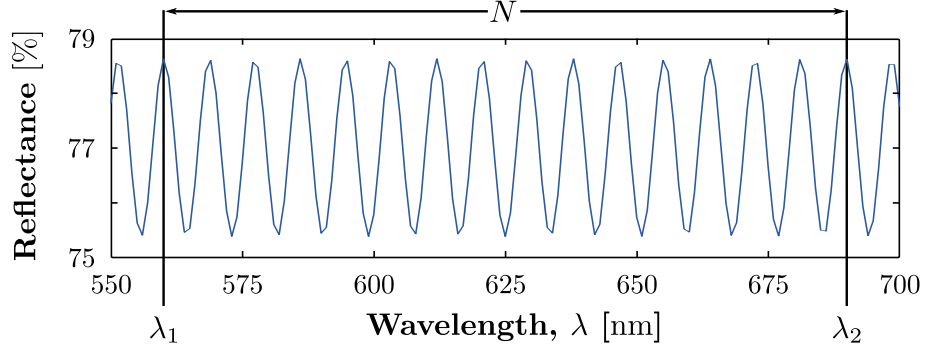
Figure 3.8: The above idealised reflectance spectra with $N = 16$ maxima, $\lambda_1 = 560\,\text{nm}$ and $\lambda_2 = 690\,\text{nm}$ which would indicate a cell thickness, $\text{h} = 24\,\mu\text{m}$ calculated using Eq. (3.16).

3.3.6   Verifying alignment

The penultimate stage of the process was to fill the LC cell with the LC-colloid mixture, and to seal the cell edges with UV-sensitive glue, as described above. Whilst observing through a polarising microscope, LC cells with homeotropic alignment were steadily heated above the associated phase transition T_c, and then cooled back down. The microscope ocular can then be removed to observe the interference pattern, an *isogyre* or *conoscopic cross*, to determine the type and success of the alignment layer [237]. The conoscopic image is produced in the back focal plane of the microscope objective and confirms the presence of birefringence, indicating its orientation with respect to $\hat{n}$. An off-centre conoscopic cross implies the optic axis is inclined at some angle with respect to the axis of the microscope.

Figure 3.9 shows the conoscopic pattern observed for an LC cell with homeotropic alignment. In this case, $\hat{n}$ is normal to the glass surface so no birefringence is observed because the phase is uniaxial and the optic axis is normal to the substrates.

To verify planar alignment, the LC cell was viewed between crossed polarisers and the minimum and maximum transmission observed as the LC was rotated relative to the crossed polarisers.
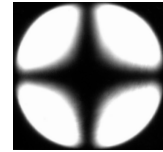
Figure 3.9: Conoscopic interference image for an anisotropic liquid crystal illustrating homeotropic alignment.

Finally, the LC cell is then adhered to the surface of a microscope slide using nail varnish and a schematic of a LC sample cell can be seen in Fig. 3.10.
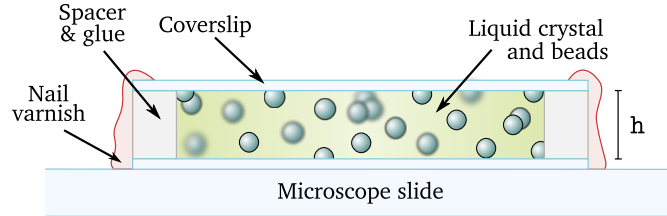
Figure 3.10: A LC sample cell contains microspheres e.g. polystyrene (PS) and silica (SC) beads, dispersed in nematic LC. Cell thickness h, measured using reflectance spectroscopy, ranged between approximately $20 - 40\,\mu$m whilst particle radius varied between $2 - 10\,\mu$m. The LC cell is adhered to a microscope slide using nail varnish.

3.4   Summary

This chapter has introduced some important characteristics of and concepts relating to liquid crystals, along with the chosen materials and the prepartion process for producing the samples used in this work.

Chapter 4

Optical Setup

This chapter details the design and implementation of the laser tweezing system. The main components of the system are discussed, including the optical setup, the sample, and imaging and particle tracking. Following this, the calibration of position and trapping power is presented with associated quantities, and the effect of heating, drift and noise is discussed.

4.1   Laser tweezing system

The optical layout of the laser tweezing system, built around a commercially available Leica [248] inverted optical microscope, is shown in Fig. 4.1, which can be divided into three main parts; (i) the laser tweezers, (ii) the microscope optics and (iii) the visual tracking system. All optics were secured to a $\sim 2.55\,\mathrm{m}$ by $1.25\,\mathrm{m}$ isolation table manufactured by Melles Griot [249], which could be floated to eliminate external vibrations. The laboratory was thermostatically controlled between 21 and $23\,^{\circ}\mathrm{C}$, and assumed to be stable in this range.

Laser tweezers

The trapping laser source was provided by a Laser Quantum [250] low noise, continuous wave, diode pumped solid state (DPSS) Neodymium Doped Yttrium Orthovanadate ($\mathrm{Nd:YVO_4}$) laser able to produce a power of up to $1.1\,\mathrm{W}$, operating at a wavelength λ of $1064\,\mathrm{nm}$ with a $\mathrm{TEM_{00}}$ beam profile.
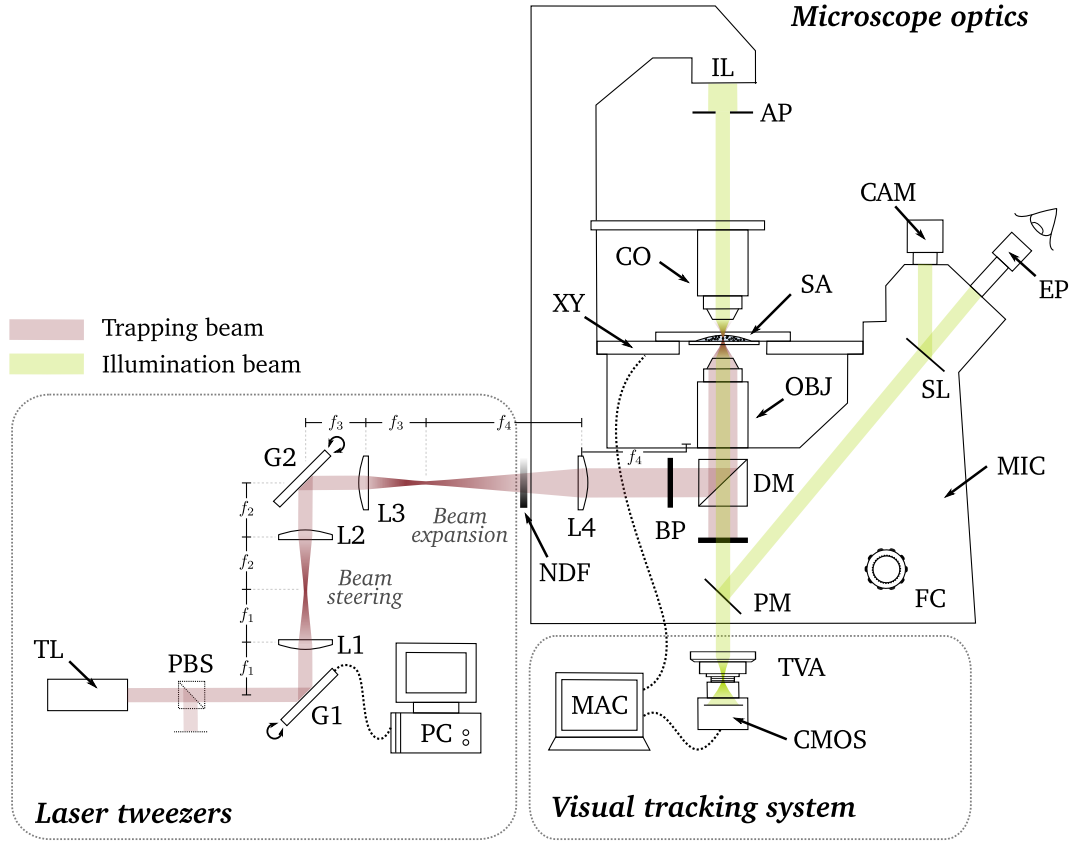
Figure 4.1: The laser tweezing system. *Laser tweezers*: 1064 nm wavelength trapping laser (TL), polarising beamsplitter (PBS), beam expansion and beam steering lenses (L1–L4), and galvanometer-controlled mirrors (G1,G2) with computer control (PC). Trapping power is accurately controlled using a variable neutral density filter (NDF). *Microscope optics*: A dichroic mirror (DM) directs the trapping beam to the 100× oil-immersion microscope objective lens (OBJ) with numerical aperture NA = 1.30. The trapping beam is tightly focussed into the sample (SA) attached to a translation stage (XY). The illumination beam (IL) is directed to the sample via a variable aperture (AP) and condenser lens (CO). Both beams are directed towards a viewing eyepiece (EP) and camera (CAM) via an internal prism (PM) and sliding beamsplitter (SL). The axial position of OBJ can be altered using the focus control (FC) or a joystick (not shown). *Visual tracking system*: a bandpass filter (BP) blocks the trapping beam. A 0.5× Leica TV Adapter (TVA) and a CMOS camera is linked to an Apple MAC for high-speed imaging and particle tracking. MAC is also used for controlling XY. *See text for further details*.

The trapping beam encounters the collimating, beem steering and beam expansion lenses (L1–L4) whose focal lengths are given in Table 4.1 (p. 106). Lenses L1–L3 were adjustable in all three dimensions using an XY adjustable lens mount, mounted on a micrometer translation stage to adjust the lens' position along the optical axis, z. The trapping beam slightly overfilled the back aperture of the microscope objective lens (OBJ). Two fast scanning galvanometer-controlled mirrors (G1,G2) provide accurate beam positioning and the option to generate multiple, time-shared traps via PC control. A variable neutral density filter (NDF) was used to accurately control the laser power and placed immediately before the back port of the microscope to prevent the high power laser beam from damaging the filter's coating.

Microscope optics

The optical arrangement is built around a commercially available Leica [248] DM IRB inverted optical microscope; a common arrangement chosen for its ease of use, integrated style, stability and suitability for biological samples and measurements in low-light level conditions. The microscope has a trinocular head and two additional ports; back fluorescence and side port, providing significant flexibility.

The trapping laser beam entered the back fluorescence port of the microscope and the second half of the beam expander (L4) was contained within the microscope body itself, approximately 65 mm from the back port entrance.

The illumination beam is provided by a 12 V, 100 W halogen bulb with a tungsten filament. An Edmund Optics [251] dichroic hot mirror (DM), selectively reflected wavelengths greater than 700 nm whilst transmitting anything below, therefore transmitting the illumination beam to the visual imaging system and reflecting the trapping beam upwards to the microscope objective lens for safety reasons. The microscope objective was an infinity-corrected Zeiss [252] EC Plan Neofluar oil-immersion objective lens with $100\times$ magnification and numerical aperture, NA = 1.30 (described in further detail in Section 4.1.1). The condenser lens was the Leica [248] S70/0.30 which has a free working distance of 70 mm and NA = 0.30. The thickness of DM dictated that the optical beam height should be 15.5 cm.

Table 4.1: Focal lengths for all lenses used in the laser tweezing system shown in Fig. 4.1.

	Lens		Focal length [mm]
LASER TWEEZERS	L1	f_1	40
	L2	f_2	40
	L3	f_3	60
	L4	f_4	175
MICROSCOPE OPTICS	OBJ	f_{obj}	1.5
	CO	f_{CO}	—
VISUAL TRACKING SYSTEM	0.5× TVA		—

It was necessary to ensure the trapping beam was parallel with the microscope objective's principal axis, so the optical trap focus coincided with the illumination optics of the microscope for imaging and tracking. A prism (PM) directs the trapping and illumination beams to the trinocular head to allow viewing through the eyepiece and an additional camera can be used for imaging, linking to a TV monitor for example.

It was possible to block the trapping beam in three places; before reaching (a) the sample, (b) the tracking system, both achieved using a bandpass filter (BP), or (c) the trinocular head using a sliding beamsplitter (SL), consisting of a short pass filter which transmitted $< 1\%$ of radiation above 1050 nm, to switch between 100 % to either the camera or eyepieve (EP), or 50 % to both. For safety, two additional short pass filters were placed in the eyepieces to protect the user from harmful laser radiation.

Transverse and axial sample positioning was achieved using a Prior Scientific [253] Proscan motorised translation stage which could either be controlled manually, using a joystick (not shown), or National Instruments (NI) [254] Lab-VIEW software. The programs were heavily based on those written by two PhD students; Tiffany Wood and Amanda Wright [168, 255] and were modified by the author. Further details of sample positioning are given in Section 4.2.1.

Visual tracking system

Particles were imaged and tracked in real-time using a CMOS (Complementary Metal Oxide Semiconductor) camera manufactured by Prosilica [256] and the NI LabVIEW control software with an Apple Macbook [257]. This is described in further detail in Section 4.3. When necessary, it was also possible to observe the sample via the eyepieces at the trinocular head with a colour charge-coupled device (CCD) camera (Model TK-C1381, JVC) connected to the top port, linked to a TV monitor.

The remainder of Section 4.1 will discuss the important components of the system in further detail.

4.1.1   Microscope objective

As mentioned in Section 2.1, in order to optically trap microscopic particles, it is necessary to expand the trapping beam to slightly overfill the back aperture of the microscope objective lens to ensure the maximum gradient force is produced at the centre of the optical trap. Tightly focussing the laser beam creates a significant portion of rays converging at large angles on the surface of the particle. This is achieved using a microscope objective lens with a high *numerical aperture*; a dimensionless measure of the solid angle over which the objective can collect light, given by,

$$\text{NA} = n_{\text{oil}} \sin \alpha \tag{4.1}$$

where α is one-half the angular aperture of the objective and n_{oil} is the refractive index of the oil between the objective front lens and the coverslip, as shown in Fig. 4.2. Given that $n_{\text{oil}} = 1.515$ as given by the manufacturer [258] and $\text{NA} = 1.30$, $\alpha = 59°$ which corresponds to an angular aperture (or total acceptance angle) of $2\alpha \approx 118°$ where $180°$ would be the maximum.

The experiments in this thesis use an infinity-corrected Zeiss [252] EC Plan Neofluar oil-immersion microscope objective lens with $100\times$ magnification and numerical aperture, $\text{NA} = 1.30^*$. It has a working distance of $0.20\,\text{mm}$ and a field of view of $25\,\text{mm}$. The transmittance of this objective at a wavelength of $1064\,\text{nm}$ is $59 \pm 2\,\%$ [212]. The terms *EC, plan* and *(neo)fluar* refer to enhanced

---

* Now obsolete.
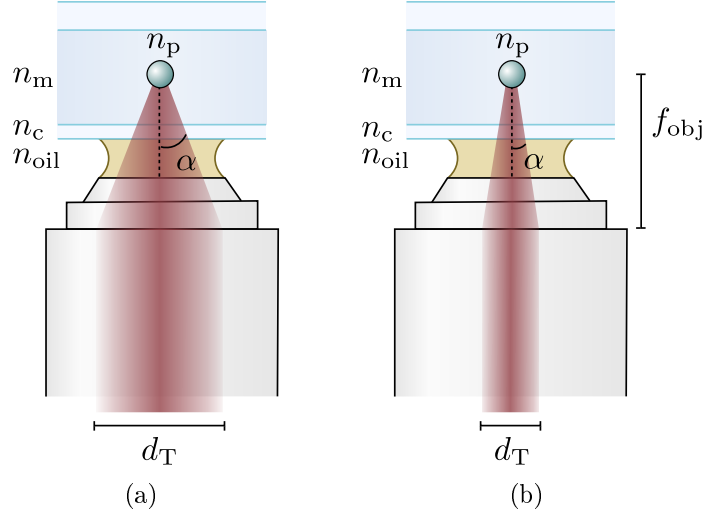
Figure 4.2: (a) For efficient optical trapping, the diameter of the trapping beam d_T should be expanded to slighly overfill the back aperture of the microscope objective to produce a sufficient number of rays converging at large angles. (b) The optical trapping force will be compromised by underfilling the microscope objective and, due to domination by the scattering force, the particle will be pushed out of the focus of the optical trap (not shown).

contrast, the total field of view being in focus i.e. a flat field of view, and the lens elements being made of fluorite or related compounds, respectively [259]. Despite a fluar objective transmitting UV and visible light, and being ideal for fluorescence microscopy, it works well with this setup.

As described earlier in this chapter, the trapping beam's diameter d_T should be expanded to slightly overfill the back aperture of the objective, as shown in Fig. 4.2(a), to ensure the tightest possible optical trap focus is achieved and provide true three dimensional confinement [36]. To achieve this, lenses L3 and L4 (Fig. 4.1) comprised a beam expander which expanded the trapping beam by a factor 2.9.

Figure 4.2(b) illustrates the effect of underfilling the objective lens; reducing the angle with which trapping rays impinge on the surface of the particle and thereby reducing the trapping force. If α is not significantly large, the scattering force $\mathbf{F}_{scat}$ will dominate and the particle will be pushed out of the optical trap's focus.

Higher values of NA allow increasingly oblique rays to enter the objective front lens, producing a more highly-resolved image. The finest detail that can

be resolved with the objective is given by the radius of the diffraction-limited Airy disk, equal to $0.61\lambda/\text{NA}$. Therefore, a lens with a larger NA will provide better resolution than that of a lower NA, and also display a brighter image due to its ability to collect more light. However, high NA lenses have working distances which restrict optical trapping to tens of microns into the sample in addition to a reduced depth of field [36]. For this laser tweezing system, if the trapping beam were being used for imaging, the limit of spatial resolution would be approximately $500\,\text{nm}$. Imaging with white light limits the spatial resolution to approximately $200\,\text{nm}$. However, the optimum spatial resolution at the detector is dictated by the Nyquist limit where the diffraction-limited resolution of the microscope should be matched to two detector pixels. [259]

4.1.1.1 Refractive index mismatch

With oil-immersion objectives, the immersion oil is index-matched with the glass coverslip, i.e. $n_{\text{oil}} = n_{\text{c}} = 1.515$, as well as with the objective lens. However, there is a refractive index mismatch between the glass coverslip and the host medium e.g. water $n_{\text{m}} = 1.33$ which, due to spherical aberrations [260], reduces the quality of the optical trap focus as trap depth Z_{T} increases. This alters the optical trap focus such that it reduces the objective's physical focal length f_{obj} to an effective focal length f_{eff} as shown in Fig. 4.3.

As given by Eq. (4.1), the angles to the normal for the rays travelling through the coverslip and oil α_1, and travelling through the host medium α_2 are given by,

$$\alpha_1 = \sin^{-1}\left(\frac{\text{NA}}{n_{\text{oil}}}\right), \tag{4.2}$$

$$\alpha_2 = \sin^{-1}\left(\frac{\text{NA}}{n_{\text{m}}}\right). \tag{4.3}$$

Thus, the combined thickness of the immersion oil and the coverslip is given by

$$\ell = \frac{0.5d_{\text{T}} - Z_{\text{T}}\tan\alpha_2}{\tan\alpha_1} \tag{4.4}$$

where Fig. 4.3 shows $f_{\text{eff}} = \ell + Z_{\text{T}}$ [260]. Again, as mentioned in Section 3.3, one may need to consider dispersion, where refractive indices are wavelength
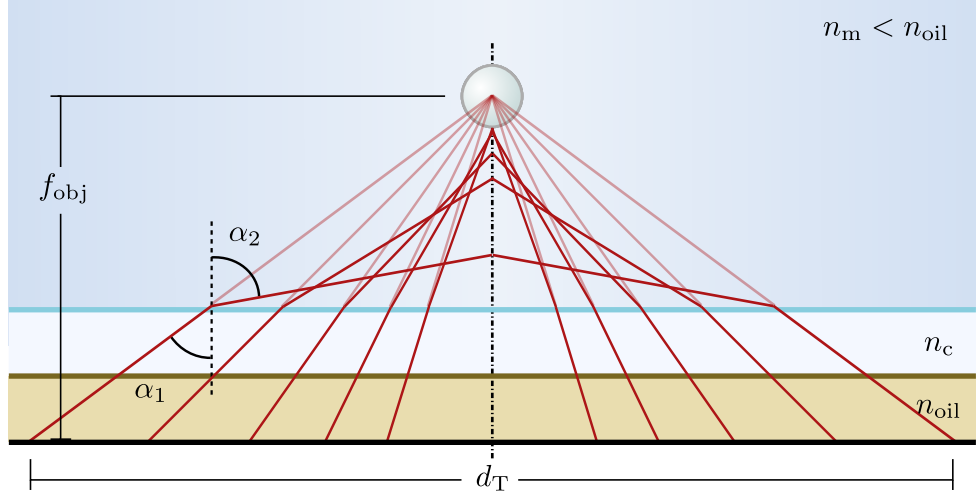
Figure 4.3: The refractive index mismatch between the combination of coverslip and immersion oil, n_c and n_{oil}, respectively, and that of the sample's host medium, n_m causes spherical aberration of the trapping beam. This acts to elongate the optical trap focus region and reduce the microscope objective's actual focal length to an effective focal length f_{eff}.

dependent [243].

The LabVIEW program written to control the microscope translation stage, *StageControl.vi* calculates f_{eff} for a given trap depth Z_T as described in a previous PhD thesis by Tiffany Wood [168].

4.1.2 Lateral trap positioning

The lateral position of the optical trap focus could be adjusted using the GSI Lumonics [261] galvanometer-controlled mirrors, chosen for their high speed, affordability and large deflection angle with a maximum of $\pm 50°$. Silver mirrors were attached to each galvanometer which had a diameter of $5\,\mathrm{mm}$ and with a reflectance of $98\,\%$ at $1064\,\mathrm{nm}$. [255]

Each galvanometer and two lenses comprise a *transfer lens sytem* which translate the trapping beam in the back focal plane (BFP) of the microscope objective, creating a lateral displacement of the trap focus in the sample plane. As shown in Fig. 4.4(a), lenses L1 and L2 create a plane AA which is conjugate to the plane BB; the microscope objective's BFP. Angular rotation of G1 located at AA causes a lateral displacement of the trap focus. The figure also illustrates
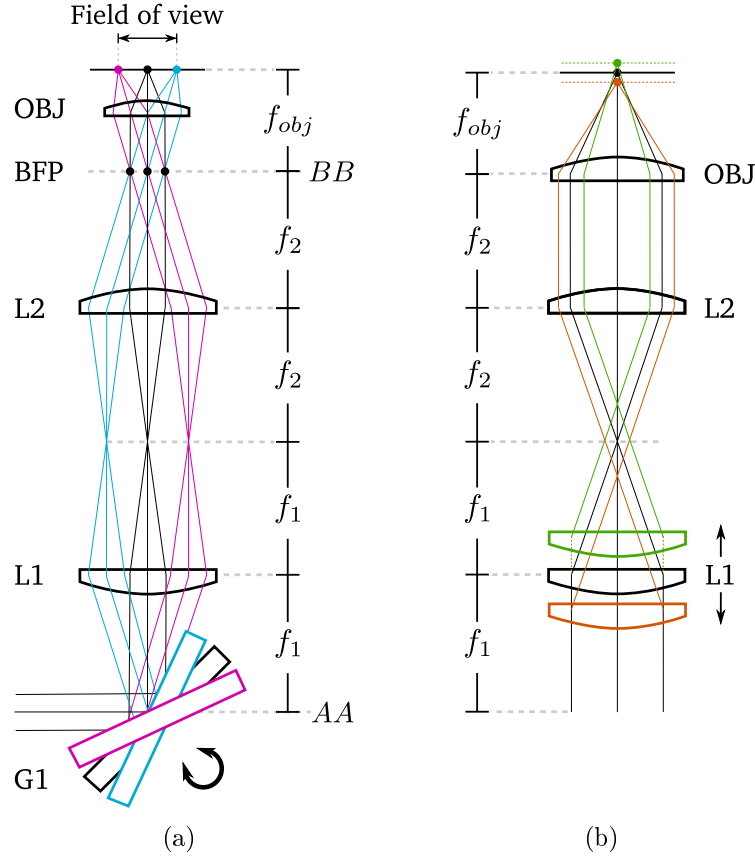
Figure 4.4: (a) Lateral trap positioning where galvanometer-controlled mirrors (G1,G2) and lenses L1–L4 create the two conjugate planes AA and BB. (b) Axial trap positioning where L1 is translated to axially translate the optical trap focus.

that whilst the angle of the rays arriving at BFP are changed, the trapping beam remains centred on the BFP of the objective. Thus, an angular displacement of the mirror corresponds to a lateral displacement of the optical trap in the image plane.

Displacement of the trap focus in x and y can be controlled independently where G1 and G2 control displacement in y and x, respectively. Hence, Fig. 4.4(a) corresponds to y trap displacement and a second transfer lens system, comprised of G2, L3 and L4 to create conjugate planes CC and DD, corresponds to x trap displacement.

4.1.3   Axial trap positioning

The lens system shown in Fig. 4.4(b) allowed for precise control of the axial position of the optical trap focus. This was especially useful to overcome chromatic aberrations which cause the trapping and illumination beams to come to alternative foci in the sample plane. The magnitude of chromatic aberrations depends on the lens' focal length, refractive index, material thickness and radii of curvature [262, 263].

Lens L1 can be translated backwards or forwards to axially translate the optical trap focus. The resulting axial translation can be calculated by applying the thin lens equation as given by

$$\frac{1}{d_o} + \frac{1}{d_i} = \frac{1}{f} \tag{4.5}$$

where, if L2 (focal length $f = f_2$) is translated by q, the object distance $d_o = f_2 + q$ and the image distance $d_i = d_{i2}$ is the distance at which an image is created to produce

$$\frac{1}{d_{i2}} = \frac{q}{f_2^2 + f_2 q}. \tag{4.6}$$

For the objective lens, $f = f_{obj}$, $d_o = -(d_{i2} - f_2)$ and d_{obj} is the distance at which the microscope objective creates an image i.e. the translated focal length. Therefore, Eq. (4.5) becomes

$$\frac{1}{d_{obj}} = \frac{1}{f_{obj}} + \frac{1}{d_{i2} - f_2} \tag{4.7}$$

and by substituting for d_{i2} from Eq. (4.6), Eq. (4.7) becomes

$$\frac{1}{d_{obj}} = \frac{f_2^2 + q f_{obj}}{f_{obj} f_2^2}. \tag{4.8}$$

As an example, moving L2 backwards, means q is positive and therefore added to the focal length f_2 to form the image distance d_{i2}. So, given that $f_2 = 40\,\mathrm{mm}$ and $f_{obj} = 1.5\,\mathrm{mm}$, for a $10\,\mathrm{mm}$ backward translation of L2, $q = 10\,\mathrm{mm}$ and the trap would be focussed at $1.486\,\mathrm{mm}$; a $14\,\mu\mathrm{m}$ decrease of f_{obj}. Instead, for a forward translation of L2, q would become negative (i.e. subtracted from the

focal length). And so, for a 10 mm forward translation of L2, $q = -10$ mm and the trap would be focussed at 1.514 mm i.e. an increase of 14 μm.

4.2   The sample

An isotropic sample consisted of polystyrene (PS) beads purchased from Poly-Sciences [245] whose diameters ranged between 2 μm and 10 μm and with a refractive index of 1.59, as detailed previously in Table 3.3 (p. 99). The beads were dispersed in distilled, deionised water and the suspension contained within the cavity of a concave microscope slide, sealed with a coverslip and nail varnish, as shown in Fig. 4.5. The sample should not have too great a bead concentration so as to avoid several surrounding beads also being pulled into the optical trap at high trapping powers. Also, it is necessary to keep particle concentrations relatively low so as to limit hydrodynamic interactions.
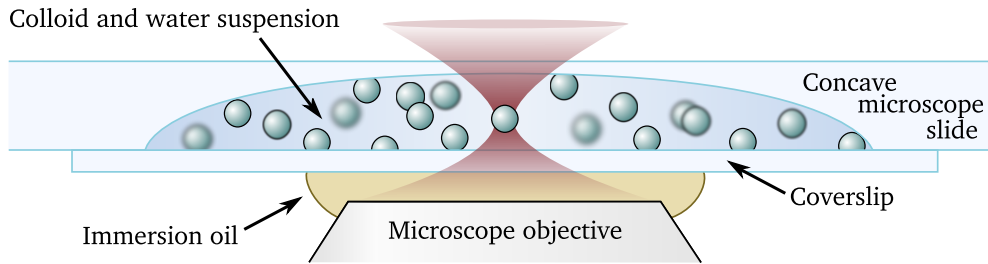
Figure 4.5: An isotropic sample cell contains a suspension of micron sized PS beads dispersed in distilled, deionised water which is sealed with a coverslip and nail varnish. The recess of the concave microscope slide had a depth of ~ 350 μm and a diameter of 15–18 mm.

The immersion oil is index-matched to the glass coverslip. Its temperature and refractive index are inversely proportional as given by the temperature coefficient; the refractive index change per °C, $-dn/dT$. It is possible to determine, and correct for, the refractive index n of a liquid at a given temperature T_1 as given by,

$$n^{T_1} = n^{T_0} - (T_1 - T_0)\frac{dn}{dT}, \qquad (4.9)$$

where n^{T_0} is the refractive index determined at room temperature T_0. In the case of immersion oil, T_0 is typically 23 °C and is stated on manufacturer datasheets [264].

This work employed immersion oil manufactured by Cargille [258] whose $dn/dT = -0.00031$ in the 15–35 °C range and $n_{\mathrm{D}}^{23} = 1.5150$.

4.2.1 Sample positioning

Transverse sample positioning was achieved using a Prior Scientific [253] Proscan motorised translation stage which could either be controlled manually, using a joystick, or via computer control. The two stepper motors for the x and y directions could achieve a linear movement of 2000 μm per revolution. Each revolution produced 200 steps, with 250 microsteps per full step. Therefore, the resolution for both the x and y directions was 50,000 microsteps/rev and 0.04 μm/microstep [255].

Axial sample positioning was adjusted also using Prior Scientific hardware with the coarse and fine focus of a third stepper motor, controlled via the joystick, a computer or a focus knob on the side of the microscope. The fine focus of the axial stepper motor could similarly achieve 50,000 microsteps per revolution. However, the linear movement is given by the Leica microscope itself, which in this case is 200 μm per revolution. Therefore, the resolution for the z direction is 0.004 μm/microstep [255].

A custom program was written with the LabVIEW interface to control the speed, acceleration and position of the translation stage and the axial position of the microscope objective. This program, *StageControl.vi*, also allowed the user to measure the stage's position and trap depth, and apply a displacement function. The program read out position in user units (uu) where $1\,\mathrm{uu} \equiv 1\,\mu\mathrm{m}$ of motion for all three axes x, y, z.

4.3 Imaging and particle tracking

The position or displacement of a trapped particle can be detected in two different ways; with imaging and non-imaging techniques. Imaging techniques, such as using a video or CCD camera, for example, allow observation of the particle's position in real time and accurate position measurement once pixel calibration has been performed. With video based imaging techniques, the position of a trapped

particle can be determined to within $\sim 5\,\text{nm}$ or better [53]. Whilst cameras offer simultaneous multi-particle detection, there is often a discrepancy between the video acquisition (or frame) rate — typically $\sim$25–120 Hz — and either the optical trap's intrinsic bandwidth ($\sim$kHz) or the particle's resonant frequency which ranges from 10–1000 Hz [53].

The requirements of an optical imaging system are a high numerical aperture condenser lens to ensure as much of the scattered downstream light is collected and focussed onto a position sensitive device. The limitations of such a system are that it can be very expensive and condenser lenses are typically oil-immersion and therefore, limit the physical size of the sample. In addition, these systems are particularly sensitive to alignment.

Non-imaging techniques can offer greater accuracy, such as back focal plane interferometry (BFPI) as described be Gittes and Schmidt [265], which measures a trapped particle's lateral and axial displacement by monitoring the far-field interference pattern created at the BFP of a collecting lens. This pattern is caused by the trapping laser light interferring with the laser light scattered by the trapped particle whose intensity is independent of the position of the laser focus within the sample plane [122, 265]. The same is not true with video microscopy. A quadrant photodiode (QPD) can be used for multiple tracking of particles which employ time-sharing of the optical trap, which is not used here. Also, QPDs can be used if the polarisation of the trapping laser is split to make two traps where some QPDs are now sensitive to the polarisation of the light they are detecting. Similarly, it is possible to incorporate more than one trapping laser and QPDs which are wavelength sensitive can be used for particle tracking. Therefore, each of these arrangements require the incorporation of more than one QPD into the system.

Optical and video-based detection modes are often used in tandem to accurately determine position whilst still observing multiple particles, and subsequently observing trapping in real-time or to perform mutual calibration. BFPI is favourable due to its speed and sensitivity with the potential to measure less than 0.1 nm in all three dimensions. [4]

A QPD is characterised by the detector sensitivity, β, which can be estimated from an uncalibrated power spectrum, $S_v(f)$. For small displacements x, $\text{V} = \beta x$, where V is the detector signal, giving β in units of $\text{V}\,\text{m}^{-1}$. The uncalibrated power
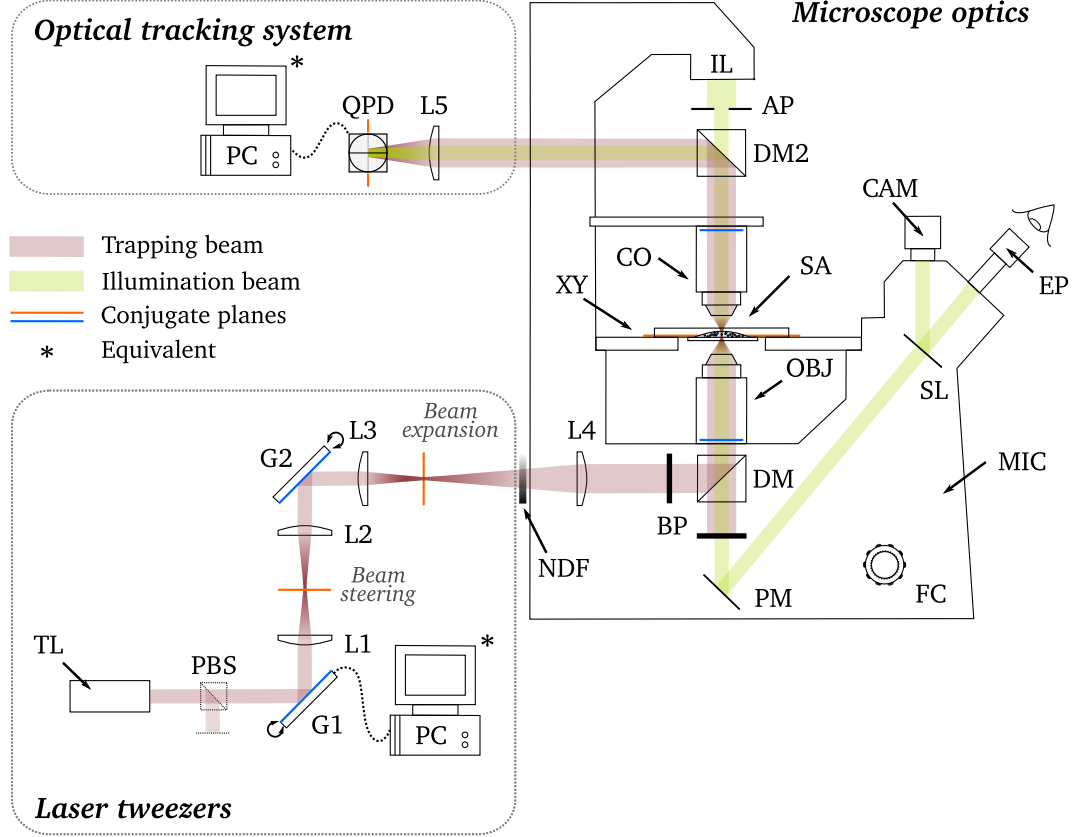
Figure 4.6: Laser tweezing system with an *optical tracking system*: a second dichroic mirror (DM2) directs the trapping and illumination beams toward the quadrant photodiode (QPD) via a focussing lens (L5). The PC collects the interferometric signal from the QPD. Blue and orange lines indicate those planes which are conjugate to one another. All other components are as detailed in Fig. 4.1.

spectrum, $S_v(f) = \beta^2 S(f)$ and β can be found by multiplying both sides by f^2. The product $f^2 S_v(f)$ reaches a plateau value when $f \gg f_c$ [122].

Initially, this project employed BFPI in a forward-scattering arrangement for sensitive tracking of individual particles. The optical setup is shown in Fig. 4.6. The notable difference from Fig. 4.1 is the *optical* tracking system. The QPD (TO8S, Roithner LaserTechnik [266]), consisting of four quadrants of photodiode active area fabricated on a single chip with a peak responsivity at 900 nm, was mounted in a cage system and placed in an optical plane *conjugate* to the sample plane. The electronics for optical amplification of the QPD signal were relatively small and housed in a box with the QPD itself. A custom written LabVIEW program acquired, displayed and saved the voltage signals produced by the incident IR light. The collecting objective (CO) in this arrangement was a 50× ULWD

Olympus MPlan objective [267]. The design and implementation of the QPD is attributed to Nicholas Roberts.

Data obtained from the QPD were analysed using *tweezercalib*, a MATLAB [268] program developed by Hansen *et al.* [227, 269] used for precise and reliable calibration and measurement. The program also provided correction for aliasing, close promixity to surfaces and QPD filtering. The average file size for 10 s of position fluctuation data recorded at a frequency of 50 kHz, with 500,000 samples per channel was over 6 MB with several files produced per measurement and per experiment, requiring significant post-processing. This was all compounded by the disadvantage of only being able to track individual particles.

4.3.1   High-speed video microscopy

Whilst QPDs are traditionally used for particle tracking, using them to track more than two particles is technically complicated. Video based techniques have been employed for particle tracking [156, 270] but until fairly recently, video microscopy offered insufficient bandwidth to reach the trap's corner frequency and were, therefore, unsuitable for monitoring Brownian motion. The option of reducing f_c by increasing the medium's fluid viscosity rarely presents itself and is often impractical. High speed video cameras, such as low-cost CMOS cameras, can record the positions of multiple particles in real-time simultaneously, offering frame rates reaching many kHz by controlling the field of view, with an accuracy reaching the thermal limit as discussed by Gibson *et al.* [217].

Tracking of multiple particles is particularly useful for monitoring multiply trapped particles as in the case of holographic optical tweezers. Unfortunately, one possible drawback of video-based tracking, when compared with using a QPD, is achieving accurate axial tracking. However, successful axial tracking with video-based tracking has been achieved with a number of different methods including using out-of-focus images of trapped particles [271, 272], a side-on viewing angle [273] and stereomicroscopy [274].

With a view to extending the laser tweezing system to be able to manipulate and track multiple particles in microfluidic systems for example, this project subsequently employed high-speed video microscopy (HSVM) for particle tracking as shown in Fig. 4.1. A CMOS camera imaged and tracked optically trapped par-

Table 4.2: Important specifications of the now obsolete Prosilica [256] EC 1280 CMOS camera chosen for high-speed video microscopy.

Specification	Value
Resolution	1280×1024
Sensor type	2/3" CMOS progressive scan
Pixel size (μm)	6.7 × 6.7
Maximum frame rate	24 fps
Lens mount	C-mount
Interface type	IEEE-1394
Exposure range	10 μs to 10 s
Region of Interest (ROI)	Independent control of x and y; 1 pixel resolution
Frame rate at 100×100 ROI	890 fps
Video colour	Monochrome
Support	NI LabVIEW supported
Ouput Format	8 bits/pixel
Spectral sensitivity range	400–1000 nm
Housing size (L×W×H) (mm)	28×46×33
Weight	77 g

ticles in real-time. The Prosilica [256] EC 1280 was connected to an Apple [257] Macbook via the FireWire 800 port which offers data transfer of up to 800 Mbps. Some important specifications of the chosen CMOS camera — which, at the time of writing had become obsolete since purchase — are listed in Table 4.2.

Programs were written in LabVIEW to handle the images acquired from the CMOS camera; *SimpleCam.vi* and *SimpleAnalysis.vi* were used for tracking individual particles and real-time analysis of particle tracking data, respectively. It would be relatively straightforward to modify these programs for tracking and analysing multiple particles.

The bandpass filter placed before the CMOS camera allowed the optical trap to be visualised e.g. for alignment purposes, eliminated for tracking or calibration purposes and prevented damaging the CMOS chip.

The arrangement of the CMOS camera with a Leica C-mount 0.5× TV adapter shown in Fig. 4.1, provided a magnification of ∼63×, determined from position calibration for the CMOS camera (see Section 4.4.1).

Width × Height (pixels)	Bandwidth (Hz)
1280 × 1064	23
100 × 100	400
64 × 64	455
40 × 40	500
16 × 16	533

Table 4.3: Achievable bandwidth given by *SimplaeCam.vi* for user-selected regions of interest (ROI). These values compare well with that quoted in Table 4.2.

(μ_x, μ_y, σ_z)
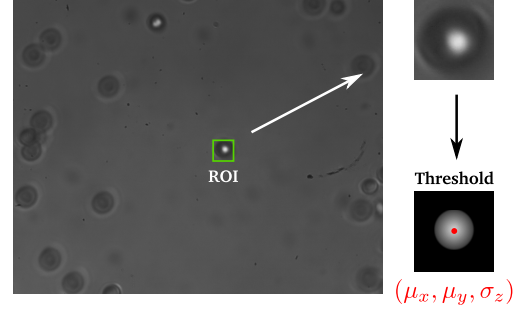
Figure 4.7: Particle tracking in LabVIEW: the image shows a user-selected region of interest (ROI) surrounding the trapped particle to increase frame rate. The program then allows the user to apply of a threshold for accurate measurement of the centroid and standard deviation of the particle image (μ_x, μ_y, σ_z).

For high-speed particle tracking in LabVIEW, the IMAQ Vision Toolkit was utilised where the user selects a region of interest (ROI) surrounding the trapped particle as shown in Fig. 4.7. This process can dramatically increase the frame rate from tens of Hz upto as much as a kHz. Table 4.3 quotes the achievable bandwidth given by *SimpleCam.vi* for user-selected tegions of interest. Typically, experiments were performed with the ROI defined around the edges of the optically trapped bead (with the ROI area in pixels dependent on particle size). A bandwidth of $\approx 250\,\mathrm{Hz}$ and recording times $\sim 10\,\mathrm{s}$, would produce small data files; $< 500\,\mathrm{kB}$. A threshold is then applied to produce a white on dark circular image of the particle.

Alternative particle tracking algorithms were applied for lateral and axial tracking. For lateral tracking, the particle's centre of mass (CoM) co-ordinates are determined using LabVIEW's centroid algorithm, found to be superior to edge detection and circle recognition algorithms. It works by computing the image's centre of energy in pixels as given by the following equations;

$$\mu_x = \frac{\sum(\mathtt{X}p_i)}{\sum(p_i)} \tag{4.10}$$

$$\mu_y = \frac{\sum(\mathtt{Y}p_i)}{\sum(p_i)} \tag{4.11}$$

where X and Y are the pixel co-ordinates from the top left-hand corner of the image and p_i is the pixel value; the numerical value of each 8-bit pixel from 0 (black) to 255 (white). Hence, intensity variation across the thresholded image of the bead during tracking plays a role.

Initially, an attempt was made to perform axial tracking by calculating a histogram of positions. However, this was extremely crude and insufficient to detect Brownian motion.

Axial tracking was improved with quick implementation achieved using a dynamic-link library (DLL) and line-fitting algorithm which together calculate the standard deviation of the particle's image. As suggested by Crocker and Grier [270], if the particle's centroid is the mean, the standard deviation is proportional to the size, or defocus, of the particle. Therefore, the standard deviation of the image is calculated as follows;

$$\sigma_z = \sqrt{(S_{xx} - \mu_x)^2 + (S_{yy} - \mu_y)^2} \tag{4.12}$$

where S_{xx} and S_{yy} are the sum of squares of x and y pixels, respectively [275]. All data are then queued and either saved to file or analysed in real-time.

4.4   Calibration

Position calibration converts position and displacement of a particle in camera pixels to micrometers. For this work, it was also necessary to perform trapping power calibration as the power of the trapping beam is accurately controlled using a variable neutral density filter. This section shall detail the process of position and trapping power calibration.

The laser tweezing system also needs to be calibrated for trap stiffness with a variety of methods to choose from. Trap stiffness calibration for the laser tweezing system employed in this work is presented in Chapter 5, with comparison between three popular calibration methods.

4.4.1   Position calibration

Position calibration was performed by moving a bead immobilised on the surface of a coverslip, due to van der Waals adhesion, a known distance x using the calibrated translation stage, therefore allowing position in pixels to be converted to microns. This was performed for the x and y directions in real-time using the region of interest feature in the LabVIEW program *SimpleCam.vi*.
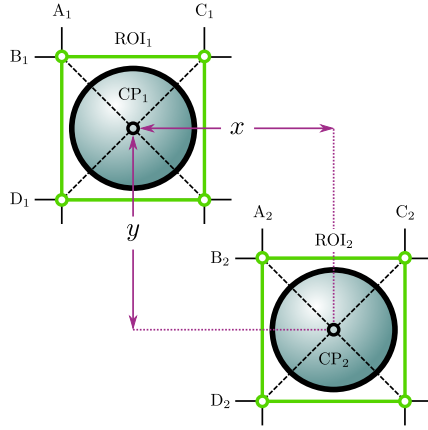
Figure 4.8: For position calibration, the user can create a region of interest (ROI) around a bead immoblised on the surface of the coverslip. The stage is then translated a known distance in the x or y direction, and the ROI then 'dragged' on the screen to the bead's new location. The difference in the bead's initial and final centre point positions, $\mathrm{CP_1}$ and $\mathrm{CP_2}$, respectively allows pixels to be converted to microns.

As can be seen in Fig. 4.8, a distance x is measured in pixels by calculating the difference between the centre point of the bead's initial position $\mathrm{CP_1}$ and the bead's final position $\mathrm{CP_2} = x + \mathrm{CP_1}$ where $\mathrm{CP_1} = (x_1, y_1)$ and $\mathrm{CP_2} = (x_2, y_2)$, which were written into the functionality of the LabVIEW program. The ROI box could be dragged to ensure its area, in pixels^2, remained constant. The expressions used to calculate x, y and the ROI area are given by

$$\mathrm{ROI}_i = |(\mathrm{C}_i - \mathrm{A}_i)(\mathrm{D}_i - \mathrm{B}_i)| \tag{4.13}$$

$$x = \frac{\mathrm{A_2} - \mathrm{A_1} + \mathrm{C_2} - \mathrm{C_1}}{2} \tag{4.14}$$

$$y = \frac{\mathrm{B_2} - \mathrm{B_1} + \mathrm{D_2} - \mathrm{D_1}}{2}. \tag{4.15}$$

The calibration factor for the CMOS camera was 9.33 pixels/μm, giving a magnification M of 63× and a field of view of $137 \times 110 \, \mu\mathrm{m}^2$, where each pixel represented approximately 107 nm × 107 nm. The calibration was also verified using a graticule placed in the sample plane.

4.4.2   Trapping power calibration

The relationship between the current, `I` supplied by the laser's power supply unit (PSU) and the output laser power `P` is shown in Fig. 4.9, illustrating a strong linear relationship.

However, varying trapping power P_T using the laser's PSU potentially introduces noise, increasing the error on measurements which involve detection of the trapped bead's Brownian motion, and can alter the beam properties, including the Gaussian beam profile necessary for laser tweezers. Therefore, the trapping power was precisely controlled by translating a variable NDF across the laser beam. Figure 4.10 shows the relationship between trapping power P_T in mW at the sample and micrometer translation of the variable NDF. A value of P_T could be calculated for a given micrometer reading from the equation of the fitted curve or a Matlab program written by the author. The point $\square$ corresponds to a micrometer reading $F_v \approx 22$ mm and therefore $P_T \approx 82$ mW. The point $\triangle$ corresponds to P_T with no NDF across the trapping beam ($F_v = 0$ mm) and is thus, the maximum P_T of the laser tweezing system; 122 ± 3 mW.

The experimental data in Fig. 4.10 shows some deviation from the expected relationship, such as slight increases in P_T despite increased translation of the NDF across the beam. Also, since the NDF had no filtration coatings at $F_v = 0$, the drop from maximum P_T to the initial 'filtered' power is unexpected. This might suggest the NDF is causing beam aberration or perhaps some reflections within the laser tweezing system due to the angle of the NDF relative to the beam and optics.

4.5   Heating, drift and noise

For complete calibration, it was important to observe any effect the illumination and laser beams had on the sample. Position fluctuation data of untrapped beads were recorded following short and long exposure to both the illumination beam and laser beam. It was observed that the illumination beam had a negligible effect, being an incoherent halogen light source. Water has a measurable absorption at 1064 nm; $\epsilon_w = 5.5 \times 10^{-4}$ cm^{-1}. In a sample with a depth of 100 μm and
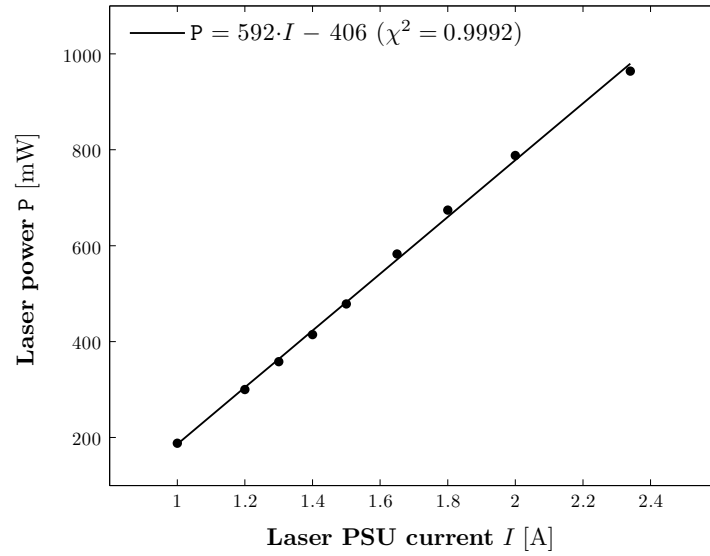
Figure 4.9: Linear relationship between the laser's output power `P` and the current of the laser power supply unit (PSU) `I`.
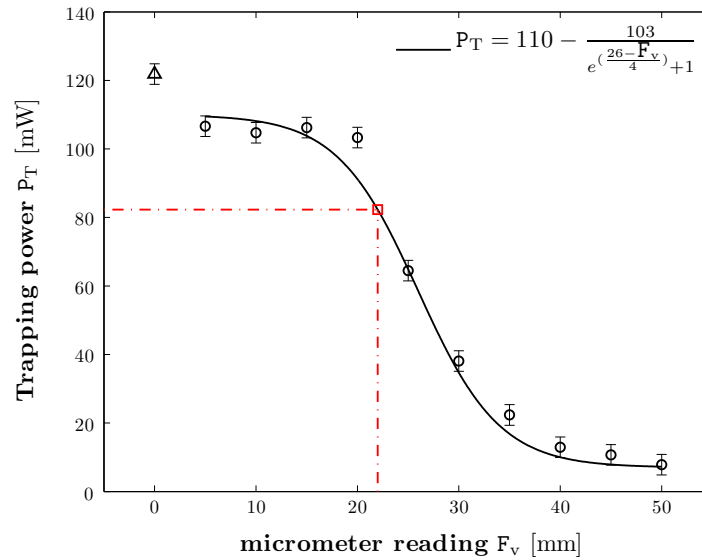
Figure 4.10: Trapping power P_T as a function of micrometer reading for the variable neutral density filter (NDF) F_v. The point $\square$ corresponds to a micrometer reading of $\approx 22\,\text{mm}$ and therefore, $P_T \approx 82\,\text{mW}$. The point $\triangle$ corresponds to P_T with no NDF in place ($F_v = 0\,\text{mm}$) and is thus, the maximum P_T of the laser tweezing system; $122 \pm 3\,\text{mW}$.

for trapping powers > 100 mW, the temperature of the aqueous suspension will increase by approximately 1 K/100 mW [276]. With reference to Fig. 4.10, it is reasonable to assume the trapping power at the sample did not exceed 140 mW.

As described by Neuman and Block [53], the environment in which laser tweezing experiments are performed can affect the sensitivity, stability and signal-to-noise ratio (SNR), namely temperature variations, acoustic noise, mechanical vibrations and air convection. These lead to slow, large-scale drift and low-frequency vibrations.

Drift within the system can lead to a reduced value of κ due to an increased positional variance. Correction for drift can be achieved by fitting a third degree polynominal to the original data and subtracting the polynomial fit to obtain drift-corrected position data as employed by Osterman [277].

Figure 4.11 illustrates this process using position time series data in the x direction for a 6 µm PS bead in water optically trapped with $P_T = 65$ mW, recorded using high-speed video microscopy. Drift on the order of 40 nm over 120 seconds was observed[†]. The solid line (blue) is the third order polynominal fit to the original data and the dashed line (black) illustrates the third order polynomial fit to the drift-corrected data i.e. zero drift. As listed in Table 4.4, this 40 nm drift introduced a 4 pN/µm discrepancy in κ_x.

Table 4.4: Order of magnitude values illustrating how drift leads to an underestimation of κ_x. In this case, a drift on the order of 40 nm per 120 seconds introduced a 4 pN/µm discrepancy in κ_x (see Fig. 4.11).

		$\sigma_x^2 \equiv \langle x^2 \rangle$ [nm^2]	κ_x [pN/µm]
——————	Original with drift	366	11
· — · — · —	Drift-corrected	271	15

In an effort to minimise the ambient sources of noise, the laser tweezing system was placed on a floating optical table, all optics were mechanically secured and placed as close to the optical table as possible to limit resonance and vibration. All free optics were also enclosed in a light-tight box, to reduce air convection, and

---

[†] Please note: lengthy recording times such as 120 seconds would typically be avoided in order to minimise drift and external vibrations but is used here for illustration, where small scale drift might still be present on shorter time scales.
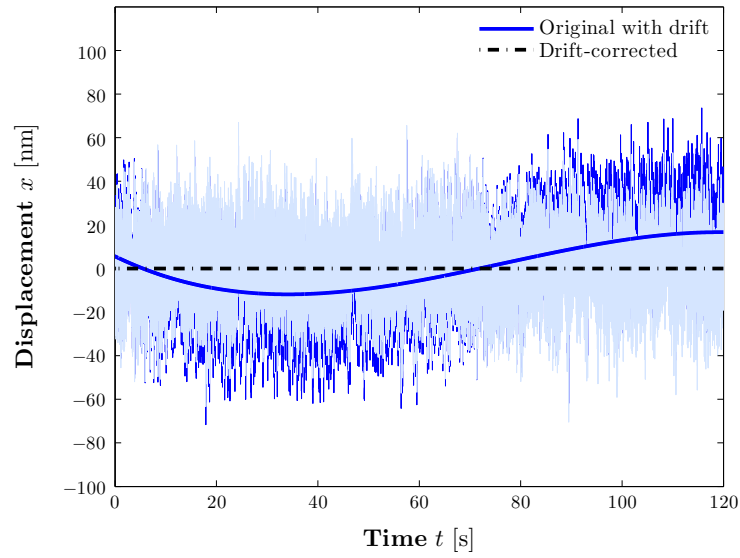
(a)
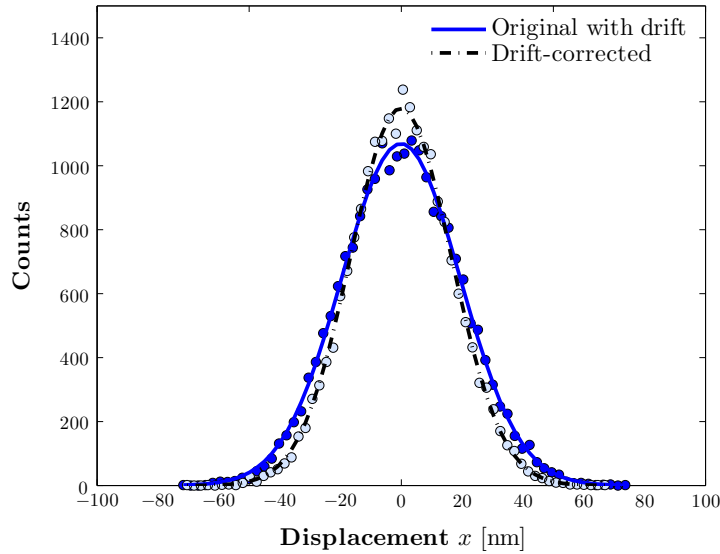
(b)

Figure 4.11: (a) Position time series in the x direction for a 6 μm PS bead in water optically trapped with $P_T = 65$ mW. The solid line (blue) is the third degree polynomial fit to the original data whilst the dashed line (black) illustrates zero drift. This polynominal fit is subtracted from the original data to obtain drift-corrected data (light blue overlaid). (b) Drift affects the associated Gaussian distribution, showing an increased positional variance and therefore, an underestimated trap stiffness as given in Table 4.4 (p. 124).

power supplies, computing and heat sources were located away from the table, e.g. on an overhead shelf or unconnected table. The laboratory in which the experiments were performed was thermostatically controlled between 21–23 °C.

4.6 Summary

This chapter has described the design and implementation of the laser tweezing system used for the work in this thesis. The main components of the laser tweezing system were discussed, including the optical setup, the sample, and imaging and particle tracking. This was followed by descriptions of position and trapping power calibration with associated quantities, and the effect of heating, drift and noise has been discussed.

Chapter 5

Laser Tweezing in Isotropic and Simple Systems

Prior to performing experiments in anisotropic, liquid crystal systems, it was important to characterise the laser tweezers in isotropic and simple systems. This chapter is split into two sections; trap stiffness calibration and investigation of factors affecting lateral and axial tweezing.

Firstly, the chapter presents and compares the results from three different methods of calibration. Experiments were then conducted to investigate the effect specific factors have on the lateral and axial trap stiffness, such as a particle's proximity to a surface, spherical aberration of the optical trap focus, and particle size and refractive index. The properties of the sample chamber are also discussed.

All results in this, and subsequent chapters, employed the laser tweezing system shown in Fig. 4.1, which uses high-speed video microscopy to perform particle tracking.

5.1   Trap stiffness calibration

Trap stiffness calibration can be achieved by recording and analysing an optically trapped particle's position, either in the time or frequency domain. This can either be performed using passive or active techniques where a range of options exist. These include analysis of a trapped particle's Brownian motion, equipar-

tition of energy and associated power spectra, and performing viscous drag force measurements [53, 278, 279].

Performing viscous drag force measurements allows calibration to be achieved relative to either stage or trap motion whilst bead immobilsation facilitates calibration relative to stage motion. Both Brownian motion analysis and viscous drag force measurements are valid only for spherical objects requiring particle diameter and viscosity of the host medium to be known *a priori* [135]. Equipartition theory is often used in combination with Brownian motion analysis in order to eliminate this requirement, as well as particle shape and depth within the sample, in order to calibrate trap stiffness. However, these characteristics will still have an effect on the calibration and their exclusion may produce results which are not truly representative of the trap characteristics [53].

Trap stiffnesses in the x, y and z directions were calibrated using (a) the equipartition (EQ) method, (b) the viscous drag (VD) force method and (c) the PSD method, whilst varying the power of the trapping laser beam. The trapping power P_T was precisely controlled by translating a variable NDF across the laser beam, the calibration for which is given in Section 4.4.2. The three methods used for trap stiffness measurements are described in the following three subsections. All calibration methods use $6\,\mu m$ PS beads suspended in water to allow for direct comparison.

5.1.1   Equipartition method

The equipartition (EQ) method is a passive technique often used to perform trap stiffness calibration by recording and analysing an optically trapped particle's position as a function of time. It is then possible to determine trap stiffness κ as described in Section 2.2.2. Calculation of κ can be made using either Eq. (2.7) where the variance $\langle x^2 \rangle$ is determined from the particle's trajectory, by fitting a Gaussian to the histogram of positions as given by Eq. (2.12) or, finally, by fitting a parabola to the optical potential $U(x)$ as given by Eq. (2.10) ideally to the $\pm 1\sigma$ harmonic region.

Trajectories for a range of trapping powers P_T were acquired with a recording time of $10\,s$ and κ calculated in three dimensions as described in the paragraph above. All data were an average of three measurements and corrected for drift
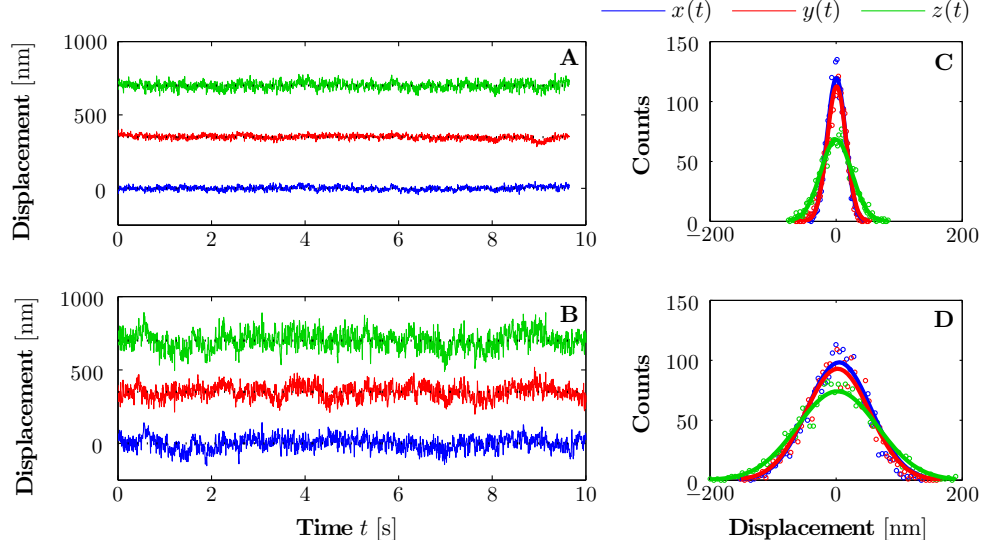
Figure 5.1: Trajectories of a 6 μm PS bead held in a strong (**A**, $P_T = 122\,\text{mW}$) and weak (**B**, $P_T = 10\,\text{mW}$) optical trap. Offsets have been applied to the y and z trajectories, respectively, to visually differentiate their traces. Also shown are the associated histogram of positions and Gaussian fit for the strong (**C**) and weak trap (**D**).

as described in Section 4.5. Each bead was trapped at a constant trap depth $Z_T = 25\,\text{μm}$. Figure 5.1 shows the trajectory of a 6 μm PS in three dimensions and the associated Gaussian distributions when held in a strong and weak optical trap; $P_T = 122\,\text{mW}$ (top) and $P_T = 10\,\text{mW}$ (bottom), respectively.

As described in Section 2.2.2, for large displacements of the bead from the centre of the optical trap, the potential U is no longer harmonic and a Gaussian distribution is insufficient to describe it. Therefore, to determine κ in the harmonic region, the parabolic fit to the potential data is confined to $\pm 1\sigma$ as shown by the solid lines in Fig. 5.2.

For comparison, the trap stiffness in all three dimensions using the three methods of analysis of the particle trajectory for the EQ method are summarised in Table 5.1. In general, κ tends to be overestimated by calculating the variance from the particle's trajectory, and underestimated by fitting a Gaussian to the histogram of positions. The average value of κ from all three methods is very close to that obtained from fitting to the $\pm 1\sigma$ region of the optical potential.

Figure 5.3 shows the linear relationship between κ and P_T in three dimensions. Each value of κ is calculated from the optical potential well and is an average of
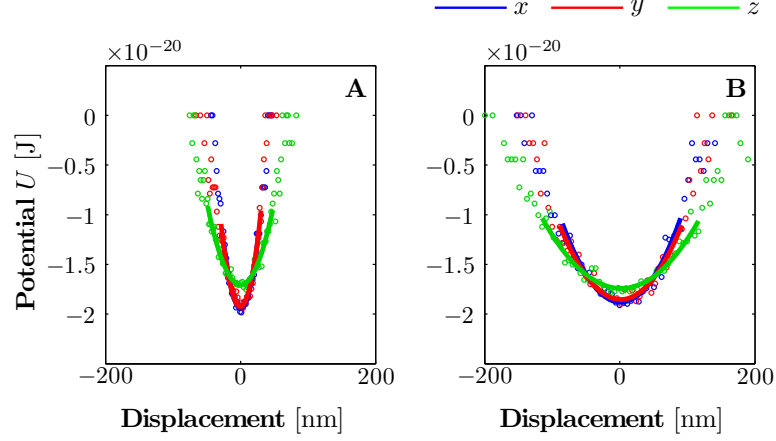
Figure 5.2: Optical potential well for a strong (**A**) and weak (**B**) trap, associated with the trajectories and Gaussian distributions shown in Fig. 5.1. The solid lines represent the parabolic fit to the harmonic region ($\pm 1\sigma$).

three measurements. Trapping power P_T is calculated using the relation between laser beam power and the position of the neutral density filter (Fig. 4.10). The difference in lateral and axial trap stiffnesses is clear, where $\kappa_x > \kappa_y > \kappa_z$. Values of trap stiffness per unit P_T for each dimension (i.e. gradient and associated error) are given in Table 5.2 (p. 137) which compares the three different trap stiffness calibration methods.

Table 5.1: Trap stiffness values in all three dimensions calculated using different statistical analysis methods applied to data obtained with the EQ method (Fig. 5.1).

P_T [mW]	Analysis method	κ_x [pN/µm]	κ_y [pN/µm]	κ_z [pN/µm]
	Trajectory	21.7	17.0	6.6
122	Gaussian fit	19.1	18.0	6.7
	Potential fit ($\pm 1\sigma$)	21.0	20.3	6.7
	Trajectory	2.0	1.8	1.1
10	Gaussian fit	1.6	1.5	1.0
	Potential fit ($\pm 1\sigma$)	2.1	1.8	1.0
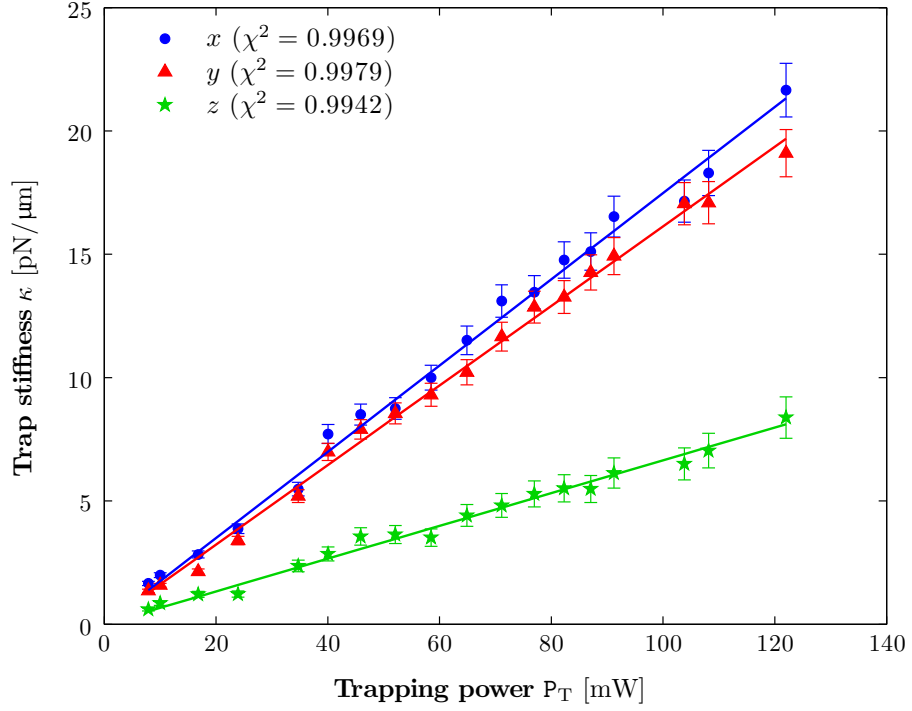
Figure 5.3: Linear relationship between κ and trapping power P_T in all three dimensions using data obtained with the EQ method. One can observe the difference in lateral and axial trap stiffness such that $\kappa_x > \kappa_y > \kappa_z$. Values of trap stiffness per unit P_T for each dimension (i.e. gradient and associated error) are given in Table 5.2 (p. 137).

5.1.2   Viscous drag method

Since the EQ method is a passive method of calibration, the trapped bead can escape from the optical trap and be recaptured during acquisition, which can lead to anomalous values for κ. Therefore, it is advantageous to compare trap stiffness values with an active method of calibration, such as the viscous drag (VD) method.

A known Stokes' viscous drag force $\mathbf{F}_S$ was applied to optically trapped $6\,\mu\text{m}$ PS beads by oscillating the translation stage with a periodic displacement wave function of constant amplitude $\mathbb{A} = 50\,\mu\text{m}$. Varying the oscillation frequency ω of the displacement function varied the viscous drag speed $\mathbf{v}$ and thus, varied $\mathbf{F}_S$. This method is equivalent to translating the trapped particle whilst the surrounding medium remains stationary.

A triangular displacement function was employed in this work, which pro-

duces a square wave of particle displacement and applied force. A sinusoidal displacement function also works well, corresponding to a cosine wave of particle displacement and force [54].

The bead's displacement x and y from the optical trap centre was measured for a range of P_T. This allowed determination of the trap stiffness κ, where bead displacement and the optical restoring force $\mathbf{F}_T$ are directly proportional; $\mathbf{F}_T = \kappa\mathbf{x}$, as described previously in Section 2.2.1.

This method can also be used to perform calibration of trapping *force* by calculating the viscous drag force required to remove the bead from the optical trap as a function of P_T. This is referred to as the *escape force method* and is advantageous in a laser tweezing system devoid of calibrated position detection. It is important to note however, that escape forces relate to properties at the extremities of the optical trap, where the relationship between optical restoring force and displacement becomes non-linear [54]. As such, it is non-trivial to determine trap stiffnesses using the escape force method.

The LabVIEW program *StageControl.vi* was used to apply the displacement functions, which is based on a LabVIEW program written by Tiffany Wood as part of a previous PhD project using laser tweezers [168]. The program was modified by the author to record the position of the translation stage during the displacement function, specifically after each pass. This provided a direct measure of the response of the translation stage to the commands issued.

Oscillation frequencies were varied between 0.1 and 4 Hz, with increments of 0.1 Hz possible, offering viscous drag speeds between 5 μm/s and 200 μm/s. This corresponds to a viscous drag force range of 0.25 − 10 pN for a 6 μm PS bead. Whilst this range would likely prove insufficient for experiments involving the escape velocity of a trapped particle, specifically at high powers, it was sufficient here in order to measure particle displacement as a function of applied viscous drag forces.

Figure 5.4 shows the y position of a 6 μm PS bead with a displacement function of $\omega = 2$ Hz applied to the translation stage in the y direction. This displacement function corresponds to a viscous drag force $\mathbf{F}_S = 2.54$ pN. The PS bead is optically trapped at $P_T = 65$ mW and a trap depth $Z_T = 25$ μm. The plot shows the raw data (light red), the smoothed data after Savitzky-Golay filtering in
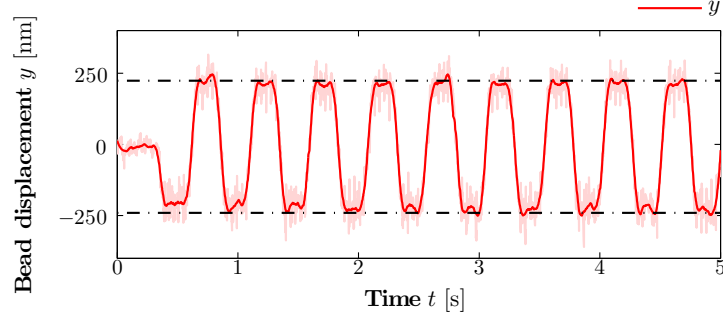
Figure 5.4: Displacement of a $6\,\mu\text{m}$ PS bead optically trapped at $\text{P}_\text{T} = 65\,\text{mW}$ with an oscillation frequency $\omega = 2\,\text{Hz}$ displacement function applied to the translation stage in the y direction. This corresponds to a viscous drag force $\mathbf{F}_\text{S} = 2.54\,\text{pN}$. The plot shows the raw data (light red), the smoothed data (red overlaid) after Savitzky-Golay filtering in Matlab [232], and the average positive and negative y displacement (dash-dot black).

Matlab [232] (red overlaid) and the average positive and negative y displacement (dash-dot black).

The linear relationship between viscous drag force $\mathbf{F}_S$ and bead displacement can be seen in Fig. 5.5 for two trapping powers; (a) $122\,\text{mW}$ and (b) $65\,\text{mW}$.
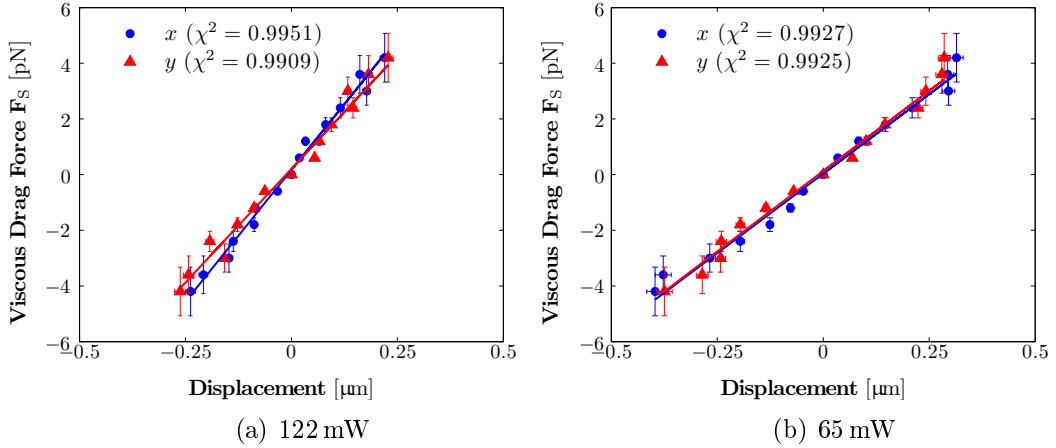
(a) $122\,\text{mW}$ (b) $65\,\text{mW}$

Figure 5.5: The relationship between viscous drag force $\mathbf{F}_\text{S}$ and particle displacement in the x and y directions for two different trapping powers P_T; (a) $122\,\text{mW}$ and (b) $65\,\text{mW}$.

Finally, Fig. 5.6 shows the linear relationship between trap stiffness κ and trapping power P_T in the x and y directions with data acquired with the VD method. The values of trap stiffness per unit P_T for each dimension (i.e. gradient
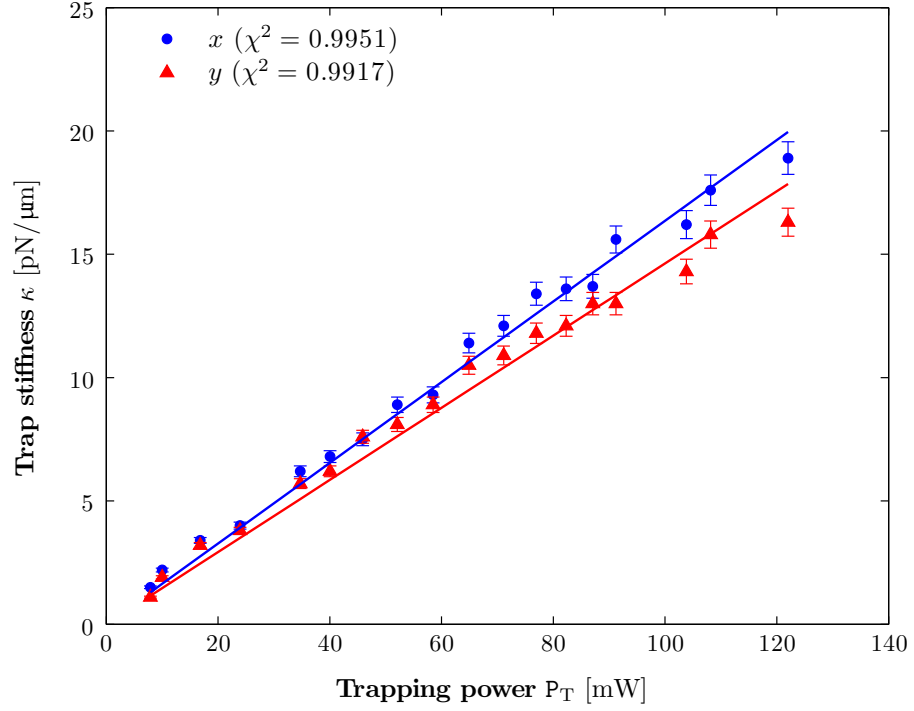
Figure 5.6: Linear relationship between trap stiffness κ and trapping power $\mathtt{P_T}$ for the x and y direction. Data were acquired with the viscous drag (VD) method and values of trap stiffness per unit $\mathtt{P_T}$ for each dimension (i.e. gradient and associated error) are given in Table 5.2 (p. 137).

and associated error) are given in Table 5.2 (p. 137).

Viscous drag force calibration in the axial direction is less straightforward. The particle may escape from the optical trap with negative axial trap displacement and then be recaptured upon return of the trap in the positive axial direction. In addition, axial trapping in an inverted arrangement is aided by the force due to gravity. Two previous PhD projects applied a viscous drag force in the axial direction whilst simultaneously translating the optical trap in the lateral plane to prevent the bead being recaptured [168, 255]. Unfortunately, viscous drag force measurements were not obtained for the axial direction in this project. However, viscous drag calibration in the x and y directions show good agreement with the passive methods of calibration (see Table 5.2, p. 137).

5.1.3 PSD method

Another passive method of trap stiffness calibration involves analysing the position of an optically trapped particle in the frequency domain. As described in Section 2.2.3, the Fourier transform of the particle's Brownian motion within the optical trap allows the trap stiffness to be determined from the characteristic roll-off frequency f_c of the power spectrum, as given in Eq. (2.17).

Position fluctuation data of an optically trapped 6 μm PS bead were recorded whilst varying P_T to calculate f_c and, thus, κ in three dimensions. This was achieved with real-time PSD analysis using the LabVIEW program *SimpleAnalysis.vi*[*] which obtains f_c from the Lorentzian fit to the Fourier transformed position fluctuation data.

The program also calculates the viscosity η of the medium surrounding the particle using Eq. (2.20) following user-input of the trapped particle's radius. The calculation of η relies on the fact that at correlation time $\tau = 0$, the ACF in Eq. (2.21) reduces to $\langle x^2 \rangle$, as described in Section 2.2.4. Finally, the program provided the option to apply a time averaging filter to the power spectrum and the author modified the program further to export the resulting PSD data and associated Lorentzian fit for x, y and z to a tab delimited text file.

Figure 5.7 shows the PSD for a 6 μm PS bead suspended in water optically trapped at $P_T = 65\,\text{mW}$ and $Z_T = 25\,\text{μm}$. The data and associated Lorentzian fit in each dimension are averaged over at least 50 scans. The figure illustrates the direct proportionality between κ and f_c in agreement with Eq. (2.17). Thus, the relative values of the corner frequency in each dimension show that $\kappa_x > \kappa_y > \kappa_z$, which is in agreement with the previous two calibration methods.

The raw data in Fig. 5.7 show some deviation from the theoretical fit at low frequencies which can be attributed to laser noise, low-frequency drift and any heating in the sample. Deviations at higher frequencies are associated with vibrational noise, aliasing effects, and motion blur due to the limited bandwidth of the CMOS camera [222].

---

[*] Written with the help of R. Bowman and largely based on programs written by the Optics Research Group at The University of Glasgow, which are available for public download, URL: `www.gla.ac.uk/schools/physics/research/groups/optics/research/optical tweezers/software/` [275].
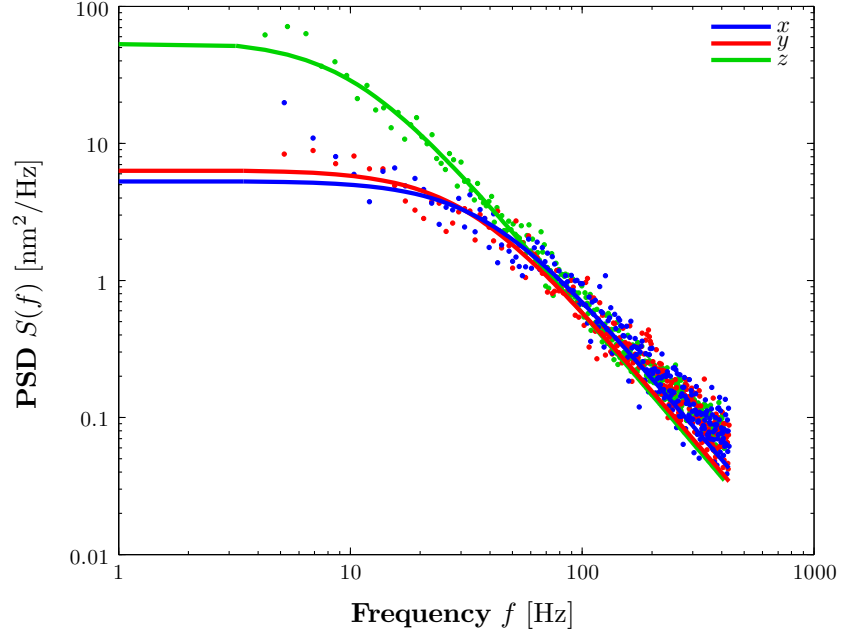
Figure 5.7: Power spectral density $S(f)$ for a $6\,\mu$m PS bead optically trapped at $P_T = 65\,$mW and $Z_T = 25\,\mu$m. Trap stiffness κ and corner frequency f_c are directly proportional as given by Eq. (2.17) thus, illustrating $\kappa_x > \kappa_y > \kappa_z$.
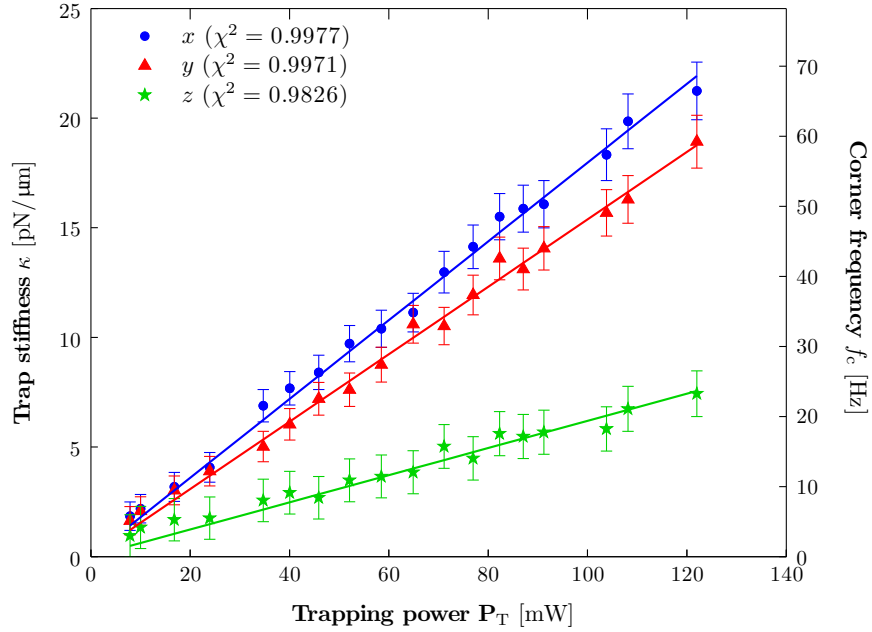
Figure 5.8: Linear relationship between trap stiffness κ and trapping power P_T in all three dimensions determined using the PSD method. The second vertical axis shows the linear relationship between f_c and P_T. The plot illustrates the differences in lateral trap stiffness; $\kappa_x > \kappa_y > \kappa_z$. Values of trap stiffness per unit P_T for each dimension (i.e. gradient and associated error) are given in Table 5.2 (p. 137).

The expected linear relationship between P_T and κ in all three dimensions is shown in Fig. 5.8. The data were obtained using the PSD method and each data point corresponds to an f_c value obtained from a Lorenztian fit averaged over ~50 scans. Values of trap stiffness per unit P_T for each dimension (i.e. gradient and associated error) are given in Table 5.2 (p. 137).

5.1.4 Trap stiffness calibration summary

Trap stiffness calibration for the laser tweezing system was performed using three different methods; equipartition, viscous drag and PSD analysis. Values of trap stiffness per unit trapping power P_T for all three dimensions are given in Table 5.2, with the exception of the VD method which was determined in the lateral dimensions only. These values correspond to the gradient and associated error from Figs. 5.3, 5.6 and 5.8. All values are statistically consistent.

Table 5.2: Comparison of trap stiffnesses per unit trapping power for each calibration method; equipartition (EQ), viscous drag (VD) and power spectral density (PSD) analysis. All values are statistically consistent with one another.

Method	Trap stiffness [pN/μm mW]		
	κ_x/P_T	κ_y/P_T	κ_z/P_T
EQ	0.175 ± 0.004	0.160 ± 0.004	0.065 ± 0.002
VD	0.163 ± 0.003	0.146 ± 0.003	—
PSD	0.180 ± 0.005	0.154 ± 0.004	0.062 ± 0.002

5.2 Factors affecting laser tweezing in three dimensions

As detailed in Chapter 4, development of the laser tweezing system allowed accurate particle tracking in the axial direction in addition to the lateral directions, using high-speed video microscopy. This provided the opportunity to characterise the laser tweezing system in all three dimensions where a selection of factors were investigated and shall be described in this section.

Firstly, the effect due to the proximity of a surface to the trapped particle and the application of Faxén's Law is investigated. This is followed by studying the effect due to spherical aberrations of the optical trap focus. Finally, the particle's size and refractive index is studied and the effect of the sample chamber properties is discussed.

5.2.1   Particle's proximity to a surface

As described in Section 2.3, the viscous drag force felt by a particle increases due to the close proximity of a surface, such as the coverslip. It is possible to apply a correction to the viscous drag coefficient γ, as given by Stokes' Law, to account for the proximity of one wall, known as Faxén's correction. Equations (2.28) and (2.29) can be used to calculate the corrected viscous drag coefficient in both the lateral and axial directions; $\gamma_\parallel$ and $\gamma_\perp$, respectively, which are a function of particle radius r and trap depth Z_T.

All plots in Section 5.1 and the values quoted in Table 5.2 are calculated using γ given by Stokes' Law, i.e. excluding any effect due to the proximity of the coverslip. This subsection aims to quantify this effect.

Trap stiffnesses for a 6 µm PS bead suspended in water were calculated using the PSD method as described in Section 5.1.2. The trapping power P_T was held constant at 65 mW whilst varying trap depth Z_T between 3 and 40 µm. The dependence of trap stiffness on Z_T for the lateral and axial directions is shown in Fig. 5.9. Figures 5.9(a) and (b) illustrate the difference in κ when calculated using γ from Stokes' Law or using $\gamma_\parallel$ and $\gamma_\perp$ from Faxén's Law. Each data point in both figures is an average of three measurements and the x and y directions have been averaged together in Fig. 5.9(a). Values of κ at small trap depths have a greater error due to $\gamma_\parallel$ and $\gamma_\perp$ having a strong dependence on r and Z_T [280].

In Fig. 5.9, the effect of the coverslip's proximity on κ can be seen in the data determined using Stokes' Law. At trap depths $Z_\mathrm{T} \lesssim 10$ µm, the particle experiences a weaker trap stiffness. Using Faxén's Law to determine κ evaluates the trap stiffness the particle *would* experience if the coverslip had no effect. At $Z_\mathrm{T} = 5$ µm, trap stiffness in the lateral and axial directions increases by 51% and 191%, respectively. The 3-fold increase in κ_z seems particularly high and as the axial trap stiffness is weaker than the lateral trap stiffness — on the order of 4

(a)

(b)
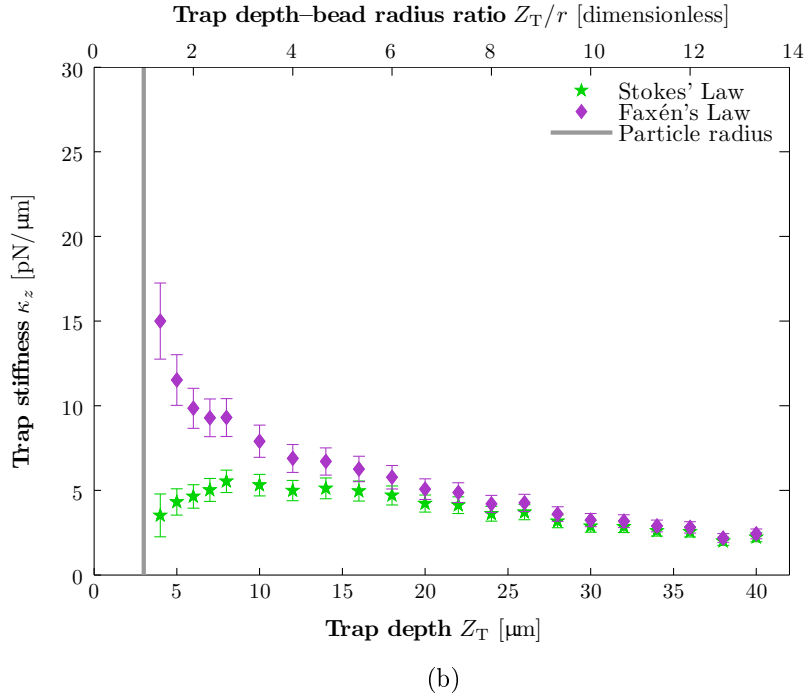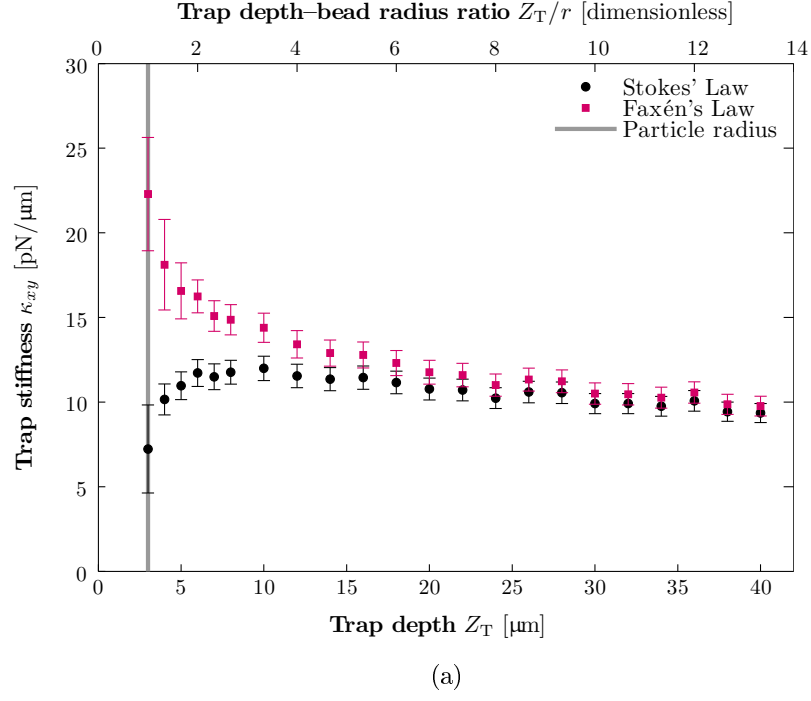
Figure 5.9: The dependence of trap stiffness κ on trap depth Z_T in the (a) lateral and (b) axial directions. Here, κ has either been calculated using Stokes' viscous drag coefficient γ or those with Faxén's correction for coverslip proximity in the lateral and axial direction, $\gamma_\parallel$ and $\gamma_\perp$, respectively. Data were obtained using the PSD method and each point is an average of three measurements

times weaker — perhaps Faxén's Law is accounting for effects other than those due to the proximity of the coverslip.

The other effect to note in Figs. 5.9(a) and (b) is the decrease in trap stiffness at $Z_T \gtrsim 12\,\mu m$. This is attributed to spherical aberrations of the optical trap and an attempt is made to quantify this effect in Section 5.2.2.

5.2.2 Spherical aberrations

Laser tweezing experiments are usually performed at large trap depths in order to limit the effect of coverslip proximity, as described in Section 5.2.1, and to prevent the particle adhering to the coverslip. However, as described in Section 4.1.1.1, when using high NA oil-immersion objectives, the trapping beam experiences spherical aberration due to the refractive index mismatch between the immersion oil and the trapping sample's host medium, typically water. This effect, shown in Fig. 4.3, increases with trap depth and affects the trap stiffness, and thus the optical trapping force.

Vermeulen *et al.* demonstrated lateral and axial stiffness with no dependence on trap depth for $2\,\mu m$ silica and polystyrene particles when trapping with a water-immersion objective, compared with a strong dependence for an oil-immersion objective. There are no spherical aberrations present when using a water-immersion objective because refraction of the beam at both the water-glass and glass-water interfaces has a compensatory effect [280].

As shown in Section 5.2.1, a reduction in the lateral and axial trap stiffnesses at small trap depths is observed due to the increased viscous drag close to the coverslip. However, despite accounting for this with Faxen's correction, a steady, continual drop in lateral and axial trap stiffness is observed for trap depths $Z_T \gtrsim 10\,\mu m$. This decrease is attributed to spherical aberration of the optical trap.

The effect due to spherical aberrations can be clearly seen in Fig. 5.10. The plots show the position distribution of a 6μm PS bead suspended in water and optically trapped at $P_T = 65\,mW$ for two different trap depths; $Z_T = 10\,\mu m$ and $Z_T = 40\,\mu m$. The reduction in lateral trap stiffnesses with increasing Z_T is observed in Fig. 5.10(a), where an increased standard deviation σ_{xy} is observed. This agrees with an even broadening of the trap focus in the lateral plane.

(a) Top view

(b) Side view (x)

(c) Side view (y)
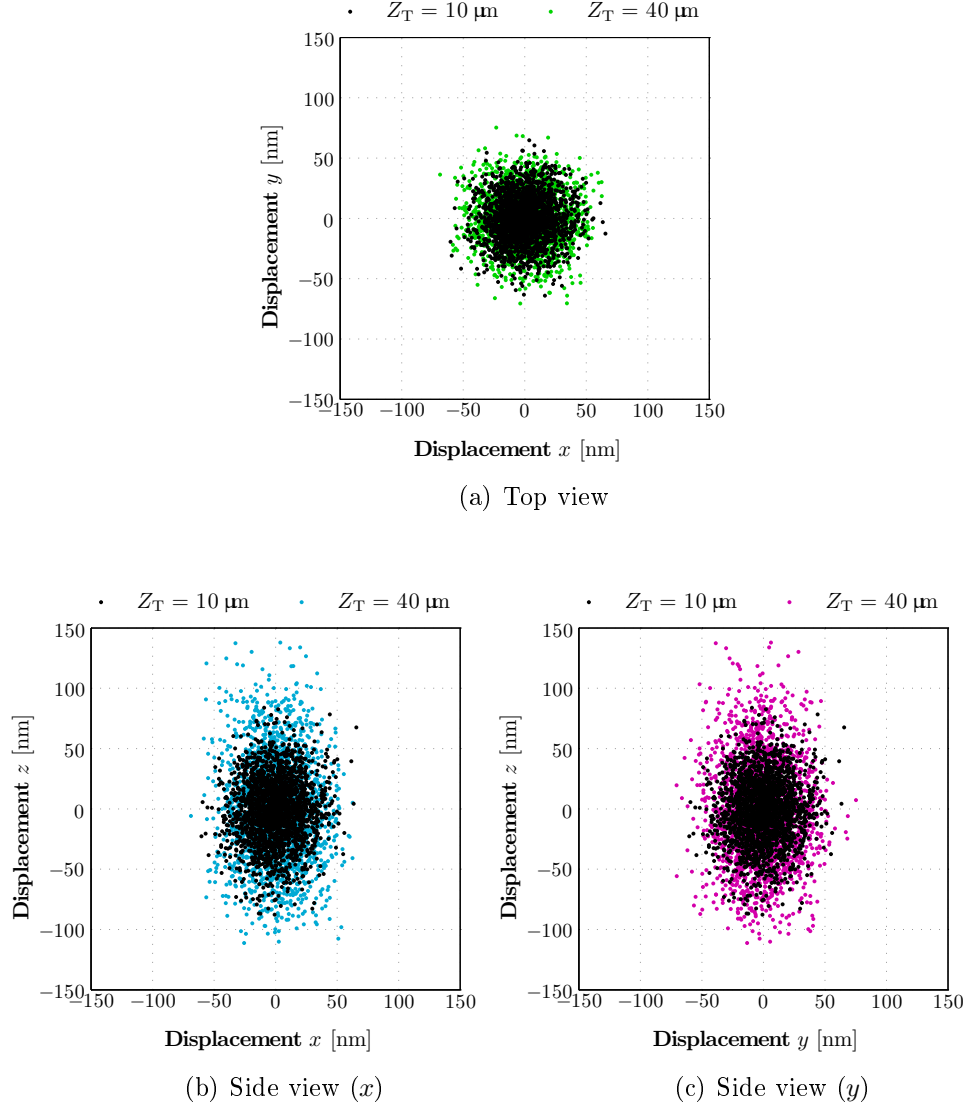
Figure 5.10: Position distributions of a $6\,\mu\text{m}$ PS bead suspended in water and optically trapped at $\texttt{P}_\text{T} = 65\,\text{mW}$ recorded at two different trap depths; $Z_\text{T} = 10\,\mu\text{m}$ and $Z_\text{T} = 40\,\mu\text{m}$. Increased standard deviations illustrate (a) an even broadening of the optical trap focus in the lateral direction and (b),(c) a significantly elongated optical trap focus in the axial direction.

The increased standard deviation σ_z leading to a reduced κ_z is far more pronounced than in the lateral directions. The elongated focus in the axial direction created due to spherical aberrations is apparent in Figs. 5.10(b) and (c), which show a side view of the position distribution from x and y, respectively.

An attempt was made to quantify the effect due to spherical aberrations. Figure 5.11 shows a linear fit to the axial and lateral trap stiffnesses for $Z_\text{T} >$
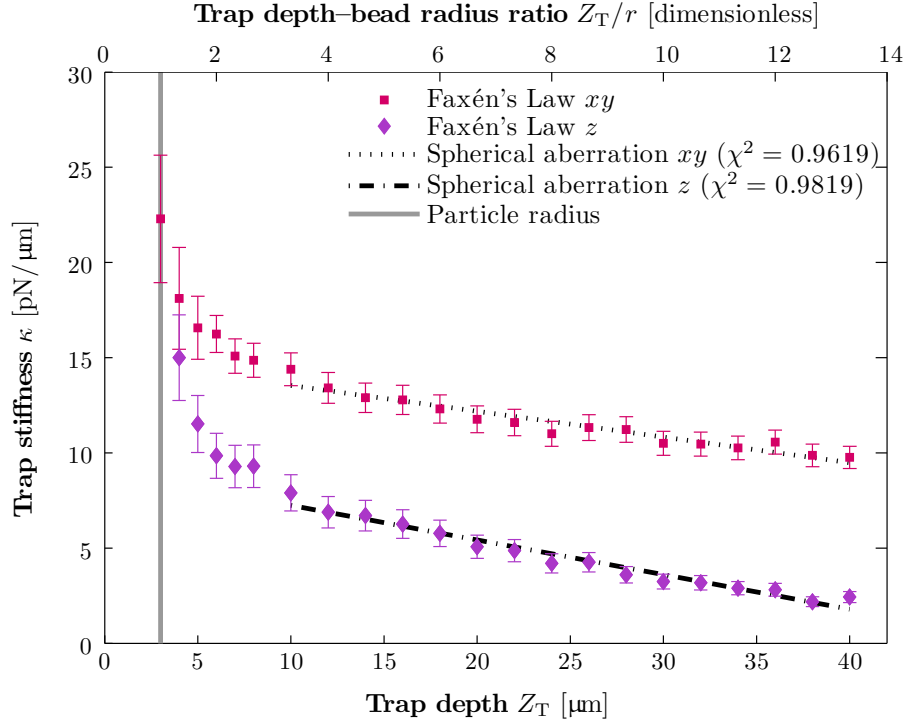
Figure 5.11: Lateral and axial trap stiffnesses; κ_{xy} (red squares) and κ_z (purple diamonds) calculated using Faxén's Law as a function of trap depth Z_T. Thus, the data shown is the corrected data from Fig. 5.9. The dashed lines represent a linear decrease in stiffness due to spherical aberration of the optical trap focus. They correspond to a 42 % and 75 % drop in κ_{xy} and κ_z, respectively.

$10\,\mu\text{m}$ after Faxén's correction has been applied to the data (Fig. 5.9). Between trap depths of 10 and $40\,\mu\text{m}$, the linear fits indicate a 42 % drop in κ_{xy}, with a 75 % drop in κ_z. This corresponds to a linear decrease of 1.4 % and 2.5 % per micron of trap depth in κ_{xy} and κ_z, respectively.

These values are in good agreement with those published in the literature, including a linear decrease of $1.6\,\%/\mu\text{m}$, and a $1.76\,\%/\mu\text{m}$ [280], although this is 1.5 times less than the linear decrease indicated in this work, it is of the right order of magnitude.

Dienerowitz *et al.* illustrated that 1st order spherical aberrations created when using a high NA oil-immersion objective lens can be compensated for using aberration correction with an SLM. They increased the trap stiffness by a factor of 3 and maintained a constant trap stiffness over a range of $50\,\mu\text{m}$ into the sample [281].

5.2.3   Sample chamber properties

Fabricated liquid crystal cells are significantly thinner than isotropic samples; on the order of 25–40 μm compared with ∼350 μm. As discussed in Section 5.2.1, the particle's proximity to the coverslip surface acts to increase the viscous drag experienced by the particle and thus, a reduction in trap stiffness is observed in both the lateral and axial directions. Therefore, it was necessary to consider if the particle being in close proximity to *both* coverslip surfaces had any effect on the trap stiffness.

A LC cell is comprised of two coverslips sandwiched together, therefore the area available for tweezing remained constant at 18×18 mm. To minimise the effect of the boundary wall provided by the spacers, tweezing was performed well away from the edge of the coverslip.

Faxén's Law corrects for the proximity of a single surface only (Eqs. (2.28) and (2.29)). However, Felgner *et al.* [231] employed the reflection method to derive an expression for the modification of Stokes' viscous drag coefficient due to the proximity of two surfaces;

$$\gamma_{\mathrm{RM}} = \gamma \left(1 + \frac{9r}{16} \left\{ \frac{1}{Z_{\mathrm{T}}} - \frac{1}{\mathrm{h} - Z_{\mathrm{T}}} \right\} \right) \tag{5.1}$$

where h is the thickness of the sample chamber, and Z_{T} and r have their usual definitions of trap depth and particle radius.

In the case of sample chambers with a small thickness, it is not possible to reduce the effect due to the coverslip surface(s). Therefore, one may consider accounting for their effect by calculating the viscous drag coefficient directly from Eq. (5.1).

5.2.4   Particle size

Trap stiffness is dependent on the size of the optically trapped particle. Since laser tweezing experiments in anisotropic systems employ particle's of differing size, it was important to investigate any effect this may have on the trap stiffness in an isotropic system.

For larger particles, i.e. those with diameter $d \gg \lambda$, a decrease in trap stiffness proportional to the inverse of the radius r^{-1} is expected. This is because, although maximum trapping force is independent of particle size, the trapping rays cover a larger distance. Therefore, a larger bead must traverse a larger distance in order to produce the same force as that of a smaller bead. Comparatively, particles in the Rayleigh regime, where $d \ll \lambda$, stiffness is expected to rise with increasing diameter with the increase proportional to r^3 [56, 230].

Trap stiffnesses in the lateral and axial directions were determined using the PSD method for a range of PS beads suspended in water. The beads were optically trapped at a constant $Z_\mathrm{T} = 25\,\mu\mathrm{m}$. Figure 5.12 shows the variation in κ_{xy} and κ_z per unit trapping power $\mathtt{P_T}$ with increasing particle radius. Each data point is an average of three measurements where κ_x and κ_y have also been averaged together.
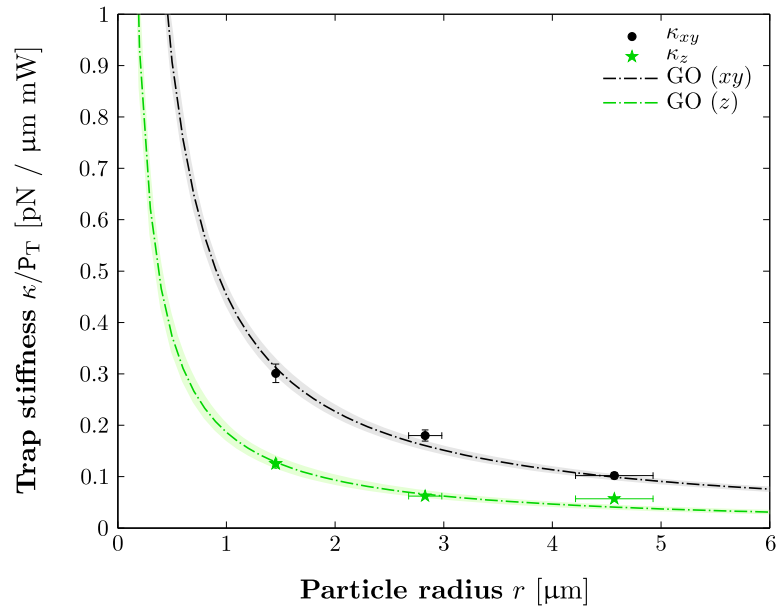
Figure 5.12: Lateral and axial trap stiffnesses as a function of particle radius for PS beads, where each data point is an average of three measurements. The dashed lines are a least squares curve fit to the data corresponding to the geometrical optics (GO) regime where $\kappa \propto r^{-1}$. Error bars are plotted if larger than the points themselves. The light grey and green areas correspond to the standard error of the least squares curve fit. Errors in r are those quoted by the manufacturer (Table 3.3, p. 99).

The dashed lines in Fig. 5.12 are the least squares curve fits to the data and correspond to the geometrical optics (GO) regime. The decrease in κ_{xy} and

κ_z closely resembles the expected nonlinear decrease proportional to r^{-1} where $\kappa_{xy} = 0.45\,\mathrm{pN/\mu m}$ mW and $\kappa_z = 12\,\mathrm{pN/\mu m}$ mW per micron of particle radius. This is also in good agreement with the literature. Viana *et al.* [282] measured the axial trap stiffness per local power using optical tweezers, where Brownian motion time decay values from the ACF were used to calculate trap stiffness. They also observed an asymptotic relationship between κ and r following the geometrical optics model.

Although the drop is nonlinear, the data in Fig. 5.12 shows a 66 % and 54 % drop in κ_{xy} and κ_z, respectively, over the range of radii. Comparatively, both the fits indicate the same 68 % drop in both κ_{xy} and κ_z over the range of radii measured. There appears to be a weaker dependence of κ on r found in this work than previously reported [282] and in comparison, one would expect a higher κ value for the $r = 1.45\,\mathrm{\mu m}$ PS bead in Fig. 5.12. This suggests the system is underestimating κ due to an underestimation of f_c; a consequence of noise within the system, such as optical misalignment, which the power spectrum is sensitive to [53, 118].

5.2.5   Particle refractive index

As explained in Section 2.1.1, for successful optical trapping, the criterion between particle refractive index n_p and medium refractive index n_m; $n_p > n_m$, should be satisfied. In a system where water is the medium surrounding the trapped particle, typical laser tweezing experiments employ polystyrene or silica as the probe bead. Polystyrene particles are favourable since they produce the larger difference between n_p and n_m, thereby exerting a greater trapping force.

Measurements of κ_{xy} and κ_z for a $10\,\mathrm{\mu m}$ (nominal) SC bead were comparable with values for a PS bead of the same size. With an increase in n_p of 0.03 from SC ($n_p = 1.56$) to PS ($n_p = 1.59$), values indicated an 11 % and 17 % increase in κ_{xy} and κ_z, respectively. This increase in κ for increasing n_p is as expected in accordance with Eq. (2.30).

However, the range investigated here is insufficient to provide conclusive evidence of the change in κ due to n_p. Determining the change in κ over SC beads with a range of radii would provide a more precise method of investigating how trap stiffness changes as a function of n_p. Also, the range studied should be larger

with options including soda lime glass beads ($n_\mathrm{p} = 1.51$), SiO_x-coated PS beads ($n_\mathrm{p} = 1.45$) and plain silica beads ($n_\mathrm{p} = 1.37$) [283].

5.3   Summary

This chapter details the characterisation of the laser tweezing system in isotropic and simple systems beginning first with trap stiffness calibration, where three different techniques are compared; equipartition, viscous drag and PSD. Also given are results which investigate the factors affecting lateral and axial trap stiffnesses.

Each of the three calibration methods employed achieve good accuracy and are consistent. The VD method shows slightly improved accuracy compared with the EQ and PSD methods as they are passive methods of calibration. Since it is in the frequency domain, the PSD method is superior as it provides more details about the particle's motion and thus, the properties of the optical trap.

In addition, the PSD method, in conjunction with real-time analysis, provides a fast, visual measure of the trap strength. It allows immediate observation of any factors affecting the trap, such as aliasing, motion blur, or vibrational and instrument noise which induce additional peaks in the power spectra. Also, any mis-alignment in the optical trap or particle detection produces non-Lorentzian power spectra [53]. The calibration values detailed herein apply to the results in the remainder of the thesis, unless otherwise stated.

Experiments were conducted to investigate factors which affect the lateral and axial trap stiffness and an effort made to quantify them for this laser tweezing system. Both the lateral and axial trap stiffness was found to decrease with increasing proximity to a surface, significantly so as the trap depth approaches the radius of the trapped particle.

Similarly, the refractive index mismatch between the surrounding medium and the glass coverslip induced aberrations in the optical trap focus, whose effect increased with increasing trap depth. This was found to occur more strongly in the axial direction than the lateral direction. It was decided that Z_T between 10 and 15 µm provided a sufficient separation between the particle and the coverslip to minimise surface effects whilst also minimising the effect due to spherical

aberrations. From this point onwards, any calulations involving the viscous drag coefficient will calculate the value directly from Eqs. (2.28) and (2.29) in order to account for surface effects. There will be no correction applied for spherical aberrations.

In the case of LC cells, where the average cell thickness h was between 20–40 μm, the particle will experience an increased viscous drag force due to the proximity of both surfaces. It is expected that the particle will also feel the same effects due to spherical aberration of the optical trap focus as in larger cells.

Finally, the properties of the particle were considered, namely the particle's size and refractive index. It was found that the lateral and axial trap stiffness decreased with increasing particle radii, with a decrease proportional to r^{-1}, as expected. Measurements of lateral and axial trap stiffnesses for a PS and SC bead of approximately the same radius indicated an increase in stiffness with increasing particle refractive index; i.e. increased trap stiffnesses for the PS bead.

Chapter 6

Laser Tweezing in Water–Glycerol Mixtures

The study of a material's flow or deformation using microscopic particles, also known as microrheology, has seen increased interest in recent years. The field examine's the viscoelastic properties of complex fluids in order to better understand and characterise them.

Laser tweezers are often employed to study viscoelastic behaviour since they permit localised investigation in as little as picolitres of fluid. Microrheological techniques can be divided into two main types; passive and active. Passive microrheology observes the free motion of probe particles, whilst active microrheology observes their motion under the application of an external driving force.

It is possible to characterise simple and purely viscous fluids, such as water and glycerol, by their viscosity. Glycerol, for example, exhibits Newtonian fluid behaviour due to the short polymer chains present [77, 225]. With the addition of water, glycerol (bulk viscosity $\sim 1.4 \, \mathrm{Pa\,s}$) becomes significantly less viscous [284].

The relationship between viscosity and glycerol content in water–glycerol (WG) mixtures has been well characterised. Cheng [285] developed an empirical formula to calculate the viscosity of WG mixtures for varying temperatures and concentrations of glycerol. More recently, Trejo González, Longinotti and Corti [286] collated data and described a range of models for predicting and determining the viscosity of WG mixtures, specifically in the supercooled region ($< 273 \, \mathrm{K}$).

Laser tweezers have been used to study the viscosity of WG mixtures with varying glycerol concentration. Parkin *et al.* [77] employed optically rotating particles using microlitres of mixture whilst Guzmán *et al.* [287] measured the power spectral density of optically trapped particles under the application of an oscillatory viscous drag force. Brau *et al.* [284] also used an active method; observation of an optically trapped bead's motion whilst it experiences a viscous drag force. However, they kept their analysis of the WG mixtures in the time domain.

To further test the capabilities of the system reported here, laser tweezing experiments were performed in WG mixtures in order to probe microscopic viscosity. Crucial to this method is accurate position calibration since all methods rely on observation of the particle's position relative to the centre of the optical trap.

6.1   Theoretical calculations

As described by Cheng [285], the dynamic viscosity of a water–glycerol mixture η_{wg} is related to the dynamic viscosity of the water and glycerol components; η_{w} and η_{g}, respectively

$$\eta_{\mathrm{wg}} = \eta_{\mathrm{w}}^{\zeta}\eta_{\mathrm{g}}^{1-\zeta} \tag{6.1}$$

where the weighting factor ζ varies between 0 and 1. Equation (6.1) can also be rewritten as

$$\eta_{\mathrm{wg}} = \eta_{\mathrm{g}}\exp(\mathtt{A}\zeta) \tag{6.2}$$

where $\mathtt{A} = \ln(\eta_{\mathrm{w}}/\eta_{\mathrm{g}})$.

Cheng also derived an expression for calculating ζ as a function of mass fraction Φ_{m} and temperature T (here in °C);

$$\zeta = 1 - \Phi_{\mathrm{m}} + \frac{a(T)b(T)(1-\Phi_{\mathrm{m}})\Phi_{\mathrm{m}}}{a(T)\Phi_{\mathrm{m}} + b(T)(1-\Phi_{\mathrm{m}})} \tag{6.3}$$

with coefficients $a = 0.705 - 0.0017T$ and $b = (4.9 + 0.036T)a^{2.5}$. Therefore, in

order to calculate `A` as given in Eq. (6.2), one must calculate η_w and η_g as follows;

$$\eta_\mathrm{w} = 1.790 \exp\left(\frac{(-1230 - T)T}{36100 + 360T}\right) \tag{6.4}$$

$$\eta_\mathrm{g} = 12100 \exp\left(\frac{(-1233 + T)T}{9900 + 70T}\right) \tag{6.5}$$

and in order to calculate Φ_m, it is necessary to calculate the mass of water and glycerol, m_w and m_g, respectively. This begins by calculating the temperature dependent densities of water and glycerol as follows

$$\rho_\mathrm{w} = 1000\left(1 - \left|\frac{T - 4}{622}\right|^{1.7}\right) \tag{6.6}$$

$$\rho_\mathrm{g} = 1277 - 0.654T \tag{6.7}$$

which can be combined with the volume of water and glycerol, V_w and V_g, to determine m_w and m_g. Thus,

$$\Phi_\mathrm{m} = \frac{m_\mathrm{g}}{m_\mathrm{g} + m_\mathrm{w}} = \frac{\rho_\mathrm{g}V_\mathrm{g}}{\rho_\mathrm{g}V_\mathrm{g} + \rho_\mathrm{w}V_\mathrm{w}} \tag{6.8}$$

and the percentage by weight (% w/w) is simply Φ_m multiplied by 100. The density of the WG mixture can be evaluated as

$$\rho_\mathrm{wg} = \rho_\mathrm{g}\Phi_\mathrm{m} + \rho_\mathrm{w}(1 - \Phi_\mathrm{m}), \tag{6.9}$$

and the kinematic viscosity of the WG mixture is then $\nu_\mathrm{wg} = \eta_\mathrm{wg}/\rho_\mathrm{wg}$.

6.2   Sample preparation

Water–glycerol mixtures were prepared by diluting anhydrous glycerol ($> 99\%$ $C_3H_5(OH)_3$, Sigma-Aldrich [288]) in distilled water to produce four concentrations; 10 %, 25 %, 50 % and 75 % (w/w). The solutions were mixed using an ultrasonic bath. Dried polystyrene beads with a diameter of 6 μm were added to each WG mixture to produce relatively low bead concentrations, on the order of 5 % solids by weight.

A small amount of each WG mixture was used to create a sample in the same way as the isotropic samples (Fig. 4.5). Thus, they had an area of 18×18 mm and a depth $\sim 350 \, \mu$m.

6.3   Microviscometry

The laser tweezing system (Fig. 4.1) was used as a microviscometer, by applying both active and passive techniques to determine the dynamic viscosity in WG mixtures of varying glycerol concentration.

It was first of all necessary to determine the trap stiffness κ in each of the WG mixtures using a technique which does not require its viscosity to be known *a priori* [284]. The EQ method was used to record the position of optically trapped particles in each of the WG mixtures at a range of P_T. Trap stiffness is then calculated from the equipartition of energy theorem (Eq. (2.7)).

All experiments were performed at a constant trap depth $Z_T = 10 \, \mu$m so as to minimise the effects due to the proximity of the coverslip and spherical aberration of the optical trap focus as discussed in Sections 5.2.1 and 5.2.2.

6.3.1   Active microviscometry

The viscosity of a fluid can be measured using laser tweezers and the application of a Stokes' viscous drag force. When the particle is subject to a fluid flow, and if the particle remains trapped, the viscous drag force is balanced by the optical restoring force. As described in Section 2.2.1, if κ is known, this technique permits viscosity η to be determined as given by;

$$\eta = \frac{\kappa \mathbf{x}}{6 \pi r \mathbf{v}} \tag{6.10}$$

where r is particle radius, $\mathbf{v}$ is the velocity of the particle's motion and $\mathbf{x}$ is its subsequent displacement from the optical trap centre.

As described in Section 5.1.2, a known Stokes' viscous drag force $\mathbf{F}_S$ was applied to optically trapped beads in each of the WG mixtures by oscillating the translation stage with a triangular wave displacement function of constant

(a)

(b)
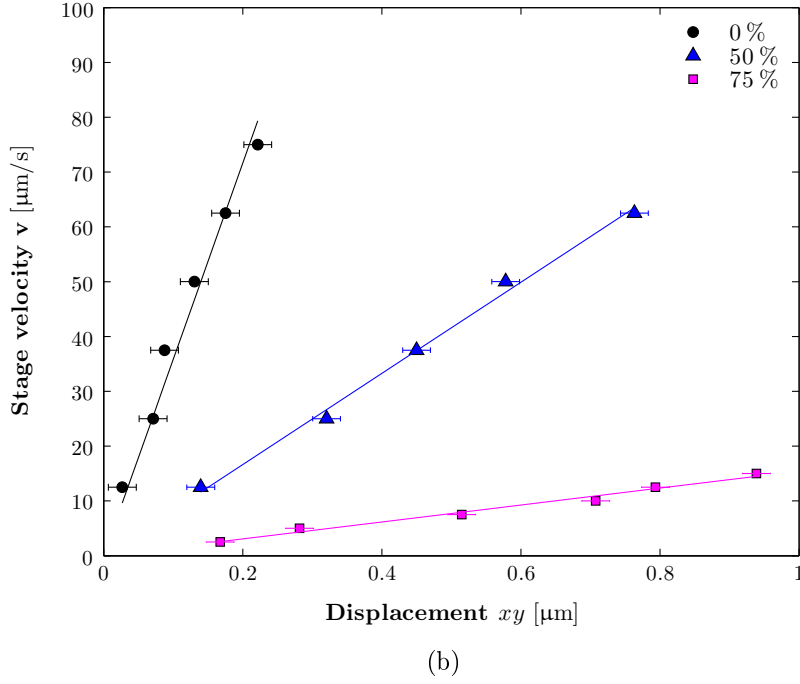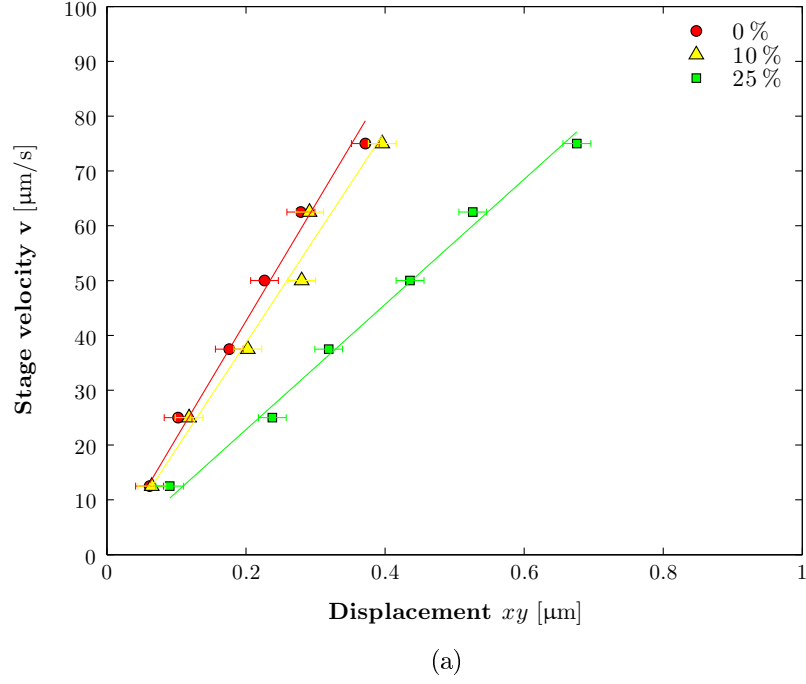
Figure 6.1: For a viscous drag force applied to an optically trapped particle, there exists a linear relationship between stage velocity and lateral particle displacement xy which allows calculation of the medium viscosity η from Eq. (6.10). The plots correspond to the displacement of $6\,\mu$m PS beads in WG mixtures with varying glycerol concentration for (a) 0, 10 and 25 % concentrations at $\mathtt{P_T} = 65\,$mW and (b) 0, 50 and 75 % at $\mathtt{P_T} = 122\,$mW.

amplitude 50 µm. Displacement of the 6 µm PS bead from the optical trap centre was measured for a range of P_T. The viscosity η_{wg} was then calculated using Eq. (6.10), where κ had been determined for each WG mixture using the EQ method.

Figure 6.1 shows the linear dependence of an optically trapped particle's displacement from the optical trap centre on stage velocity for four WG mixtures. This dependence is compared for a 6 µm PS bead in 0, 10 and 25 % glycerol for $P_T = 65$ mW (Fig. 6.1(a)) and in 0, 50 and 75 % glycerol for $P_T = 122$ mW (Fig. 6.1(b)).

Each data point in Fig. 6.1 is an average of two measurements of the displacement, where x and y and positive and negative displacements have been averaged together.

As expected from Eq. (6.10), the particle's displacement from the optical trap centre increases with increasing glycerol concentration. This is because each mixture becomes more viscous with the increased addition of glycerol, thereby exerting a greater viscous drag on the particle. Also shown is the reduction in particle displacement with increased trapping power P_T, as expected.

6.3.2   Passive microviscometry

The PSD method is often used as a calibration method (Section 5.1.3) and has been combined with Stokes' viscous drag to calculate η_{wg} [287]. This work employs the PSD method independently, as a passive technique to determine η_{wg}. This allows direct comparison to values determined using an active technique on the same laser tweezing system.

The power spectrum of an optically trapped bead's Brownian motion is given by Eq. (2.19). The characteristic roll-off frequency of this motion, due to the confinement imposed by the optical trap, is given in Eq. (2.17). This method allows the viscosity η of the medium surrounding the trapped particle to be determined using the corner frequency f_c as follows;

$$\eta = \frac{\kappa}{12\pi^2 r f_c} \tag{6.11}$$

where κ for each WG mixture is pre-determined, in this case using the EQ method.

For each of the WG mixtures, position fluctuation data of optically trapped 6 μm PS beads were recorded whilst varying P_T. This data was Fourier transformed and analysed in real-time with the LabVIEW program *SimpleAnalysis.vi* which obtains f_c from the Lorentzian fit to the data.
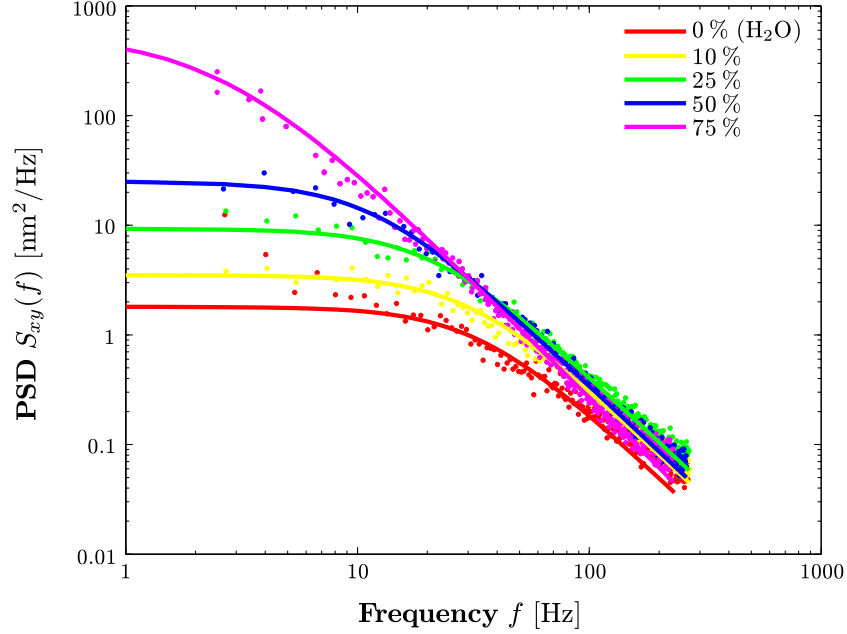
Figure 6.2: Lateral power spectra (PSD) $S_{xy}(f)$ for 6 μm PS beads optically trapped in WG mixtures of varying glycerol concentration; 0 (water), 10, 25, 50 and 75 %. The decrease in f_c corresponds to an increase in the viscosity of the WG mixture η_{wg}. The plots showing concentrations 0, 10 and 25 % were trapped with $P_T = 65$ mW whilst those for 50 and 75 % correspond to $P_T = 122$ mW.

Figure 6.2 shows the lateral PSD for a 6 μm PS bead in four different WG mixtures; 10, 25, 50 and 75 %, compared with that of water (0 %). Each spectra is an average of ∼50 scans, where x and y have been averaged together, and each value of f_c was obtained from three spectra.

In agreement with Eq. (6.11), the decrease in f_c in Fig. 6.2 corresponds to an increase in η_{wg} as glycerol concentration is increased.

For clarity, the spectra in Fig. 6.2 for 0, 10 and 25 % glycerol correspond to $P_T = 65$ mW whilst those for 50 and 75 % glycerol correspond to $P_T = 122$ mW.

6.4 Discussion

Dynamic viscosities of WG mixtures η_{wg} were measured using both an active and passive microviscometry technique and calculated using Eqs. (6.10) and (6.11). Figure 6.3 shows the calculated values of η_{wg} using the VD and PSD methods; Figs. 6.3(a) and 6.3(b), respectively. Also shown are Cheng's model for a temperature of 32 and 40 °C [285]. For comparison, the figures also show the line corresponding to a temperature of 22 °C.

The results are in good agreement with one another showing an increase in η_{wg} with increasing glycerol concentration. Both Figs. 6.3(a) and 6.3(b) show a decrease in η_{wg} with increased trapping power $\mathrm{P_T}$, suggesting a corresponding increase in the temperature of the WG mixture.

For Fig. 6.3(a), the error in η_{wg} is calculated from the standard deviation of κ_x and κ_y, determined for each WG mixture using the EQ method, and the error on each gradient in Fig. 6.1. Similarly, in Fig. 6.3(b) the standard deviation of κ_x and κ_y, and three measurements of f_c for each WG mixture, are combined in quadrature to calculate the error in η_{wg}.

The remainder of this section will discuss the effect of laser-induced heating in WG mixtures and application of laser tweezing to investigate the effect refractive index has on trap stiffness.

6.4.1 Laser-induced heating

It is known that the tightly focussed spot created in laser tweezing experiments can cause laser-induced heating of the medium in and around the optical trap focus as discussed by Peterman, Gittes and Schmidt [289]. They developed a model which incorporates the conditions and geometry of the experiment. Incidentally, they compared the laser-induced heating when trapping polystrene and silica beads in both water and glycerol (pure).

Contrary to earlier models, they discovered when using PS and SC beads, laser light absorption in the solvent surrounding the particle was the most important contribution to heating, and not heating within the trapped particle itself. They found that the heating effect in water was substantially smaller than in glycerol.

(a)

(b)
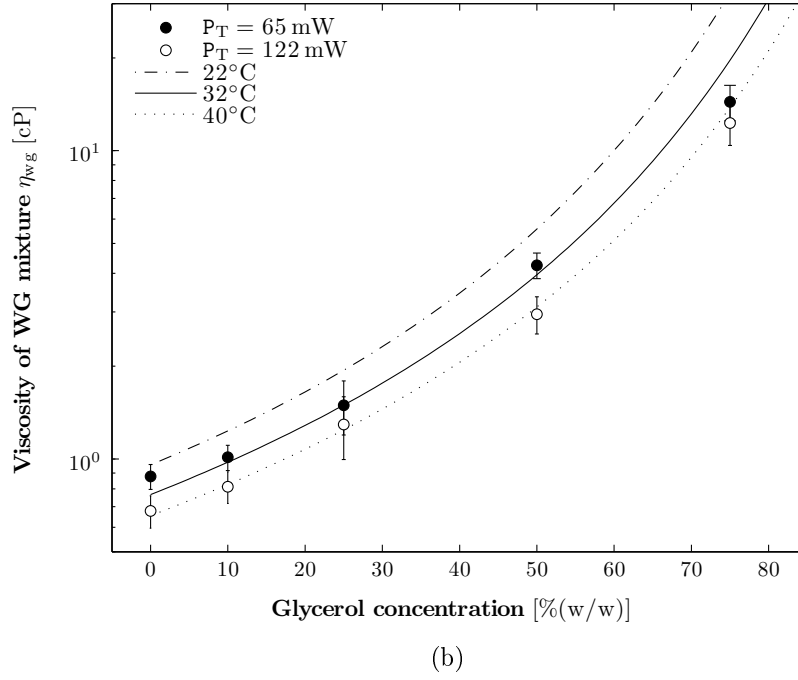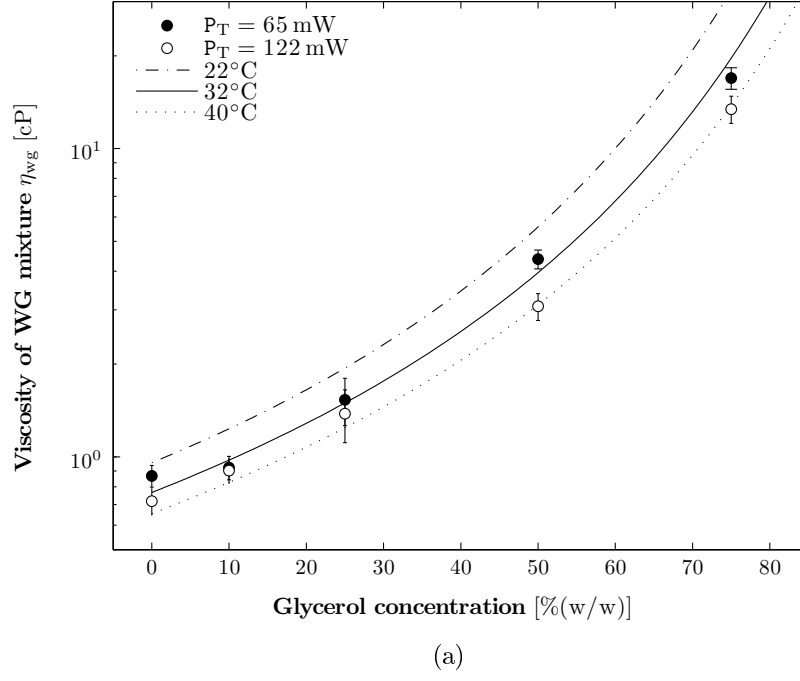
Figure 6.3: Dynamic viscosities of WG mixtures η_{wg} as a function of glycerol concentration where data is obtained using (a) the VD method and (b) the PSD method. Each of the lines correspond to η_{wg} at different temperatures; 22, 32 and 40 °C, as given by Cheng's model [285]. The data is plotted on a semi-logarithmic axis allowing closer inspection of η_{wg} at low glycerol concentrations. *See the text for further details.*

Finally, they observed that the laser-induced heating effect in glycerol increased with increasing trap depth since the coverslip acts as a heat sink.

The VD and PSD techniques produce values of η in water of $0.87 \pm 0.07\,\mathrm{cP}$ and $0.88 \pm 0.08\,\mathrm{cP}$, which are each within one standard deviation of the accepted value of $0.89\,\mathrm{cP}$ at $25\,°\mathrm{C}$. In both Figs. 6.3(a) and 6.3(b), a decrease in η_{wg} is observed between $\mathsf{P_T} = 65$ and $122\,\mathrm{mW}$. This suggests an increase in temperature with increasing $\mathsf{P_T}$. Both datasets shift from a line of best fit of $32\,°\mathrm{C}$ toward that of $40\,°\mathrm{C}$, both given by Cheng's model [285].

For data obtained using the VD method in Fig. 6.3(a), the decrease in η_{wg} with increasing $\mathsf{P_T}$ is less when compared with the PSD method data. Assuming the laser is indeed heating the WG mixture surrounding the particle, this is an intuitive result. As the translation stage is oscillated, the position of the particle and thus the optical trap focus is constantly changing and reducing the time it spends in one location. This may therefore act to reduce the localised temperature and hence increase the observed value of η_{wg}. This implies the speed of the trapped particle is greater than the time it takes for the fluid to reach thermal equilibrium. Viscous drag speeds employed in this work were up to $75\,\mathrm{\mu m/s}$ with the exception of the $75\,\%$ WG mixture, where the maximum stage speed for these measurements was $15\,\mathrm{\mu m/s}$. Peterman, Gittes and Schmidt employed viscous drag speeds $\sim 1\,\mathrm{\mu m/s}$ which is slow enough to allow thermal equilibrium in glycerol to a distance of $10\,\mathrm{\mu m}$; $\sim 1\,\mathrm{ms}$.

In accordance with Eq. (6.11), the decrease in η_{wg} in Fig. 6.3(b) implies an increase in f_{c} which is proportional to κ. As stated above, the decrease in η_{wg} using the passive PSD technique is greater than shown in data obtained using the active VD method. This implies a greater temperature increase with increasing $\mathsf{P_T}$ which is in agreement with the idea that a fast moving particle allows less time for thermal equilibrium. This is negated in passive experiments where the trapped particle, and therefore the optical trap, remains fixed in a single location in the fluid.

Both datasets show a greater shift of η_{wg} as glycerol concentration increases, with particular attention drawn to concentrations 50 and $75\,\%$. This suggests a greater temperature increase as the viscosity of the WG mixture becomes closer to that of pure glycerol. This is in agreement with the general trend shown by Peterman, Gittes and Schmidt; the temperature increase is significantly more in

glycerol than in water.

In pure glycerol, Peterman, Gittes and Schmidt's model predicts a temperature increase on the order of $38\,°C/W$ for pure glycerol at this trap depth $(10\,\mu m)$. This would correspond to an increase on the order of $2\,°C$ for an increase of $57\,mW$ as is the case here. Therefore, the indicated $8\,°C$ increase is larger than expected and all mixtures are diluted. Both experimental data and the model in the aforementioned work illustrates the relatively small influence of particle size on the heating effect. Therefore, the discrepancy cannot be accounted for due to trapping larger beads than those used by Peterman, Gittes and Schmidt [289].

6.4.2   Refractive index mismatch

As given by Eqs. (2.4) and (2.5), the trapping force felt by the particle depends on the angle of refraction of the rays impinging upon its surface (see also Fig. 2.1). As the refractive index of the medium moves towards that of the particle, the angles of refraction at the particle surface are reduced. This in turn reduces the momentum change and thus, the induced gradient force as shown in Fig. 2.2. Therefore, the stiffness of the optical trap depends on the refractive index difference between the particle and the surrounding medium as given by Eq. (2.30).

There exists a greater refractive index difference between the particle and the surrounding medium in water compared with that of pure glycerol as well as WG mixtures. This leads to a refractive index mismatch when measuring the trap stiffness in these media. Brau *et al.* [284] showed that this effect can be corrected for by normalising the measured trap stiffness in the WG mixture κ_{wg} by the relative refractive index. This allows the expected trap stiffness in water κ_{w} to be obtained as given by

$$\kappa_{\mathrm{w}} = \kappa_{\mathrm{wg}}\,\frac{n_{\mathrm{p}} - n_{\mathrm{w}}}{n_{\mathrm{p}} - n_{\mathrm{wg}}} \tag{6.12}$$

where n_{p}, n_{w} and n_{wg} are the refractive indices of the particle, water and WG mixture, respectively.

Rearrangement of Eq. (6.12) illustrates the linear inverse proportionality between κ_{wg} and the relative refractive index, or n-factor (fractional term in Eq. (6.12)). Therefore, a plot of κ_{wg} against the inverse of the n-factor at a given $\mathrm{P_T}$ would yield a value of the corresponding κ_{w} from the gradient.

Table 6.1: Refractive indices of water–glycerol mixtures n_{wg} with varying glycerol concentration prepared as (% v/v) and (% w/w) taken from references [284, 290]. *See the text for further details.*

Glycerol (% v/v)	Refractive index n_{wg}	Glycerol (% w/w)	Refractive index n_{wg}
0	1.3328	0	1.3330
10	1.3476	10	1.3448
25	1.3688	25	1.3640
50	1.4043	50	1.3981
75	1.4418	75	1.4353
100	1.4718	100	1.4740

Brau et al. [284] illustrated that a plot of κ_{wg} against trapping power shows a decrease in the trap stiffness with increasing glycerol concentration. However, once the refractive index correction has been applied as per Eq. (6.12), all data points collapse into a single line to allow κ_{w} to be determined.

The refractive index of WG mixtures increases linearly with glycerol concentration as shown in Table 6.1. These values were determined by Brau *et al.* [284] from refractometer measurements who also employed a trapping beam with a wavelength of 1064 nm. It is important to note that these values correspond to glycerol concentration measured in %(v/v) and as such, there will be some variation in n_{wg}. Unfortunately, the publication does not explicitly state which wavelength or temperature these refractive indices correspond to, therefore it is assumed to be at the trapping wavelength of 1064 nm and room temperature. For comparison, n_{wg} at 589 nm and 20 °C for WG mixtures in %(w/w) are also provided, obtained from the *CRC Handbook of Chemistry and Physics* (1973) [290].

The effect of refractive index changes on κ_{wg} can be seen in Fig. 6.4 which show position distributions for a 6 μm PS bead optically trapped in WG mixtures 0, 10 and 25 % at $\mathrm{P_T} = 65$ mW and 0, 50 and 75 % at $\mathrm{P_T} = 122$ mW. An increase in the positional variance is observed, albeit slight, corresponding to a reduction in κ as given by the equipartition of energy theorem (Eq. (2.7)).

Figure 6.5 shows the inverse proportionality between trap stiffness and the relative refractive index or *n*-factor of Eq. (6.12) for two trapping powers; $\mathrm{P_T} = 65$ mW and $\mathrm{P_T} = 122$ mW. The data were obtained using the EQ method. Each

(a) 65 mW   (b) 122 mW
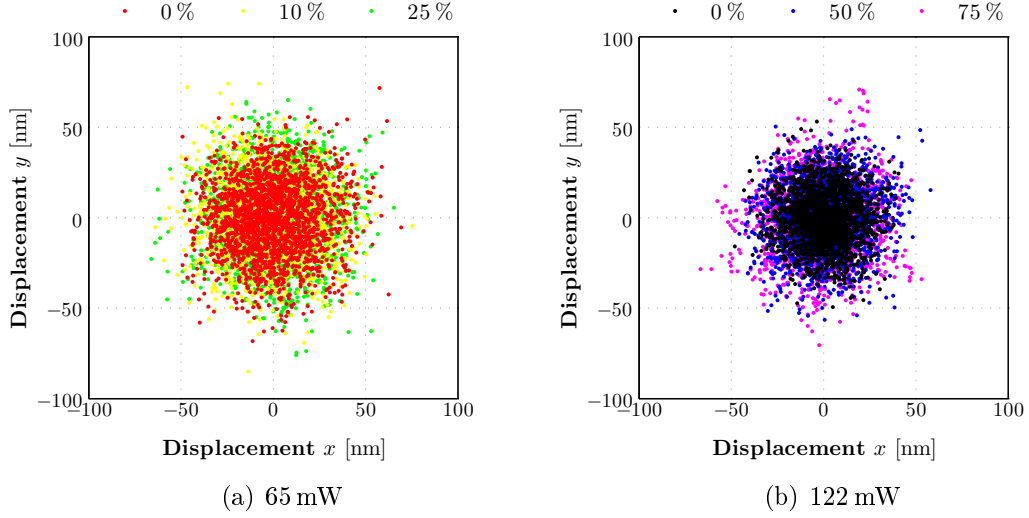
Figure 6.4: Position distributions of 6 μm polystyrene (PS) beads suspended in water–glycerol mixtures with varying glycerol concentration for (a) 0 %, 10 % and 25 % at $P_T = 65$ mW and (b) 0 %, 50 % and 75 % at $P_T = 122$ mW. The trap depth remained constant at $Z_T = 10$ μm.

data point is an average of three measurements of κ, where κ_x and κ_y have been averaged together. Thus, the plotted error bars correspond to the standard deviation of κ_{wg}. Each line represents a linear least squares fit to the data.

The effect of refractive index becomes more significant as trapping power increases. The same effect is observed by Brau *et al.* [284]. They noted the introduction of low-frequency errors when calculating κ at high glycerol concentrations due to the increased viscosity. This effect appears not to be present here which could be attributed to the lower trapping powers employed in this work. In addition, measurements were not made for 100 % glycerol.

A value for the expected trap stiffness if there were no refractive index changes is determined from the gradient of the linear fits in Fig. 6.5. The corresponding values of lateral trap stiffness κ_w are 10.61 ± 0.33 pN/μm and 20.52 ± 0.29 pN/μm for trapping powers of 65 mW and 122 mW, respectively. These values are consistent with those obtained using the PSD method for the same values of P_T and $Z_T = 10$ μm; 11.99 ± 0.72 pN/μm and 20.04 ± 1.20 pN/μm.

However, a caveat: the *n*-factor in Fig. 6.5 is calculated using the refractive indices determined by Brau *et al.* (Table 6.1) where the temperature specifically, is unknown.
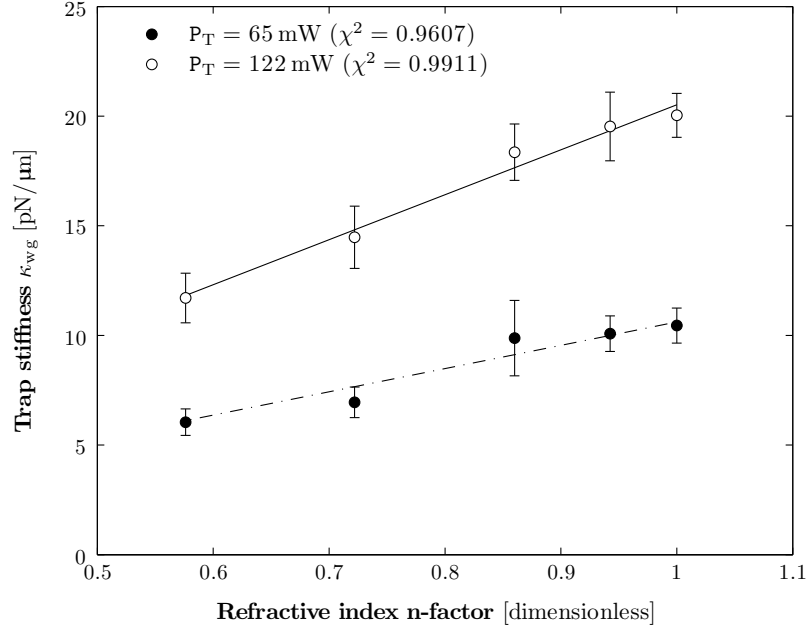
Figure 6.5: The linear relationship between lateral trap stiffness in water–glycerol mixtures κ_{wg} and the inverse of the n-factor as given by Eq. (6.12). As glycerol concentration is increased, the refractive index of the mixture also increases toward the particle's refractive index. This acts to reduce the optical trap stiffness. The gradient of each linear fit gives a value for the expected value of κ_{w} if no refractive index mismatch between the mixtures were present. Each data point is an average of three measurements of κ_{wg}, where κ_x and κ_y have been averaged together. Thus, the plotted error bars correspond to the standard deviation of κ_{wg} and each line represents a linear least squares fit to the data.

This technique could be employed to measure refractive indices of fluids if κ can be determined with high precision.

6.5   Summary

This chapter has presented the results of employing the laser tweezing system as a tool for microviscometry using both an active and passive technique. The results were obtained using the laser tweezing system shown in Fig. 4.1, which uses high-speed video microscopy to perform particle tracking.

Dynamic viscosities of WG mixtures η_{wg} with varying glycerol concentration were determined. In agreement with Cheng's model [285], η_{wg} increased with increasing glycerol concentration. The results suggested laser-induced heating

in the mixtures, specifically with greater glycerol concentration. However, this was larger than expected compared with the literature [289]. There was a slight difference in the temperature increase between the active and passive techniques, where the particle's motion in the active technique may allow insufficient time for thermal equilibrium.

The results may also suggest other intricacies of the experimental situation. As shown by Peterman, Gittes and Schmidt [289], the coverslip acts as a heat sink where the laser-induced heating effect increases with increasing trap depth. In this work, the particle may be positioned further ahead of the optical trap focus than a measurement of Z_T suggests, thus lying further away from the coverslip than believed and thereby experiencing a greater laser-induced heating effect. However, this is unlikely to account for such a greater than expected discrepancy as the heating effect is not strongly dependent on trap depth. There may also exist an underestimation of the value of P_T at the sample which could account for the greater increase in temperature due to the trapping laser beam. A more in depth investigation is required to definitively conclude whether the changes in η_{wg} are indeed due to laser-induced heating.

This chapter also detailed the use of the laser tweezing system for detecting changes in refractive index of the medium and its effect on the optical trap stiffness. As glycerol concentration is increased so does the refractive index of the mixture. This acts to reduce the optical trap stiffness. However, this can be corrected for to show that an expected value for the trap stiffness can still be determined from this data. Similarly, this technique could be employed to measure refractive indices of fluids if trap stiffness can be determined to a high precision.

This work used refractive index values published in the literature for the WG mixtures, where some discrepancy will exist due to the temperature, wavelength and the method of mixture preperation e.g. ($\% \, w/w$) versus ($\% \, v/v$). Ideally, refractive indices of the WG mixtures should be determined in-house at 1064 nm for ($\% \, w/w$) concentrations, using reflectance spectroscopy, for example. Also, measuring n_{wg} as a function of temperature would allow correction for refractive index changes due to any laser-induced heating.

Chapter 7

Laser Tweezing in Liquid Crystals

Analysis of optically trapped colloids provides practically pertinent details about the host medium. Studying the characteristics of liquid crystalline media attracts increasing interest due to their impact in the advancement of electro-optic systems and display technology.

Laser tweezers are a popular and successful technique for investigating LC media, as they often require only very small volumes of liquid crystal ($\sim \mu$L) and also facilitate investigations in a predominantly viscous regime.

This chapter details laser tweezing experiments using polystyrene (PS) and silica (SC) beads dispersed in different liquid crystal mixtures with homeotropic and planar alignment. Active and passive measurement techniques were employed to determine the anisotropic viscosities of the LC mixtures; viscous drag and PSD analysis. More specifically, this allowed determination of effective and local anistropic shear viscosity coefficients. All experiments employed the laser tweezing shown in Fig. 4.1. The results in this chapter are compared with those available in the literature which have employed (a) optical tweezers and (b) a shear flow measurement technique.

This chapter begins with a consideration of the experimental conditions including the Ericksen number, the LC cells themselves and the alignment of the LC at the particle surface. This is followed by the experimental detail and results of the active and passive microviscometry employed. Finally, a discussion is presented on distortion of the LC director $\hat{n}$, colloidal interactions within the LC and the effect of the refractive index contrast.

7.1 Experimental conditions

One should consider the experimental environment in which laser tweezing experiments are being performed, particularly in LC mixtures. The first of these important considerations for LC mixtures is the degree of viscoelasticity of the system, characterised by the Ericksen number. In addition, attention should be paid to the alignment of the LC at the surface of colloids dispersed within it. This section will examine these aspects, and their impact in laser tweezing experiments, in further detail.

7.1.1 Ericksen number E_{r}

In a liquid crystal, the contribution of elastic forces to the Stokes' viscous drag force can be quantified using the Ericksen number E_{r} as given in Eq. (3.14). At low Ericksen number $E_{\mathrm{r}} \ll 1$, elastic forces exceed viscous forces and so any elastic distortions of the LC director $\hat{n}$ due to the flow field i.e. the particle's motion, are considered negligible.

The Ericksen number can be minimised by controlling the velocity length scale v_{∞}. In the active viscous drag (VD) experiments, the translation stage was moved at a maximum speed of $70 \, \mu\mathrm{m/s}$. With characteristic values for the Frank elastic constant $K_i \sim 10 \, \mathrm{pN}$ and Leslie coefficient $\alpha_4 \sim 10^{-2} \, \mathrm{Ns/m^2}$ [168, 291], the smallest bead, $2 \, \mu\mathrm{m}$ PS, gives an average value of $E_{\mathrm{r}} \sim 0.03$. For the largest bead, $10 \, \mu\mathrm{m}$ PS, on average $E_{\mathrm{r}} \sim 0.14$. Therefore, using the chosen colloids and LC mixtures, the experimental environment would remain in the low Ericksen number regime, $E_{\mathrm{r}} \ll 1$.

As given by Eq. (3.14), it is only if the stage were to be moved at a speed $v \gtrsim 400 \, \mu\mathrm{m/s}$ and $v \gtrsim 2000 \, \mu\mathrm{m/s}$ for the $10 \, \mu\mathrm{m}$ and $2 \, \mu\mathrm{m}$ PS beads, respectively, that elastic forces would begin to equal viscous forces i.e. $E_{\mathrm{r}} \sim 1$. Specific values of E_{r} for SC beads are not discussed as they fall within the desirable range for E_{r} at the chosen radii.

In passive PSD experiments, the velocity length scale v_{∞} for an optically trapped particle undergoing Brownian motion (i.e. the Brownian velocity) will range between approximately $1.8 \, \mathrm{mm/s}$ and $0.2 \, \mathrm{mm/s}$ depending on particle den-

sity and radius. These values are calculated using the radii of the 2 and 10 μm nominal PS beads, respectively (Table 3.3).

These velocities correspond to $0.14 \leqslant E_\mathrm{r} \leqslant 0.85$, depending on the combination of particle radius and density, and the liquid crystal of choice, as shown in Fig. 7.1. Clearly, this largely facilitates experiments in the low Ericksen number regime, $E_\mathrm{r} \ll 1$. Comparatively, some combinations would present a system approaching $E_\mathrm{r} \sim 1$.
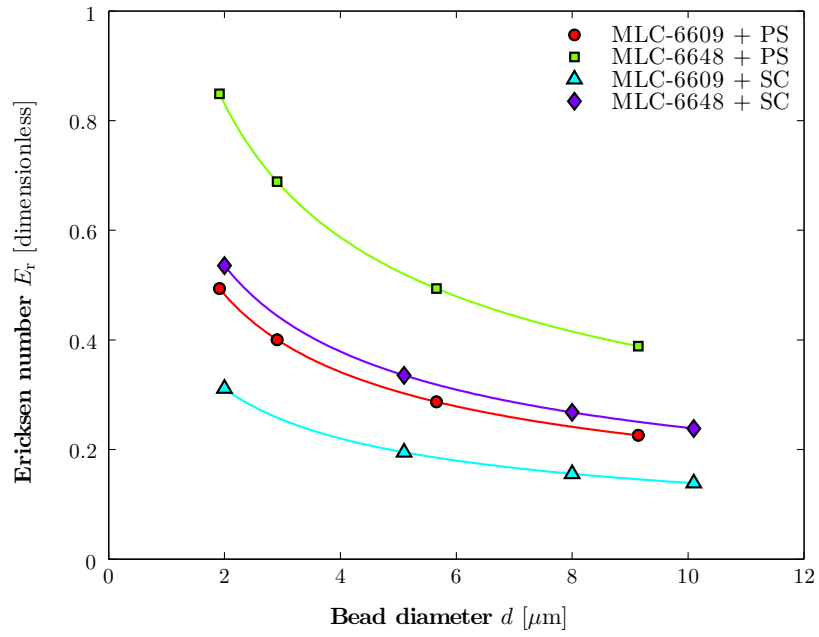
Figure 7.1: Calculated Ericksen number E_r from Eq. (3.14) as a function of bead radius listed in Table 3.3. These values correspond to passive laser tweezing experiments where the velocity length scale v_∞ is the velocity of the particle's Brownian motion.

Figure 7.1 also shows that, since smaller colloids have an increased Brownian velocity, E_r can be minimised in passive techniques by using larger colloids. Similarly, choosing a LC with a higher Frank elastic constant K_i will minimise E_r. In this case, $K(6609) > K(6648)$ [155, 168, 292].

7.1.2 Liquid crystal cells

Table 7.1: The liquid crystal and bead combinations used in this work. LC cells with planar (P) and homeotropic (H) alignment were used for both. The Ericksen number E_r given by Eq. (3.14) are calculated for the VD and PSD methods where all values are < 1.

LC	Particle properties	Alignment P	Alignment H	Ericksen number, E_r VD	Ericksen number, E_r PSD
MLC-6648	2 µm SC	✓	✓	0.04	0.54
MLC-6609	6 µm PS	✓	✓	0.06	0.29

The colloidal suspensions were prepared at relatively low concentrations of typically 2–4 % solids by weight. To minimise any distortion of the LC director, particles of relatively small diameter; 2 µm in MLC-6648 and 6 µm in MLC-6609, were dispersed using ultrasound. The LC and colloid combinations used are given in Table 7.1, where P and H indicate planar and homeotropic alignment, respectively. Also shown in the table are calculated values of E_r for the VD and PSD methods. Calculations for the VD method use the maximum velocity of 70 µm/s whilst those for the PSD method use the Brownian velocity of the associated particle radii.

LC cells were fabricated as described in Section 3.3 where the coverslip surfaces were treated to achieve planar and homeotropic alignment of the LC relative to the coverslip surface. Their thickness h, measured using reflectance spectroscopy (Section 3.3.5), varied between 25.3 µm and 36.1 µm with an error $\sigma_h \sim 8$–10 %.

7.1.3 Surface anchoring

Planar and homeotropic alignment of the LC director $\hat{n}$ relative to the coverslip surface was performed as described in Section 3.3.6. For a planar LC with good alignment, no light should be transmitted through the LC when viewed between crossed polarisers. This was observed within the bulk of the nematic. However, small, bright regions were also observed, corresponding to director distortion around the particles dispersed within the cell. The distortion of $\hat{n}$ around the particle means it is no longer parallel to either polariser, thereby allowing light

transmission. For a well-aligned homeotropic LC cell, a central conoscopic cross should be observed. The bulk alignment of the LC director $\hat{n}$ should be largely unaffected by colloidal dispersions at the relatively low concentrations used here; $\sim 2\text{--}4\,\%$. Any shift in the conoscopic image was likely due to regions of poor alignment of the LC at the coverslip surfaces.

Chain-like structures were observed for $2\,\mu\text{m}$ SC beads dispersed in MLC-6648 with planar alignment, as shown in Fig. 7.2. This suggests the LC molecules are homeotropically aligned at the colloid surface as detailed in Section 3.2.4. The particles experience a strong attraction to one another in the direction of $\hat{n}$ and the formation of particle chains lowers the free energy of the system.

It is most likely that a Saturn-ring director field is present, shown in Fig. 3.7(b) (p. 96), as these most commonly occur for particles with $r < 5\,\mu\text{m}$ [167, 168, 242]. For this type of director field, the homeotropic surface anchoring is weak, in comparison to topological defects which are due to strong homeotropic anchoring. This creates an isotropic distribution relative to the large convergence angle of the rays impinging upon the particle surface and hence minimises any anisotropy of the trapping forces. One may therefore assume an effective refractive index $\bar{n} = \sqrt{2n_{\text{o}}^2 + n_{\text{e}}^2/3}$, which gives 1.515 for both MLC-6648 and MLC-6609 [200].
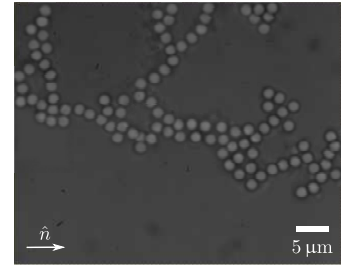
Figure 7.2: Chain-like structure of $2\,\mu\text{m}$ SC beads dispersed in MLC-6648 with planar alignment. This indicates the LC molecules are homeotropically aligned at the particle surface.

Planar anchoring at the particle surface, generates clustering of beads [293]. There was some evidence of this for SC beads in hometropic cells of MLC-6648. The formation of clusters indicates the long-range attractive forces. Although repulsive forces are also present where the particles remain seperated. It was possible to trap individual SC beads and detach them from the surrounding particles, where this was more easily achieved with smaller 'clumps' of beads. It was also possible to pull two clumps of beads apart using the laser tweezers.

7.1.4   Trapping power and depth

As shown by Smalyukh *et al.* [184], quantitative studies of particle dynamics in laser tweezers can be performed with relatively low trapping powers. In materials with low birefringence Δn, which is true of the LCs used here, reorientation of $\hat{n}$ due to the trapping laser is weaker than for high Δn. These materials thus possess a higher threshold power before realignment of $\hat{n}$, allowing greater trapping forces to be applied.

The trap depth was kept constant at $Z_T = 10\,\mu m$ in order to minimise the effect due to the proximity of the coverslip and spherical aberration of the optical trap focus, as discussed in Sections 5.2.1 and 5.2.2. However, it is expected that any spherical aberrations will be small as the average refractive index of the LC is close to the refractive index of the glass coverslip. Similarly, unlike laser tweezing in water, increasing trap depth is unlikely to reduce the trapping forces as the birefringence is low; $\Delta n \sim 0.07$ for the chosen LCs (Table 3.2, p. 98). Higher values of Δn will weaken the trapping force due to significant light defocussing, which acts to increase the width of the optical trap [152, 200].

Thicknesses of each LC cell h were measured using reflectance spectroscopy as described in Section 3.3.5. The values ranged between approximately $20-40\,\mu m$ with an error $\sigma_h \sim 8\text{--}10\,\%$.

7.2   Microviscometry in liquid crystals

Experiments to determine the viscosity coefficients of LCs using laser tweezers relies on the fact that an optically trapped bead's motion in a given dimension will differ depending on whether the plane is parallel or perpendicular to $\hat{n}$. Since motion of an optically trapped bead depends on the viscosity of the host medium, it is therefore possible to determine viscosity coefficients by observation of this motion as described in Section 3.1.3. As evidence of the LC's anisotropic viscosity, one would expect to observe an anisotropic dynamic response from the optically trapped colloid, dependent upon the orientation of the axes relative to $\hat{n}$.

As detailed in Chapter 2, a number of statistical methods exist to detect differences in position fluctuations of an optically trapped bead. For example, one

would expect to observe anisotropy in the Gaussian distribution of particle positions, the autocorrelation and mean squared displacement functions, the power spectrum and the viscous drag force experienced by the optically trapped colloid. Whilst none of these methods are suitable for *calibration* of laser tweezers in a viscoelastic media [206], such as a LC, they offer valuable information about the characteristics of colloidal dispersions.

PS and SC beads with a range of diameters were dispersed in two LC mixtures with homeotropic and planar alignment. As described in Chapter 3, for a homeotropically aligned LC cell, both the x and y directions are perpendicular to the LC director $\hat{n}$ whilst z is parallel. For a LC cell with planar alignment, depending on the transverse orientation of the LC cell, either the x or y direction is parallel to $\hat{n}$, whilst z is perpendicular. See also Fig. 3.5 (p. 92) and Table 3.1 (p. 93).

Laser tweezing has previously been employed to determine the effective viscosities $\eta_{\text{eff}}^{\perp}$ and $\eta_{\text{eff}}^{\parallel}$ of MLC-6648 [167]; the effective viscosities perpendicular and parallel to $\hat{n}$. These experiments were performed in the low Ericksen number regime and employed active microviscometry, specifically the escape force method, to measure viscosity. This therefore provided a direct comparison of viscosity values, where the work detailed in this thesis determines viscocity values using passive microviscometry with high-speed video microscopy.

In addition, Pasechnik *et al.* [189] determined anisotropic shear viscosity coefficients η_1, η_2 and η_3 for MLC-6609 using traditional shear flow experiments. Therefore, this facilitated a comparison between anisotropic viscosity coefficients given in the literature, determined with an alternative technique. It also provided an opportunity to compare viscosity values determined in the low Ericksen number regime, as here, with those not in this regime, as in reference [189].

Prior to performing laser tweezing experiments in anisotropic media, it is often necessary to perform calibration of force and/or trap stiffness as the trapping and viscous forces also become anisotropic. In the case of liquid crystals, this calibration requires observing the particle dynamics relative to the director $\hat{n}$. However, this can be avoided by using particles with high refractive indices $n_{\text{p}} \gg n_{\text{o}}$ and n_{e}. Also, choosing LC's with relatively small birefringence, trap stiffness can be considered practically independent of $\hat{n}$ around the particle [184, 200].

With sufficient birefringence, dielectric anisotropy and clearing temperature (see Table 3.2, p. 98), the LC mixtures MLC-6648 and MLC-6609 made suitable LCs for laser tweezing experiments. Experiments were perfomed using the laser tweezing system shown in Fig. 4.1 (p. 104), where initial development allowed accurate particle tracking in all three dimensions using high-speed video microscopy as described in Section 4.3.1. This enhancement allowed media to be probed in three dimensions including examination of anisotropic viscosity of LCs.

7.2.1 Passive microviscometry

The characteristic corner frequency f_c of an optically trapped colloid's PSD is inversely proportional to the drag coefficient γ as given by Eq. (2.17), and hence the viscosity. This treatment can be applied to liquid crystals if experiments are performed in the low Ericksen number regime as described in Section 7.1.1.

One would expect to observe differences in the power spectrum of an optically trapped bead's position fluctuations depending on a given direction's relation to $\hat{n}$. Fitting a Lorenztian to the PSD data to obtain f_c allows determination of the LC's effective anisotropic viscosity coefficients $\eta_{\text{eff}}^{\perp}$ and $\eta_{\text{eff}}^{\parallel}$ as given by Eq. (2.20).

MLC-6648

Figures 7.3 and 7.4 show the PSD and associated Lorenztian fit in the x, y and z directions for an optically trapped $2\,\mu\text{m}$ SC bead dispersed in MLC-6648 with homeotropic and planar alignment, respectively. The PSD and associated Lorenztian fit are filtered i.e. averaged, over ~ 100 scans and the plots shown are an average of three separate measurements. Values of the effective viscosities $\eta_{\text{eff}}^{\perp}$ and $\eta_{\text{eff}}^{\parallel}$ obtained from the Lorentzian fit to PSD data are presented in Table 7.2 on p. 182.

For a homeotropically aligned cell in Fig. 7.3, both the x and y directions are perpendicular to the LC director $\hat{n}$ meaning they both experience $\eta_{\text{eff}}^{\perp}$ which is confirmed by the similarity in f_c values. The z direction is parallel with $\hat{n}$ and would therefore, experience $\eta_{\text{eff}}^{\parallel}$. The value of $f_c(z)$ is approximately $45\,\%$ of $f_c(x)$ and $f_c(y)$. We know that $\kappa_{xy} > \kappa_z$, but the result also illustrates a reduced viscosity since we would expect a further reduced value of $f_c(z)$ if the disparity
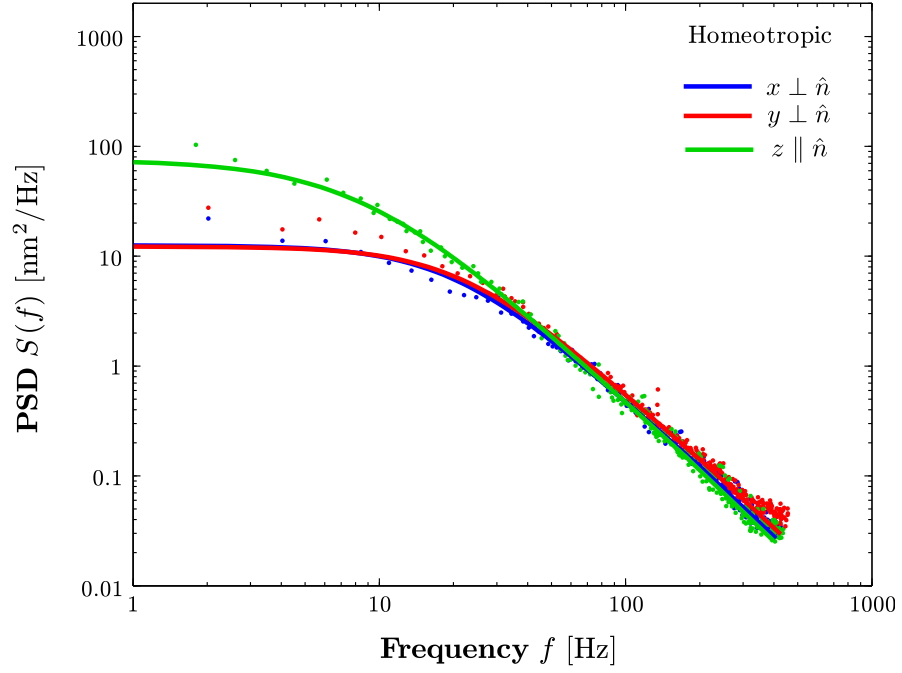
Figure 7.3: PSD for $2\,\mu\text{m}$ SC beads in MLC-6648 trapped with a trap stiffness $\kappa_{xy} \approx 20\,\text{pN/}\mu\text{m}$ (measured in water) with homeotropic alignment; $f_c(x) = 19.8 \pm 2.0\,\text{Hz}$, $f_c(y) = 21.6 \pm 2.1\,\text{Hz}$ and $f_c(z) = 9.1 \pm 0.9\,\text{Hz}$.
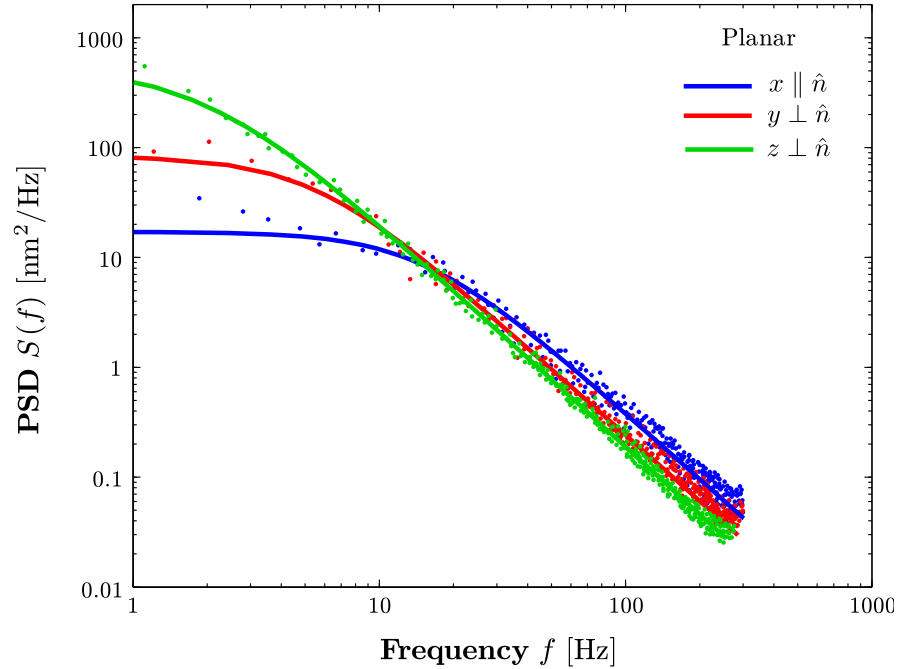
Figure 7.4: PSD for $2\,\mu\text{m}$ SC beads in MLC-6648 trapped with a trap stiffness $\kappa_{xy} \approx 20\,\text{pN/}\mu\text{m}$ (measured in water) with planar alignment; $f_c(x) = 15.0 \pm 1.7\,\text{Hz}$, $f_c(y) = 5.4 \pm 0.6\,\text{Hz}$, $f_c(z) = 2.3 \pm 0.3\,\text{Hz}$.

between lateral and axial trap stiffness were the only effect.

In comparison, for a cell with planar alignment, the x and z directions are parallel to $\hat{n}$ whilst y is perpendicular, producing clearly different PSD plots, as shown in Fig. 7.4. This is again evident from the difference in corner frequencies; $f_c(x) > f_c(y)$, on the order of three times greater. Here, $f_c(x) > f_c(z)$, ~ 6 times greater, which can be partly attributed to the difference between κ_x and κ_z, although it is greater than expected from calibration data in water shown in Section 5.1.

MLC-6609

Figures 7.5 and 7.6 show the PSD and associated Lorenztian fit in the x, y and z directions for an optically trapped 6 μm PS bead dispersed in MLC-6609 with homeotropic and planar alignment, respectively. The PSD and associated Lorenztian fit are filtered i.e. averaged, over ~ 100 scans. Values of the effective viscosities $\eta_{\text{eff}}^{\perp}$ and $\eta_{\text{eff}}^{\parallel}$ obtained from the Lorentzian fit to PSD data are presented in Table 7.2 on p. 182.

For the homeotropic cell of MLC-6609, the corner frequencies in all three dimensions are of a similar value. It is reasonable to conclude from this data that the optically trapped particle experiences a similar effective viscosity $\eta_{\text{eff}}^{\perp}$ in x and y whilst in the z direction, although $\kappa_{xy} > \kappa_z$, this direction experiences a reduced effective viscosity $\eta_{\text{eff}}^{\parallel}$.

For the planar cell of MLC-6609, $f_c(x) > f_c(y) > f_c(z)$. Taking into account the differences between lateral and axial κ, this therefore suggests the optically trapped particle experiences a different effective viscosity in the x direction compared with the y and z direction; $\eta_{\text{eff}}^{\parallel}$ and $\eta_{\text{eff}}^{\perp}$, respectively.

7.2.2 Active microviscometry

This section details results obtained using active microviscometry in order to compare passive microviscometry results for this laser tweezing system. One would expect to observe anisotropy in the particle's motion when subjected to a viscous drag force in directions parallel and perpendicular to $\hat{n}$.
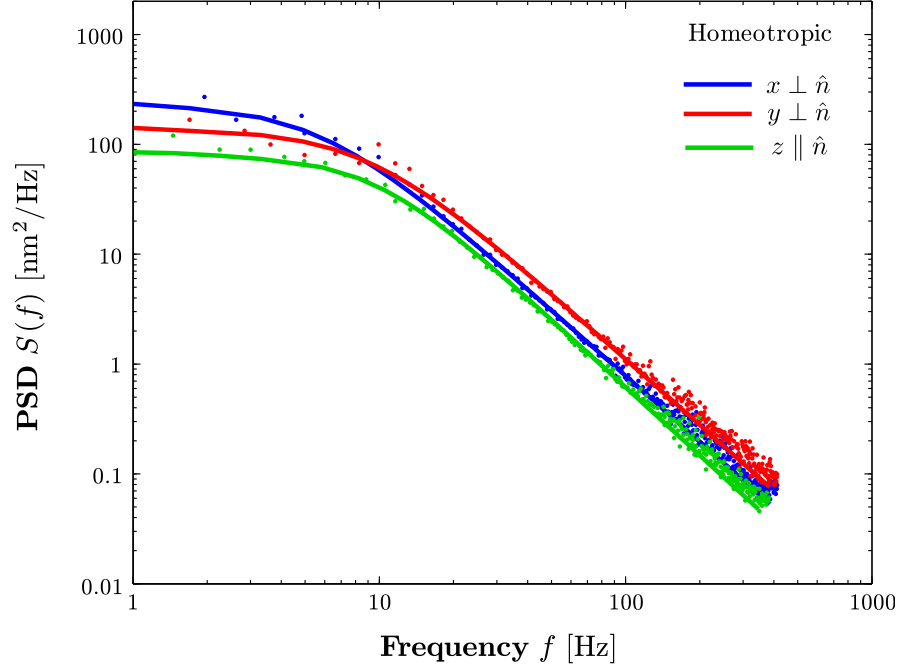
Figure 7.5: PSD for a 6 μm PS bead in MLC-6609 trapped with a trap stiffness $\kappa_{xy} \approx 20\,\mathrm{pN/\mu m}$ (measured in water) with homeotropic alignment, $f_\mathrm{c}(x) = 6.0 \pm 0.7\,\mathrm{Hz}$, $f_\mathrm{c}(y) = 9.0 \pm 1.0\,\mathrm{Hz}$, $f_\mathrm{c}(z) = 8.0 \pm 0.8\,\mathrm{Hz}$.
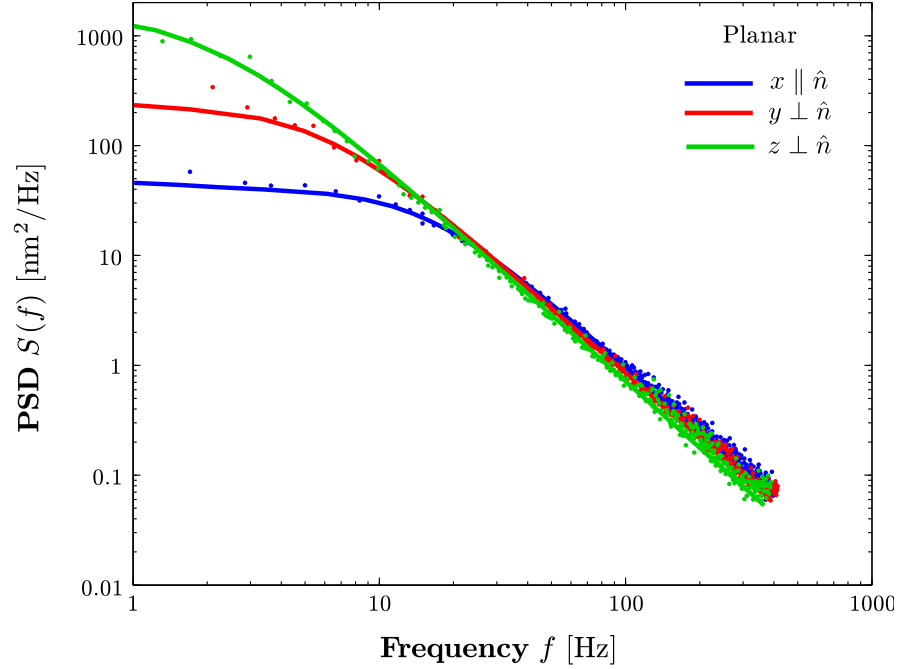
Figure 7.6: PSD for a 6 μm PS bead in MLC-6609 trapped with a trap stiffness $\kappa_{xy} \approx 20\,\mathrm{pN/\mu m}$ (measured in water) with planar alignment, $f_\mathrm{c}(x) = 12.7 \pm 1.3\,\mathrm{Hz}$, $f_\mathrm{c}(y) = 5.9 \pm 0.6\,\mathrm{Hz}$, $f_\mathrm{c}(z) = 3.1 \pm 0.4\,\mathrm{Hz}$.

The increase in viscosity experienced by a colloid immersed in a LC relative to water was reflected in the reduction in speed at which a bead became located at the optical trap centre. This effect was directly proportional with increasing P_T, in agreement with reports in the literature [155, 184]. The particle withstood significantly less viscous drag speeds than that of a PS or SC bead of the same size in water, trapped at the same power. In addition, the optically trapped bead in the LC responded to a viscous drag force with a large displacement from the optical trap centre where the bead appeared to be 'tethered'. This is likely to be the elastic Saturn-ring surrounding the particle, created due to the quadrapolar symmetry of the homeotropic director orientation at the particle surface. It is indeed possible to manipulate the Saturn-ring with laser tweezers, including fusing them together to entangle particles [294, 295].

As stated above, in the low Ericksen number regime $E_r \ll 1$, elastic distortions of the LC director $\hat{n}$ are considered negligible. Similarly, the laser tweezing experiments are performed in the Reynold's number Re $\ll 1$ ($\lesssim 10^{-5}$). Therefore, the viscous drag acting on a particle immersed in the LC can be described by Stokes' law. This allows the viscosity to be determined in the same way as for a purely viscous fluid; using Eq. (6.10).

As in Sections 5.1.2 and 6.3.1, a known Stokes' viscous drag force $\mathbf{F}_S$ was applied to optically trapped beads in each of the LC mixtures by oscillating the translation stage with a triangular displacement function. In an effort to eliminate any measurement errors due to the particle tracking and analysis system, the active escape force (EF) method was employed to probe anisotropic viscosity of LCs.

The escape force is the minimum force required to cause a bead to escape from the optical trap, defined as

$$\mathbf{F}_{esc} = 6\pi\eta r \mathbf{v}_{esc} \tag{7.1}$$

where $\mathbf{v}_{esc}$ is the velocity of the surrounding fluid, or in this case the sample stage, when the particle is released from the optical trap. At this point, $\mathbf{F}_{esc}$ is considered as the maximum trapping force proportional to the maximum displacement $\mathbf{F}_{max} = -\kappa \mathbf{x}_{max}$, such that;

$$\mathbf{F}_{max} = 6\pi\eta r \mathbf{v}_{esc}, \tag{7.2}$$

or, using Eq. (2.30), this is equivalently;

$$\frac{Qn_{\mathrm{m}}\mathsf{P}_{\mathrm{T}}}{c} = 6\pi\eta r \mathbf{v}_{\mathrm{esc}}. \tag{7.3}$$

Measuring $\mathbf{v}_{\mathrm{esc}}$ as a function of P_{T} will thus allow determination of η.

It is possible to determine the trapping efficiency Q experimentally if η is known, as described in Section 2.4. However, Q can also be calculated theoretically using a Matlab program developed by Niemien *et al.*; the '*Optical tweezers computational toolbox*' [296]. Thus, the trapping force $\mathbf{F}$ for a range of P_{T} can be calculated using Eq. (2.30).

Figures 7.7(a) and 7.7(b) show the calculated lateral efficiency Q_{xy} as a function of particle position. The axial trap efficiency Q_z is also shown for comparison. Each of the figures correspond to SC and PS beads, respectively, where the host medium is either of the LC mixtures; MLC-6648 or MLC-6609, since they have the same average refractive index $\bar{n}$.

Figures 7.8(a) and 7.8(b) show the calculated lateral trapping forces $\mathbf{F}_{xy}$ for SC and PS beads, respectively, as a function of particle position. The figures show five plots of $\mathbf{F}_{xy}$ corresponding to P_{T} between 10 and 50 mW calculated using Eq. (2.30) and the theoretical values of Q_{xy}. The units of position are given in units of the trapping laser wavelength $\lambda = 1064$ nm. The plots show expected results; (i) $Qxy > Q_z$, (ii) both Q and $\mathbf{F}_{xy}$ increase with particle size, and (iii) $\mathbf{F}_{xy}$ increases with P_T. A linear relationship exists between Q and P_{T}, thus allowing values of Q and $\mathbf{F}_{\mathrm{max}}$ to be determined for a given P_{T}.

MLC-6648

The escape velocity of 2 μm SC beads trapped in MLC-6648 was measured for planar and homeotropic cells. The trapping power P_{T} was kept constant between $10-50$ mW and the stage velocity increased until the bead escaped from the optical trap. The viscous drag force was applied in both the x and y directions in order to probe $\eta_{\mathrm{eff}}^{\perp}$ and $\eta_{\mathrm{eff}}^{\parallel}$.

It was realised that when measuring $\eta_{\mathrm{eff}}^{\parallel}$, the necessary values of $\mathbf{v}_{\mathrm{esc}}$ for a 2 μm SC bead to escape from the optical trap would exceed the chosen maximum stage velocity of 70 μm/s. Therefore, measurements were made at additional values of

(a)

(b)
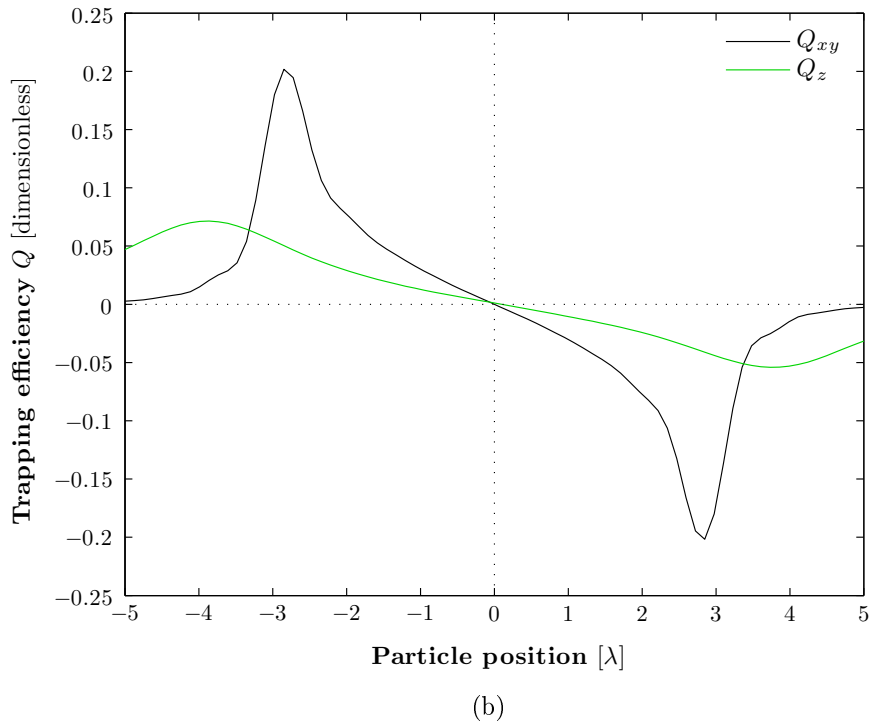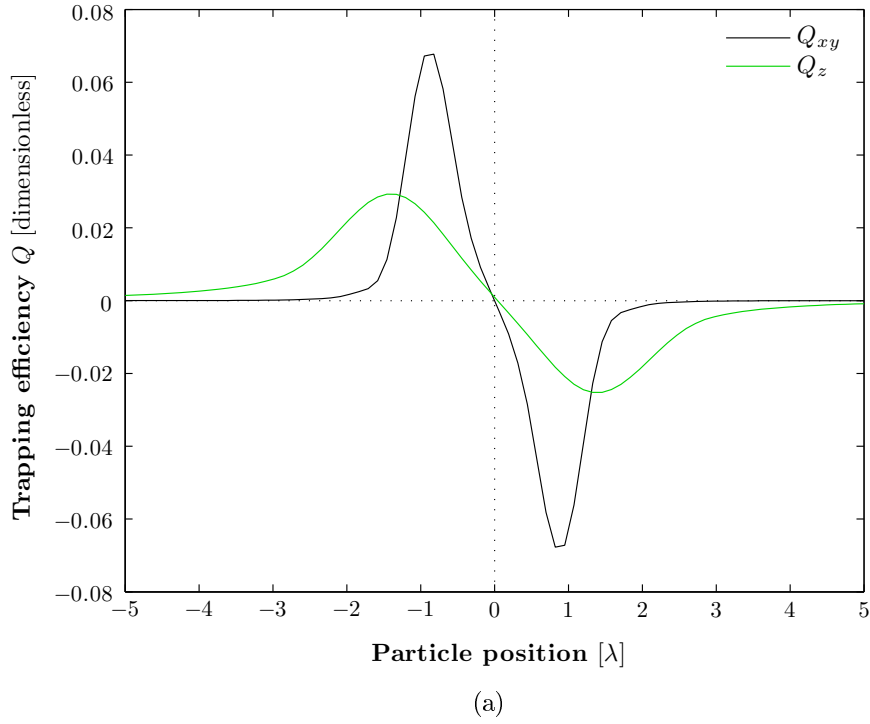
Figure 7.7: Calculated lateral and axial trapping efficiencies Q_{xy} and Q_z for (a) 2 μm SC beads ($n_p = 1.56$) and (b) 6 μm PS beads ($n_p = 1.59$) dispersed in either of the LC mixtures with average refractive index $\bar{n} = 1.515$.

(a)
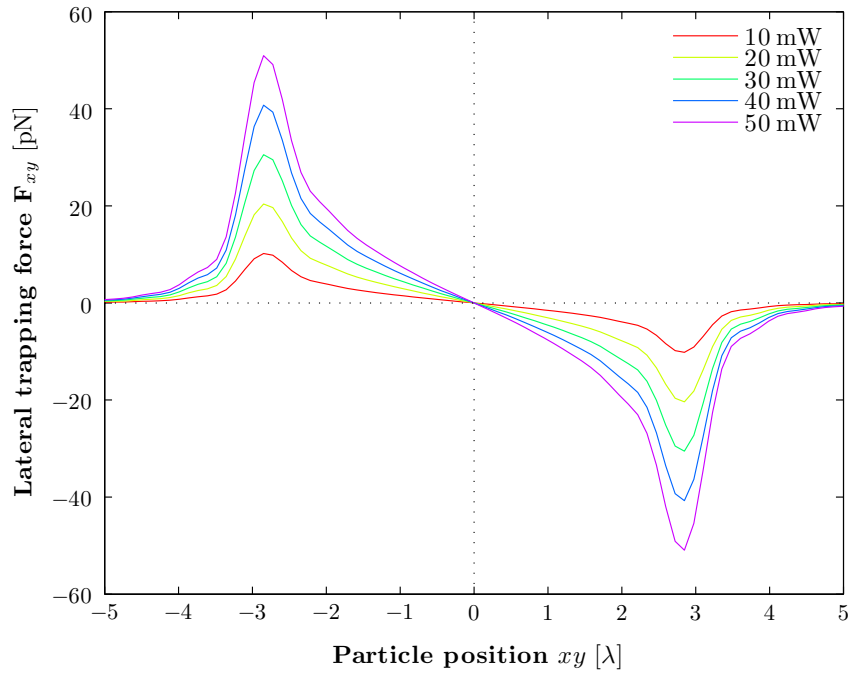
(b)

Figure 7.8: Calculated lateral trapping force $\mathbf{F}_{xy}$ for (a) $2\,\mu\mathrm{m}$ SC beads ($n_{\mathrm{p}} = 1.56$) and (b) $6\,\mu\mathrm{m}$ PS beads ($n_{\mathrm{p}} = 1.59$) dispersed in either of the LC mixtures with average refractive index $\bar{n} = 1.515$. Values of Q_{xy} and Q_z are determined for 5 trapping powers $\mathrm{P_T}$ between 10 and $50\,\mathrm{mW}$.

P_T.

Figures 7.9(a) and 7.9(b) show escape velocity $\mathbf{v}_{esc}$ of a 2 µm SC bead in planar and homeotropically-aligned cells of MLC-6648, respectively, as a function of P_T. Each point is an average of two measurements in a single LC cell. The corresponding values of η_{eff} are given in Table 7.2 (p. 182) where error contributions are from the linear fit, the particle radius and the error on Q_{xy}, given as 1 % [296].

As expected $\eta_{eff}^{\perp} > \eta_{eff}^{\parallel}$. This is in agreement with the literature, which report escape velocities differing by approximately a factor of 2 when comparing motion across and along $\hat{n}$ [153, 167]. Also, the values are in good agreement with η_{eff} values determined using passive microviscometry.

Using values for $\eta_{eff}^{\perp}$ and $\eta_{eff}^{\parallel}$, measured using passive microviscometry (Table 7.2, p. 182), predictions of $\mathbf{v}_{esc}$ of a 6 µm PS bead optically trapped in MLC-6609 were made as a function of P_T. These predictions, shown in Fig. 7.10, are for motion along and across $\hat{n}$ in cells with both planar and homeotropic alignment in three dimensions.

(a)

(b)
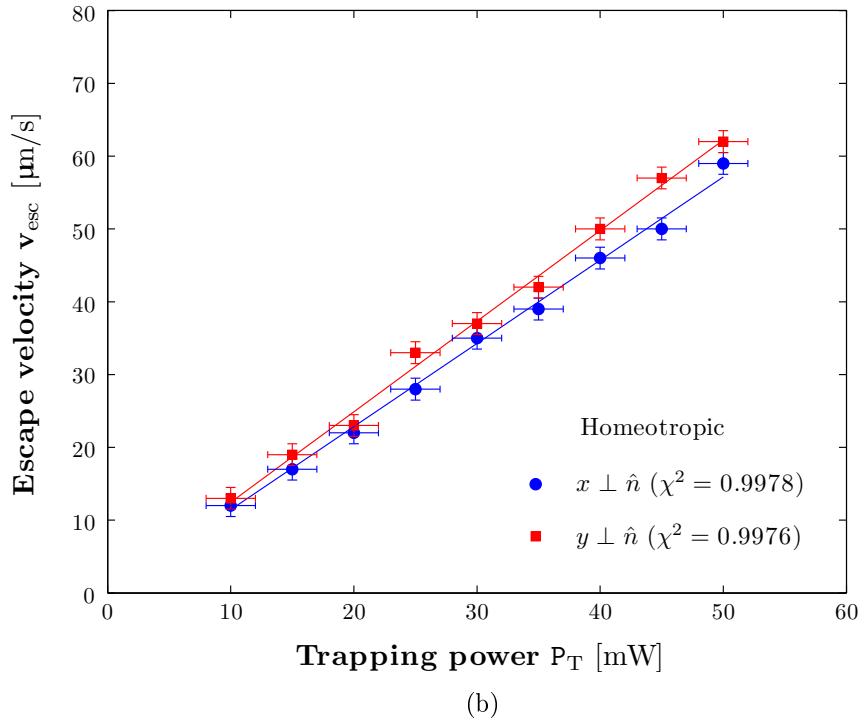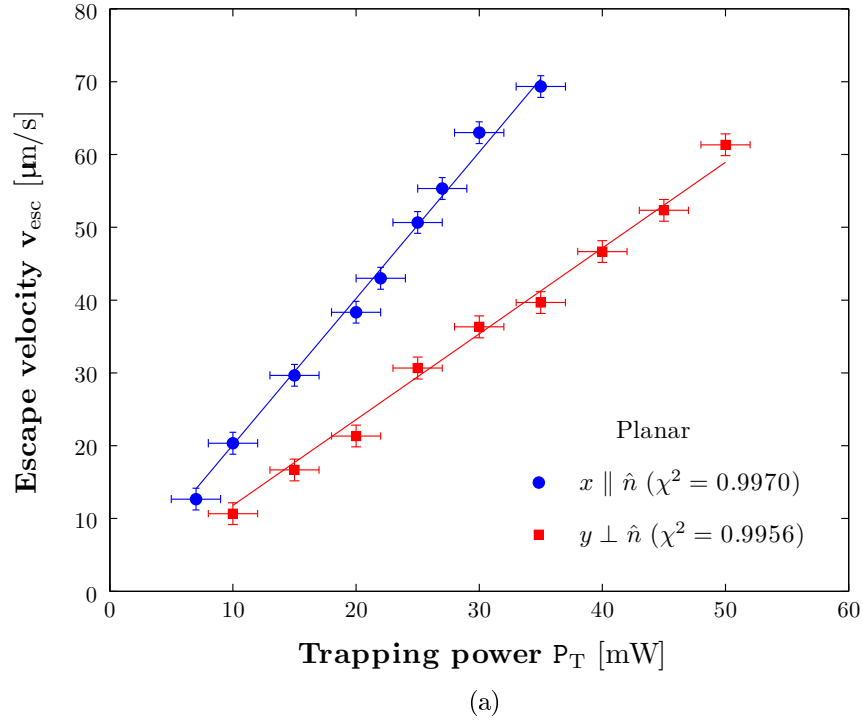
Figure 7.9: Escape velocity of $2\,\mu$m SC beads as a function of trapping power for (a) planar and (b) homeotropically-aligned cells of MLC-6648. As expected, the results illustrate $\eta_{\text{eff}}^{\perp} > \eta_{\text{eff}}^{\parallel}$.

(a)

(b)
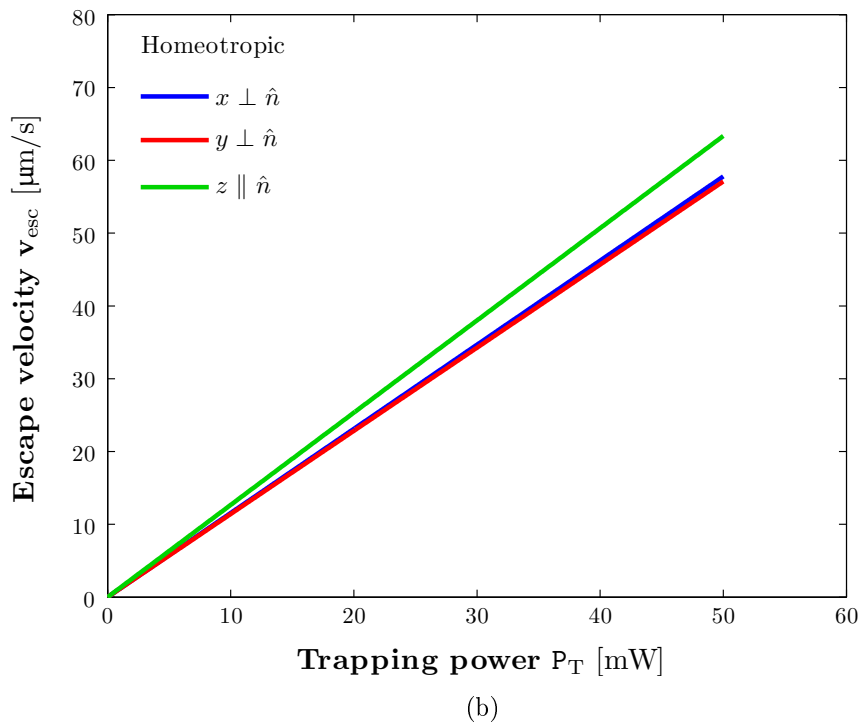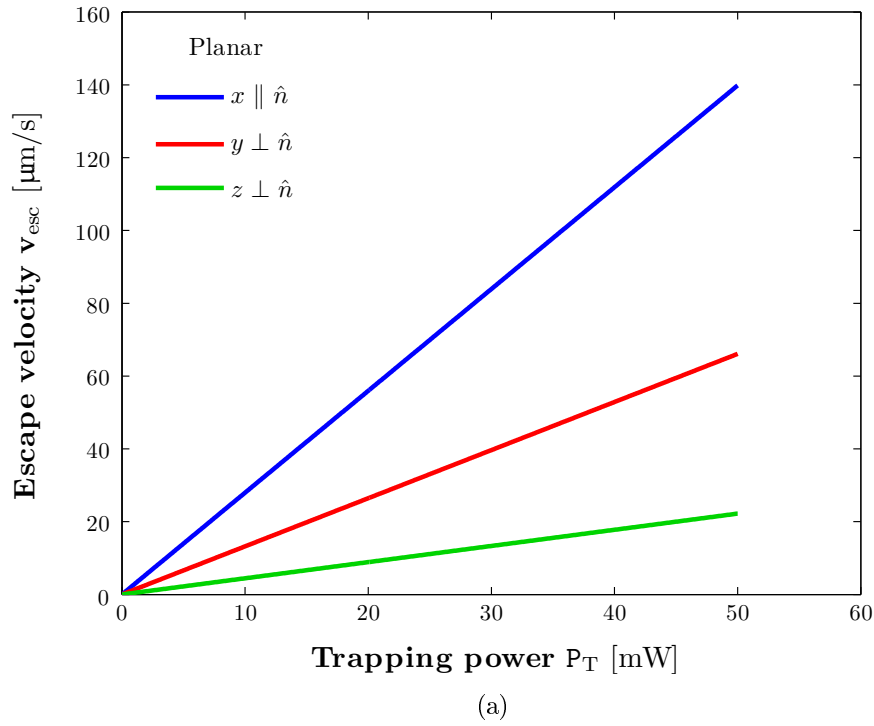
Figure 7.10: Predicted values of the escape velocity of $6\,\mu$m PS beads as a function of trapping power for (a) planar and (b) homeotropically-aligned cells of MLC-6609. Values were calculated using theoretically determined values of lateral and axial trapping efficiencies Q_{xy} and Q_z and η_{eff} values measured using passive microviscometry.

7.2.3 Effective viscosities $\eta_{\text{eff}}^{\perp}$ and $\eta_{\text{eff}}^{\parallel}$

Figure 7.11 compares $\eta_{\text{eff}}^{\parallel}$ and $\eta_{\text{eff}}^{\perp}$ determined for homeotropic and planar cells of MLC-6648 and MLC-6609 using both passive and active microviscometry. The results illustrate the observed anisotropy using both methods. On average, the value was found to be close to the average bulk viscosity values of each LC.
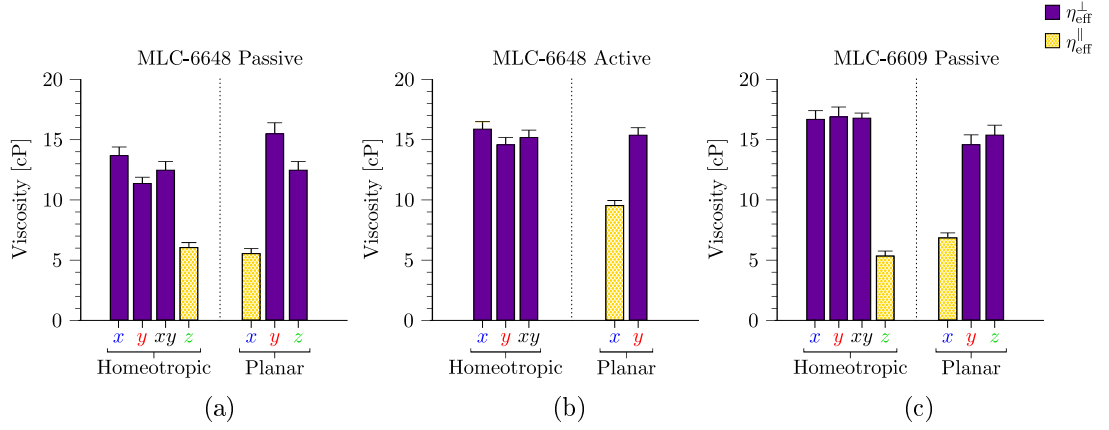
Figure 7.11: Comparison of effective anisotropic viscosities $\eta_{\text{eff}}^{\perp}$ and $\eta_{\text{eff}}^{\parallel}$ calculated for homeotropic and planar samples of MLC-6648 using (a) passive and (b) active microviscometry, and (c) for samples of MLC-6609 using passive microviscometry. The labels x, y and z correspond to values obtained using the power spectra for that direction, whilst xy denotes the average of x and y i.e. the lateral direction.

Calculated values of $\eta_{\text{eff}}^{\perp}$ and $\eta_{\text{eff}}^{\parallel}$ are summarised in Table 7.2 where the quoted errors are the standard error on the mean and the number of measurements on separate cells are given in brackets. Again, x, y and z correspond to values obtained for that direction, whilst xy denotes the average of x and y i.e. the lateral direction.

7.3 Discussion

Power spectral density analysis in conjunction with computer controlled laser tweezers and high-speed video microscopy to perform particle tracking have been used to investigate the anisotropic viscosity of two nematic LCs; MLC-6609 and MLC-6648 in the low Ericksen number regime $E_{\text{r}} \ll 1$.

Table 7.2: Values of effective viscosities $\eta^{\parallel}_{\text{eff}}$ and $\eta^{\perp}_{\text{eff}}$ for MLC-6648 and MLC-6609 with homeotropic and planar alignment, determined using passive and active microviscometry. All values are in good agreement with previous work [167, 189], see the text for more detail. The quoted errors are the standard error on the mean and the number of measurements are given in brackets. A single centiPoise cP is equivalent to 0.001 Pa s.

Liquid crystal	η_{eff} [cP]	Passive Microviscometry		Active Microviscometry	
		Homeotropic	Planar	Homeotropic	Planar
MLC-6648	$\eta^{\perp}_{\text{eff}}$	13.7 ± 0.7 (3) x 11.4 ± 0.5 (3) y 12.5 ± 0.7 (3) xy	15.5 ± 0.9 (2) y 13.0 ± 0.7 (2) z	15.9 ± 0.6 (2) x 14.6 ± 0.6 (2) y 15.2 ± 0.6 (2) xy	15.4 ± 0.6 (2) y
	$\eta^{\parallel}_{\text{eff}}$	6.1 ± 0.4 (2) z	5.6 ± 0.4 (2) x		9.02 ± 0.4 (2) x
MLC-6609	$\eta^{\perp}_{\text{eff}}$	16.7 ± 0.7 (2) x 16.9 ± 0.8 (2) y 16.8 ± 0.4 (2) xy	14.6 ± 0.8 (2) y 15.4 ± 0.9 (2) z		
	$\eta^{\parallel}_{\text{eff}}$	5.4 ± 0.4 (2) z	6.9 ± 0.4 (2) x		

With reference to Table 7.2, the effective viscosity values $\eta_{\text{eff}}^{\perp}$ and $\eta_{\text{eff}}^{\parallel}$, determined for MLC-6648 in this work agree well with values obtained previously using an alternative form of laser tweezing; applying known viscous drag forces to an optically trapped particle relative to the director $\hat{n}$ [167]. They are also in good agreement with the flow viscosity quoted by the manufacturer [244].

Similarly, values of $\eta_{\text{eff}}^{\perp}$ for MLC-6609 determined in this work agree well with the flow viscosity. However, there is a considerable difference (a factor of 2) with other viscosity measurements made on large volumes of material, using shear flow experiments, which were not in the low Ericksen number regime [189].

7.3.1 Surface anchoring ratio $\eta_{\text{eff}}^{\perp}/\eta_{\text{eff}}^{\parallel}$

The results also allow discussion on the anchoring of the LC at the particle surface, characterised by the ratio $\eta_{\text{eff}}^{\perp}/\eta_{\text{eff}}^{\parallel}$. Calculated values are given in Table 7.3. There is considerable variation in the values where all are higher than expected. Stark *et al.* [167] theoretically predicted that for strong and weak homeotropic anchoring, the ratio should be 2 and 1.3, respectively, although the transition is a continuum. These results confirm the previous observation from active measurements [167] that strong anchoring is implied.

Table 7.3: The ratio $\eta_{\text{eff}}^{\perp}/\eta_{\text{eff}}^{\parallel}$ characterises the strength of the anchoring at the particle surface where a value of 2.0 and 1.3 would correspond to strong and weak homeotropic anchoring, respectively.

Liquid crystal	Passive value		Active value	
	Homeotropic	Planar	Homeotropic	Planar
MLC-6648	2.0 ± 0.4	2.5 ± 0.2		1.7 ± 0.4
MLC-6609	3.1 ± 0.8	2.2 ± 0.5		

7.3.2 Trap stiffness

It is possible to estimate corresponding values of trap stiffness κ using values of f_{c} and η_{eff}. These back-calculated values are given in Table 7.4. All values were higher than expected, on the order of 2 times higher, for any of the directions

Table 7.4: Comparison of back-calculated values of trap stiffness κ in MLC-6648, MLC-6609 and water determined using passive microviscometry. PS and SC correspond to polystyrene and silica beads, respectively.

Material	Particle properties		Trap stiffness κ (pN/μm)					
			x		y		z	
			Hometropic	Planar	Homeotropic	Planar	Homeotropic	Planar
MLC-6648	2 μm	SC	32.1 ± 1.5	10.0 ± 1.0	29.2 ± 1.4	10.0 ± 1.0	19.7 ± 1.2	10.6 ± 1.0
MLC-6609	6 μm	PS	36.0 ± 2.6	31.3 ± 2.1	23.0 ± 2.1	17.0 ± 1.4	15.3 ± 1.7	17.0 ± 1.9
Water	6 μm	PS	~ 20		~ 20		~ 7	

when compared with the same trapping power for a $6\,\mu$m polystyrene bead in water.

For homeotropic cells of MLC-6648, the refractive index difference δn between the particle and the medium has decreased when compared with trapping in water $n_\mathrm{w} = 1.33$. One would therefore expect κ to decrease in line with this. However, these results are contrary to that prediction and the values are also greater than the corresponding value in water $\kappa_\mathrm{w} \approx 20\,pN\mu$m.

For planar cells of MLC-6648, the values of κ_x and κ_y are in agreement with the predicted decrease in κ compared with κ_w as δn has decreased. The agreement between these numbers suggests trap stiffness is relatively independent of $\hat{n}$ at the particle surface. However, since passive microviscometry observes Brownian motion, one would expect to see a difference in κ relative to $\hat{n}$, as shown by Smalyukh *et al.* [184]. The value of κ_z is thus, greater than both κ_x and κ_y; an unexpected result.

The discrepancy between the values of $\kappa_\perp$ for the homeotropic and planar cells of MLC-6648 ($\kappa_{x/y}$ and κ_y, respectively) suggest that the trap stiffness is weaker in a planarly aligned cell. However, in both these cell types, motion perpendicular to the director corresponds to the trapping beam experiencing only the ordinary refractive index n_o. Thus, trap stiffness should not deviate too greatly. A possible explanation is the idea that the trapping beam converging at such high angles, $\sim 60\,^\circ$, causing it to experience a component of the LC's extraordinary refractive index n_e. This contribution would act to increase the apparent value of κ.

For homeotropic cells of MLC-6609, the value of κ_z is a factor of 2 smaller than κ_x and κ_y, however is larger than expected when comparing with the corresponding value of the lateral trap stiffness κ_w. For planar cells of MLC-6609, κ_x is once more overestimated relative to κ_w. However, κ_y is lower than κ_w, in line with a decrease in refractive index difference δn. The value of κ_z is a factor of 2 smaller than κ_x and κ_y, whilst being larger than expected when compared with κ_w.

Interestingly, unlike MLC-6648, there appears to be very little discrepancy between $\kappa_\perp$ for the homeotropic and planar cells suggesting there is a negligible effect due to the trapping beam experiencing a component of n_e. There is however, a discrepancy for some values of $\kappa_\parallel$, where $\kappa_\parallel$ for homeotropic and planar cells (κ_z

and κ_x, respectively) differs by a factor of 2. This suggests there is an unaccounted for difference between the alignment types, or perhaps an erroneous reading.

Possible sources for the inflated value of κ include the LabVIEW program *SimpleAnalysis.vi* itself. The program filters the Lorenztian data to increase precision. However, the measurement of the variance from the ACF is unfiltered and any instantaneous errors which underestimate $\langle x^2 \rangle$, $\langle y^2 \rangle$ and $\langle z^2 \rangle$ will propagate into the measurement of η and thus, κ.

Similarly, the program requires user input of the temperature T which is proportional to κ. Overestimation of T is possible, particularly for low P_T. There is, of course, the effect of the cells being handmade, where an alignment layer rather than an applied electric field is used to align $\hat{n}$. Therefore, any weaknesses in the alignment layer may affect the particle dynamics.

In both isotropic and LC cells, the particle was held away from the coverslip surface ($\sim 10\,\mu\text{m}$) so as to minimise any boundary effects. As such, the increased trap stiffness values imply that the influence of the surfaces is much more important for LC systems, and perhaps other non-Newtonian fluids, than for isotropic materials. Also, these discrepancies are unlikely to be due to aberrations of the trapping beam, which has a greater effect in the axial (z) direction.

7.3.3   Refractive index

The refractive index difference δn between that of the particle and the LC's ordinary and extraordinary refractive indices are given in Table 7.5. Both values of δn for silica beads are significantly small compared with the refractive index when trapping SC beads in water; 0.23. This suggests trapping of SC beads is theoretically forbidden and successful trapping may be due to the contribution of the laser beams electric field or the creation of a high-n region or 'cloud' around the particle. It may be necessary to take into consideration dispersion; the wavelength dependence of n [243].

As described in Section 3.2.2, at large values of P_T, reorientation of $\hat{n}$ occurs. The resultant effect is that the particle 'falls into' the optical trap despite being located a significant distance from it, e.g. $10\,\mu\text{m}$, as a shown by Mušević *et al.* [182]. They showed the particle appeared to be attracted to a 'ghost' particle

Table 7.5: Calculated values of the refractive index differences δn_e and δn_o; the differences between the particle's refractive index n_p and the extraordinary and ordinary refractive indices of the chosen liquid crystals, n_e and n_o, respectively, as given previously in Tables 3.2 and 3.3.

		MLC-6609	MLC-6648
Polystyrene (PS)	$\delta n_e = n_p - n_e$	**0.0386**	0.0443
	$\delta n_o = n_p - n_o$	**0.1163**	0.1144
Silica (SC)	$\delta n_e = n_p - n_e$	0.0086	**0.0143**
	$\delta n_o = n_p - n_o$	0.0863	**0.0844**

where the laser beam had reorientated $\hat{n}$ or partially melted the LC. It was achieved at a trapping power of $64\,\mathrm{mW}$, close to but greater than the power employed in passive microviscometry of MLC-6609. It is important to note, in their experiments the particle refractive index $n_p > n_e$ and n_o.

The insertion of a wave plate, taking into consideration the dichroic mirrors in the setup so as not to produce circularly polarised light, would allow investigation into whether the trapping laser beam is causing the optical Fréedericksz transition. Values of δn for PS beads in MLC-6609 are also relatively small when compared with trapping in water; 0.26. However, they are at least a factor of ~ 3 times larger than for SC beads in MLC-6648, even when considering the average refractive index $\bar{n}$.

Incidentally, the ordinary and extraordinary refractive indices of the chosen LC materials provided by the manufacturer are determined for $589.3\,\mathrm{nm}$ and at $20\,°\mathrm{C}$ (Table 3.2, p. 98). As with the water–glycerol mixtures, it would be advantageous to determine each LC's pair of refractive indices at the trapping laser wavelength; $1064\,\mathrm{nm}$. This would therefore allow conclusive evaluation of refractive index differences δn. Determining these as a function of temperature would also be worthwhile.

7.3.4   Particle tracking

It was often difficult to obtain a good quality image of the particle in order to achieve accurate particle tracking. An example of this is shown in Fig. 7.12 for a 6 μm PS bead optically trapped in MLC-6609. The image shows the particle before and after applying a threshold to eliminate the background. In such cases, the intensity at the particle centre was insufficient to create a circular image with

Figure 7.12: Image of a 6 μm PS bead optically trapped in MLC-6609 before (left) and after (right) a threshold has been applied for accurate particle tracking.

a bright centre. Similarly, the particle often didn't stand out from the background due to the LC's opacity, thereby reducing the illumination beam through the LC cell.

7.3.5   LC cell geometry

As discussed, one possible reason for discrepancies in η_{eff} is distortion of $\hat{n}$; including the strength of the alignment layer and the laser trapping beam. However, the geometry of the LC cell and the particle's location may also have an effect. Since the LC cells are made of 18 mm × 18 mm coverslips, their only support is provided by the spacers, located far from the

Figure 7.13: Director distortion of planar (top) and homeotropic (bottom) LC cells due to 'dipping' of the coverslip.

centre of the LC cell. Figure 7.13 illustrates how 'dipping' at the centre can affect the components of viscosity experienced by the particle. For a planar cell , a contribution is made to the z direction from any director 'tilt' in the x and y directions, as shown to the right. For a homeotropic cell however, a contribution is made to both the x and y directions due to any director tilt in the z axis.

7.4   Summary

This chapter presented the results of active and passive microviscosity of two liquid crystal mixtures; MLC-6648 and MLC-6609, using the escape force method and the PSD method, respectively. The measured quantities provided evidence of the difference in viscosity depending on the axes' orientation relative to the director $\hat{n}$. As expected, in all cases, $\eta_{\text{eff}}^{\perp} > \eta_{\text{eff}}^{\parallel}$. Predictions were made for a particle's anisotropic escape velocity in three dimensions in both planar and homeotropic cells of MLC-6609. A discussion was provided which takes into account some of the factors affecting tweezing in anistropic liquid crystalline media, including reorientation of the director by the trapping laser beam, surface anchoring, cell geometry and accurate particle tracking.

Despite some discrepancies from both expected values of η_{eff} in the literature and those obtained with active microviscometry, the combination of laser tweezers and power spectral density analysis provides an alternative method to obtain accurate results for anisotropic viscosities in good agreement with previous work. There is merit for further investigation into whether there is a simple insensitivity of this method to the LC's anisotropy or whether it is indeed obtaining different local viscosities.

Chapter 8

Conclusion and Future Work

This chapter aims to conclude and summarise the findings of the research carried out and presented in this thesis. This is followed by suggestions of future work with details of their possible implementation.

8.1 Research summary

The aim of the research presented in this thesis was to use laser tweezers to investigate the microfluidics of both simple and isotropic systems, and anisotropic liquid crystalline systems. At the start of the conducted research, several methods were available for investigating anisotropic systems, including the passive method of observing the power spectral density of the Brownian motion of optically trapped colloids.

Prior to any measurements in anisotropic systems, it was important to calibrate the laser tweezing system; power, position and trap stiffness specifically, and then characterise its performance in well understood systems. The inherited laser tweezing system employed optical particle tracking with the use of a quadrant photodiode. However, with a view to extending the system to multi-trapping with holographic optical tweezers (HOTs) and increasing the speed of measurement and analysis, high-speed video microscopy was employed for imaging and particle tracking. The virtual instrument software, LabVIEW [254], was employed to acquire and analyse data in real time, also allowing data export.

Three dimensional trap stiffness calibration was performed using both active and passive techniques. The passive techniques were divided into time and frequency domain analysis. The acquisition of an optically trapped bead's trajectory and analysis in the time domain allowed calculation of κ from the equipartition of energy theorem. This method does not require the host medium's viscosity to be known *a priori*. Fourier transformation of the position fluctuation data allows κ to be calculated using frequency domain analysis, which provides additional details about the experimental conditions, including sources of noise and vibration and any issues with alignment of the optical trap.

The active viscous drag force method was employed in two dimensions to compare with the passive calibration techniques. All results compared well with one another. An attempt was also made to quantify factors affecting laser tweezing experiments and their impact on κ. These included the proximity of a surface to the optically trapped particle, spherical aberration of the optical trap due to the mismatch between the coverslip surface and the host medium i.e. water, and particle size and refractive index. The results showed fairly good agreement with the theory and experimental data in the literature.

The laser tweezing system was then used for microviscometry; measurements of small changes in viscosity. The active and passive methods of calibration were employed as measurement techniques also. The chosen system for investigation were water–glycerol (WG) mixtures with varying glycerol mass fraction since the viscosity of the mixture in relation to glycerol concentration is well characterised. The mixtures exhibit Newtonian fluid behaviour meaning viscous forces dominate over elastic forces and the fluid's viscosity can be described by Stokes' law.

The results of microviscosity for four WG mixtures with mass fraction $10 \leqslant \Phi_{\mathrm{m}} \leqslant 0.75$ followed the expected trend of increasing viscosity with glycerol concentration in agreement with theoretical predictions [285]. In addition, the relationship agreed well with experimental data presented in the literature which also employed laser tweezers [77, 284, 287]. However, there was some indication of laser-induced heating with a magnitude greater than expected; on the order of $10\,°C$, when compared with both theoretical predictions and experimental data [289]. Changes in κ were also observed between the different WG mixtures, where the change was accounted for due to the decrease in refractive index difference between that of the particle and the mixture as glycerol concentration

increased. Again, this agreed well with the literature [284].

Finally, both active and passive microviscometry were employed to probe the anisotropic viscosity of two LC mixtures. Using laser tweezers provides the opportunity to perform experiments in both the low Reynold's and Ericksen number regimes. This therefore means viscous forces dominate allowing the medium viscosity to be described by Stokes' Law and any distortion of the LC director $\hat{n}$ is considered negligible.

PSD analysis and escape force experiments were performed to observe the dynamics of optically trapped beads to infer the viscosity in directions parallel and perpendicular to the liquid crystal director $\hat{n}$. The anisotropic nature of the particle dynamics provided evidence of the anisotropic viscosity exhibited by LCs.

Effective viscosity coefficients of each LC mixture relative to $\hat{n}$; across and along it, $\eta_{\text{eff}}^{\perp}$ and $\eta_{\text{eff}}^{\parallel}$, respectively, were determined using the active and passive methods. LC cells with planar and homeotropic alignment were used where, as expected, the viscosity experienced by an optically trapped bead was greater along rather than across $\hat{n}$; such that $\eta_{\text{eff}}^{\perp} > \eta_{\text{eff}}^{\parallel}$.

The values of η_{eff} determined in this work for MLC-6648 were in good agreement with values quoted in the literature, which had also been determined using laser tweezers [167]. The values also compare well with the flow viscosity, provided by the manufacturer [244]. However, some disparity existed between the two different techniques and also between planar and homeotropic cells. The associated values of κ seemed to deviate from what is expected and also infer a higher trap stiffness than measured in water for an equivalent trapping power.

A passive method only was used to determine $\eta_{\text{eff}}^{\perp}$ and $\eta_{\text{eff}}^{\parallel}$ for the mixture MLC-6609 where the Mięsowicz coefficients for this mixture have been determined in the bulk using a shear flow method and presented in the literature [189]. Although the results deviated from the aforementioned work, the values determined in this work correspond to local viscosity values in the low Ericksen number regime, whilst theirs were not.

Again, corresponding values of κ suggest the particle is experiencing a greater trap strength in the LC than for the same optical trapping power in water. A discussion was given on possible reasons for the overestimation of κ, which include particle tracking and analysis, an overestimation of sample temperature at

low trapping powers P_T and regions of poor alignment due to the LC cell being handmade.

Also given are predicted values of the escape velocity for an optically trapped particle in MLC-6609. These values are determined using known quantities and theoretically calculated values of the lateral and axial trapping efficiencies.

Measurement of $\eta_{\text{eff}}^{\perp}$ and $\eta_{\text{eff}}^{\parallel}$ also provides a measure of the anchoring of $\hat{n}$ at the particle surface as given by the ratio $\eta_{\text{eff}}^{\perp}/\eta_{\text{eff}}^{\parallel}$. The observation of chain-like structures in LC cells with planar alignment suggested weak hometropic anchoring and, thus, the presence of a Saturn-ring defect. This was visible in planar samples where the Saturn-ring itself could be tweezed and the bead appeared to be tethered. For strong and weak homeotropic anchoring this ratio is 2 and 1.3, respectively. Calculated values for planar cells of both LC mixture suggest strong homeotropic anchoring, although the transition between the two is a continuum. The values of the effective viscosity ratio in the homeotropic cells suggests a degree of homeotropic anchoring at the particle surface, which is expected at the poles, although planar alignment may be expected.

Finally, factors affecting laser tweezing in LCs were discussed. These included the creation of high-index regions around the particle and reorientation of $\hat{n}$ due to the trapping beam creating attractive regions. This results in the particle being pulled into the trap from some distance away. Such an effect allows optical trapping in a situation which would ordinarily be considered unachievable; i.e. when there is an insufficient refractive index contrast between particle and medium. Also, an insufficient intensity distribution of the optically trapped bead has an effect on particle tracking and thus, on measured values of η_{eff}.

8.2 Conclusion and relevance

Some important conclusions can be drawn from the work carried out. Within the limitations of the equipment, funding and time available, the results obtained during the project indicate the laser tweezing system is suitable for detecting microscopic changes in viscosity. The results also indicate a system capable of investigating anistropic particle dynamics, specifically to study anisotropic viscosity of liquid crystalline media.

The combination of PSD analysis and high-speed video microscopy has provided a fast method of observing the microfluidics of isotropic and anisotropic systems. Alternatives include combining active and passive techniques, or optically rotating particles to perform microviscometry [77, 287]. The speed of data acquisition and analysis used in this work may have come at the expense of high precision and accuracy. Considering this trade-off, video microscopy could be thought of as less favourable than optical based imaging, using a quadrant photodiode, for example. The choice of imaging method is a trade-off between a 'plug-and-play' system and extra effort in terms of alignment, with considerable attention paid to the desired precision and accuracy.

Many naturally occurring materials possess anisotropic characteristics, including biological systems, such as cell membranes and lipids. The study of their anisotropic behaviour could have far-reaching consequences, including medical diagnostics. Laser tweezers continue to receive increasing research interest and investment where the technique can be implemented with an Apple iPad, and all other necessary components, of course [28]. Laser tweezing research in liquid crystals is relevant to the progression of switchable display technologies.

8.3 Future work

The work carried out in this thesis highlights a number of areas for further investigation. This section will discuss future work and some suggestions for their implementation.

8.3.1 Laser tweezers

Improvements were made to the inherited laser tweezers system, most notably incorporating a high speed CMOS camera to image and track optically trapped colloids. There are still some areas which would benefit from improvement by upgrading the optical components, as shall be detailed herein.

Optical setup

To optimise optical trapping, the optical setup could be improved with some of the following changes. The inclusion of an aperture at the focal point of the beam expander would provide spatial filtering to improve the quality of the radial intensity profile of the output beam. The aperture should have a radius approximately equal to that of the Gaussian beam at the focus of the beam expander [297].

Eliminating the periscope from the optical setup might reduce additional deviations of the trapping beam therefore improving alignment, in addition to improving laser safety. This could be achieved with the addition of an elevated breadboard to bring all optics to the correct height in order to enter the back port of the microscope at 15.5 cm without the necessity for a periscope.

Of great importance in microscopy is the delivery of the illumination beam, especially for achieving optimum image quality, resolution and contrast. This is of particular relevance to the work in this thesis which utilises the illumination beam for particle tracking and is reliant on a particle with good contrast to the background. Brightfield imaging was used for the work in this thesis, which provided sufficient illumination. However, Köhler illumination is significantly superior, providing uniform sample illumination and allowing for contrast and resolution control [259, 298].

The combination of condenser and microscope objective used in this work were not compatible for successful Köhler illumination. More specifically, the Leica S70/0.30 condenser provided brightfield illumination for microscope objectives between 0.25× and 40× without the need for a field diaphragm. The 100× microscope objective chosen for this work and, in fact, necessary for optical trapping therefore falls outside this range. Unfortunately, Köhler illumination was not possible for the S70/0.30 condenser and as such, the field diaphragm needed to achieve this type of illumination was not supplied with the Leica microscope.

The choice of condenser also plays a significant role for image quality. Choosing a condenser lens with a numerical aperture which closely matches that of the microscope objective, for example, would greatly improve the resolution of the image [259]. Other condensers available with the Leica microscope; S23/0.53 and S1/0.90 would allow brightfield illumination with objective magnifications from

5× and 10×, respectively, upto 100×. These condensers would also allow for Köhler illumination with the inclusion of a field diaphragm.

It would be advantangeous to detect particles which are displaced from the optical trap centre. One way to achieve this is through the use of a Wollaston prism, which consists of two orthogonal prisms cemented together such that their optic axes are perpendicular. The prism creates a pair of orthogonal, linearly polarised beams from randomly polarised light. Wollaston prisms have been used to create multiple optical traps and, in conjuction with a quarter-wave plate, to create two circularly polarised traps; one left, one right [74]. However, with reference to this work, one could use two Wollaston prisms to allow differential interference contrast (DIC) imaging* where the two beams are recombined and interfere, having travelled different optical path lengths. The resulting interference pattern gives a 3D relief appearance corresponding to the optical density of the sample to emphasise features, e.g. particle edges, but is not topographically accurate. If the particle is centred in the optical trap, the output beam will match that of the input beam. If, however, the beam is off-centre, a phase lag is introduced between the two beams to produce elliptically polarised light, where the degree of ellipticity gives a measure of the particle's displacement.

Integrated microscopy

The laser tweezing system is built around a commercially available optical microscope which is particularly useful if looking at biological samples. However, it does limit access to the trapping beam and can make aligning the trapping beam with the back aperture of the microscope objective difficult. A custom-built laser tweezing system, where all optical components are accessible — specifically for alignment purposes — might streamline the setup and alignment procedure. However, a commercially available system often has increased stability in comparison to a custom built setup, which should be a significant consideration when observing a particle's Brownian motion.

---

* Similar to phase contract imaging with the exclusion of a diffraction halo.

High-speed particle tracking

The CMOS camera used in this work to perform high-speed video microscopy can achieve kHz frame rates. However, that depends on the region of interest and is often not easily achieved in reality. Faster cameras have been employed with frame rates on the order of 10,000 frames per second [299]. The achievable frame rate of the camera, and crucially the practically achievable frame rate for the setup concerned compared with what is theoretically possible, should be thoroughly considered. More specifically, evaluating whether acquisition frame rate plays a role, possibly producing erroneous results suggested by this work, is crucial for video-based microscopy.

8.3.2   Multitrapping

The laser tweezing system had the potential for multi-trapping via time-sharing of the trapping beam with galvanometer-controlled mirrors. However, an alternative and popular method for generating multiple traps involves using a spatial light modulator, essentially a computer controlled diffractive optical element, and computer generated holograms to individually address multiple optical traps with ease and at significant speeds e.g. ~ 100 traps at $100\,\text{Hz}$ [69].

A significant consideration in the use of a SLM is the expense; some of which can be in excess of £15,000. However, this is considered a reasonable sacrifice considering the breadth of application of a SLM. In addition to multiple laser tweezers, they also offer the opportunity to create different and novel beam shapes including Laguerre-Gaussian. Thus, allowing the transfer of orbital angular momentum to induce particle rotation. Aberration correction can also be achieved with an SLM.

A suggested route of investigation for this project was the use of a SLM to create multiple optical traps in order to study two-bead cross correlation interactions. Specifically, this would have shed light on the interaction between colloids dispersed in liquid crystalline media due to the attractive and repulsive forces due to distortion and alignment of the director at the particle surface.

As an aside, multi-trapping can also be used to verify good calibration, by observing the cross-correlation of the motion of a trapped particle in the x and y
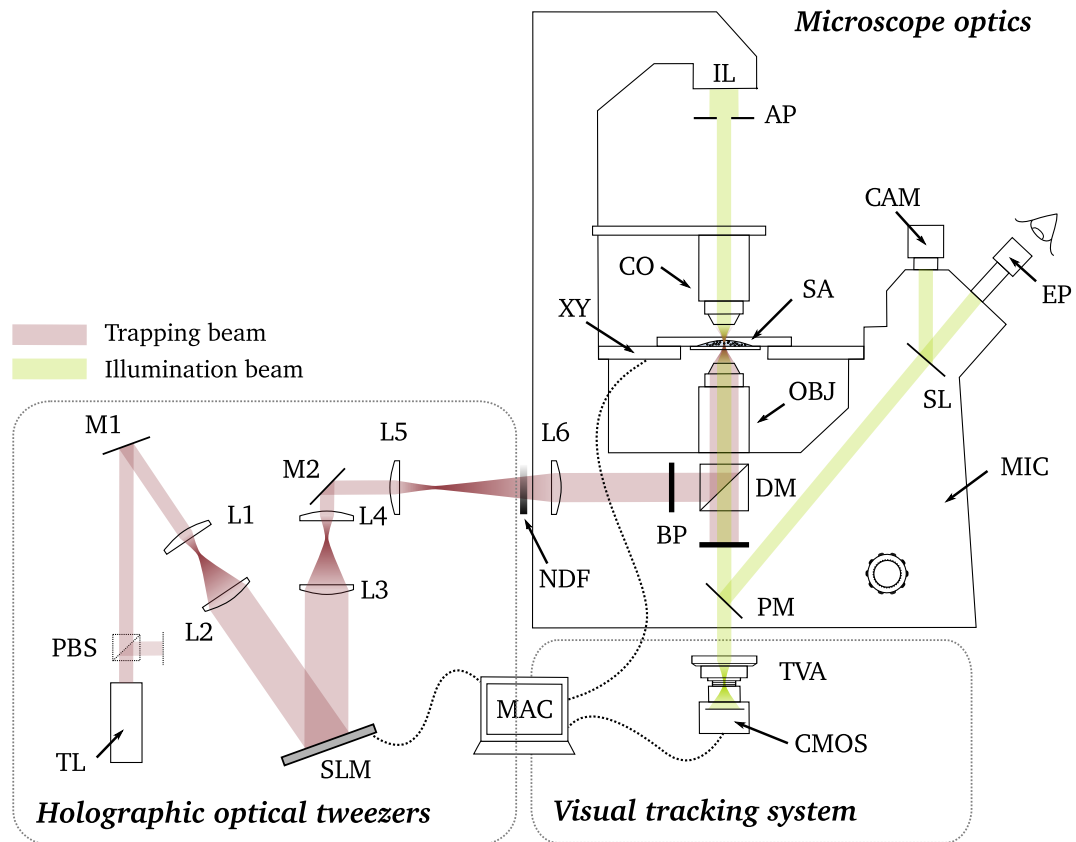
Figure 8.1: The holographic optical tweezers (HOTs) system: 1064 nm wavelength trapping laser (TL) and variable neutral density filter (NDF). Beam expansion lenses (L1,L2) and directing mirror M1 to direct trapping beam onto phase only spatial light modulator (SLM) controlled using Apple MAC. Lenses L3-L6 direct the trapping beam into the inverted microscope. *Microscope optics* and *Visual tracking system* are the same as in Fig. 4.1 (p. 104).

directions. The resulting function should be independent and as such, no correlation between their motion should exist.

A brief investigation into the use of a SLM with this laser tweezing system was performed. This provided a feasibility study of its integration with the current system, in terms of alignment, optics and footprint, and also the ease with which holographic optical trapping could be implemented.

The fundmentals of HOTs are rooted in holography which conventionally works by interfering a reference wave with one scattered from a three-dimensional object to create a hologram which preserves the phase and amplitude informa-

Table 8.1: Focal lengths for all lenses used in the holographic optical tweezers (HOTs) setup shown in Fig. 8.1.

	Lens		Focal length [mm]
	L1	f_1	25.4
	L2	f_2	200
HOLOGRAPHIC	L3	f_3	25.4
OPTICAL	L4	f_4	200
TWEEZERS	L5	f_5	60
	L6	f_6	175

tion of object and you are, thus, able to reconstruct it in three dimensions. Using a SLM, it is possible to produce amplitude and phase-only holograms, which affect only the amplitude or the phase of the the incoming beam, respectively. Computer-generated hologram is employed, where there is no object. Instead, the desired image is known, e.g. multiple traps, and so the diffracting object required to create this image is created.

The SLM display consists of nematic liquid crystal pixels, each of which modulates the phase of the light reflected from it. The phase-only pattern displayed on the surface of the SLM is called a *kinoform*, where complex arrangements can be calculated to generate many discrete traps [300]. As shown in Fig. 8.2, it is often necessary for the angle of incidence of the incoming beam be as small as possible (preferably $< 10°$), to ensure (i) the maximum amount of light exits each pixel and (ii) the light interacts with the liquid crystal in the correct orientation. It is imperative to carefully consider the algorithm chosen for kinoform calculation; this is a trade-off between the kinoform's optical efficiency and computation time [301].

Figure 8.2 illustrates the basic optical process for generating multiple optical traps with an SLM; a computer-controlled diffractive optical element. The proposed and built setup is shown in Fig. 8.1 and the focal lengths of the chosen lenses are given in Table 8.1. For further details on HOTs, the reader is directed toward references [62, 63].

The chosen SLM was a reflective, pure phase Hamamatsu [302] LCoS-SLM[†] X10468-03 and was integrated into the original laser tweezers setup to modulate

---

[†] LCoS: Liquid crystal on silicon
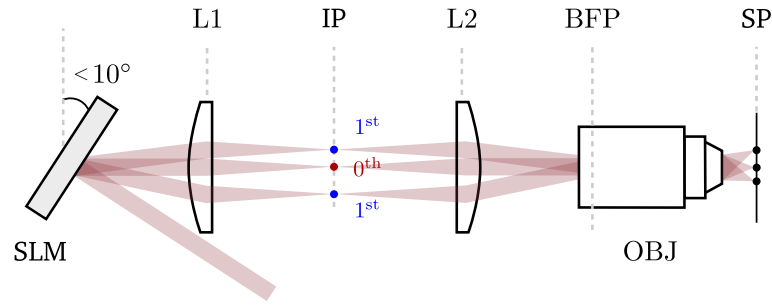
Figure 8.2: Holographic optical tweezers (HOTs) employ a spatial light modulator (SLM) to generate multiple, individually-addressable optical traps using computer generated holograms. The spatial light modulator (SLM) creates individually adressable optical traps in the sample plane (SP) by focussing the orders created in the imaging plane (IP) onto the back focal plane (BFP) of the microscope objective (OBJ) using a set of lenses (L1,L2).

the wavefront of the trapping laser beam. It was chosen for its suitability for the laser's operating wavelength (1064 nm), high light utilisation efficiency (95 %) and high damage threshold, which significantly exceeds the power in this system (1 W).

It was possible to control the SLM using software supplied by Hammamatsu or using custom programs written in LabVIEW. A single optical trap was achieved and successful optical trapping achieved in a microfluidic channel as shown in Fig. 8.3. Typically, microfluidic devices or 'chips' are made using PDMS or PMMA where channels are either directly milled into the solid polymer with a computer controlled milling machine with drill dimensions down to $\sim$100 μm. Alternatively, if a number

Figure 8.3: Optically trapped 2 μm polystyrene bead in distilled, deionised water using holographic optical tweezers generated with a spatial light modulator (SLM). The trapped bead is approximately $12r$ from the wall of the microfluidic channel (left).

of copies are required, a metal template is first fabricated, into which a liquid polymer is injected the liquid polymer, known as injection moulding. In both cases, the channels are usually sealed with an adhesive layer. A 'true' microfluidic device has at least one dimension less than 1 mm [303].

8.3.3   Liquid crystals

There is considerable scope of future work for investigating liquid crystals with laser tweezers. The suggestions made here are those which are practical with the current laser tweezing system or with some enhancement, and would provide a positive contribution to a selection of research areas.

To further understand the effect the trapping beam has on the liquid crystal, specifically the director, one could introduce a wave plate, taking into consideration the dichroic mirrors in the setup so as not to produce circularly polarised light. This would allow investigation into whether the trapping laser beam is causing the optical Fréedericksz transition which either reorientates the director or melts a region of the LC and thus, could be facilitating trapping which would otherwise be forbidden [176, 182, 183].

In microrheology and laser tweezers, some consider passive techniques inferior to active techniques. If the optical trap remains stationary, the particle can be continually released and re-trapped without indication, thus producing erroneous results. Any effect this may have had on the results presented in this thesis can be investigated further by combining active and passive techniques. For example, Guzmán et al. [287] measured the power spectral density of optically trapped particles under the application of an oscillatory viscous drag force, where the frequency peak was proportional to the viscosity of the media surrounding the trapped particle, in this case, water-glycerol mixtures. This method may also be applicable to colloids dispersed in LCs.

Similarly, to assist characterisation of surface anchoring at the LC-colloid interface, one could introduce crossed polarisers to observe the liquid crystal surrounding the trapped particle. This could also be expanded to observe particle interactions in liquid crystals where multi-trapping with HOTs (as described in Section 8.3.2) provides a suitable method of doing so. Understanding the interaction between particles dispersed in liquid crystals has potential for self-assembled devices, topological soft materials and applications in photonics.

It would be advantageous to extend the range of liquid crystal mixtures studied in this work where MLC-7023, manufactured by Merck, also meets the criteria for achieving efficient laser tweezing, with a birefringence $\Delta n = 0.0609$, dielectric anisotropy $\Delta \varepsilon = 7.9$ and clearing temperature $T_c = 79.5°$C. Unfortunately, the

flow viscosity is now quoted, therefore potentially making comparison measured viscosity values different. Preliminary investigations were performed with this LC mixture where it was found to be difficult to align and evidence suggested the addition of colloids may have caused some variation in T_{c}.

The results presented in this thesis could be further enhanced by observing the effects of temperature, trapping beam polarisation, trap depth and cell thickness, and their effect on LCs. It would be possible to use, for example, a Linkam THMS600 heating and freezing controlled using a TMS 93 temperature controller would be a suitable candidate for temperature control of LC cells, specifically in an inverted arrangement in line with that of the microscope. However, it should be noted that immersion oil is inversely proportional to temperature which should be accounted for with any heating or cooling of the sample. In addition, to prevent any damage to the microscope objective, the temperature range for investigations should be limited to an appropriate range. For the Leica microscope objective using in this work, 0–60 °C would be suitable.

There are some other interesting applications which nominate areas for investigation. Carbon nanotubes offer great promise for novel light-weight composites which are superstrong. However, they are required to be well dispersed and preferably, be aligned within the composite. Choosing liquid crystals as the dispersive media provides a very effective method for imposing their organisation [304, 305]. Therefore, trapping of carbon nanotubes may provide insight into these structures including their interaction with one another when dispersed in a LC.

References

[1] Einstein, A. Zur Quantentheorie der Strahlung (Translation: On the Quantum Theory of Radiation). *Physikalische Zeitschrift* **18**: 121 (1917). English translation in: B. L. van der Waerden, editor, Sources of Quantum Mechanics, Volume 5, 63-77 (Dover Publications, 1968) ISBN: **0486618811**. *Cited on page 32.*

[2] Ashkin, A. Acceleration and trapping of particles by radiation pressure. *Physical Review Letters* **24**(4): 156–159 (1970). DOI: **10.1103/PhysRevLett.24.156**. *Cited on pages 37, 38 & 39.*

[3] Ashkin, A., Dziedzic, J.M., Bjorkholm, J.E. and Chu, S. Observation of a Single-Beam Gradient Force Optical Trap for Dielectric Particles. *Optics Letters* **11**(5): 288–290 (1986). DOI: **10.1364/OL.11.000288**. *Cited on pages 37, 38 & 39.*

[4] Moffitt, J.R., Chemla, Y.R., Smith, S.B. and Bustamante, C. Recent Advances in Optical Tweezers. *Annual Review of Biochemistry* **77**(1): 205–228 (2008). DOI: **10.1146/annurev.biochem.77.043007.090225**. *Cited on pages 37, 53, 69 & 115.*

[5] Gould, R.G. The LASER, Light Amplification by Stimulated Emission of Radiation. In P.A. Franken and R.H. Sands (editors), The Ann Arbor Conference on Optical Pumping (Ann Arbor, the University of Michigan, 1959), 128. *Cited on page 38.*

[6] Maiman, T.H. Stimulated Optical Radiation in Ruby. *Nature* **187**(4736): 493–494 (1960). DOI: **10.1038/187493a0**. *Cited on page 38.*

[7] Lebedev, P.N. The Experimental Study of the Pressure of Light (Untersuchungen über die Druckkräfte des Lichtes). *Annalen der Physik* **6**(11): 433–458 (1901). DOI: **10.1002/andp.19013111102**. *Cited on pages 38 & 39.*

[8] Nichols, E.F. and Hull, G.F. A Preliminary Communication on the Pressure of Heat and Light Radiation. *Physical Review (Series I)* **13**(5): 307 (1901). DOI: **10.1103/PhysRevSeriesI.13.307**. *Cited on pages 38 & 39.*

[9] McGloin, D. Optical tweezers: 20 years on. *Philosophical Transactions of the Royal Society A: Mathematical, Physical and Engineering Sciences* **364**(1849): 3521–3537 (2006). DOI: **10.1098/rsta.2006.1891**. *Cited on pages 38 & 39.*

[10] Padgett, M.J., Molloy, J.E. and McGloin, D. (editors). Optical tweezers: methods and applications. Series in optics and optoelectronics (Chapman and Hall/CRC, Taylor and Francis Group, 2010). *Cited on pages 38, 39, 44 & 53.*

[11] Ashkin, A. and Dziedzic, J.M. Optical Levitation by Radiation Pressure. *Applied Physics Letters* **19**(8): 283–285 (1971). DOI: `10.1063/1.1653919`. *Cited on page 38.*

[12] Ashkin, A. and Dziedzic, J.M. Radiation Pressure on a Free Liquid Surface. *Physical Review Letters* **30**(4): 139 (1973). DOI: `10.1103/PhysRevLett.30.139`. *Cited on page 38.*

[13] Ashkin, A. and Dziedzic, J.M. Optical Levitation of Liquid Drops by Radiation Pressure. *Science* **187**(4181): 1073–1075 (1975). DOI: `10.1126/science.187.4181.1073`. *Cited on page 38.*

[14] Ashkin, A. and Dziedzic, J.M. Observation of a New Nonlinear Photoelectric Effect Using Optical Levitation. *Physical Review Letters* **36**(5): 267 (1976). DOI: `10.1103/PhysRevLett.36.267`. *Cited on page 38.*

[15] Ashkin, A. and Dziedzic, J.M. Optical levitation in high vacuum. *Applied Physics Letters* **28**(6): 333–335 (1976). DOI: `10.1063/1.88748`. *Cited on page 38.*

[16] Ashkin, A. and Dziedzic, J.M. Feedback stabilization of optically levitated particles. *Applied Physics Letters* **30**(4): 202–204 (1977). DOI: `10.1063/1.89335`. *Cited on page 38.*

[17] Ashkin, A. and Dziedzic, J.M. Observation of Resonances in the Radiation Pressure on Dielectric Spheres. *Physical Review Letters* **38**(23): 1351 (1977). DOI: `10.1103/PhysRevLett.38.1351`. *Cited on page 38.*

[18] Ashkin, A. and Dziedzic, J.M. Observation of light scattering from nonspherical particles using optical levitation. *Applied Optics* **19**(5): 660–668 (1980). DOI: `10.1364/AO.19.000660`. *Cited on page 38.*

[19] Ashkin, A. and Dziedzic, J.M. Optical trapping and manipulation of viruses and bacteria. *Science* **235**(4795): 1517–1520 (1987). DOI: `10.1126/science.3547653`. *Cited on pages 38 & 53.*

[20] Ashkin, A., Dziedzic, J.M. and Yamane, T. Optical trapping and manipulation of single cells using infrared laser beams. *Nature* **330**(6150): 769–771 (1987). DOI: `10.1038/330769a0`. *Cited on pages 38 & 53.*

[21] Ashkin, A. History of optical trapping and manipulation of small-neutral particle, atoms, and molecules. *IEEE Journal of Selected Topics in Quantum Electronics* **6**(6): 841–856 (2000). DOI: `10.1109/2944.902132`. *Cited on pages 39 & 69.*

[22] Smith, S.P., Bhalotra, S.R., Brody, A.L., Brown, B.L., Boyda, E.K. and Prentiss, M. Inexpensive optical tweezers for undergraduate laboratories. *American Journal of Physics* **67**(1): 26–35 (1999). DOI: `10.1119/1.19187`. *Cited on page 39.*

[23] Pastel, R., Struthers, A., Ringle, R., Rogers, J., Rohde, C. and Geiser, P. Laser trapping of microscopic particles for undergraduate experiments. *American Journal of Physics* **68**(11): 993–1001 (2000). DOI: 10.1119/1.1286048. *Cited on page 39.*

[24] Bechhoefer, J. and Wilson, S. Faster, cheaper, safer optical tweezers for the undergraduate laboratory. *American Journal of Physics* **70**(4): 393–400 (2002). DOI: 10.1119/1.1445403. *Cited on page 39.*

[25] Appleyard, D.C., Vandermeulen, K.Y., Lee, H. and Lang, M.J. Optical trapping for undergraduates. *American Journal of Physics* **75**(1): 5–14 (2007). DOI: 10.1119/1.2366734. *Cited on pages 39 & 72.*

[26] Rocha, M.S. Optical tweezers for undergraduates: Theoretical analysis and experiments. *American Journal of Physics* **77**(8): 704–712 (2009). DOI: 10.1119/1.3138698. *Cited on page 39.*

[27] Mas, J., Farré, A., Cuadros, J., Juvells, I. and Carnicer, A. Understanding Optical Trapping Phenomena: A Simulation for Undergraduates. *IEEE Transactions on Education* **54**(1): 133–140 (2011). DOI: 10.1109/TE.2010.2047107. *Cited on page 39.*

[28] Bowman, R.W., Gibson, G., Carberry, D., Picco, L., Miles, M. and Padgett, M.J. iTweezers: optical micromanipulation controlled by an Apple iPad. *Journal of Optics* **13**(4): 044002 (2011). DOI: 10.1088/2040-8978/13/4/044002. *Cited on pages 40, 46 & 194.*

[29] Blickle, V. and Bechinger, C. Realization of a micrometre-sized stochastic heat engine. *Nature Physics* **8**(2): 143–146 (2011). DOI: 10.1038/nphys2163. *Cited on page 40.*

[30] Ohlinger, A., Deak, A., Lutich, A.A. and Feldmann, J. Optically Trapped Gold Nanoparticle Enables Listening at the Microscale. *Physical Review Letters* **108**(1): 018101 (2012). DOI: 10.1103/PhysRevLett.108.018101. *Cited on page 40.*

[31] Cojoc, D., Garbin, V., Ferrari, E., Businaro, L., Romanato, F. and Di Fabrizio, E. Laser trapping and micro-manipulation using optical vortices. *Microelectronic Engineering* **78-79**: 125–131 (2005). DOI: 10.1016/j.mee.2004.12.017. *Cited on page 40.*

[32] Alpmann, C., Bowman, R., Woerdemann, M., Padgett, M. and Denz, C. Mathieu beams as versatile light moulds for 3D micro particle assemblies. *Optics Express* **18**(25): 26084–26091 (2010). DOI: 10.1364/OE.18.026084. *Cited on pages 41 & 43.*

[33] Yao, A.M. and Padgett, M.J. Orbital angular momentum: origins, behavior and applications. *Advances in Optics and Photonics* **3**(2): 161–204 (2011). DOI: 10.1364/AOP.3.000161. *Cited on pages 40, 41 & 42.*

[34] Padgett, M.J. Orbital angular momentum, optical spanners, and rotational frequency shift. In Laser Resonators III (SPIE, San Jose, CA, USA, 2000), volume 3930, 130–143. DOI: 10.1117/12.385396. *Cited on pages 40, 41 & 42.*

[35] Kennedy, S.A., Szabo, M.J., Teslow, H., Porterfield, J.Z. and Abraham, E.R.I. Creation of Laguerre-Gaussian laser modes using diffractive optics. *Physical Review A* **66**(4): 043801 (2002). DOI: 10.1103/PhysRevA.66.043801. *Cited on page 42.*

[36] Dholakia, K., Reece, P. and Gu, M. Optical micromanipulation. *Chemical Society Reviews* **37**(1): 42–55 (2008). DOI: 10.1039/b512471a. *Cited on pages 42, 44, 52, 53, 68, 108 & 109.*

[37] Molloy, J.E. and Padgett, M.J. Lights, action: optical tweezers. *Contemporary Physics* **43**(4): 241–258 (2002). DOI: 10.1080/00107510110116051. *Cited on pages 42 & 44.*

[38] Simpson, N.B., McGloin, D., Dholakia, K., Allen, L. and Padgett, M.J. Optical tweezers with increased axial trapping efficiency. *Journal of Modern Optics* **45**(9): 1943 – 1949 (1998). DOI: 10.1080/09500349808231712. *Cited on pages 42, 43, 68, 84 & 85.*

[39] Prentice, P., MacDonald, M., Frank, T., Cuschier, A., Spalding, G., Sibbett, W., Campbell, P. and Dholakia, K. Manipulation and filtration of low index particles with holographic Laguerre-Gaussian optical trap arrays. *Optics Express* **12**(4): 593–600 (2004). DOI: 10.1364/OPEX.12.000593. *Cited on page 42.*

[40] Gahagan, K.T. and Swartzlander, J.G.A. Optical vortex trapping of particles. *Optics Letters* **21**(11): 827–829 (1996). DOI: 10.1364/OL.21.000827. *Cited on page 42.*

[41] Padgett, M., Courtial, J. and Allen, L. Light's Orbital Angular Momentum. *Physics Today* **57**(5): 35–40 (2004). DOI: 10.1063/1.1768672. *Cited on page 42.*

[42] Sato, S., Ishigure, M. and Inaba, H. Optical trapping and rotational manipulation of microscopic particles and biological cells using higher-order mode Nd:YAG laser beams. *Electronics Letters* **27**(20): 1831–1832 (1991). DOI: 10.1049/el:19911138. *Cited on page 42.*

[43] Pampaloni, F. and Enderlein, J. Gaussian, Hermite-Gaussian, and Laguerre-Gaussian beams: A primer (2004). Electronic resource. Date Accessed: April 14, 2011. URL: arxiv.org/abs/physics/0410021v1. *Cited on page 42.*

[44] Arlt, J., Garces-Chavez, V., Sibbett, W. and Dholakia, K. Optical micromanipulation using a Bessel light beam. *Optics Communications* **197**(4-6): 239–245 (2001). DOI: 10.1016/S0030-4018(01)01479-1. *Cited on page 43.*

[45] López-Mariscal, C., Gutiérrez-Vega, J.C., Milne, G. and Dholakia, K. Orbital angular momentum transfer in helical Mathieu beams. *Optics Express* **14**(9): 4182–4187 (2006). DOI: 10.1364/OE.14.004182. *Cited on page 43.*

[46] Maurer, C., Jesacher, A., Bernet, S. and Ritsch-Marte, M. What spatial light modulators can do for optical microscopy. *Laser & Photonics Reviews* **5**(1): 1863–8899 (2010). DOI: 10.1002/lpor.200900047. *Cited on pages 44 & 46.*

[47] Booth, M.J. Adaptive optics in microscopy. *Philosophical Transactions of the Royal Society A: Mathematical, Physical and Engineering Sciences* **365**(1861): 2829–2843 (2007). DOI: 10.1098/rsta.2007.0013. *Cited on page 44.*

[48] Theofanidou, E., Wilson, L., Hossack, W.J. and Arlt, J. Spherical aberration correction for optical tweezers. *Optics Communications* **236**(1-3): 145–150 (2004). DOI: 10.1016/j.optcom.2004.03.009. *Cited on page 44.*

[49] Nash, R., Bowman, S., Bradley, C. and Conan, R. A Prototype Optical Tweezer System Employing Adaptive Optics Technology. *International Journal of Optomechatronics* **4**(3): 306–324 (2010). DOI: 10.1080/15599612.2010.512379. *Cited on page 44.*

[50] Yuan, X., Zhang, Y., Cao, R., Zhao, X., Bu, J. and Zhu, S. Dynamic steering beams for efficient force measurement in optical manipulation. *Chinese Optics Letters* **9**(3): 031201 (2011). DOI: 10.3788/COL201109.031201. *Cited on pages 44 & 45.*

[51] Powell, J.A. The Development of a DPSS Laser Scanning Optical Tweezer System. Ph.D. thesis, University of Manchester (2000). *Cited on page 44.*

[52] Hanes, Richard, D.L., Jenkins, Matthew, C. and Egelhaaf, Stefan, U. Combined holographic-mechanical optical tweezers: Construction, optimization, and calibration. *Review of Scientific Instruments* **80**(8): 083703 (2009). DOI: 10.1063/1.3196181. *Cited on page 44.*

[53] Neuman, K.C. and Block, S.M. Optical trapping. *Review of Scientific Instruments* **75**(9): 2787–2809 (2004). DOI: 10.1063/1.1785844. *Cited on pages 45, 53, 68, 69, 72, 75, 79, 115, 124, 128, 145 & 146.*

[54] Visscher, K., Gross, S.P. and Block, S.M. Construction of multiple-beam optical traps with nanometer-resolution position sensing. *IEEE Journal of Selected Topics in Quantum Electronics* **2**(4): 1066–1076 (1996). DOI: 10.1109/2944.577338. *Cited on pages 45, 75 & 132.*

[55] Pattanaporkratana, A., Park, C.S., Maclennan, J.E. and Clark, N.A. Direct measurement of interaction forces between islands on freely suspended smectic C films using multiple optical tweezers. *Ferroelectrics* **344**(1): 71–80 (2006). DOI: 10.1080/00150190600966862. *Cited on page 45.*

[56] Simmons, R.M., Finer, J.T., Chu, S. and Spudich, J.A. Quantitative measurements of force and displacement using an optical trap. *Biophysical Journal* **70**(4): 1813–1822 (1996). DOI: 10.1016/S0006-3495(96)79746-1. *Cited on pages 45 & 144.*

[57] Vermeulen, K.C., van Mameren, J., Stienen, G.J.M., Peterman, E.J.G., Wuite, G.J.L. and Schmidt, C.F. Calibrating bead displacements in optical tweezers using acousto-optic deflectors. *Review of Scientific Instruments* **77**(1): 013704–6 (2006). DOI: 10.1063/1.2165568. *Cited on page 45.*

[58] Valentine, M.T., Guydosh, N.R., Gutiérrez-Medina, B., Fehr, A.N., Andreasson, J.O. and Block, S.M. Precision steering of an optical trap by electro-optic deflection. *Optics Letters* **33**(6): 599–601 (2008). DOI: 10.1364/OL.33.000599. *Cited on page 45.*

[59] Greenleaf, W.J., Frieda, K.L., Abbondanzieri, E.A., Woodside, M.T. and Block, S.M. High-resolution single-molecule optical trapping measurements of transcription with basepair accuracy: instrumentation and methods. In Optical Trapping and Optical Micromanipulation IV (SPIE, San Diego, CA, USA, 2007), volume 6644, 664406–8. DOI: 10.1117/12.739631. *Cited on pages 45, 54 & 55.*

[60] Dufresne, E.R. and Grier, D.G. Optical tweezer arrays and optical substrates created with diffractive optics. *Review of Scientific Instruments* **69**(5): 1974–1977 (1998). DOI: 10.1063/1.1148883. *Cited on page 46.*

[61] MacDonald, M.P., Spalding, G.C. and Dholakia, K. Microfluidic sorting in an optical lattice. *Nature* **426**(6965): 421–424 (2003). DOI: 10.1038/nature02144. *Cited on page 46.*

[62] Curtis, J.E., Koss, B.A. and Grier, D.G. Dynamic holographic optical tweezers. *Optics Communications* **207**(1-6): 169–175 (2002). DOI: 10.1016/S0030-4018(02)01524-9. *Cited on pages 46 & 199.*

[63] Padgett, M. and Di Leonardo, R. Holographic optical tweezers and their relevance to lab on chip devices. *Lab on a Chip* **11**(7): 1196–1205 (2011). DOI: 10.1039/C0LC00526F. *Cited on pages 46 & 199.*

[64] Reicherter, M., Haist, T., Wagemann, E.U. and Tiziani, H.J. Optical particle trapping with computer-generated holograms written on a liquid-crystal display. *Optics Letters* **24**(9): 608–610 (1999). DOI: 10.1364/OL.24.000608. *Cited on page 46.*

[65] Liesener, J., Reicherter, M., Haist, T. and Tiziani, H.J. Multi-functional optical tweezers using computer-generated holograms. *Optics Communications* **185**(1-3): 77–82 (2000). DOI: 10.1016/S0030-4018(00)00990-1. *Cited on page 46.*

[66] Čižmár, T., Mazilu, M. and Dholakia, K. In situ wavefront correction and its application to micromanipulation. *Nature Photonics* **4**(6): 388–394 (2010). DOI: 10.1038/nphoton.2010.85. *Cited on page 46.*

[67] Whyte, G., Gibson, G., Leach, J., Padgett, M., Robert, D. and Miles, M. An optical trapped microhand for manipulating micron-sized objects. *Optics Express* **14**(25): 12497–12502 (2006). DOI: 10.1364/OE.14.012497. *Cited on page 46.*

[68] Pacoret, C., Bowman, R., Gibson, G., Haliyo, S., Carberry, D., Bergander, A., Regnier, S. and Padgett, M. Touching the microworld with force-feedback optical tweezers. *Optics Express* **17**(12): 10259–10264 (2009). DOI: `10.1364/OE.17.010259`. *Cited on page 46.*

[69] Preece, D., Bowman, R., Linnenberger, A., Gibson, G., Serati, S. and Padgett, M. Increasing trap stiffness with position clamping in holographic optical tweezers. *Optics Express* **17**(25): 22718–22725 (2009). DOI: `10.1364/OE.17.022718`. *Cited on pages 46 & 197.*

[70] Di Leonardo, R., Ianni, F. and Ruocco, G. Computer generation of optimal holograms for optical trap arrays. *Optics Express* **15**(4): 1913–1922 (2007). DOI: `10.1364/OE.15.001913`. *Cited on page 46.*

[71] Keshoju, K., Xing, H. and Sun, L. Magnetic field driven nanowire rotation in suspension. *Applied Physics Letters* **91**(12): 123114 (2007). DOI: `10.1063/1.2789184`. *Cited on page 47.*

[72] Neuman, K. Single-molecule micromanipulation techniques. *Annual review of materials science* **37**(1): 33–67 (2007). DOI: `10.1146/annurev.matsci.37.052506.084336`. *Cited on pages 47, 48, 53, 54 & 79.*

[73] Deniz, A.A., Mukhopadhyay, S. and Lemke, E.A. Single-molecule biophysics: at the interface of biology, physics and chemistry. *Journal of the Royal Society Interface* **5**(18): 15–45 (2008). DOI: `10.1098/rsif.2007.1021`. *Cited on pages 47, 48 & 53.*

[74] Leach, J., Mushfique, H., di Leonardo, R., Padgett, M. and Cooper, J. An optically driven pump for microfluidics. *Lab on a Chip* **6**(6): 735–739 (2006). DOI: `10.1039/b601886f`. *Cited on pages 47, 49, 51 & 196.*

[75] Asavei, T., Loke, V.L.Y., Barbieri, M., Nieminen, T.A., Heckenberg, N.R. and Rubinsztein-Dunlop, H. Optical angular momentum transfer to microrotors fabricated by two-photon photopolymerization. *New Journal of Physics* **11**(9): 093021 (2009). DOI: `10.1088/1367-2630/11/9/093021`. *Cited on pages 47 & 51.*

[76] Bishop, A.I., Nieminen, T.A., Heckenberg, N.R. and Rubinsztein-Dunlop, H. Optical microrheology using rotating laser-trapped particles. *Physical Review Letters* **92**(19): 198104 (2004). DOI: `10.1103/PhysRevLett.92.198104`. *Cited on pages 47, 49 & 51.*

[77] Parkin, Simon, J., Knoner, G., Nieminen, Timo, A., Heckenberg, Norman, R. and Rubinsztein-Dunlop, H. Picoliter viscometry using optically rotated particles. *Physical Review E: Statistical, Nonlinear, and Soft Matter Physics* **76**(4): 041507 (2007). DOI: `10.1103/PhysRevE.76.041507`. *Cited on pages 47, 49, 51, 52, 148, 149, 191 & 194.*

[78] Daria, V.R., Go, M.A. and Bachor, H.A. Simultaneous transfer of linear and orbital angular momentum to multiple low-index particles. *Journal of Optics* **13**(4): 044004 (2011). DOI: 10.1088/2040-8978/13/4/044004. *Cited on page 47.*

[79] Higurashi, E., Sawada, R. and Ito, T. Optically induced angular alignment of trapped birefringent micro-objects by linearly polarized light. *Physical Review E* **59**(3): 3676 (1999). DOI: 10.1103/PhysRevE.59.3676. *Cited on page 47.*

[80] Eriksen, R.L., Rodrigo, P.J., Daria, V.R. and Gluckstad, J. Spatial light modulator-controlled alignment and spinning of birefringent particles optically trapped in an array. *Applied Optics* **42**(25): 5107–5111 (2003). DOI: 10.1364/AO.42.005107. *Cited on page 49.*

[81] Parkin, S.J.W., Knoner, G., Nieminen, T.A., Heckenberg, N.R. and Rubinsztein-Dunlop, H. Microrheology of microlitre samples: probed with rotating optical tweezers. In Optical Trapping and Optical Micromanipulation IV (SPIE, San Diego, CA, USA, 2007), volume 6644, 66440. DOI: 10.1117/12.735492. *Cited on pages 49 & 51.*

[82] Zhong, M.C., Zhou, J.H., Ren, Y.X., Li, Y.M. and Wang, Z.Q. Rotation of birefringent particles in optical tweezers with spherical aberration. *Applied Optics* **48**(22): 4397–4402 (2009). DOI: 10.1364/AO.48.004397. *Cited on page 49.*

[83] Chen, L., Lee, S., Choo, J. and Lee, E.K. Continuous dynamic flow micropumps for microfluid manipulation. *Journal of Micromechanics and Microengineering* **18**(1): 013001 (2008). DOI: 10.1088/0960-1317/18/1/013001. *Cited on pages 49 & 52.*

[84] Manzo, C., Paparo, D., Marrucci, L. and Janossy, I. Light-induced rotation of dye-doped liquid crystal droplets. *Physical Review E* **73**(5): 051707 (2006). DOI: 10.1103/PhysRevE.73.051707. *Cited on pages 49 & 60.*

[85] Friese, M.E.J., Nieminen, T.A., Heckenberg, N.R. and Rubinsztein-Dunlop, H. Optical alignment and spinning of laser-trapped microscopic particles. *Nature* **394**(6691): 348–350 (1998). DOI: 10.1038/28566. *Cited on pages 49 & 51.*

[86] Yu, T., Cheong, F.C. and Sow, C.H. The manipulation and assembly of CuO nanorods with line optical tweezers. *Nanotechnology* **15**(12): 1732–1736 (2004). DOI: 10.1088/0957-4484/15/12/005. *Cited on page 49.*

[87] Zhang, J., Kim, H.I., Oh, C.H., Sun, X.D. and Lee, H. Multidimensional manipulation of carbon nanotube bundles with optical tweezers. *Applied Physics Letters* **88**(5): 053123 (2006). DOI: 10.1063/1.2172020. *Cited on page 49.*

[88] Zhang, J.L., Kim, T.G., Jeoung, S.C., Yao, F.F., Lee, H. and Sun, X.D. Controlled trapping and rotation of carbon nanotube bundle with optical tweezers. *Optics Communications* **267**(1): 260–263 (2006). DOI: 10.1016/j.optcom.2006.06.031. *Cited on page 49.*

[89] Khan, M., Sood, A.K., Mohanty, S.K., Gupta, P.K., Arabale, G.V., Vijaymo-hanan, K. and Rao, C.N.R. Optical trapping and transportation of carbon nanotubes made easy by decorating with palladium. *Optics Express* **14**(1): 424–429 (2006). DOI: `10.1364/OPEX.14.000424`. *Cited on page 49.*

[90] Tanaka, K., Yamabe, T. and Fukui, K. The Science and Technology of Carbon Nanotubes (Elsevier, 1999). *Cited on page 49.*

[91] Monthioux, M., Serp, P., Flahaut, E., Razafinimanana, M., Laurent, C., Peigney, A., Bacsa, W. and Broto, J.M. Introduction to Carbon Nanotubes. In B. Bhushan (editor), Springer Handbook of Nanotechnology (Springer Berlin Heidelberg, 2010), 47–118. Third edition. DOI: `10.1007/978-3-642-02525-9_3`. *Cited on page 49.*

[92] Král, P. and Sadeghpour, H.R. Laser spinning of nanotubes: A path to fast-rotating microdevices. *Physical Review B* **65**(16): 161401 (2002). DOI: `10.1103/PhysRevB.65.161401`. *Cited on page 49.*

[93] Khan, M., Sood, A.K., Deepak, F.L. and Rao, C.N.R. Optically driven nanorotors: Experiments and model calculations. *Journal of Nanoscience and Nanotechnology* **7**(6): 1800–1803 (2007). DOI: `10.1166/jnn.2007.719`. *Cited on page 50.*

[94] Mohanty, S.K., Gupta, P.K. and Verma, R.S. Self-rotation of an assembly of two or more, cylindrical objects in optical tweezers: A simple approach for realization of optically driven micromotors. *Current Science* **93**(5): 695–698 (2007). *Cited on pages 50 & 52.*

[95] Carberry, D.M. and et al. Calibration of optically trapped nanotools. *Nanotechnology* **21**(17): 175501 (2010). DOI: `10.1088/0957-4484/21/17/175501`. *Cited on page 50.*

[96] Phillips, D.B., Carberry, D.M., Simpson, S.H., Schäfer, H., Steinhart, M., Bowman, R., Gibson, G.M., Padgett, M.J., Hanna, S. and Miles, M.J. Optimizing the optical trapping stiffness of holographically trapped microrods using high-speed video tracking. *Journal of Optics* **13**(4): 044023 (2011). DOI: `10.1088/2040-8978/13/4/044023`. *Cited on page 50.*

[97] Friese, M.E.J., Rubinsztein-Dunlop, H., Gold, J., Hagberg, P. and Hanstorp, D. Optically driven micromachine elements. *Applied Physics Letters* **78**(4): 547–549 (2001). DOI: `10.1063/1.1339995`. *Cited on pages 50 & 51.*

[98] Metzger, N.K., Mazilu, M., Kelemen, L., Ormos, P. and Dholakia, K. Observation and simulation of an optically driven micromotor. *Journal of Optics* **13**(4): 044018 (2010). DOI: `10.1088/2040-8978/13/4/044018`. *Cited on page 51.*

[99] Neale, S.L., MacDonald, M.P., Dholakia, K. and Krauss, T.F. All-optical control of microfluidic components using form birefringence. *Nature Materials* **4**(7): 530–533 (2005). DOI: `10.1038/nmat1411`. *Cited on page 51.*

[100] Loke, V.L.Y., Asavei, T., Nieminen, T.A., Heckenberg, N.R. and Rubinsztein-Dunlop, H. Optical microrotors: theory, design and fabrication. In Optical Trapping and Optical Micromanipulation IV (SPIE, San Diego, CA, USA, 2007), volume 6644, 66440U–9. DOI: 10.1117/12.735341. *Cited on page 51.*

[101] Parkin, S., Knoner, G., Singer, W., Nieminen, T.A., Heckenberg, N.R. and Rubinsztein-Dunlop, H. Optical Torque on Microscopic Objects. In Laser Manipulation of Cells and Tissues (Elsevier Academic Press Inc., 2007), volume 82 of *Methods in Cell Biology*, 525–561. DOI: 10.1016/S0091-679X(06)82019-4. *Cited on page 51.*

[102] Asavei, T., Nieminen, T.A., Heckenberg, N.R. and Rubinsztein-Dunlop, H. Fabrication of microstructures for optically driven micromachines using two-photon photopolymerization of UV curing resins. *Journal of Optics A: Pure and Applied Optics* **11**(3): 034001 (2009). DOI: 10.1088/1464-4258/11/3/034001. *Cited on page 51.*

[103] Nieminen, T.A., Asavei, T., Loke, V.L.Y., Heckenberg, N.R. and Rubinsztein-Dunlop, H. Symmetry and the generation and measurement of optical torque. *Journal of Quantitative Spectroscopy and Radiative Transfer* **110**(14-16): 1472–1482 (2009). DOI: 10.1016/j.jqsrt.2009.03.013. *Cited on page 51.*

[104] Asavei, T., Nieminen, T.A., Heckenberg, N.R. and Rubinsztein-Dunlop, H. Use of shape induced birefringence for rotation in optical tweezers. In K. Dholakia and G.C. Spalding (editors), Optical Trapping and Optical Micromanipulation VII (SPIE, San Diego, California, USA, 2010), volume 7762, 77621C–8. DOI: 10.1117/12.861793. *Cited on page 51.*

[105] Whitesides, G.M. The origins and the future of microfluidics. *Nature* **442**(7101): 368–373 (2006). DOI: 10.1038/nature05058. *Cited on pages 51 & 52.*

[106] Hansen, C.L., Skordalakes, E., Berger, J.M. and Quake, S.R. A robust and scalable microfluidic metering method that allows protein crystal growth by free interface diffusion. *Proceedings of the National Academy of Sciences* **99**(26): 16531–16536 (2002). DOI: 10.1073/pnas.262485199. *Cited on page 51.*

[107] Zheng, B., Tice, J.D., Roach, L.S. and Ismagilov, R.F. A Droplet-Based, Composite PDMS/Glass Capillary Microfluidic System for Evaluating Protein Crystallization Conditions by Microbatch and Vapor-Diffusion Methods with On-Chip X-Ray Diffraction. *Angewandte Chemie International Edition* **43**(19): 2508–2511 (2004). DOI: 10.1002/anie.200453974. *Cited on page 51.*

[108] Shim, J.u., Cristobal, G., Link, D.R., Thorsen, T. and Fraden, S. Using Microfluidics to Decouple Nucleation and Growth of Protein Crystals. *Crystal Growth & Design* **7**(11): 2192–2194 (2007). DOI: 10.1021/cg700688f. *Cited on page 51.*

[109] Boer, G., Johann, R., Rohner, J., Merenda, F., Delacretaz, G., Renaud, P. and Salathe, R.P. Combining multiple optical trapping with microflow manipulation for the rapid bioanalytics on microparticles in a chip. *Review of Scientific Instruments* **78**(11): 116101 (2007). DOI: 10.1063/1.2804768. *Cited on page 52.*

[110] Yager, P., Edwards, T., Fu, E., Helton, K., Nelson, K., Tam, M.R. and Weigl, B.H. Microfluidic diagnostic technologies for global public health. *Nature* **442**(7101): 412–418 (2006). DOI: `10.1038/nature05064`. *Cited on pages 52 & 53.*

[111] Applegate, R.W., Schafer, D.N., Amir, W., Squier, J., Vestad, T., Oakey, J. and Marr, D.W.M. Optically integrated microfluidic systems for cellular characterization and manipulation. *Journal of Optics A: Pure and Applied Optics* **9**(8): S122–S128 (2007). DOI: `10.1088/1464-4258/9/8/S03`. *Cited on page 52.*

[112] Lin, C.C., Chen, A. and Lin, C.H. Microfluidic cell counter/sorter utilizing multiple particle tracing technique and optically switching approach. *Biomedical Microdevices* **10**(1): 55–63 (2008). DOI: `10.1007/s10544-007-9109-8`. *Cited on page 52.*

[113] Williams, M.C. Optical Tweezers: Measuring Piconewton Forces (2002). Electronic Resource. Date Accessed: April 11, 2011 URL: `biophysics.org/Portals/1/PDFs/Education/williams.pdf`. *Cited on pages 53 & 68.*

[114] Coirault, C., Pourny, J.C., Lambert, F. and Lecarpentier, Y. Optical tweezers in biology and medicine. *M S: Medecine Sciences* **19**(3): 364–367 (2003). DOI: `10.1051/medsci/2003193364`. *Cited on page 53.*

[115] Thalhammer, S. Laser microtools in cell biology and molecular medicine. *Laser physics* **13**(5): 681–691 (2003). *Cited on page 53.*

[116] Toner, M. Blood-on-a-chip. *Annual review of biomedical engineering* **7**(1): 77–103 (2005). DOI: `10.1146/annurev.bioeng.7.011205.135108`. *Cited on page 53.*

[117] Neuman, K.C. and Nagy, A. Single-molecule force spectroscopy: optical tweezers, magnetic tweezers and atomic force microscopy. *Nature Methods* **5**(6): 491–505 (2008). DOI: `10.1038/nmeth.1218`. *Cited on page 53.*

[118] Woodside, M.T. and Valentine, M.T. Single-Molecule Manipulation Using Optical Traps. In P. Hinterdorfer and A. Oijen (editors), Handbook of Single-Molecule Biophysics (Springer New York, 2009), 341–370. DOI: `10.1007/978-0-387-76497-9_12`. *Cited on pages 53, 54, 75 & 145.*

[119] Roberts, N.W. and Needham, M.G. A mechanism of polarized light sensitivity in cone Photoreceptors of the goldfish Carassius auratus. *Biophysical Journal* **93**(9): 3241–3248 (2007). DOI: `10.1529/biophysj.107.112292`. *Cited on page 53.*

[120] Alexander, T., Pellegrino, P.M. and Gillespie, J.B. Near-infrared surface-enhanced-Raman-scattering-mediated detection of single optically trapped bacterial spores. *Applied Spectroscopy* **57**(11): 1340–1345 (2003). DOI: `10.1366/000370203322554482`. *Cited on page 53.*

[121] Svoboda, K., Schmidt, C.F., Schnapp, B.J. and Block, S.M. Direct observation of kinesin stepping by optical trapping interferometry. *Nature* **365**(6448): 721–727 (1993). DOI: `10.1038/365721a0`. *Cited on page 53.*

[122] Allersma, M.W., Gittes, F., deCastro, M.J., Stewart, R.J. and Schmidt, C.F. Two-dimensional tracking of ncd motility by back focal plane interferometry. *Biophysical Journal* **74**(2): 1074–1085 (1998). DOI: `10.1016/S0006-3495(98)74031-7`. *Cited on pages 53, 69, 77, 115 & 116.*

[123] Abbondanzieri, E.A., Greenleaf, W.J., Shaevitz, J.W., Landick, R. and Block, S.M. Direct observation of base-pair stepping by RNA polymerase. *Nature* **438**(7067): 460–465 (2005). DOI: `10.1038/nature04268`. *Cited on page 54.*

[124] Perkins, T.T. Optical traps for single molecule biophysics: a primer. *Laser & Photonics Reviews* **3**(1-2): 203–220 (2009). DOI: `10.1002/lpor.200810014`. *Cited on page 55.*

[125] Greenleaf, W.J. and Block, S.M. Single-Molecule, Motion-Based DNA Sequencing Using RNA Polymerase. *Science* **313**(5788): 801 (2006). DOI: `10.1126/science.1130105`. *Cited on page 55.*

[126] Huisstede, J.H.G., Subramaniam, V. and Bennink, M.L. Combining optical tweezers and scanning probe microscopy to study DNA-protein interactions. *Microscopy Research and Technique* **70**(1): 26–33 (2007). DOI: `10.1002/jemt.20382`. *Cited on page 55.*

[127] Mao, H.B. and Luchette, P. An integrated laser-tweezers instrument for micro-analysis of individual protein aggregates. *Sensors and Actuators B: Chemical* **129**(2): 764–771 (2008). DOI: `10.1016/j.snb.2007.09.052`. *Cited on page 55.*

[128] Chen, Y.F., Blab, G.A. and Meiners, J.C. Stretching Submicron Biomolecules with Constant-Force Axial Optical Tweezers. *Biophysical Journal* **96**(11): 4701–4708 (2009). DOI: `10.1016/j.bpj.2009.03.009`. *Cited on page 55.*

[129] Fernandes, H.P., Fontes, A., de Thomaz, A.A., Barbosa, L.C., Barjas-Castro, M.L. and Cesar, C.L. Studying red blood cell agglutination by measuring membrane viscosity with optical tweezers. In Optical Trapping and Optical Micromanipulation IV (SPIE, San Diego, CA, USA, 2007), volume 6644, 66440M–7. DOI: `10.1117/12.734284`. *Cited on page 55.*

[130] Fontes, A., Barjas Castro, M.L., Brandão, M.M., Fernades, H.P., Thomaz, A.A., Huruta, R.R., Pozzo, L.Y., Barbosa, L.C., Costa, F.F., Saad, S.T.O. and Cesar, C.L. Mechanical and electrical properties of red blood cells using optical tweezers. *Journal of Optics* **13**(4): 044012 (2011). DOI: `10.1088/2040-8978/13/4/044012`. *Cited on page 55.*

[131] Ghosh, A., Sinha, S., Dharmadhikari, J.A., Roy, S., Dharmadhikari, A.K., Samuel, J., Sharma, S. and Mathur, D. Euler buckling-induced folding and rotation of red blood cells in an optical trap. *Physical Biology* **3**(1): 67 (2006). DOI: `10.1088/1478-3975/3/1/007`. *Cited on page 55.*

[132] Saraogi, V., Padmapriya, P., Paul, A., Tatu, U.S. and Natarajan, V. Change in spectrum of Brownian fluctuations of optically trapped red blood cells due

to malarial infection. *Journal of Biomedical Optics* **15**(3): 037003 (2010). DOI: `10.1117/1.3427142`. *Cited on page 56.*

[133] Appleyard, D.C. and Lang, M.J. Active particle control through silicon using conventional optical trapping techniques. *Lab on a Chip* **7**(12): 1837–1840 (2007). DOI: `10.1039/b711507e`. *Cited on page 56.*

[134] Ohta, A.T., Chiou, P.Y., Han, T.H., Liao, J.C., Bhardwaj, U., McCabe, E.R.B., Yu, F.Q., Sun, R. and Wu, M.C. Dynamic cell and microparticle control via optoelectronic tweezers. *Journal of Microelectromechanical Systems* **16**(3): 491–499 (2007). DOI: `10.1109/JMEMS.2007.896717`. *Cited on page 56.*

[135] Andersson, M., Madgavkar, A., Stjerndahl, M., Wu, Y., Tan, W., Duran, R., Niehren, S., Mustafa, K., Arvidson, K. and Wennerberg, A. Using optical tweezers for measuring the interaction forces between human bone cells and implant surfaces: System design and force calibration. *Review of Scientific Instruments* **78**(7): 074302–8 (2007). DOI: `10.1063/1.2752606`. *Cited on pages 56 & 128.*

[136] Wang, M. Optical forces for noninvasive cellular analysis. *Applied optics* **42**(28): 5765–5773 (2003). DOI: `10.1364/AO.42.005765`. *Cited on page 56.*

[137] Guck, J., Ananthakrishnan, R., Mahmood, H., Moon, T.J., Cunningham, C.C. and Käs, J. The optical stretcher: A novel laser tool to micromanipulate cells. *Biophysical Journal* **81**(2): 767–784 (2001). DOI: `10.1016/S0006-3495(01)75740-2`. *Cited on page 56.*

[138] Guck, J., Schinkinger, S., Lincoln, B., Wottawah, F., Ebert, S., Romeyke, M., Lenz, D., Erickson, H.M., Ananthakrishnan, R., Mitchell, D., Käs, J., Ulvick, S. and Bilby, C. Optical deformability as an inherent cell marker for testing malignant transformation and metastatic competence. *Biophysical Journal* **88**(5): 3689–3698 (2005). DOI: `10.1529/biophysj.104.045476`. *Cited on page 56.*

[139] Capitanio, M., Maggi, D., Vanzi, F. and Pavone, F.S. FIONA in the trap: the advantages of combining optical tweezers and fluorescence. *Journal of Optics A: Pure and Applied Optics* **9**(8): S157–S163 (2007). DOI: `10.1088/1464-4258/9/8/S07`. *Cited on page 57.*

[140] Xie, C.G. and Li, Y.Q. Raman spectra and optical trapping of highly refractive and nontransparent particles. *Applied Physics Letters* **81**(6): 951–953 (2002). DOI: `10.1063/1.1497437`. *Cited on page 57.*

[141] Petrov, D.V. Raman spectroscopy of optically trapped particles. *Journal of Optics A: Pure and Applied Optics* **9**(8): S139–S156 (2007). DOI: `10.1088/1464-4258/9/8/S06`. *Cited on page 57.*

[142] Heng, X., Hsiao, E., Psaltis, D. and Yang, C. An optical tweezer actuated, nanoaperture-grid based Optofluidic Microscope implementation method. *Optics Express* **15**(25): 16367–16375 (2007). DOI: `10.1364/OE.15.016367`. *Cited on page 57.*

[143] Juan, M.L., Righini, M. and Quidant, R. Plasmon nano-optical tweezers. *Nature Photonics* **5**(6): 349–356 (2011). DOI: `10.1038/nphoton.2011.56`. *Cited on pages 57 & 58.*

[144] Grigorenko, A. Mind the trap. *Nature Photonics* **2**(6): 382–382 (2008). DOI: `10.1038/nphoton.2008.98`. Interview by Amber Jenkins. *Cited on page 58.*

[145] Righini, M., Girard, C. and Quidant, R. Light-induced manipulation with surface plasmons. *Journal of Optics A: Pure and Applied Optics* **10**(9): 093001 (2008). DOI: `10.1088/1464-4258/10/9/093001`. *Cited on page 58.*

[146] Righini, M., Volpe, G., Girard, C., Petrov, D. and Quidant, R. Surface Plasmon Optical Tweezers: Tunable Optical Manipulation in the Femtonewton Range. *Physical Review Letters* **100**(18): 186804 (2008). DOI: `10.1103/PhysRevLett.100.186804`. *Cited on page 58.*

[147] Righini, M., Zelenina, A.S., Girard, C. and Quidant, R. Parallel and selective trapping in a patterned plasmonic landscape. *Nature Physics* **3**(7): 477–480 (2007). DOI: `10.1038/nphys624`. *Cited on page 58.*

[148] Grigorenko, A.N., Roberts, N.W., Dickinson, M.R. and Zhang, Y. Nanometric optical tweezers based on nanostructured substrates. *Nature Photonics* **2**(6): 365–370 (2008). DOI: `10.1038/nphoton.2008.78`. *Cited on page 58.*

[149] Mohanty, S. Liquid crystals – The fourth phase of matter. *Resonance* **8**(11): 52–70 (2003). DOI: `10.1007/BF02837958`. *Cited on pages 58, 87 & 95.*

[150] Lavrentovich, O.D. Polarization Microscope Images of Liquid Crystals (2010). Electronic Resource. Date Accessed: May 9, 2011. URL: `www.nsf.gov/news/mmg/index.cfm`. *Cited on page 59.*

[151] Castellano, J.A. Liquid Gold: The Story of Liquid Crystal Displays and the Creation of an Industry (World Scientific Publishing Company, 2005). Page 274. *Cited on page 59.*

[152] Smalyukh, I., Kuzmin, A.N., Kachynski, A.V., Prasad, P.N. and Lavrentovich, O.D. Optical trapping of colloidal particles and measurement of the defect line tension and colloidal forces in a thermotropic nematic liquid crystal. *Applied Physics Letters* **86**(2): 021913 (2005). DOI: `10.1063/1.1849839`. *Cited on pages 60 & 168.*

[153] Smalyukh, I., Senyuk, B.I., Shiyanovskii, S.V., Lavrentovich, O.D., Kuzmin, A.N., Kachynski, A.V. and Prasad, P.N. Optical trapping, manipulation, and 3D imaging of disclinations in liquid crystals and measurement of their line tension. *Molecular Crystals and Liquid Crystals* **450**(1): 279–295 (2006). DOI: `10.1080/15421400600587787`. *Cited on pages 60 & 178.*

[154] Smalyukh, I., Kaputa, D.S., Kachynski, A.V., Kuzmin, A.N. and Prasad, P.N. Optical trapping of director structures and defects in liquid crystals using laser tweezers. *Optics Express* **15**(7): 4359–4371 (2007). DOI: `10.1364/OE.15.004359`. *Cited on page 60.*

[155] Trivedi, R.P., Engström, D. and Smalyukh, I.I. Optical manipulation of colloids and defect structures in anisotropic liquid crystal fluids. *Journal of Optics* **13**(4): 044001 (2011). DOI: `10.1088/2040-8978/13/4/044001`. *Cited on pages 60, 97, 165 & 174.*

[156] Hasnain, I.A. and Donald, A.M. Microrheological characterization of anisotropic materials. *Physical Review E* **73**(3): 031901 (2006). DOI: `10.1103/PhysRevE.73.031901`. *Cited on pages 60 & 117.*

[157] Kawamura, M., Ye, M. and Sato, S. Optical trapping and manipulation system using liquid-crystal lens with focusing and deflection properties. *Japanese Journal of Applied Physics Part 1: Regular Papers Brief Communications and Review Papers* **44**(8): 6098–6100 (2005). DOI: `10.1143/JJAP.44.6098`. *Cited on page 60.*

[158] Hands, P.J.W., Tatarkova, S.A., Kirby, A.K. and Love, G.D. Modal liquid crystal devices in optical tweezing: 3D control and oscillating potential wells. *Optics Express* **14**(10): 4525–4537 (2006). DOI: `10.1364/OE.14.004525`. *Cited on page 60.*

[159] Hands, P.J.W., Tatarkova, S.A., Kirby, A.K. and Love, G.D. Optical tweezing beam control using liquid crystal adaptive optical elements. In Optical Trapping and Optical Micromanipulation III (SPIE, San Diego, CA, USA, 2006), volume 6326, 63262U–8. DOI: `10.1117/12.679421`. *Cited on page 60.*

[160] Pasechnik, S.V., Chigrinov, V.G. and Shmeliova, D.V. Liquid Crystals (Wiley-VCH, 2009). Page 170. *Cited on page 60.*

[161] Tamai, N., Ito, T. and Masuhara, H. Second- and third-harmonic generation from optically trapped liquid crystal droplet. *Japanese Journal of Applied Physics Part 2: Letters* **35**(5A): L547–L550 (1996). DOI: `10.1143/JJAP.35.L547`. *Cited on page 60.*

[162] Juodkazis, S., Shikata, M., Takahashi, T., Matsuo, S. and Misawa, H. Fast optical switching by a laser-manipulated microdroplet of liquid crystal. *Applied Physics Letters* **74**(24): 3627–3629 (1999). DOI: `10.1063/1.123203`. *Cited on page 60.*

[163] Juodkazis, S., Shikata, M., Takahashi, T., Matsuo, S. and Misawa, H. Size dependence of rotation frequency of individual laser trapped liquid crystal droplets. *Japanese Journal of Applied Physics Part 2: Letters* **38**(5A): L518–L520 (1999). DOI: `10.1143/JJAP.38.L518`. *Cited on page 60.*

[164] Juodkazis, S., Matsuo, S., Murazawa, N., Hasegawa, I. and Misawa, H. High-efficiency optical transfer of torque to a nematic liquid crystal droplet. *Applied Physics Letters* **82**(26): 4657–4659 (2003). DOI: `10.1063/1.1588366`. *Cited on page 60.*

[165] Murazawa, N., Juodkazis, S., Matsuo, S. and Misawa, H. Control of the molecular alignment inside liquid-crystal droplets by use of laser tweezers. *Small* **1**(6): 656–661 (2005). DOI: `10.1002/smll.200500038`. *Cited on page 60.*

[166] Wood, T.A., Gleeson, H.F., Dickinson, M.R. and Wright, A.J. Mechanisms of optical angular momentum transfer to nematic liquid crystalline droplets. *Applied Physics Letters* **84**(21): 4292–4294 (2004). DOI: 10.1063/1.1753067. *Cited on pages 60 & 63.*

[167] Gleeson, H.F., Wood, T.A. and Dickinson, M. Laser manipulation in liquid crystals: an approach to microfluidics and micromachines. *Philosophical Transactions of the Royal Society A: Mathematical, Physical and Engineering Sciences* **364**(1847): 2789–2805 (2006). DOI: 10.1098/rsta.2006.1855. *Cited on pages 60, 61, 63, 93, 167, 169, 178, 182, 183 & 192.*

[168] Wood, T.A. Optical trapping and liquid crystals. Ph.D. thesis, The University of Manchester (2004). *Cited on pages 60, 63, 93, 96, 106, 110, 132, 134, 164, 165 & 167.*

[169] Yang, Y., Brimicombe, P.D., Roberts, N.W., Dickinson, M.R., Osipov, M. and Gleeson, H.F. Continuously rotating chiral liquid crystal droplets in a linearly polarized laser trap. *Optics Express* **16**(10): 6877–6882 (2008). DOI: 10.1364/OE.16.006877. *Cited on pages 60 & 63.*

[170] Murazawa, N., Juodkazis, S. and Misawa, H. Laser manipulation of a smectic liquid-crystal droplet. *European Physical Journal E* **20**(4): 435–439 (2006). DOI: 10.1140/epje/i2006-10033-1. *Cited on page 60.*

[171] Ito, K. and Kimura, M. Optically Induced Rotation of Microcylinders Made of Photopolymerizable Nematic Liquid Crystal. *Japanese Journal of Applied Physics* **49**(4): 040208 (2010). DOI: 10.1143/JJAP.49.040208. *Cited on page 60.*

[172] Murazawa, N., Juodkazis, S., Jarutis, V., Tanamura, Y. and Misawa, H. Viscosity measurement using a rotating laser-trapped microsphere of liquid crystal. *Europhysics Letters* **73**(5): 800–805 (2006). DOI: 10.1209/epl/i2005-10457-7. *Cited on page 61.*

[173] Murazawa, N., Juodkazis, S., Tanamura, Y. and Misawa, H. Rheology measurement at liquid-crystal water interface using laser tweezers. *Japanese Journal of Applied Physics Part 1: Regular Papers Brief Communications and Review Papers* **45**(2A): 977–982 (2006). DOI: 10.1143/JJAP.45.977. *Cited on page 61.*

[174] Abedin, K.S., Kerbage, C., Fernandez-Nieves, A. and Weitz, D.A. Optical manipulation and rotation of liquid crystal drops using high-index fiber-optic tweezers. *Applied Physics Letters* **91**(9): 091119 (2007). DOI: 10.1063/1.2775321. *Cited on page 61.*

[175] Brasselet, E., Murazawa, N., Juodkazis, S. and Misawa, H. Statics and dynamics of radial nematic liquid-crystal droplets manipulated by laser tweezers. *Physical Review E* **77**(4): 041704 (2008). DOI: 10.1103/PhysRevE.77.041704. *Cited on page 61.*

[176] Škarabot, M., Ravnik, M., Babič, D., Osterman, N., Poberaj, I., Žumer, S., Muševič, I., Nych, A., Ognysta, U. and Nazarenko, V. Laser trapping of low refractive

index colloids in a nematic liquid crystal. *Physical Review E* **73**(2): 021705 (2006). DOI: `10.1103/PhysRevE.73.021705`. *Cited on pages 61, 95 & 201.*

[177] Poulin, P., Stark, H., Lubensky, T.C. and Weitz, D.A. Novel colloidal interactions in anisotropic fluids. *Science* **275**(5307): 1770–1773 (1997). DOI: `10.1126/science.275.5307.1770`. *Cited on page 61.*

[178] Poulin, P. Novel phases and colloidal assemblies in liquid crystals. *Current Opinion in Colloid & Interface Science* **4**(1): 66–71 (1999). DOI: `10.1016/S1359-0294(99)00009-6`. *Cited on page 61.*

[179] Meeker, S.P., Poon, W.C.K., Crain, J. and Terentjev, E.M. Colloid-liquid-crystal composites: An unusual soft solid. *Physical Review E* **61**(6): R6083 (2000). DOI: `10.1103/PhysRevE.61.R6083`. *Cited on page 61.*

[180] Iwashita, Y. and Tanaka, H. Optical manipulation of defects in a lyotropic lamellar phase. *Physical Review Letters* **90**(4): 045501 (2003). DOI: `10.1103/PhysRevLett.90.045501`. *Cited on page 61.*

[181] Yada, M., Yamamoto, J. and Yokoyama, H. Direct observation of anisotropic interparticle forces in nematic colloids with optical tweezers. *Physical Review Letters* **92**(18): 185501 (2004). DOI: `10.1103/PhysRevLett.92.185501`. *Cited on page 61.*

[182] Muševič, I., Škarabot, M., Babič, D., Osterman, N., Poberaj, I., Nazarenko, V. and Nych, A. Laser trapping of small colloidal particles in a nematic liquid crystal: Clouds and ghosts. *Physical Review Letters* **93**(18): 187801 (2004). DOI: `10.1103/PhysRevLett.93.187801`. *Cited on pages 61, 95, 186 & 201.*

[183] Lev, B., Nych, A., Ognysta, U., Chernyshuk, S.B., Nazarenko, V., Skarabot, M., Poberaj, I., Babic, D., Osterman, N. and Musevic, I. Anisotropic laser trapping in nematic colloidal dispersion. *European Physical Journal E* **20**(2): 215–219 (2006). DOI: `10.1140/epje/i2006-10015-3`. *Cited on pages 61 & 201.*

[184] Smalyukh, I., Kachynski, A.V., Kuzmin, A.N. and Prasad, P.N. Laser trapping in anisotropic fluids and polarization-controlled particle dynamics. *Proceedings of the National Academy of Sciences of the United States of America* **103**(48): 18048–18053 (2006). DOI: `10.1073/pnas.0608698103`. *Cited on pages 62, 168, 169, 174 & 185.*

[185] Tatarkova, S.A., Burnham, D.R., Kirby, A.K., Love, G.D. and Terentjev, E.M. Colloidal Interactions and Transport in Nematic Liquid Crystals. *Physical Review Letters* **98**(15): 157801 (2007). DOI: `10.1103/PhysRevLett.98.157801`. *Cited on page 62.*

[186] Kumar, A. Calculation of optical parameters of liquid crystals. *Acta Physica Polonica A* **112**(6): 1213–1221 (2007). *Cited on page 62.*

[187] Miesowicz, M. Liquid Crystals in my Memories and Now – the Role of Anisotropic Viscosity in Liquid Crystals Research. *Molecular Crystals and Liquid Crystals* **97**(1-4): 1–11 (1983). DOI: `10.1080/00268948308073137`. *Cited on page 62.*

[188] Smith, N.J., Tillin, M.D. and Sambles, J.R. Direct optical quantification of backflow in a 90 degrees twisted nematic cell. *Physical Review Letters* **88**(8): 088301 (2002). DOI: `10.1103/PhysRevLett.88.088301`. *Cited on page 62.*

[189] Pasechnik, S.V., Chigrinov, V.G., Shmeliova, D.V., Tsvetkov, V.A. and Voronov, A.N. Anisotropic shear viscosity in nematic liquid crystals: new optical measurement method. *Liquid Crystals* **31**(4): 585–592 (2004). DOI: `10.1080/02678290410001667371`. *Cited on pages 62, 63, 169, 182, 183 & 192.*

[190] Mieda, Y. and Furutani, K. Micromanipulation method using backflow effect of liquid crystals. In 2006 IEEE International Symposium on Micro-NanoMechatronics and Human Science (Nagoya, JAPAN, 2006), 208–213. DOI: `10.1109/MHS.2006.320279`. *Cited on page 62.*

[191] Vanbrabant, P.J.M., Dessaud, N. and Stromer, J.F. Temperature influence on the dynamics of vertically aligned liquid crystal displays. *Applied Physics Letters* **92**(9): 091101 (2008). DOI: `10.1063/1.2889448`. *Cited on page 63.*

[192] Kneppe, H. and Schneider, F. Determination of the viscosity coefficients of the liquid-crystal MBBA. *Molecular Crystals and Liquid Crystals* **65**(1-2): 23–37 (1981). DOI: `10.1080/00268948108076128`. *Cited on page 63.*

[193] Graf, H.H., Kneppe, H. and Schneider, F. Shear and rotational viscosity coefficients of two nematic liquid crystals. *Molecular Physics: An International Journal at the Interface Between Chemistry and Physics* **77**(3): 521–538 (1992). DOI: `10.1080/00268979200102591`. *Cited on page 63.*

[194] Stark, H. and Ventzki, D. Non-linear Stokes drag of spherical particles in a nematic solvent. *Europhysics Letters* **57**(1): 60 (2002). DOI: `10.1209/epl/i2002-00541-0`. *Cited on page 63.*

[195] Loudet, J.C., Hanusse, P. and Poulin, P. Stokes drag on a sphere in a nematic liquid crystal. *Science* **306**(5701): 1525–1525 (2004). DOI: `10.1126/science.1102864`. *Cited on page 63.*

[196] Verhoeff, A.A., van Rijssel, J., de Villeneuve, V.W.A. and Lekkerkerker, H.N.W. Orientation dependent Stokes drag in a colloidal liquid crystal. *Soft Matter* **4**(8): 1602–1604 (2008). DOI: `10.1039/b804236e`. *Cited on page 63.*

[197] Sanders, J.L., Dickinson, M.R. and Gleeson, H.F. Laser tweezers for determining anisotropic viscosity coefficients of nematic liquid crystals. In G.C. Spalding and K. Dholakia (editors), Optical Trapping and Optical Micromanipulation VII (SPIE, San Diego, California, USA, 2010), volume 7762, 776221–9. DOI: `10.1117/12.862853`. *Cited on pages 63 & 79.*

[198] Takahashi, K., Ichikawa, M. and Kimura, Y. Direct measurement of force between colloidal particles in a nematic liquid crystal. *Journal of Physics: Condensed Matter* **20**(7) (2008). DOI: `10.1088/0953-8984/20/7/075106`. *Cited on page 63.*

[199] Shahzamanian, M.A. and Shoarinejad, S. Dynamics of two colloidal particles immersed in a nematic liquid crystal. *Journal of Physics: Condensed Matter* **19**(15): 156101 (2007). DOI: `10.1088/0953-8984/19/15/156101`. *Cited on page 63.*

[200] Smalyukh, I., Lavrentovich, O.D., Kuzmin, A.N., Kachynski, A.V. and Prasad, P.N. Elasticity-mediated self-organization and colloidal interactions of solid spheres with tangential anchoring in a nematic liquid crystal. *Physical Review Letters* **95**: 157801 (2005). DOI: `10.1103/PhysRevLett.95.157801`. *Cited on pages 63, 167, 168 & 169.*

[201] Kondo, N., Iwashita, Y. and Kimura, Y. Dependence of interparticle force on temperature and cell thickness in nematic colloids. *Physical Review E* **82**(2): 020701 (2010). DOI: `10.1103/PhysRevE.82.020701`. *Cited on page 64.*

[202] Kotar, J., Babic, D., Vilfan, M., Copic, M. and Poberaj, I. Magneto-optic tweezers studies of interactions in liquid crystal colloids. *Molecular Crystals and Liquid Crystals* **450**(1): 297–304 (2006). DOI: `10.1080/15421400600587837`. *Cited on page 64.*

[203] Dierking, I., Biddulph, G. and Matthews, K. Electromigration of microspheres in nematic liquid crystals. *Physical Review E* **73**(1): 011702 (2006). DOI: `10.1103/PhysRevE.73.011702`. *Cited on page 64.*

[204] Škarabot, M., Tkalec, U. and Muševič, I. Transport and crystallization of colloidal particles in a thin nematic cell. *European Physical Journal E* **24**(1): 99–107 (2007). DOI: `10.1140/epje/i2007-10218-0`. *Cited on page 64.*

[205] Dierking, I., Cass, P., Syres, K., Cresswell, R. and Morton, S. Electromigration of microspheres in ferroelectric smectic liquid crystals. *Physical Review E* **76**(2): 021707 (2007). DOI: `10.1103/PhysRevE.76.021707`. *Cited on page 64.*

[206] Fischer, M. and Berg-Sørensen, K. Calibration of trapping force and response function of optical tweezers in viscoelastic media. *Journal of Optics A: Pure and Applied Optics* **9**(8): S239–S250 (2007). DOI: `10.1088/1464-4258/9/8/S18`. *Cited on pages 65 & 169.*

[207] Pralle, A., Prummer, M., Florin, E.L., Stelzer, E.H.K. and Horber, J.K.H. Three-dimensional high-resolution particle tracking for optical tweezers by forward scattered light. *Microscopy Research and Technique* **44**(5): 378–386 (1999). DOI: `10.1002/(SICI)1097-0029(19990301)44:5<378::AID-JEMT10>3.0.CO;2-Z`. *Cited on page 68.*

[208] Rohrbach, A. and Stelzer, E.H.K. Three-dimensional position detection of optically trapped dielectric particles. *Journal of Applied Physics* **91**(8): 5474–5488 (2002). DOI: `10.1063/1.1459748`. *Cited on page 68.*

[209] van Mameren-Schotvanger, J. Integrating single-molecule visualization and DNA micromanipulation. Ph.D. thesis, Vrije Universiteit Amsterdam (2008). *Cited on pages 68 & 71.*

[210] Nieminen, T.A., Knoner, G., Heckenberg, N.R. and Rubinsztein-Dunlop, H. Physics of optical tweezers. In Laser Manipulation of Cells and Tissues (Elsevier Academic Press Inc., 2007), volume 82 of *Methods in Cell Biology*, 207–236. DOI: `10.1016/S0091-679X(06)82006-6`. *Cited on page 68.*

[211] Ashkin, A. Forces of a single-beam gradient laser trap on a dielectric sphere in the ray optics regime. *Biophysical Journal* **61**(2): 569–582 (1992). DOI: `10.1016/S0006-3495(92)81860-X`. *Cited on pages 69, 70, 71 & 84.*

[212] Svoboda, K. and Block, S.M. Biological Applications of Optical Forces. *Annual Review of Biophysics and Biomolecular Structure* **23**(1): 247–285 (1994). DOI: `10.1146/annurev.bb.23.060194.001335`. *Cited on pages 69, 70 & 107.*

[213] Chiou, A., Wei, M.T., Chen, Y.Q., Tseng, T.Y., Liu, S.L., Karmenyan, A. and Lin, C.H. Optical Trapping and Manipulation for Biomedical Applications Biophotonics. In L. Pavesi and P.M. Fauchet (editors), Biophotonics (Springer Berlin Heidelberg, 2008), Biological and Medical Physics, Biomedical Engineering, 249–273. DOI: `10.1007/978-3-540-76782-4_14`. *Cited on page 69.*

[214] Keen, S., Leach, J., Gibson, G. and Padgett, M.J. Comparison of a high-speed camera and a quadrant detector for measuring displacements in optical tweezers. *Journal of Optics A: Pure and Applied Optics* **9**(8): S264–S266 (2007). DOI: `10.1088/1464-4258/9/8/S21`. *Cited on page 73.*

[215] Florin, E.L., Pralle, A., Stelzer, E.H.K. and Horber, J.K.H. Photonic force microscope calibration by thermal noise analysis. *Applied Physics A: Materials Science and Processing* **66**: S75–S78 (1998). DOI: `10.1007/s003390051103`. *Cited on page 74.*

[216] Gittes, F. and Schmidt, C.F. Chapter 8 Signals and Noise in Micromechanical Measurements. In M.P. Sheetz (editor), Methods in Cell Biology (Academic Press, 1997), volume 55, 129–156. DOI: `10.1016/S0091-679X(08)60406-9`. *Cited on pages 77, 78 & 79.*

[217] Gibson, G.M., Leach, J., Keen, S., Wright, A.J. and Padgett, M.J. Measuring the accuracy of particle position and force in optical tweezers using high-speed video microscopy. *Optics Express* **16**(19): 14561–14570 (2008). DOI: `10.1364/OE.16.014561`. *Cited on pages 79, 80 & 117.*

[218] Hester, B.C., Crawford, A., Kishore, R.B., Helmerson, K., Halas, N.J. and Levin, C. Optical trapping of nanoshells. In Optical Trapping and Optical Micromanipulation IV (SPIE, San Diego, CA, USA, 2007), volume 6644, 66441B. DOI: `10.1117/12.735276`. *Cited on page 79.*

[219] Li, M. and Arlt, J. Trapping multiple particles in single optical tweezers. *Optics Communications* **281**(1): 135–140 (2008). DOI: `10.1016/j.optcom.2007.09.032`. *Cited on page 79.*

[220] Otto, O., Gutsche, C., Kremer, F. and Keyser, U.F. Optical tweezers with 2.5 kHz bandwidth video detection for single-colloid electrophoresis. *Review of Scientific Instruments* **79**(2): 023710–6 (2008). DOI: `10.1063/1.2884147`. *Cited on page 79.*

[221] Pesce, G., De Luca, A.C., Rusciano, G., Netti, P.A., Fusco, S. and Sasso, A. Microrheology of complex fluids using optical tweezers: a comparison with macrorheological measurements. *Journal of Optics A: Pure and Applied Optics* **11**(3): 034016 (2009). DOI: `10.1088/1464-4258/11/3/034016`. *Cited on page 79.*

[222] Wong, W.P. and Halvorsen, K. The effect of integration time on fluctuation measurements: calibrating an optical trap in the presence of motion blur. *Optics Express* **14**(25): 12517–12531 (2006). DOI: `10.1364/OE.14.012517`. *Cited on pages 79 & 135.*

[223] Czerwinski, F., Richardson, A.C. and Oddershede, L.B. Quantifying Noise in Optical Tweezers by Allan Variance. *Optics Express* **17**(15): 13255–13269 (2009). DOI: `10.1364/OE.17.013255`. *Cited on page 80.*

[224] Henderson, S., Mitchell, S. and Bartlett, P. Position correlation microscopy: probing single particle dynamics in colloidal suspensions. *Colloids and Surfaces A: Physicochemical and Engineering Aspects* **190**(1-2): 81–88 (2001). DOI: `10.1016/S0927-7757(01)00667-7`. *Cited on page 82.*

[225] Yao, A., Tassieri, M., Padgett, M. and Cooper, J. Microrheology with optical tweezers. *Lab on a Chip* **9**(17): 2568–2575 (2009). DOI: `10.1039/b907992k`. *Cited on pages 82 & 148.*

[226] Schäffer, E., Norrelykke, S.F. and Howard, J. Surface forces and drag coefficients of microspheres near a plane surface measured with optical tweezers. *Langmuir* **23**(7): 3654–3665 (2007). DOI: `10.1021/la0622368`. *Cited on page 83.*

[227] Tolić-Nørrelykke, I.M., Berg-Sørensen, K. and Flyvbjerg, H. MatLab program for precision calibration of optical tweezers. *Computer Physics Communications* **159**(3): 225–240 (2004). DOI: `10.1016/j.cpc.2004.02.012`. *Cited on pages 84 & 117.*

[228] Wright, W.H., Sonek, G.J. and Berns, M.W. Parametric study of the forces on microspheres held by optical tweezers. *Applied Optics* **33**(9): 1735–1748 (1994). DOI: `10.1364/AO.33.001735`. *Cited on page 84.*

[229] Wright, A.J., Wood, T.A., Dickinson, M.R., Gleeson, H.F. and Mullin, T. The transverse trapping force of an optical trap: factors affecting its measurement. *Journal of Modern Optics* **50**(10): 1521–1532 (2003). DOI: `10.1080/09500340308235226`. *Cited on page 84.*

[230] Bartlett, P. and Henderson, S. Three-dimensional force calibration of a single-beam optical gradient trap. *Journal of Physics: Condensed Matter* **14**(33): 7757 (2002). DOI: `10.1088/0953-8984/14/33/314`. *Cited on pages 85 & 144.*

[231] Felgner, H., Müller, O. and Schliwa, M. Calibration of light forces in optical tweezers. *Applied Optics* **34**(6): 977–982 (1995). DOI: `10.1364/AO.34.000977`. *Cited on pages 85 & 143.*

[232] MATLAB version 7.12.0.635 (R2011a). Natick, Massachusetts: The MathWorks Inc., 2011. *Cited on pages 85 & 133.*

[233] Tam-Chang, S.W. and Huang, L. Chromonic liquid crystals: properties and applications as functional materials. *Chemical Communications* **44**(17): 1957–1967 (2008). DOI: `10.1039/B714319B`. *Cited on page 87.*

[234] Vertogen, G. and de Jeu, W.H. Thermotropic Liquid Crystals, Fundamentals, volume 45 of *Springer Series in Chemical Physics* (Springer Verlag, Berlin, 1988). Pages 5; 78 (in citation order). *Cited on pages 88 & 94.*

[235] de Gennes, P.G. and Prost, J. The Physics of Liquid Crystals. The International Series on Monographs on Physics (Oxford University Press, 1993), second edition. Pages 10; 43 (in citation order). *Cited on pages 88 & 94.*

[236] Collings, P.J. and Hird, M. (editors). Introduction to Liquid Crystals: Chemistry and Physics. The Liquid Crystal Book Series (CRC Press, Taylor & Francis Group, 1997). Pages 228-233; 195-200; 32; 202-210 (in citation order). *Cited on pages 88, 90 & 94.*

[237] Oswald, P. and Pieranski, P. Nematic and Cholesteric Liquid Crystals: Concepts and Physical Properties Illustrated by Experiments. The Liquid Crystals Book Series (CRC Press, Taylor & Francis Group, 2005). Pages 87-92; 108-113; 206-207 (in citation order). *Cited on pages 90, 95 & 101.*

[238] Demus, D., Goodby, J.W., Gray, G.W., Spiess, H.W. and Vill, V. (editors). Physical Properties of Liquid Crystals (Wiley-VCH Verlag GmbH, 1999). DOI: `10.1002/9783527613946`. Pages 352-354. *Cited on page 91.*

[239] Blinov, L.M. Structure and Properties of Liquid Crystals (Springer, 2011), first edition. Pages 199; 278 (in citation order). *Cited on pages 94 & 99.*

[240] Marquis, F., Meystre, P., Wright, E.M. and Kaplan, A.E. Dynamics of the optical Freedericksz transition. *Physical Review A* **36**(2): 875 (1987). DOI: `10.1103/PhysRevA.36.875`. *Cited on page 95.*

[241] Yamamoto, R. Simulating Particle Dispersions in Nematic Liquid-Crystal Solvents. *Physical Review Letters* **87**(7): 075502 (2001). DOI: `10.1103/PhysRevLett.87.075502`. *Cited on page 96.*

[242] Anderson, V.J., Terentjev, E.M., Meeker, S.P., Crain, J. and Poon, W.C.K. Cellular solid behaviour of liquid crystal colloids 1. Phase separation and morphology. *The European Physical Journal E: Soft Matter and Biological Physics* **4**(1): 11–20 (2001). DOI: `10.1007/PL00013680`. *Cited on pages 96 & 167.*

[243] Saleh, B.E. and Teich, M.C. Fundamentals of Photonics (Wiley, Hoboken, N.J. :, 2007), second edition. Page 179. *Cited on pages 97, 110 & 186.*

[244] Merck Sharp and Dohme Limited. Hertford Road, Hoddesdon, Hertfordshire, EN11 9BU, UK. *Cited on pages 98, 183 & 192.*

[245] Polysciences Europe GmbH. Handelsstrasse 3, D-69214 Eppelheim, Germany. *Cited on pages 99 & 113.*

[246] Fisher Scientific UK Limited (Part of Thermo Fisher Scientific). Bishop Meadow Road, Loughborough, Leicestershire, LE11 5RG, UK. *Cited on page 99.*

[247] Goodman, A.M. Optical interference method for the approximate determination of refractive index and thickness of a transparent layer. *Applied Optics* **17**(17): 2779–2787 (1978). DOI: `10.1364/AO.17.002779`. *Cited on page 100.*

[248] Leica Microsystems. Davy Avenue, Knowhill, Milton Keynes, Buckinghamshire, MK5 8LB, UK. *Cited on pages 103 & 105.*

[249] CVI Melles Griot. 200 Dorado Place SE, Albuquerque, NM 87123, USA. *Cited on page 103.*

[250] Laser Quantum UK. Emery Court, Vale Road, Stockport, Cheshire, SK4 3GL, UK. *Cited on page 103.*

[251] Edmund Optics. Unit 1, Opus Avenue, Nether Poppleto, York, YO26 6BL, UK. *Cited on page 105.*

[252] Carl Zeiss Ltd. P O Box 78, Welwyn Garden City, Hertfordshire, AL7 1LU, UK. *Cited on pages 105 & 107.*

[253] Prior Scientific Instruments Ltd. 3-4 Fielding Industrial Estate, Wilbraham Road, Fulbourn, Cambridge, CB21 5ET, UK. *Cited on pages 106 & 114.*

[254] National Instruments (NI) Corporation (UK) Ltd. Measurement House, Newbury Business Park, London Road, Newbury, Berkshire, RG14 2PZ, UK. *Cited on pages 106 & 190.*

[255] Wright, A.J. Factors affecting the characterisation of an optical trap using the viscous drag force method. Ph.D. thesis, The University of Manchester (2004). *Cited on pages 106, 110, 114 & 134.*

[256] Allied Vision Technologies GmbH (previously Prosilica). Taschenweg 2a, 07646 Stadtroda, Germany. *Cited on pages 107 & 118.*

[257] Apple Sales International. Hollyhill Industrial Estate, Hollyhill, Cork, Republic of Ireland. *Cited on pages 107 & 118.*

[258] Cargille Laboratories. 55 Commerce Road, Cedar Grove, NJ 07009, USA. *Cited on pages 107 & 114.*

[259] Hibbs, A.R. Confocal Microscopy for Biologists (Springer, 2004). Chapter 2: Understanding Microscopy. *Cited on pages 108, 109 & 195.*

[260] Rohrbach, A. and Stelzer, E.H.K. Trapping forces, force constants, and potential depths for dielectric spheres in the presence of spherical aberrations. *Applied Optics* **41**(13): 2494–2507 (2002). DOI: `10.1364/AO.41.002494`. *Cited on page 109.*

[261] GSI Lumonics. Cosford Lane, Swift Valley, Rugby, Warwickshire, CV21 1QN, UK. *Cited on page 110.*

[262] Hecht, E. Optics (Addison Wesley Longman, Inc., Reading, Mass. :, 1998), third edition. Pages 159, 248 and 271. *Cited on page 112.*

[263] Fischer, P., Carruthers, A.E., Volke-Sepulveda, K., Wright, E. M. Brown, C.T.A., Sibbett, W. and Dholakia, K. Enhanced optical guiding of colloidal particles using a supercontinuum light source. *Optics Express* **14**(12): 5792–5802 (2006). DOI: `10.1364/OE.14.005792`. *Cited on page 112.*

[264] Wheeler, B. and Wilson, L.J. Practical Forensic Microscopy: A Laboratory Manual (John Wiley & Sons, 2008). Page 194. *Cited on page 113.*

[265] Gittes, F. and Schmidt, C.F. Interference model for back-focal-plane displacement detection in optical tweezers. *Optics Letters* **23**(1): 7–9 (1998). DOI: `10.1364/OL.23.000007`. *Cited on page 115.*

[266] Roithner LaserTechnik. Wiedner Hauptstrasse 76, 1040 Vienna, Austria. *Cited on page 116.*

[267] Olympus Microscopy. KeyMed House, Stock Road, Southend-on-Sea, Essex, SS2 5QH. *Cited on page 117.*

[268] Mathworks. Matrix House, Cambridge Business Park, Cambridge, CB4 0HH, UK. *Cited on page 117.*

[269] Hansen, P.M., Tolić-Nørrelykke, I.M., Flyvbjerg, H. and Berg-Sørensen, K. tweezercalib 2.1: Faster version of MatLab package for precise calibration of optical tweezers. *Computer Physics Communications* **175**(8): 572–573 (2006). DOI: `10.1016/j.cpc.2006.07.009`. *Cited on page 117.*

[270] Crocker, J.C. and Grier, D.G. Methods of Digital Video Microscopy for Colloidal Studies. *Journal of Colloid and Interface Science* **179**(1): 298–310 (1996). DOI: `10.1006/jcis.1996.0217`. *Cited on pages 117 & 120.*

[271] Zhang, Z. and Menq, C.H. Three-dimensional particle tracking with subnanometer resolution using off-focus images. *Applied Optics* **47**(13): 2361–2370 (2008). DOI: `10.1364/AO.47.002361`. *Cited on page 117.*

[272] Silburn, S.A., Saunter, C.D., Girkin, J.M. and Love, G.D. Multidepth, multiparticle tracking for active microrheology using a smart camera. *Review of Scientific Instruments* **82**(3): 033712–6 (2011). DOI: `10.1063/1.3567801`. *Cited on page 117.*

[273] Perch-Nielsen, I., Rodrigo, P. and Glückstad, J. Real-time interactive 3D manipulation of particles viewed in two orthogonal observation planes. *Optics Express* **13**(8): 2852–2857 (2005). DOI: 10.1364/OPEX.13.002852. *Cited on page 117.*

[274] Bowman, R., Preece, D., Gibson, G.M. and Padgett, M.J. Stereoscopic particle tracking for 3D touch, vision and closed-loop control in optical tweezers. *Journal of Optics* **13**(4): 044003 (2011). DOI: 10.1088/2040-8978/13/4/044003. *Cited on page 117.*

[275] Bowman, R. The University of Glasgow, Personal Communication (2009-2011). *Cited on pages 120 & 135.*

[276] Kuo, S.C. A Simple Assay for Local Heating in Optical Tweezers. In M.P. Sheetz (editor), Methods in Cell Biology (Academic Press, Harcourt Brace & Company, San Diego, 1998), volume 55, 43–45. DOI: 10.1016/S0091-679X(08)60401-X. *Cited on page 124.*

[277] Osterman, N. TweezPal – Optical tweezers analysis and calibration software. *Computer Physics Communications* **181**(11): 1911–1916 (2010). DOI: 10.1016/j.cpc.2010.07.024. *Cited on page 124.*

[278] Berg-Sørensen, K. and Flyvbjerg, H. Power spectrum analysis for optical tweezers. *Review of Scientific Instruments* **75**(3): 594–612 (2004). DOI: 10.1063/1.1645654. *Cited on page 128.*

[279] Deng, Y., Bechhoefer, J. and Forde, N.R. Brownian motion in a modulated optical trap. *Journal of Optics A: Pure and Applied Optics* **9**(8): S256–S263 (2007). DOI: 10.1088/1464-4258/9/8/S20. *Cited on page 128.*

[280] Vermeulen, K.C., Wuite, G.J.L., Stienen, G.J.M. and Schmidt, C.F. Optical trap stiffness in the presence and absence of spherical aberrations. *Applied Optics* **45**(8): 1812–1819 (2006). DOI: 10.1364/AO.45.001812. *Cited on pages 138, 140 & 142.*

[281] Dienerowitz, M., Gibson, G., Bowman, R. and Padgett, M. Holographic aberration correction: optimising the stiffness of an optical trap deep in the sample. *Optics Express* **19**(24): 24589–24595 (2011). DOI: 10.1364/OE.19.024589. *Cited on page 142.*

[282] Viana, N.B., Rocha, M.S., Mesquita, O.N., Mazolli, A., Neto, P.A.M. and Nussenzveig, H.M. Towards absolute calibration of optical tweezers. *Physical Review E* **75**(2): 021914 (2007). DOI: 10.1103/PhysRevE.75.021914. *Cited on page 145.*

[283] Bormuth, V., Jannasch, A., Ander, M., van Kats, C.M., van Blaaderen, A., Howard, J. and Schaffer, E. Optical trapping of coated microspheres. *Optics Express* **16**(18): 13831–13844 (2008). DOI: 10.1364/OE.16.013831. *Cited on page 146.*

[284] Brau, R.R., Ferrer, J.M., Lee, H., Castro, C.E., Tam, B.K., Tarsa, P.B., Matsu-daira, P., Boyce, M.C., Kamm, R.D. and Lang, M.J. Passive and active microrheology with optical tweezers. *Journal of Optics A: Pure and Applied Optics* **9**(8): S103–S112 (2007). DOI: `10.1088/1464-4258/9/8/S01`. *Cited on pages 148, 149, 151, 158, 159, 160, 191 & 192.*

[285] Cheng, N.S. Formula for the Viscosity of a Glycerol–Water Mixture. *Industrial & Engineering Chemistry Research* **47**(9): 3285–3288 (2008). DOI: `10.1021/ie071349z`. *Cited on pages 148, 149, 155, 156, 157, 161 & 191.*

[286] Trejo González, J.A., Longinotti, M.P. and Corti, H.R. The Viscosity of Glycerol–Water Mixtures Including the Supercooled Region. *Journal of Chemical & Engineering Data* **56**(4): 1397–1406 (2011). DOI: `10.1021/je101164q`. *Cited on page 148.*

[287] Guzmán, C., Flyvbjerg, H., Köszali, R., Ecoffet, C., Forró, L. and Jeney, S. In situ viscometry by optical trapping interferometry. *Applied Physics Letters* **93**(18): 184102–3 (2008). DOI: `10.1063/1.3020713`. *Cited on pages 149, 153, 191, 194 & 201.*

[288] Sigma-Aldrich Company Ltd. The Old Brickyard, New Road, Gillingham, Dorset, SP8 4XT, UK. *Cited on page 150.*

[289] Peterman, E.J.G., Gittes, F. and Schmidt, C.F. Laser-Induced Heating in Optical Traps. *Biophysical Journal* **84**(2): 1308–1316 (2003). DOI: `10.1016/S0006-3495(03)74946-7`. *Cited on pages 155, 158, 162 & 191.*

[290] Weast, R.C. (editor). CRC Handbook of Chemistry and Physics (CRC Press, Cleveland, Ohio, 1973), 53rd edition. *Cited on page 159.*

[291] Blinov, L.M. and Chigrinov, V.G. Electrooptic Effects in Liquid Crystal Materials (Springer, New York, 1994). *Cited on page 164.*

[292] Yu, T.C., Lo, Y.L. and Huang, R.R. Determination of azimuthal anchoring strength in twisted nematic liquid crystal cells using heterodyne polarimeter. *Optics Express* **18**(20): 21169–21182 (2010). DOI: `10.1364/OE.18.021169`. *Cited on page 165.*

[293] Poulin, P. and Weitz, D.A. Inverted and multiple nematic emulsions. *Physical Review E* **57**(1): 626–637 (1998). DOI: `10.1103/PhysRevE.57.626`. *Cited on page 167.*

[294] Muševič, I. Optical manipulation and self-assembly of nematic colloids: colloidal crystals and superstructures. *Liquid Crystals Today* **19**(1): 2–12 (2010). DOI: `10.1080/13583140903395947`. *Cited on page 174.*

[295] Tkalec, U., Ravnik, M., Čopar, S., Žumer, S. and Muševič, I. Reconfigurable Knots and Links in Chiral Nematic Colloids. *Science* **333**(6038): 62–65 (2011). DOI: `10.1126/science.1205705`. *Cited on page 174.*

[296] Nieminen, Timo, A., Loke, V.L.Y., Stilgoe, A.B., Knoner, G., Branczyk, A.M., Heckenberg, N.R. and Rubinsztein-Dunlop, H. Optical tweezers computational toolbox. *Journal of Optics A: Pure and Applied Optics* **9**(8): S196 (2007). DOI: `10.1088/1464-4258/9/8/S12`. *Cited on pages 175 & 178.*

[297] Davis, C.D. Lasers and Electro-Optics: Fundamentals and Engineering (Cambridge University Press, 1996). Page 369. *Cited on page 195.*

[298] Lacey, A.J. Light Microscopy in Biology: A Practical Approach (Oxford University Press, 1999), second edition. Pages 7-10 and 31. *Cited on page 195.*

[299] Otto, O., Czerwinski, F., Gornall, J.L., Stober, G., Oddershede, L.B., Seidel, R. and Keyser, U.F. Real-time particle tracking at 10,000 fps using optical fiber illumination. *Optics Express* **18**(22): 22722–22733 (2010). DOI: `10.1364/OE.18.022722`. *Cited on page 197.*

[300] Hariharan, P. Optical holography : principles, techniques, and applications. Cambridge studies in modern optics (Cambridge University Press, 1986). *Cited on page 199.*

[301] Burnham, D.R. Microscopic applications of holographic beam shaping and studies of optically trapped aerosols. Ph.D. thesis, The University of St. Andrews (2009). *Cited on page 199.*

[302] Hamamatsu Photonics UK Ltd. 2 Howard Court, 10 Tewin Road, Welwyn Garden City, Hertfordshire, AL7 1BW, UK. *Cited on page 199.*

[303] Casabella, S. The University of Manchester, Personal Communication (2011-2012). *Cited on page 200.*

[304] Lagerwall, J.P.F. and Scalia, G. Carbon nanotubes in liquid crystals. *Journal of Materials Chemistry* **18**(25): 2890–2898 (2008). DOI: `10.1039/B802707B`. *Cited on page 202.*

[305] Schymura, S., Kühnast, M., Lutz, V., Jagiella, S., Dettlaff-Weglikowska, U., Roth, S., Giesselmann, F., Tschierske, C., Scalia, G. and Lagerwall, J. Towards Efficient Dispersion of Carbon Nanotubes in Thermotropic Liquid Crystals. *Advanced Functional Materials* **20**(19): 3350–3357 (2010). DOI: `10.1002/adfm.201000539`. *Cited on page 202.*

[306] Lee, W.M., Reece, P.J., Marchington, R.F., Metzger, N.K. and Dholakia, K. Construction and calibration of an optical trap on a fluorescence optical microscope. *Nature Protocols* **2**(12): 3226–3238 (2007). DOI: `10.1038/nprot.2007.446`. *Cited on pages 231 & 233.*

Appendices

Appendix A

Optical Alignment

It is imperative to obtain good alignment of the trapping beam and thus, the optical trap itself, so as to avoid any trap anisotropy which will affect results. Aberrations, such as spherical aberrations, astigmatism and coma, will limit the trap stiffness obtainable. Lee *et al.* [306] detail the construction and calibration of a laser tweezers system integrated with a fluorescence microscope. For comparison, this appendix details the expected images when the laser tweezers system used in this thesis is well aligned.

A.1   Alignment procedure

This section details the alignment procedure of the laser tweezing system used in this thesis, as shown in Fig. 4.1 on p. 104.

1. Remove all lenses from the optical beam path. Removing lens L4 will significantly improve the liklihood of achieving successful alignment. For this, the back of the microscope can be removed* and lens L4 can be unscrewed and removed completely.

2. Setup a periscope to obtain an optical beam height of 15.5 cm (not shown in Fig. 4.1).

3. Setup the beam steering mirrors (static or galvo-mirrors) to direct the laser trapping beam into the back port of the inverted optical microscope.

---

* Take care if removing the back of the microscope as the electronics for the microscope are housed here.

4. Use minimal laser power to verify constant beam height and no horizontal deviations throughout the optical beam path using an IR card reader and/or an IR viewfinder.

5. To verify correct vertical and horizontal alignment (again, using minimal power), an auxiliary mirror can be placed at the location where the microscope objective screws into place (into one of the holes of the revolving sextuple nosepiece) and above the **closed** aperture[†] immediately above the condenser lens. The reflection of the laser beam from this auxiliary mirror is directed towards the CMOS camera at the side port to allow observation of adjustments in real time. Ensure the laser beam hits the centre of the mirror at each point it is placed in the optical beam path. It is also possible to place the CMOS camera at the top port of the microscope, also using the Leica $0.5 \times$ HC TV adapter, for additional alignment verification. Remember, the side port slider (right hand side of the microscope body) should be in the appropriate position for directing the laser beam to either the side or top port; 'ON' and 'OFF', respectively.

6. Reinsert each lens individually and re-align the beam as in step 4, where it is advantagous to start with lenses L4 and L3 (the beam expander) in this order. For laser safety purposes, be aware of where each lens brings the beam to a focus. Some useful points to note:

   ▷ Lens L4 is mounted within a threaded tube with a length of 4.5 cm, thereby allowing its position along the optic axis to be adjusted by unscrewing it from the back of the microscope. For the beam expander to produce a collimated beam, the distance between lenses L3 and L4 should be the sum of their focal lengths; 235 mm.

   ▷ Replace the back of the microscope and fine-tune the distance between lenses L3 and L4 using the micrometer stage on which L3 is mounted.

7. Ensure the trapping beam after the beam expander is collimated and correctly expanded to slightly overfill the back aperture of the microscope objective ($\varnothing$ 5 mm). This can be problematic as the beam is now directed upwards after being reflected by the dichroic hot mirror (DM).

8. Finally, insert the microscope objective and an isotropic sample, e.g. water (with or without beads), to observe the trapping beam in the sample plane.

[†] The mirror is likely to drop through the aperture if it is open.

▷ Figure A.1 shows images of a slightly *aberrated* laser trapping beam focussed at the coverslip-water interface (top) and at increasing trap depths Z_T, with and without the illumination beam. The aberrations present are spherical, coma and astigmatism. Further adjustments to the optical alignment would produce a diffraction-limited spot, completely free of aberrations. See reference [306] for further details.

▷ Figure A.2 shows images of a $6\,\mu$m PS bead optically trapped at $P_T = 122 \pm 3\,$mW using the slightly aberrated beam shown in Fig. A.1. The
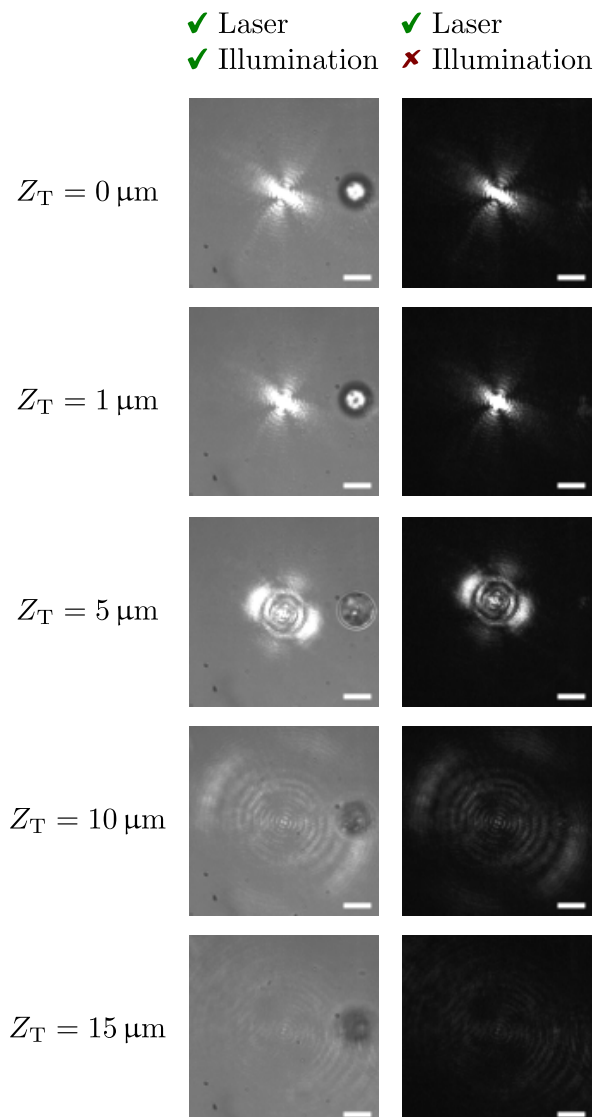
Figure A.1: Images of the laser trapping beam focussed at the coverslip-water interface (top) and at increasing trap depths; $Z_T = 1, 5, 10, 15\,\mu$m, with and without the illumination beam. The scale bar represents $5\,\mu$m.

sequence shows the trapped bead close to the coverslip-water interface and at increasing trap depths, with alternative combinations of illumination and trapping beam visible.
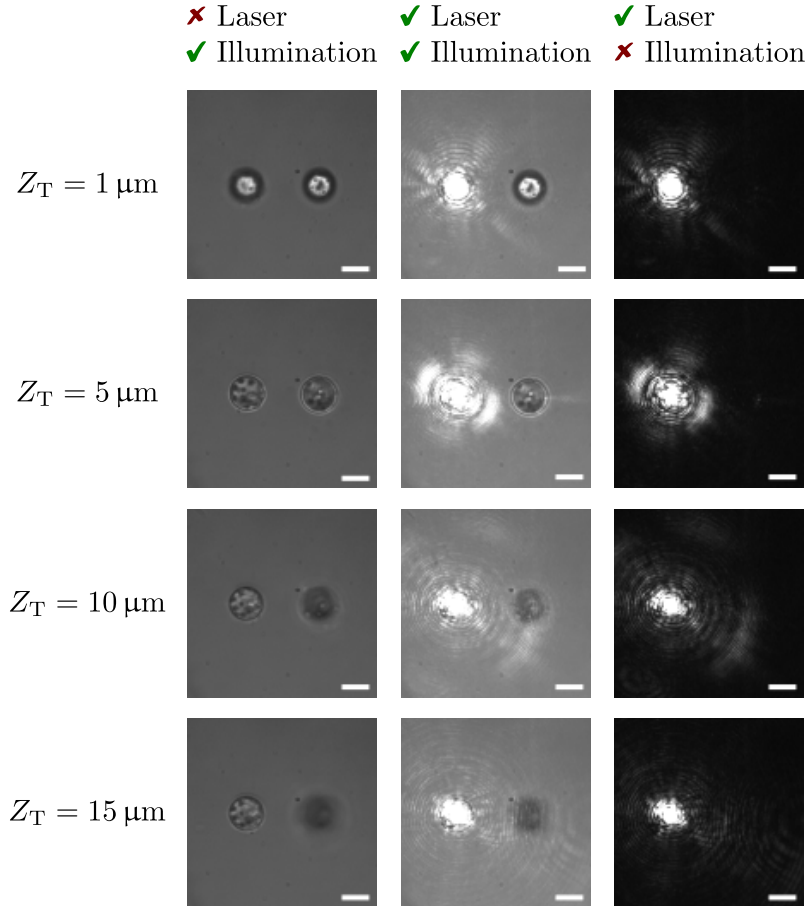
Figure A.2: Images of a $6\,\mu m$ PS bead optically trapped at $P_T = 122 \pm 3\,\text{mW}$ close to the coverslip-water interface at a trap depth of $1\,\mu m$, and at increasing trap depths; $Z_T = 5, 10, 15\,\mu m$, with alternative combinations of the illumination and laser trapping beam visible. The scale bar represents $5\,\mu m$.

Appendix B

Royal Society Discussion Meeting Paper

This appendix includes a proof of the discussion meeting paper associated with Royal Society Discussion Meeting, New frontiers in anisotropic fluid-particle composites in June 2012. The paper, entitled 'Pushing, pulling and twisting liquid crystal systems; exploring new directions with laser manipulation', will be published in a future issue of Philosophical Transactions of the Royal Society A: Mathematical, Physical and Engineering Sciences.

Pushing, pulling and twisting liquid crystal systems; exploring new directions with laser manipulation

Jennifer L Sanders, Yiming Yang, Mark R Dickinson and Helen F Gleeson [*]

School of Physics and Astronomy and The Photon Science Institute,
The University of Manchester, Manchester M13 9PL, UK

Optical tweezers are exciting tools with which to explore liquid crystal systems; the motion of particles held in laser traps through liquid crystals is perhaps the only approach that allows a low Ericksen number regime to be accessed. This offers a new method of studying the microrheology associated with micron-sized particles suspended in liquid crystal media — and such hybrid systems are of increasing importance as novel soft-matter systems. This paper describes the microrheology experiments that are possible in nematic materials and discusses the sometimes unexpected results that ensue. It also presents observations made in the inverse system; micron-sized droplets of liquid crystal suspended in an isotropic medium. Also touched upon are the remarkable light-induced changes in chirality that result in a micron-sized opto-mechanical transducer.

Keywords: Optical tweezers; liquid crystals; microfluidics; microrheology; viscosity

1. Introduction

Trapping and moving micron-sized particles in liquid crystals has provided a unique way of studying some of the fundamental properties of colloidal liquid crystal systems. In particular, this experimental approach allows the study of forces between colloidal particles in liquid crystals, the measurement of elasticity of defects, and the anisotropic viscosity coefficients of liquid crystals in the low Ericksen regime (in which the director configuration is considered not to be influenced by the particle motion) to be deduced. Rather few nematic materials have been studied using this approach, but we describe the viscosity coefficients that have been deduced for two different materials. There are two main methods of measuring viscosity; either through the release of a particle from a trap which moves at different speeds, or from an analysis of particle tracking via a power spectral density measurement.

The inverse experiment, in which micron-sized liquid crystalline droplets are held in laser traps with specific polarisation properties, allows the transfer of angular momentum to the droplets. A torque is imparted to a birefringent particle held in an optical trap through the phase shift experienced by the transmitted light. Fast, optically driven switches, rotating at speeds in excess of 1 kHz, can readily be produced from nematic droplets held in a circularly polarised beam. This paper examines some of the unexpected observations caused by nonlinear interactions of the liquid crystalline material with the trapping field. However, we have also shown that a chiral nematic

---

[*]Author for correspondence (helen.gleeson@manchester.ac.uk)

1

Jennifer Louise Sanders   236

droplet can, in some special circumstances, undergo continuous rotation in a *linearly* polarised trap, a phenomenon that is the result of optically-induced changes in chirality of the system. We touch on this remarkable effect, which results in an optically driven transducer.

2. Laser manipulation

Optical trapping, as a means to manipulate and study micron-sized dielectric particles, has advanced significantly since the first steps towards the technology were taken more than 40 years ago by Arthur Ashkin [1]. Since the successful demonstration of the first single-beam optical trap for dielectric particles by Ashkin *et al.* in 1986 [2], 'optical tweezers' — the popular name when referring to optical trapping — have become one of the most popular techniques employed for manipulating such particles and determining their characteristics, resulting in the proliferation of further innovative optical trapping technologies. The range of optical tweezing applications is rapidly growing, with the current focus on biological and microanalytical systems as well as the integration of optical tweezers with already well established investigative techniques [3].

The scope of achievements with optical tweezers continues to grow as the technique progresses alongside and in partnership with contemporary technology. The technique has seen phenomenal interest; at the time of writing, Ashkin's 1986 paper [2] had been cited more than 2,300 times! In addition, there have been several publications geared towards undergraduates understanding and experimenting with optical tweezers [4–6], illustrating the acceptance of the technique into mainstream optics.

At the start of 2011, a publication detailed the use of an Apple iPad — a thin, tablet computer controlled via a multi-touch display — to control multiple particles with laser tweezers [7], known as the *iTweezers* interface. At the end of 2011, researchers in Germany developed a microscopic heat engine; a Stirling engine, whose piston mechanism is powered by an optically trapped particle [8].

(a)   Basic principles

The magnitude of the force exerted by a laser beam with power P travelling through a medium with a refractive index $\bar{n}$ is given by

$$F = \frac{\bar{n}P}{c}Q(\delta n) \tag{2.1}$$

where Q is the optical trapping efficiency; a dimensionless constant of proportionality which can be thought of as the fraction of incident power used to exert an optical force. Q accounts for beam parameters, such as spot size, wavelength, and beam profile; and optical properties of the trapped particle, including its size, shape and mass, and refractive index relative to the surrounding medium, δn [9–11]. In the case of liquid crystals, $\bar{n}$ is an average refractive index of the ordinary and extraordinary refractive indices, n_o and n_e, respectively, given by $\bar{n} = \sqrt{2n_o^2 + n_e^2/3}$.

An optical trap is analogous to a Hookean spring where the particle behaves like an overdamped harmonic oscillator for small displacements and the optical potential is harmonic about the equilibrium position. The optical restoring force in one dimensions if given by $\mathbf{F}_{\mathrm{T}} = -\kappa\mathbf{x}$, where κ is the optical trap stiffness, and is analogous to the spring constant [4]. As such, $\mathbf{F}_{\mathrm{T}}$ acts to counteract the particle's displacement and restore it to an equilibrium position at the centre of the optical trap.

2

1
2
3
4
5
6
7
8
9
10
11
12
13
14
15
16
17
18
19
20
21
22
23
24
25
26
27
28
29
30
31
32
33
34
35
36
37
38
39
40
41
42
43
44
45
46
47
48
49
50
51
52
53
54
55
56
57
58
59
60

(b)   Optical setup

The optical layout for all experiments, built around a commercially available Leica inverted optical microscope, is shown in figure 1, which can be divided into five components; (a) optical tweezers, (b) microscope optics, (c) illumination, (d) visual tracking and (e) photodetection systems.
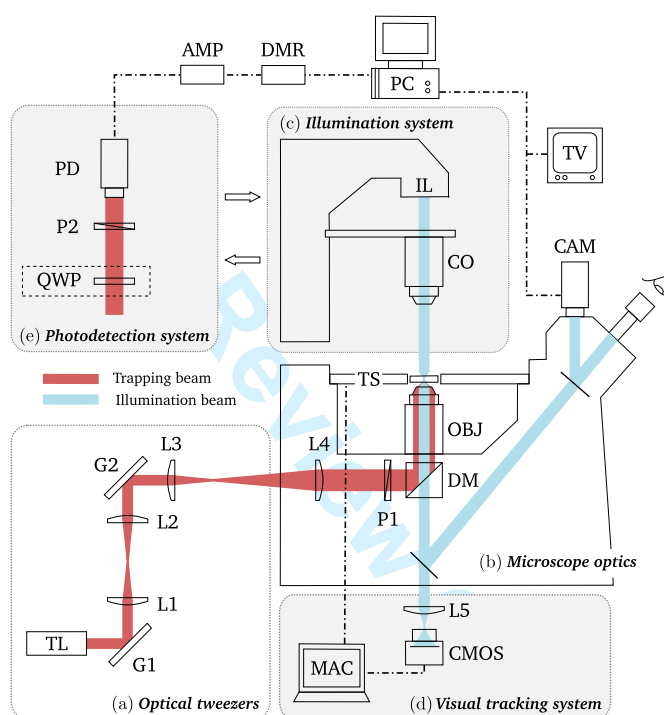
Figure 1: (*Online version in colour*) A schematic of the optical setup split up into five components. (a) *Optical tweezers*: 1064 nm wavelength trapping laser (TL), beam expansion and beam steering lenses (L1–L4), and galvanometer-controlled mirrors (G1,G2) with computer control. (b) *Microscope optics*: A dichroic mirror (DM) directs the trapping beam to the 100× oil-immersion microscope objective lens (OBJ) with numerical aperture NA = 1.30. The trapping beam is tightly focussed into the sample attached to a translation stage (TS). The axial position of OBJ can be altered using a manual focus control or joystick. (c) *Illumination system*: The illumination beam (IL) is directed to the sample via a condenser lens (CO). Both trapping and illumination beams are directed towards a viewing eyepiece and camera (CAM). (d) *Visual tracking system*: For dielectric particles dispersed in liquid crystal, a CMOS camera is linked to an Apple Mac for high-speed imaging and particle tracking. The Mac is also used for controlling the lateral position of TS and the axial position of OBJ. All control software is written in LabVIEW. (e) *Photodetection system*: a quarter-wave plate (QWP), two linear polarisers (P1,P2) and photodetector (PD) are used for detection of liquid crystal droplets. An amplifier (AMP) and discriminator (DMR) circuit connects the system to a PC for data acquisition. The illumination and photodetection systems are interchangeable, denoted by arrows. *See text for further details.*

3

The optical trapping system employs a diode-pumped solid-state, Nd:YVO$_4$ laser operating at a wavelength of 1064 nm. The optical trap is created by tightly focussing the trapping beam, achieved using a microscope objective with a high numerical aperture NA of 1.30. A dichroic mirror, which selectively reflects radiation above 700 nm, directs the trapping beam towards the objective. The position of the beam in the trapping plane is controlled using galvanometer-controlled mirrors (G1, G2) and the position of the optical trap focus is controlled using stepper motors. The trapping beam is expanded to slightly overfill the back aperture of the microscope objective to ensure the maximum gradient force is produced at the centre of the optical trap.

The sample is illuminated using a 100 W halogen bulb directed through a condenser lens. The sample can then be imaged using a digital camera, TV monitor and PC monitor or the human eye. The sample plane can also be imaged via a CMOS camera, EC 1280 manufactured by Prosilica (now Allied Vision Technologies) and an Apple Mac laptop screen which comprise the visual tracking system used for high-speed particle tracking. High-speed CMOS cameras can record the positions of multiple particles in real-time simultaneously, offering frame rates reaching several kHz by controlling the field of view, and are relatively low-cost. They also provide an accuracy reaching the thermal limit [12]. Programs were written in LabVIEW to track particles and perform real-time analysis.

The illumination system can be replaced by the photodetection system, developed to detect and characterise the rotation of optically trapped liquid crystal droplets. The system consists of two linear polarisers (P1, P2) optimised for 1064 nm, and a photodetector. The first polariser P1 is placed in the optical train prior to the sample to generate an optical trap with a high degree of linear polarisation. An amplifier and discriminator circuit connects the system to a PC where the LabVIEW interface is used for measuring light transmitted through the droplet. A quarter-wave plate (QWP) can be inserted to measure the Stokes' parameters.

3.   Anisotropic viscosity in liquid crystals

Defining LC characteristics plays a particularly significant role in improving LCD technologies [13]. For example, determining a twisted nematic LC's rotational viscosity coefficient or describing fluid flow, or '*back-flow*', effects [14] are critical for improving LCD efficiency since they influence the device's response times. Computer models for predicting back-flow effects often require several anisotropic viscosity coefficients, termed '*back-flow coefficients*', which can be determined via their relation to shear viscosity coefficients measurable in classical flow experiments [14, 15]. The effect of back-flow has itself been employed to optically trap colloids [16], illustrating that progress in understanding both LC back-flow and optical trapping in LCs can be mutually beneficial.

In the past, viscosity coeffcients have been determined by studying LC flow through a capillary via the application of a magnetic field and observing pressure differences [17, 18]. Pasechnik *et al.* [15] employed a decay flow method; inducing shear flow with optically controlled pressure differences, to determine back-flow viscosities for the LC mixture MLC-6609. For the majority of new LCs generated for LCD technology, research often focuses upon determining LC refractive indices whilst other quantities, including viscosity coefficients, remain unknown. Ignoring such back-flow effects in LCDs allows poor prediction of their functionality and limits progress.

Established techniques of liquid crystal research conduct macroscopic investigations since they examine the bulk liquid crystal. Therefore, there is a strong call for microscopic, local investigations. Research involving LC-colloidal dispersions expands the knowledge and understanding of LCs and

4

their anisotropic nature.

As in isotropic fluids, viscosity in LCs can be determined by observing the viscous, or Stokes, drag experienced by a particle moving through a fluid [19–21]. The Stokes drag is highly non-linear for particles in a nematic solvent; the colloid (acting as a quadrupole) finds it easier to diffuse parallel to $\hat{n}$ than perpendicular to it [22, 23]. Further research by Verhoeff *et al.* [24] quantised this direction-dependent Stokes drag. They demonstrated that for a colloid moving through a nematic LC, the viscous drag parallel to $\hat{n}$ was larger than the drag perpendicular to $\hat{n}$ by a factor of two. Gleeson *et al.* [20] employed the viscous drag technique with optical tweezers to measure the effective viscosities of LC mixture MLC-6648 for motion parallel and perpendicular to it. The values allowed inference of the anchoring strength of colloidal particles within the LC mixture which was in good agreement with prediction.

Passive methods of determining liquid crystal viscosity, such as observing the anisotropic Brownian motion of colloids in liquid crystalline media by analysing associated power spectra in the frequency domain, have remained largely underrepresented in the literature until recently [25]. Exploration is warranted into the idea that passive methods could be employed to understand and characterise the behaviour of viscoelastic media, including LCs.

The relationship between $\hat{n}$ and the nematic LC's fluid velocity, termed '*nematodynamics*', is described by the Ericksen-Leslie equations which include five independent Leslie coefficients α_i where $i = 1, 2, ...5$. Solutions to these equations are paramount for determining LCD switching times. These are typically calculated by determining effective viscosities in shear flow experiments; applying shear to a LC sample cell, in which $\hat{n}$ is aligned electrically or magnetically.

The effective viscosity η, of a LC medium is given by

$$\eta(\theta, \phi) = \eta_1 \sin^2 \theta \cos^2 \phi + \eta_2 \cos^2 \theta + \eta_3 \sin^2 \theta \sin^2 \phi + \eta_{12} \sin^2 \theta \cos^2 \theta \cos^2 \phi \qquad (3.1)$$

where the three principal anisotropic viscosity coefficients, η_1, η_2 and η_3 are also known as the Mięsowicz viscosity coefficients, and are concerned with back-flow effects in a LC and thus, switching times of an LC device. Here, η_{12} is the anisotropic viscosity coefficient associated with $\hat{n}$ not being parallel to either shear flow v or its gradient ∇v. Figure 2 illustrates the definition of effective viscosity in terms of $\hat{n}$ relative to v and ∇v.

In a 3D scenario, the anisotropic viscosity coefficients η_1 and η_3 occur simultaneously and are inseparable, so are given by effective viscosity $\eta_{\text{eff}}^{\perp}$ whilst η_2 is given by $\eta_{\text{eff}}^{\parallel}$.
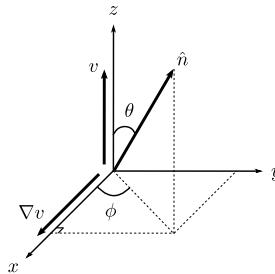

Figure 2: Orientation of the LC director $\hat{n}$ relative to the flow velocity v and flow velocity gradient ∇v.

5

Experiments with optical tweezers allow measurement of $\eta_{\text{eff}}^{\perp}$ and $\eta_{\text{eff}}^{\parallel}$ for example, by observing three dimensional position fluctuations of an optically trapped colloid immersed in the LC. For a homeotropic cell, fluctuations occurring in the z direction are parallel to $\hat{n}$, whilst those in the x and y directions are both perpendicular to $\hat{n}$. In a planar cell, fluctuations in the z direction are perpendicular to $\hat{n}$. Depending on the orientation of the planar cell, either the x or y will be parallel to $\hat{n}$.

(a)   Materials and Methods

Details of the optical tweezing of polystrene and silica beads dispersed in different liquid crystal mixtures with homeotropic and planar alignment are given below. Active and passive measurement techniques were employed to determine the anisotropic viscosities of the LC mixtures; the viscous drag force method and power spectral analysis, where these are described below. More specifically, this allowed determination of effective anistropic shear viscosity coefficients. The experiments employed the optical tweezing system shown in figure 1, specifically (a) optical tweezers, (b) microscope optics, (c) illumination system and (d) visual tracking system.

Active microviscometry

The escape force is the minimum force required to cause a particle of radius r to escape from the optical trap, defined as

$$\mathbf{F}_{\text{esc}} = 6\pi\eta r \mathbf{v}_{\text{esc}} \tag{3.2}$$

where $\mathbf{v}_{\text{esc}}$ is the velocity of the surrounding fluid, or in this case the sample stage, when the particle is released from the optical trap. At this point, $\mathbf{F}_{\text{esc}}$ is considered as the maximum trapping force proportional to the maximum displacement $\mathbf{F}_{\text{max}} = -\kappa \mathbf{x}_{\text{max}}$. $\mathbf{F}_{\text{esc}}$ can be equated to equation 2.1 to measure $\mathbf{v}_{\text{esc}}$ as a function of P, thus allowing determination of η.

Passive microviscometry

The power spectrum (PS) of an optically trapped particle's Brownian motion as a function of frequency f is given by

$$S(f) = \frac{k_B T}{\pi^2 \gamma \left(f_c^2 + f^2 \right)} \tag{3.3}$$

where k_B is Boltzmann's constant, T is temperature and the drag coefficient $\gamma = 6\pi\eta r$. The corner frequency f_c describes a characteristic roll frequency $f_c = \kappa/2\pi\gamma$. For frequencies $f \ll f_c$, the particle is confined by the optical trap and the PS remains approximately constant. Whereas, for frequencies $f \gg f_c$, the particle experiences only Brownian motion and as such, $S(f)$ is proportional to $1/f^2$ giving a slope of -2, as expected for free diffusion. Equation 3.3 has an approximate Lorentzian profile in which the two distinct regions can be seen.

It is possible to employ this analysis to determine the viscosity of the medium in which the particle is optically trapped as given by

$$\eta = \frac{k_B T}{12\pi^2 r \langle x^2 \rangle f_c} \tag{3.4}$$

6

where $\langle x^2 \rangle$ is the particle's positional variance, or the distribution of positions visited by the trapped particle during thermal fluctuations [26]. It is possible to obtain $\langle x^2 \rangle$ from either a histogram of positions visited by the particle, which has a Gaussian distribution, or the autocorrelation function at short time scales. The drag coefficient $\gamma = 6\pi\eta r$ has been incorporated into equation 3.4.

Ericksen number E_r

In a liquid crystal, the contribution of elastic forces to the Stokes' viscous drag force can be quantified using the Ericksen number $E_r = \alpha_4 v_\infty r / 2K_i$, where v_∞ and r are velocity and length scales e.g. the velocity and radius of a colloid immersed in the NLC, α_4 is a Leslie coefficient and K_i is a Frank elastic coefficient. At low Ericksen number $E_r \ll 1$, elastic forces exceed viscous forces and so any elastic distortions of the LC director $\hat{n}$ due to the flow field i.e. the particle's motion, are considered negligible.

The Ericksen number can be minimised by controlling the velocity length scale v_∞. In active viscous drag force experiments, the translation stage was moved at a maximum speed of $70\,\mu\text{m/s}$. In passive microviscometry, v_∞ is calculated as the speed of the particle's Brownian motion. With characteristic values of $K_i \sim 10\,\text{pN}$ and $\alpha_4 \sim 10^{-2}\,\text{Ns/m}^2$, maximum values of E_r are given in table 1. Thus, the chosen LC-colloid combinations facilitates experiments in the low Ericksen number regime, $E_r \ll 1$.

Liquid crystal cells

The LC cells used in this work consist of microspheres dispersed in aligned nematic LC mixture at relatively low concentrations $< 5\%$ solids by weight. The specifications of the chosen LCs and colloids are also given in table 1.

Table 1: Details of chosen liquid crystals (Merck) and particles. The Ericksen number is calculated for the viscous drag (VD) and power spectrum (PS) methods. Refractive indices are measured at $589\,\text{nm}$.

LC	material	radius r (μm)	refractive index n	VD	PS	n_o	n_e	$\bar{n}$	flow viscosity η (cP)
MLC-6648	silica	2	1.56	0.04	0.54	1.476	1.546	1.515	19
MLC-6609	polystyrene	6	1.59	0.06	0.29	1.474	1.551	1.515	20

The LC-colloid suspension is sandwiched between two coverslips, separated by Capton spacers and sealed with UV sensitive glue. The LC cell is adhered to a microscope slide using nail varnish. Cell thickness h, measured using reflectance spectroscopy, varied between approximately $25\,\mu\text{m}$ and $40\,\mu\text{m}$.

For homeotropic alignment, each coverslip was immersed in a Silane (OTMS) mixture and alignment is verified by heating and cooling the LC-filled cell past its phase transition temperature and observing a conoscopic cross. For planar alignment, Polyimide (PI) is applied and a 'rubbing' technique employed. Alignment is verified by observing minimum and maximum transmission when rotating the LC-filled cell between crossed polarisers.

7

1
2
3
4
5
6
7
8
9
10
11
12
13
14
15
16
17
18
19
20
21
22
23
24
25
26
27
28
29
30
31
32
33
34
35
36
37
38
39
40
41
42
43
44
45
46
47
48
49
50
51
52
53
54
55
56
57
58
59
60

(b)   Results

Figure 3 presents three dimensional power spectra for optically trapped $2\,\mu\text{m}$ silica and $6\,\mu\text{m}$ polystyrene beads dispersed in MLC-6648 and MLC-6609, respectively, for both homeotropic and planar alignment. Each spectra and associated Lorenztian fit are filtered i.e. averaged, over ~ 100 scans and the plots shown are an average of three separate measurements.
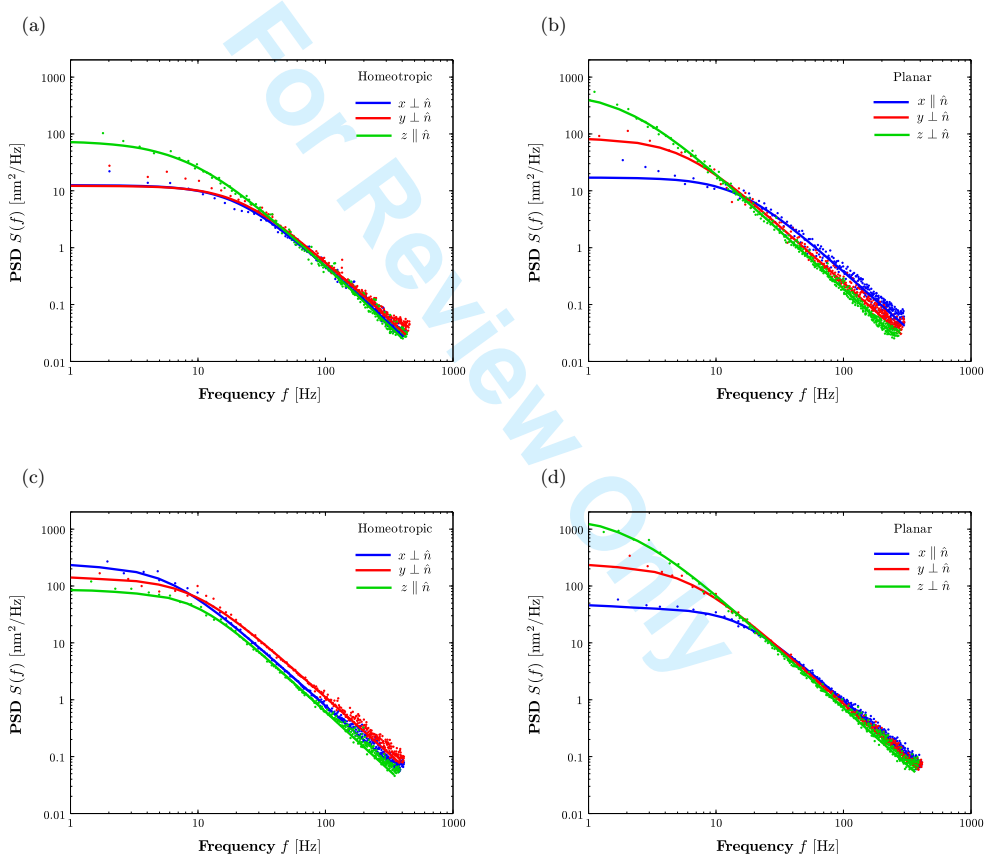

Figure 3: (*Online version in colour*) **MLC-6648**: Power spectra for $2\,\mu\text{m}$ silica beads dispersed in MLC-6648 in a cell with (a) homeotropic and (b) planar alignment. **MLC-6609**: Power spectra for $6\,\mu\text{m}$ polystyrene beads dispersed in MLC-6609 in a cell with (c) homeotropic and (d) planar alignment.

8

MLC-6648

For the homeotropic cell, both the x and y directions are perpendicular to $\hat{n}$ and so both experience $\eta_{\text{eff}}^{\perp}$ which is confirmed by the similarity in power spectra. The z direction is parallel with $\hat{n}$ and would therefore, experience $\eta_{\text{eff}}^{\parallel}$. The difference in power spectra between the three different directions can clearly be seen when comparing the corner frequencies f_c associated with the position fluctuations in each direction, x, y and z. The values of $f_c(x)$ and $f_c(y)$ both exceed $f_c(z)$ by approximately 45%. It is known that since κ_{xy} is always greater than κ_z, and so $f_c(xy) > f_c(z)$. However, we would expect a greater difference between them in water and thus the higher value of $f_c(z)$ suggests the particle is experiencing a reduced viscosity in the z direction.

In comparison, for a cell of MLC-6648 with planar alignment, the x and z directions are parallel to $\hat{n}$ whilst y is perpendicular, producing clearly different PSD plots. This is again evident from the difference in corner frequencies, where $f_c(x) > f_c(y)$, on the order of three times greater, showing that the x and y directions experience an alternative viscosity. Also, $f_c(x) > f_c(z)$ since again, lateral trap stiffness is stronger than axial trap stiffness.

MLC-6609

For the homeotropic cell of MLC-6609, the corner frequencies in all three dimensions are similar. Therefore suggesting that the optically trapped particle experiences a similar effective viscosity $\eta_{\text{eff}}^{\perp}$ in x and y whilst in the z direction, although $\kappa_{xy} > \kappa_z$, this direction experiences a reduced effective viscosity $\eta_{\text{eff}}^{\parallel}$.

For the planar cell of MLC-6609, $f_c(x) > f_c(y) > f_c(z)$. Taking into account the usual differences between lateral and axial κ, this therefore suggests the optically trapped particle experiences a different effective viscosity in the x direction compared with the y and z direction; $\eta_{\text{eff}}^{\parallel}$ and $\eta_{\text{eff}}^{\perp}$, respectively.

Effective viscosities $\eta_{\text{eff}}^{\parallel}$ and $\eta_{\text{eff}}^{\perp}$

Values of $\eta_{\text{eff}}^{\parallel}$ and $\eta_{\text{eff}}^{\perp}$ were determined for homeotropic and planar cells of MLC-6648 and MLC-6609 using both passive and active microviscometry. These results are presented in figure 4 which illustrate the observed anisotropy using both methods. The labels x, y and z correspond to values obtained using the power spectra for that direction, whilst xy denotes the average of x and y i.e. the lateral direction. On average, the value is found to be close to the average bulk viscosity values of each LC.

The results also allow discussion on the anchoring of the LC at the particle surface, described by the ratio $\eta_{\text{eff}}^{\perp}/\eta_{\text{eff}}^{\parallel}$, where calculated values are given in table 2. There is considerable variation in the values where all are high. The results confirm the previous observation from active measurements [20] that strong anchoring is implied, where $\eta_{\text{eff}}^{\perp}/\eta_{\text{eff}}^{\parallel} = 2.0$ for strong anchoring.
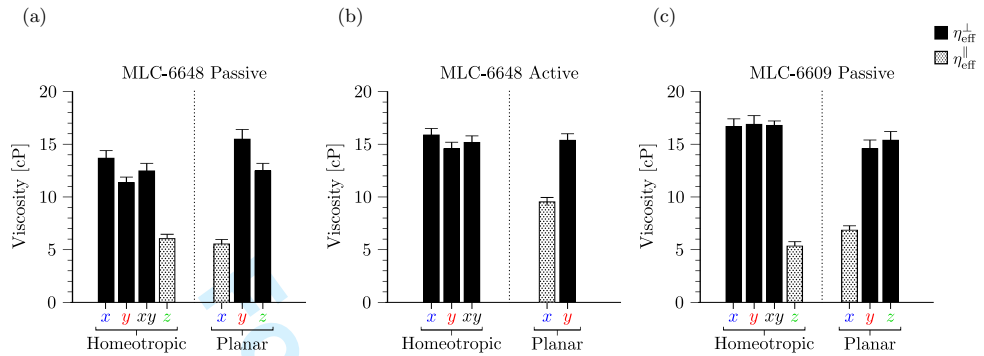
9

Figure 4: (*Online version in colour*) Comparison of effective anisotropic viscosities $\eta_{\text{eff}}^{\perp}$ and $\eta_{\text{eff}}^{\parallel}$ calculated for homeotropic and planar samples of MLC-6648 using (a) passive and (b) active microviscometry, and (c) for samples of MLC-6609 using passive microviscometry. The labels x, y and z correspond to values obtained using the power spectra for that direction, whilst xy denotes the average of x and y i.e. the lateral direction.

Table 2: The ratio $\eta_{\text{eff}}^{\perp}/\eta_{\text{eff}}^{\parallel}$ characterises the strength of the anchoring at the particle surface where a value of 2.0 and 1.3 would correspond to strong and weak homeotropic anchoring, respectively.

LC	passive value		active value	
	homeotropic	planar	homeotropic	planar
MLC-6648	2.0 ± 0.4	2.5 ± 0.2		1.7 ± 0.4
MLC-6609	3.1 ± 0.8	2.2 ± 0.5		

Chain-like structures were observed for $2\,\mu$m silica beads dispersed in MLC-6648 with planar alignment, suggesting the LC molecules are homeotropically aligned at the colloid surface. The particles experience a strong attraction to one another in the direction of $\hat{n}$ and the formation of particle chains lowers the free energy of the system.

It is most likely that a Saturn ring director field is present as these most commonly occur for particles of radii $r < 5\,\mu$m. For this type of director field, the homeotropic surface anchoring is weak, in comparison to topological defects which are due to strong homeotropic anchoring. This creates an isotropic distribution relative to the large convergence angle of the rays impinging upon the particle surface and hence minimises any anisotropy of the trapping forces. This is the reason why one may therefore assume an effective refractive index $\bar{n}$ [27].

Planar anchoring at the particle surface, generates clustering of beads [28]. There was some evidence of this for SC beads in hometropic cells of MLC-6648. The formation of clusters indicates the existence of long-range attractive forces. Although repulsive forces are also present where the particles remain separated. It was possible to trap individual silica beads and detach them from the surrounding particles.

10

Trap stiffness

It is possible to estimate corresponding values of trap stiffness κ using values of f_c and η_{eff}. These are given in table 3. For the data shown in figure 3, values of κ were significantly higher than expected, on the order of 2 times higher, for any of the directions when compared with the same trapping power for a $6\,\mu$m polystyrene bead in water. This discrepancy is unlikely to be due to aberrations of the trapping beam, which has a greater effect in the axial (z) direction.

Similarly, in both isotropic and anisotropic samples, the particle was held away from the coverslip surface ($\sim 10\,\mu$m) so as to minimise any boundary effects. As such, the increased trap stiffness values imply that the influence of the surfaces is much more important for LC systems, and perhaps other non-Newtonian fluids, than for isotropic materials.

Table 3: Values of trap stiffness κ in MLC-6648, MLC-6609 and water determined using passive microviscometry. The symbols denote the material of the trapped particle; silica ($^\triangle$) and polystyrene ($^\diamond$).

material	particle size (μm)	trap stiffness κ (pN/μm)					
		x		y		z	
		homeotropic	planar	homeotropic	planar	homeotropic	planar
MLC-6648	$2\,^\triangle$	32.1 ± 1.5	10.0 ± 1.0	29.2 ± 1.4	10.0 ± 1.0	19.7 ± 1.2	10.6 ± 1.0
MLC-6609	$6\,^\diamond$	36.0 ± 2.6	31.3 ± 2.1	23.0 ± 2.1	17.0 ± 1.4	15.3 ± 1.7	17.0 ± 1.9
Water	$6\,^\diamond$	~ 20		~ 20		~ 7	

4. Rotation of liquid crystal droplets in circularly and elliptically polarised optical tweezers

Advances and understanding of LC emulsions (LCEs) — micro-droplets of LC, coated with a surfactant, dispersed in an isotropic liquid [29] — through optical manipulation establishes the potential of liquid crystals for optically driven micromachines. In a 1996 paper, Tamai, Ito and Masuhara [30] reported second- and third-harmonic generation from optically trapped micron-sized nematic and ferroelectric liquid crystal droplets dispersed in water. This was closely followed in 1999 with Juodkazis *et al.* [31] reporting the rotation of optically trapped nematic liquid crystal droplets with circularly polarised light. Further work by the same group detailed the dependence of rotation frequency on droplet size [32] and the efficiency of optical torque transfer to droplets [33].

There have been several further reports demonstrating optical trapping and rotation of LC droplets in suspension including nematic droplets with circularly polarised light [19, 20, 34], chiral nematic droplets with linearly polarised light [20, 21], dye-doped nematic droplets using circularly and elliptically polarised light [35] and smectic liquid crystal droplets in circularly polarised light [36]. Interestingly, liquid crystal droplets have recently been used to fabricate micron-sized liquid crystal cylinders which were rotated in circularly polarised optical tweezers to measure the viscosity of the composite LC [37].

Spinning LC droplets have also been employed to measure the viscosity of the host medium, such as heavy water D_2O [38, 39]. The trapping laser beam transfers optical torque to the LC droplet and its electric field induces molecular reorganisation within the LC droplet [40]. Gleeson, Wood and Dickinson [20] discussed wave-plate behaviour as the mechanism responsible for observing LC

11

droplet rotation but cited other possible mechanisms for the optical angular momentum transfer, including anisotropic scattering, absorption and the optical Fréedericksz transition. The reasons for the underlying physical processes continue to remain elusive and of interest.

(a)   Materials and Methods

Details of the optical trapping of liquid droplets dispersed in water are given below. Experiments are performed to examine the influence of droplet geometry on trapping and rotation, with circularly and elliptically polarised trapping beams. LC droplets in optical tweezers with a linearly polarised trapping beam were also observed. The experiments employed the optical tweezing system shown in figure 1, specifically (a) optical tweezers, (b) microscope optics, (c) illumination system and (e) photodetection system.

Liquid crystal droplets

For droplets of nematic liquid crystal, E7 from Merck were used. Its high refractive index ($\Delta n = 0.225$) ensured successful optical trapping, since $\mathbf{F}_T$ increases with the droplet's refractive index. For the chiral nematic liquid crystal droplets, related chiral and achiral nematic systems were used; MDA-1444 and MDA-1445[1], also manufactured by Merck. These were chosen as they facilitated preparation of mixtures with a range of pitch lengths, which remained relatively constant as a function of temperature, a change in pitch length on the order of $1\,\mathrm{nm/^\circ C}$.

(b)   Observation of droplet rotation

A liquid crystal is intrinsically birefringent, however the birefringence of a spherical droplet depends significantly on its director configuration. One may consider this a *structural birefingence*, where schematics of the director configurations considered in this work; bipolar, twisted bipolar, radial and Frank-Pryce, are shown in figure 5.

(a)   (b)   (c)   (d)
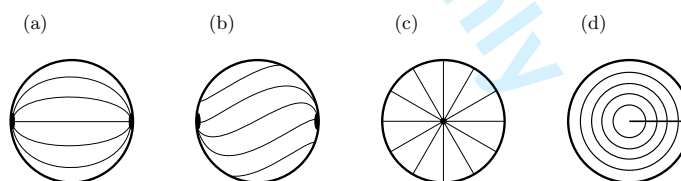
Figure 5: Director configuration of different LC droplet types: (a) bipolar, (b) twisted bipolar, (c) radial and (d) Frank-Pryce.

In circularly and elliptically polarised optical tweezers, nematic and chiral LC droplets were observed to rotate continuously as the beam polarisation direction also varied continuously, as shown in figure 6.

---

[1] Also known as BL131 and BL131a

12

Jennifer Louise Sanders   247
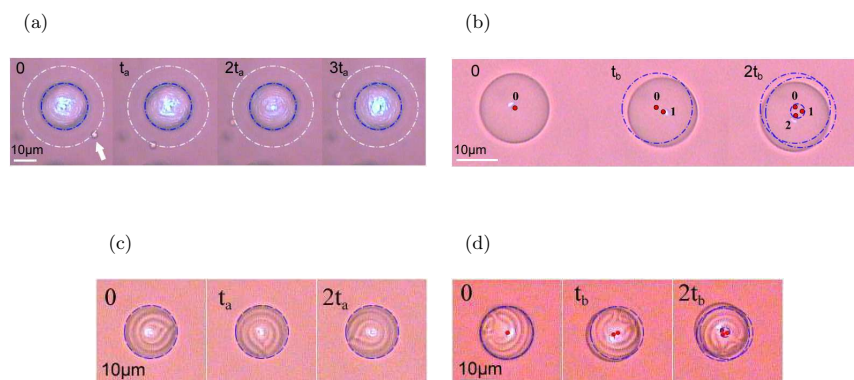
Figure 6: (*Online version in colour*) Time evolution showing the continuous rotation of nematic and chiral nematic liquid crystal droplets in circularly and elliptically polarised optical tweezers. (a) A nematic bipolar droplet rotates about its centre, where a nearby small droplet can be seen orbiting due to their hydrodynamic interaction. (b) The centre of the radial nematic droplet orbits as a circle. (c) A Frank-Pryce droplet rotates about its centre. (d) The centre of a variational Frank-Pryce droplet orbits as a circle in company with its spin rotation.

The bipolar and radial nematic droplet exhibit two different rotation mechanisms; the bipolar droplet spins in the optical trap, whilst the centre radial droplet orbits about a circle. A similar observation is made for chiral nematic droplets. The Frank-Pryce droplet spins in the optical trap in the same way as the bipolar nematic droplet, whilst some chiral droplets adopted a variational Frank-Pryce director structure, whose centre orbited about a circle similar to the radial nematic droplet. Here, the variational structure occurs because the chiral droplet structure is strongly dependent on the ratio between droplet size and pitch length. The structural transition between the twisted bipolar and Frank-Pryce structure is continuous. Finally, the twisted bipolar droplet behaved in the same way as the bipolar nematic droplet.

The rotational axis of droplets is displaced for certain droplets. We can define ℓ as the rotational axis, where $\ell = 0$ for the droplet centre. The optical torque depends on ℓ which defines the passage of light through the droplet. Optical force can be calculated numerically assuming the geometric optics regime. Values of ℓ depend on shape birefringence; the symmetry of the director structure in the droplet. Further details of rotation for each droplet type are given in table 4. The dynamics of the rotating droplet depend on optical torque, moment of inertia and drag as shall be decribed in further detail below.

As shown in figure 7, these observations allow definition of two general types of droplet rotation; (a) the spherical droplet's rotational axis is defined as parallel to the original rotational axis passing through the droplet's centre of mass or (b) the axes are displaced from one another by ℓ ($\ell \geq 0$).

(c)   Optical torque

The resultant optical torque acting upon the droplet due to the birefringent nature of the liquid crystal causes the rotation of the droplet in the optical trap. This optical torque can be quantified

13

Table 4: The rotational dynamics of each droplet type depend on its director configuration. For some droplets, its rotational axis is displaced be a distance ℓ.

| droplet type	rotationally symmetric?	ℓ (from experiment) (μm)	comments
bipolar & twisted bipolar	yes	$\ell \sim 0$	any optical reorientation of director does not break symmetry
radial	yes	$\ell > 0$ ($\sim 1.7\,\mu\text{m}$)	optical reorientation of director breaks symmetry
Frank-Pryce	no	$\ell \sim 0$	break in symmetry due to disclination can be neglected in optical force calculations
variational F-P	no	$\ell > 0$ ($\sim 1.4\,\mu\text{m}$)	significant intrinsic droplet asymmetry
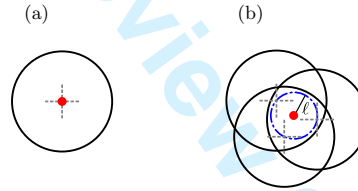
Figure 7: (*Online version in colour*) The rotational axis of a spherical droplet is displaced from the original axis by a distance ℓ. (a) If $\ell = 0$, the rotational axis passes through the droplet's centre of mass. (b) If $\ell \neq 0$, the droplet rotates about a cirle.

by calculating the change in angular momentum between the light incident upon and transmitted through the droplet.

This angular momentum change induces a torque per unit area τ [41];

$$\tau = -\frac{P}{\omega}\sin\Gamma\cos 2\phi\sin 2\theta + \frac{P}{\omega}(1-\cos\Gamma)\sin 2\phi \tag{4.1}$$

where P is the laser power per unit area, ω is its angular frequency, ϕ the degree of ellipticity and θ is the angle between the fast axis of the wave plate producing the elliptically polarised light and the optical axis of the droplet. The torque is dependent on the birefringent material's thickness d as described by the retardation of the emergent light;

$$\Gamma = \frac{2\pi}{\lambda}d\Delta n_{\text{eff}}. \tag{4.2}$$

14

Here, Δn_{eff} represents the effective birefringence; $n_o - n_e$. Thus, the retardation is the phase difference between the light field components experiencing the ordinary n_o and extraordinary n_e refractive indices of the birefringent material. Γ takes into account the droplet's director structure.

The first term in equation 4.1 is the torque due to the linearly polarised component of incident light whilst the second term is due to the change in polarisation of the light emerging from the birefringent material.

The viscosities of the droplet are much greater than that of the surrounding medium, typically and in this case, water. Therefore, the optically driven LC droplet can be regarded as the rotation of a rigid body until the optical torque no longer exists. The optical torque acting on the droplet is given by

$$\tau_d = I\frac{\mathrm{d}\alpha}{\mathrm{d}t} + D\alpha, \tag{4.3}$$

where α is the angular velocity of the droplet, and I and D are the inertia and drag-damping factor of the rotating droplet, respectively. Equation 4.3 describes the droplet's drag-damped rotational behaviour.

The moment of inertia for the droplet depends on the displacement of the parallel axis away from the centre axis; ℓ, and is given by $I_{\text{sphere}} + m\ell^2$. In addition, the drag-damping factor for the rotating droplet in water is given by $D = 8\pi\eta\left(r + \ell\right)^3$, where m and r are the mass and radius of the droplet, and η is the viscosity of the surrounding medium; water. Furthermore, τ_d also depends on ℓ since Γ is affected by each droplet's director configuration. Thus, it is possible to express equation 4.3 as a function of ℓ, $\tau_d(\ell)$, by substituting expressions for I and D.

(d) Optical reorientation of droplet director structure

The optical torque is highly dependent on the optical reorientation of the droplet's director, which, as shown in figure 6, has the ability to break the droplet's rotational symmetry about the optical trapping beam axis. Brasselet *et al.* [40] indicated the optical realignment within the radial droplet depends on the beam polarisation. They show displacement ℓ decreases with increasing beam ellipticity, tending toward zero as ellipticity approaches $\pi/4$ (circular polarisation). Figure 8 illustrates optical reorientation of a bipolar and radial droplet when held in an elliptical optical trap.

The director configuration for all droplet types along the beam axis is shown in figure 9. For the bipolar, twisted bipolar and Frank-Pryce droplets, $\ell = 0$ and is independent of beam polarisation, meaning the beam axis coincides with the rotational axis of the droplet. In these cases, Δn_{eff} is independent of the azimuthal angle ϕ where the $\hat{n}$ vectors lie perpendicular to the beam axis. Therefore, the effective birefringence is $n_a = n_e - n_o$ and so, equation 4.2 can be applied as a simple approximation for these director structures.

Conversely, for a radial droplet, $\ell \neq 0$ and its effective birefringence has a non-trivial expression;

$$\Delta n_{\text{eff}} = \frac{2\pi}{\lambda} \int_{-r\cos\theta_0}^{r\cos\theta_0} \left[\left(\frac{n_o n_e}{\sqrt{n_o^2 \sin^2\theta(z) + n_e^2 \cos^2\theta(z)}} \right) - n_o \right] dz, \tag{4.4}$$

where $\theta_0 = \arcsin(\ell/r)$ and $\theta(z) = \arctan(\ell/z)$, which is the polar angle of the $\hat{n}$ vector depending on the director position z.

15
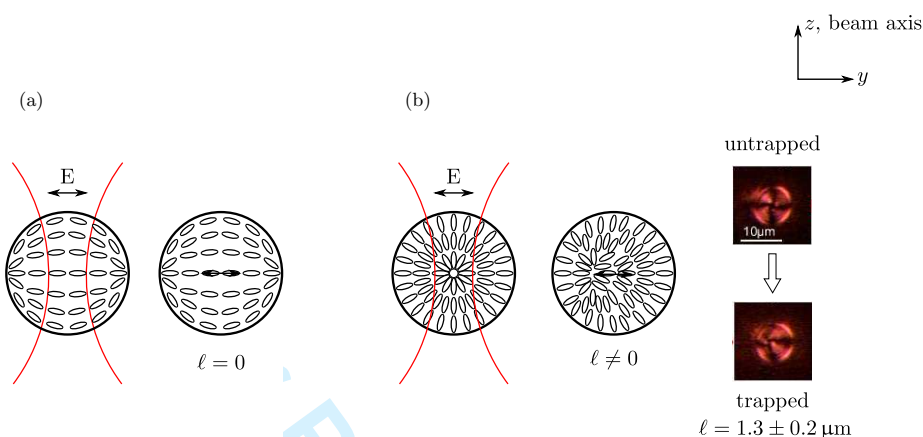
Figure 8: (*Online version in colour*) For a droplet held in an optical trap with elliptic polarisation, optical realignment does not change the symmetry of structure birefringence of (a) a bipolar droplet but causes relocation of the trapping position of (b) a radial droplet, with a displacement of $\ell \cong 1.3\,\mu\text{m}$, for example.

Figure 9: (*Online version in colour*) Director configuration of different LC droplet types when held in an optical trap: (a) bipolar, (b) twisted bipolar, (c) radial and (d) Frank-Pryce. The azimuthal angle is given by ϕ whilst $\theta(z)$ describes the polar angle of the $\hat{n}$ vector .

16

1
2
3
4
5
6
7
8
9
10
11
12
13
14
15
16
17
18
19
20
21
22
23
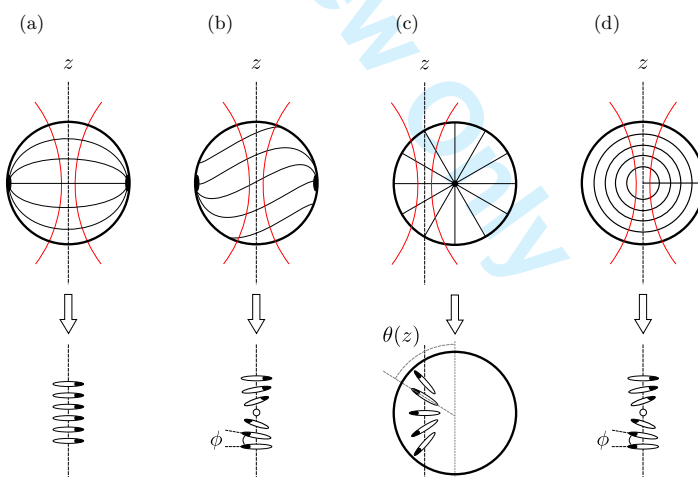24
25
26
27
28
29
30
31
32
33
34
35
36
37
38
39
40
41
42
43
44
45
46
47
48
49
50
51
52
53
54
55
56
57
58
59
60

(e)   Dynamics of droplet rotation: simulation and experiment

It is now possible to utilise the information about the droplet's trapping position ℓ and optical torque $\tau_d(\ell)$ to numerically simulate the dynamics of liquid crystal droplets in optical tweezers. To do so, θ is considered as the cumulative angle with respect to time, such that

$$\theta_i = \sum_0^{i-1} \alpha_i \left(t/N \right) \tag{4.5}$$

where the time period t is divided into N equal, small periods. Here, α_i is the angular velocity of the droplet after the i-th rotation. Substituting equations 4.2 and 4.5 into the expression for the optical torque acting on the droplet (equation 4.3), a general formula which describes the dynamics of the optically trapped droplet is produced;

$$\frac{P}{\omega} \left[-\sin \Gamma_{bi} \cos 2\phi \sin \left(\theta_0 + \sum_0^{i-1} \alpha_i \left(t/N \right) \right) + \left(1 - \cos \Gamma_{bi} \sin 2\phi \right) \right]$$
$$= \left(\frac{2}{5} mr^2 + ml^2 \right) \frac{d\alpha_i}{dt} + 8\pi\eta(r+l)^3 \alpha_n. \tag{4.6}$$

Here, N is the number of samples, θ_0 is the initial angle between the droplet director $\hat{n}$ and the major axis of the polarisation, and ϕ is again, the degree of ellipticity of the trapping beam. The subscript bi denotes bipolar.

The numerical simulations are applied for a bipolar droplet with a trapping power $P = 50\,\text{mW}$ and wavelength $\lambda = 1064\,\text{nm}$ to replicate experimental conditions. The droplet radius $r = 10\,\mu\text{m}$, trapping position $\ell = 0$ and birefringence $\Delta n = 0.2$. The viscosity of water at $20\,^\circ\text{C}$ was used $(1.003\,\text{cP})$ and $\theta_0 = \pi/3$ for all simulations.

The numerical simulations lead to plots of angular velocity α and rotated angular distance Ω as a function of time as shown in figure 10. For a circularly polarised optical trap $(\phi = \pi/4)$, the result indicates the rotational dynamics of the bipolar droplet exhibits a linear behaviour; the droplet rotates at a constant angular velocity α. Therefore, Ω increases linearly with time.

For an elliptically polarised trap $(\phi = \pi/3)$, the rotational dynamics of the bipolar droplet shows unique, non-linear behaviour, where the droplet rotates at a varying angular velocity. Furthermore, the variation in α follows a repeating and regular pattern; fast and slow. This therefore, produces a non-linear increase in Ω.

Measured optical transmission of rotating bipolar droplets in circularly and elliptically polarised optical tweezers are shown in figure 11. The droplet diameters d are $9.7 \pm 0.3\,\mu\text{m}$ and $8.9 \pm 0.3\,\mu\text{m}$, respectively. For circularly polarised optical tweezers, the period of rotation as a function of time is collected to calculate the angular frequency α of the rotating droplet. The experimental result follows the theoretical simulation with the exception of the magnitude of α. However, this discrepancy can be attributed to the experimental droplet being half the size of the simulated droplet.

For the bipolar droplet in elliptically polarised optical tweezers, the experimental result is in good agreement with the theoretical simulation. Let us consider the elliptical beam, which consists of both a linear and circular component. The circular component provides the constant optical torque whilst the linear component offers a varying optical torque depending on θ; the angle between
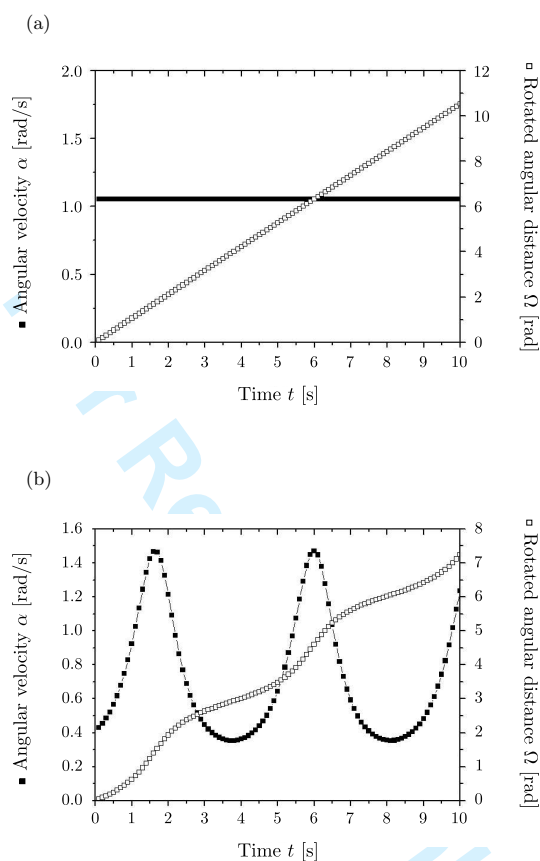
17

(a)

(b)

Figure 10: Mathematical modelling of the behaviour of a bipolar droplet held in an optical trap with (a) circular and (b) elliptical polarisation.

the beam polarisation and droplet director (see equation 4.1). This angle varies between 0 and 2π, thus the first term in equation 4.1 repeats with regular positive/negative values. This implies the optical torque due to the linear component is regularly driving and resisting the droplet's rotation.

Further experiments were conducted to examine how droplet size affected the rotational velocity of the rotating droplet. The numerical simulations were performed and experimental measurements made for bipolar droplets in elliptically polarised optical tweezers. As shown in figure 11(d), the droplet dynamics are characterised by marked non-linear behaviour where experimental measurements agree well with the numerical simulation.
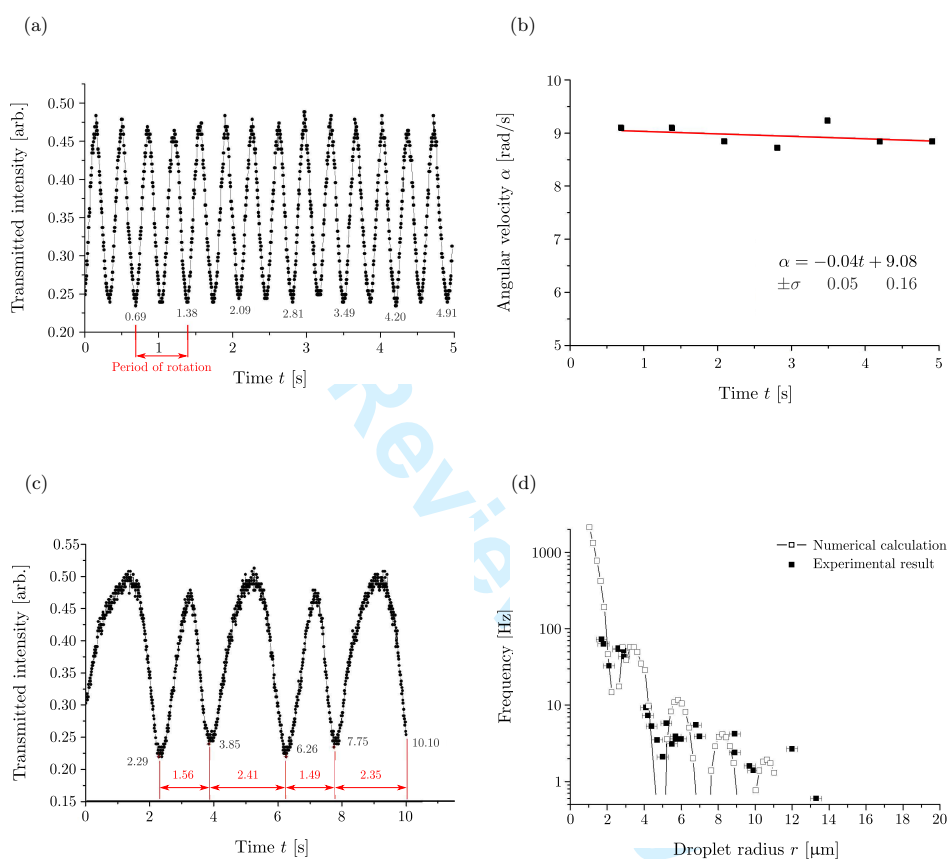
18

Figure 11: (*Online version in colour*) (a) Measured optical transmission of a rotating bipolar droplet in circularly polarised optical tweezers (ellipticity $\phi = \pi/4$). Period of rotation is marked on the figure. Droplet diameter $d = 9.7 \pm 0.3\,\mu$m. (b) Calculated angular velocity from the measured optical transmission of the rotating droplet. A linear fit to the data indicates the angular volcity here is almost constant. (c) Measured optical transmission of a rotating bipolar droplet in the elliptically polarised traps. A repeating fast-slow rotational dynamic is marked by the periodicities. Droplet diameter $d = 8.9 \pm 0.3\,\mu$m. (d) Rotational frequency of nematic bipolar droplets as a function of their radius in elliptically polarised traps ($\phi = \pi/3$). Open squares represent the numerical calculations as detailed in the text and closed squares represent the experimental measurements.

19

APPENDIX B: ROYAL SOCIETY DISCUSSION MEETING PAPER

Submitted to Phil. Trans. R. Soc. A - Issue   Page 20 of 23

5.   Rotation of liquid crystal droplets in linearly polarised optical tweezers

A numerical simulation for a bipolar droplet in linearly polarised optical tweezers ($\phi = 0$) is performed and shown in figure 12, with the same simulation parameters as for circularly and elliptically polarised beams. The simulation illustrates the bipolar droplet rotates for $\pi/3$ for $\sim 1\,\mathrm{s}$ to an equilibirum orientation with no further rotation, as would be observed for a wave plate.
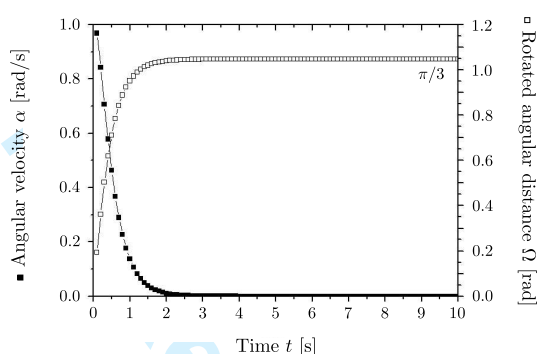

Figure 12: Mathematical modelling of the behaviour of a bipolar droplet held in an optical trap with linear polarisation ($\phi = 0$).

Figure 13 shows the time evolution of a chiral nematic liquid crystal droplet in an optical trap with linear polarisation. It illustrates that the droplet experiences a torque until the droplet's director is aligned with respect to the beam polarisation, which is also observed for a nematic liquid crystal droplet. At this point, $\phi = 0$, and thus, the torque $\tau_d = 0$. In this situation, the extraordinary and ordinary rays no longer deviate into two directions with two alternate velocities.
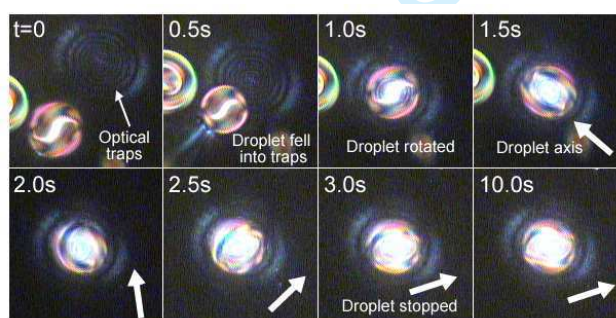
Figure 13: (*Online version in colour*) Time evolution showing the realignment of a chiral nematic liquid crystal droplet in a linearly polarized optical trap. The droplet is trapped near the focus of the laser beam, then rotates in the trap until it stops at around 3.0 s. Here, the ring pattern indicates the position of the optical trap. White arrows represent the droplet axis where the chiral droplet adopts a twisted bipolar structure.

20

A rather different rotation is observed for chiral nematic droplets of a critical size, which adopt a twisted bipolar structure as reported in Yang *et al.* [21]. The equilibrium orientation is related to the configuration of the droplet and so depends on droplet size and the pitch length of the chiral material. The rotation occurs only for small droplets of a critical size and is accompanied by a distinct vertical motion of the droplet in the trap.

The mechanism responsible for the anomalous motion of the chiral droplets is quite different from any previously reported that produces rotation of birefringent particles in optical tweezers. It relies on a photo-induced molecular rotation that induces a critical reorganisation of the liquid crystal in the droplet, followed by elastic relaxation of the photo-induced structure. A cycle of molecular reorganisation and relaxation follows. This fascinating combination of continuous rotation and linear motion when the chiral droplets are held in optical tweezers had not previously been observed and generates interesting implications for optical switching microfluidics.

6.   Conclusions

Liquid crystals and particles are fascinating media and the hybrid systems do far more than merely combine properties.

Microrheology allows measurement of local viscosity in anisotropic systems. In this case, experiments were performed in the low Ericksen number regime, where anisotropy in the liquid crystal's viscosity is observed with passive microviscometry. Values of effective viscosity obtained were close to the bulk viscosity value. However, the results produced unexpectedly high values of trap stiffness. It is possible that surface effects in the liquid crystal cell i.e. the coverslip, are influential. Therefore, it illustrates the importance of understanding how laser manipulation works in non-Newtonian systems.

The rotation of LC droplets leads to the prospect of all-optical switches. The rotation observed here depends on the droplet phase, geometry and polarisation with respect to the trapping beam. The phenomena include rotation on- and off-axes; continuous, uniform rotation; nonlinear rotation; and continual rotation until some equilibrium position is reached. The experimental observations are all readily simulated by a simple model. The novel observation of continuous rotation for specific kinds of N* droplets suggest the opportunity for an opto-mechanical transducer.

References

1 Ashkin, A. 1970 Acceleration and trapping of particles by radiation pressure. *Physical Review Letters* **24**, 156–159. (doi:10.1103/PhysRevLett.24.156).

2 Ashkin, A., Dziedzic, J. M., Bjorkholm, J. E. & Chu, S. 1986 Observation of a single-beam gradient force optical trap for dielectric particles. *Optics Letters* **11**, 288–290. (doi:10.1364/OL.11.000288).

3 Moffitt, J. R., Chemla, Y. R., Smith, S. B. & Bustamante, C. 2008 Recent advances in optical tweezers. *Annual Review of Biochemistry* **77**, 205–228. (doi:10.1146/annurev.biochem.77.043007.090225).

4 Appleyard, D. C., Vandermeulen, K. Y., Lee, H. & Lang, M. J. 2007 Optical trapping for undergraduates. *American Journal of Physics* **75**, 5–14. (doi:10.1119/1.2366734).

5 Rocha, M. S. 2009 Optical tweezers for undergraduates: Theoretical analysis and experiments. *American Journal of Physics* **77**, 704–712. (doi:10.1119/1.3138698).

21

6 Mas, J., Farré, A., Cuadros, J., Juvells, I. & Carnicer, A. 2011 Understanding optical trapping phenomena: A simulation for undergraduates. *Education, IEEE Transactions on* **54**, 133–140. (doi:10.1109/TE.2010.2047107).

7 Bowman, R. W., Gibson, G., Carberry, D., Picco, L., Miles, M. & Padgett, M. J. 2011 iTweezers: optical micromanipulation controlled by an Apple iPad. *Journal of Optics* **13**, 044002. (doi:10.1088/2040-8978/13/4/044002).

8 Blickle, V. & Bechinger, C. 2011 Realization of a micrometre-sized stochastic heat engine. *Nature Physics* **8**, 143–146. (doi:10.1038/nphys2163).

9 Simpson, N. B., McGloin, D., Dholakia, K., Allen, L. & Padgett, M. J. 1998 Optical tweezers with increased axial trapping efficiency. *Journal of Modern Optics* **45**, 1943 – 1949. (doi:10.1080/09500349808231712).

10 Wright, W. H., Sonek, G. J. & Berns, M. W. 1994 Parametric study of the forces on microspheres held by optical tweezers. *Applied Optics* **33**, 1735–1748. (doi:10.1364/AO.33.001735).

11 Wright, A. J., Wood, T. A., Dickinson, M. R., Gleeson, H. F. & Mullin, T. 2003 The transverse trapping force of an optical trap: factors affecting its measurement. *Journal of Modern Optics* **50**, 1521–1532. (doi:10.1080/09500340308235226).

12 Gibson, G. M., Leach, J., Keen, S., Wright, A. J. & Padgett, M. J. 2008 Measuring the accuracy of particle position and force in optical tweezers using high-speed video microscopy. *Optics Express* **16**, 14561–14570. (doi:10.1364/OE.16.014561).

13 Miesowicz, M. 1983 Liquid crystals in my memories and now – the role of anisotropic viscosity in liquid crystals research. *Molecular Crystals and Liquid Crystals* **97**, 1–11. (doi:10.1080/00268948308073137).

14 Smith, N. J., Tillin, M. D. & Sambles, J. R. 2002 Direct optical quantification of backflow in a 90 degrees twisted nematic cell. *Physical Review Letters* **88**, 088301. (doi:10.1103/PhysRevLett.88.088301).

15 Pasechnik, S. V., Chigrinov, V. G., Shmeliova, D. V., Tsvetkov, V. A. & Voronov, A. N. 2004 Anisotropic shear viscosity in nematic liquid crystals: new optical measurement method. *Liquid Crystals* **31**, 585–592. (doi:10.1080/02678290410001667371).

16 Mieda, Y. & Furutani, K. 2006 Micromanipulation method using backflow effect of liquid crystals. In *2006 IEEE International Symposium on Micro-NanoMechatronics and Human Science* pp. 208–213. Nagoya, JAPAN. (doi:10.1109/MHS.2006.320279).

17 Kneppe, H. & Schneider, F. 1981 Determination of the viscosity coefficients of the liquid-crystal mbba. *Molecular Crystals and Liquid Crystals* **65**, 23–37. (doi:10.1080/00268948108076128).

18 Graf, H. H., Kneppe, H. & Schneider, F. 1992 Shear and rotational viscosity coefficients of two nematic liquid crystals. *Molecular Physics: An International Journal at the Interface Between Chemistry and Physics* **77**, 521–538. (doi:10.1080/00268979200102591).

19 Wood, T. A., Gleeson, H. F., Dickinson, M. R. & Wright, A. J. 2004 Mechanisms of optical angular momentum transfer to nematic liquid crystalline droplets. *Applied Physics Letters* **84**, 4292–4294. (doi:10.1063/1.1753067).

20 Gleeson, H. F., Wood, T. A. & Dickinson, M. 2006 Laser manipulation in liquid crystals: an approach to microfluidics and micromachines. *Philosophical Transactions of the Royal Society A: Mathematical, Physical and Engineering Sciences* **364**, 2789–2805. (doi:10.1098/rsta.2006.1855).

21 Yang, Y., Brimicombe, P. D., Roberts, N. W., Dickinson, M. R., Osipov, M. & Gleeson, H. F. 2008 Continuously rotating chiral liquid crystal droplets in a linearly polarized laser trap. *Optics Express* **16**, 6877–6882. (doi:10.1364/OE.16.006877).

22 Stark, H. & Ventzki, D. 2002 Non-linear Stokes drag of spherical particles in a nematic solvent. *EPL (Europhysics Letters)* **57**, 60. (doi:10.1209/epl/i2002-00541-0).

23 Loudet, J. C., Hanusse, P. & Poulin, P. 2004 Stokes drag on a sphere in a nematic liquid crystal. *Science* **306**, 1525–1525. (doi:10.1126/science.1102864).

24 Verhoeff, A. A., van Rijssel, J., de Villeneuve, V. W. A. & Lekkerkerker, H. N. W. 2008 Orientation dependent Stokes drag in a colloidal liquid crystal. *Soft Matter* **4**, 1602–1604. (doi:10.1039/b804236e).

25 Sanders, J. L., Dickinson, M. R. & Gleeson, H. F. 2010 Laser tweezers for determining anisotropic viscosity coefficients of nematic liquid crystals. In *Optical Trapping and Optical Micromanipulation VII*

22

volume 7762 pp. 776221–9. San Diego, California, USA: SPIE. (doi:10.1117/12.862853).

26 Keen, S., Leach, J., Gibson, G. & Padgett, M. J. 2007 Comparison of a high-speed camera and a quadrant detector for measuring displacements in optical tweezers. *Journal of Optics A: Pure and Applied Optics* **9**, S264–S266. (doi:10.1088/1464-4258/9/8/S21).

27 Smalyukh, I., Lavrentovich, O. D., Kuzmin, A. N., Kachynski, A. V. & Prasad, P. N. 2005 Elasticity-mediated self-organization and colloidal interactions of solid spheres with tangential anchoring in a nematic liquid crystal. *Physical Review Letters* **95**, 157801. (doi:10.1103/PhysRevLett.95.157801).

28 Poulin, P. & Weitz, D. A. 1998 Inverted and multiple nematic emulsions. *Physical Review E* **57**, 626–637. (doi:10.1103/PhysRevE.57.626).

29 Pasechnik, S. V., Chigrinov, V. G. & Shmeliova, D. V. 2009 *Liquid Crystals*. Germany: Wiley-VCH. (doi:10.1002/9783527627660). P. 170.

30 Tamai, N., Ito, T. & Masuhara, H. 1996 Second- and third-harmonic generation from optically trapped liquid crystal droplet. *Japanese Journal of Applied Physics Part 2: Letters* **35**, L547–L550. (doi:10.1143/JJAP.35.L547).

31 Juodkazis, S., Shikata, M., Takahashi, T., Matsuo, S. & Misawa, H. 1999 Fast optical switching by a laser-manipulated microdroplet of liquid crystal. *Applied Physics Letters* **74**, 3627–3629. (doi:10.1063/1.123203).

32 Juodkazis, S., Shikata, M., Takahashi, T., Matsuo, S. & Misawa, H. 1999 Size dependence of rotation frequency of individual laser trapped liquid crystal droplets. *Japanese Journal of Applied Physics Part 2: Letters* **38**, L518–L520. (doi:10.1143/JJAP.38.L518).

33 Juodkazis, S., Matsuo, S., Murazawa, N., Hasegawa, I. & Misawa, H. 2003 High-efficiency optical transfer of torque to a nematic liquid crystal droplet. *Applied Physics Letters* **82**, 4657–4659. (doi:10.1063/1.1588366).

34 Murazawa, N., Juodkazis, S., Matsuo, S. & Misawa, H. 2005 Control of the molecular alignment inside liquid-crystal droplets by use of laser tweezers. *Small* **1**, 656–661. (doi:10.1002/smll.200500038).

35 Manzo, C., Paparo, D., Marrucci, L. & Janossy, I. 2006 Light-induced rotation of dye-doped liquid crystal droplets. *Physical Review E* **73**, 051707. (doi:10.1103/PhysRevE.73.051707).

36 Murazawa, N., Juodkazis, S. & Misawa, H. 2006 Laser manipulation of a smectic liquid-crystal droplet. *European Physical Journal E* **20**, 435–439. (doi:10.1140/epje/i2006-10033-1).

37 Ito, K. & Kimura, M. 2010 Optically induced rotation of microcylinders made of photopolymerizable nematic liquid crystal. *Japanese Journal of Applied Physics* **49**, 040208. (doi:10.1143/JJAP.49.040208).

38 Murazawa, N., Juodkazis, S., Jarutis, V., Tanamura, Y. & Misawa, H. 2006 Viscosity measurement using a rotating laser-trapped microsphere of liquid crystal. *Europhysics Letters* **73**, 800–805. (doi:10.1209/epl/i2005-10457-7).

39 Murazawa, N., Juodkazis, S., Tanamura, Y. & Misawa, H. 2006 Rheology measurement at liquid-crystal water interface using laser tweezers. *Japanese Journal of Applied Physics Part 1: Regular Papers Brief Communications and Review Papers* **45**, 977–982. (doi:10.1143/JJAP.45.977).

40 Brasselet, E., Murazawa, N., Juodkazis, S. & Misawa, H. 2008 Statics and dynamics of radial nematic liquid-crystal droplets manipulated by laser tweezers. *Physical Review E* **77**, 041704. (doi:10.1103/PhysRevE.77.041704).

41 Friese, M. E. J., Nieminen, T. A., Heckenberg, N. R. & Rubinsztein-Dunlop, H. 1998 Optical alignment and spinning of laser-trapped microscopic particles. *Nature* **394**, 348–350. (doi:10.1038/28566).

23